Gap materials interaction with femtosecond lasers in GHz-burst mode

Pierre Balage

THÈSE PRÉSENTÉE

POUR OBTENIR LE GRADE DE

DOCTEUR DE L'UNIVERSITÉ DE BORDEAUX

ÉCOLE DOCTORALE

SCIENCES PHYSIQUES ET DE L'INGENIEUR

Spécialité : Laser, Matière et Nanosciences

Par Pierre BALAGE

ETUDE DE L'INTERACTION DES MATERIAUX A GAP AVEC DES LASERS FEMTOSECONDES EN MODE RAFALE GHz

Sous la direction de : Inka MANEK-HÖNNINGER

Soutenue le 19 septembre 2024

Membres du jury :

Stefan NOLTE	Professeur	IAP, Jena	Rapporteur
Razvan STOIAN	Directeur de Recherche	LHC, St-Etienne	Rapporteur
Ottavia JEDRKIEWICZ	Docteure	CNR- IFN, Como	Examinatrice
Philippe BALCOU	Directeur de Recherche	CELIA, Bordeaux	Président
Inka MANEK-HÖNNINGER	Professeure	CELIA, Bordeaux	Directrice
John LOPEZ	Ingénieur de Recherche	CELIA, Bordeaux	Membre invité

French summary

I. Contexte scientifique :

L'usinage et la modification en volume de matériaux à gap constituent un enjeu majeur pour l'industrie, en particulier pour l'opto- et la micro-électronique. La brièveté des impulsions femtosecondes permet d'obtenir une grande qualité d'usinage en minimisant les effets collatéraux et confère la capacité unique de travailler en volume par absorption non-linéaire. Ce travail de thèse, purement expérimental, se concentre sur l'exploration des potentialités du nouveau mode rafale GHz pour la transformation des matériaux à gap et la compréhension des mécanismes d'interaction laser-matière spécifiques. Dans ce mode, chaque impulsion laser de forte intensité est remplacée par une rafale constituée de nombreuses impulsions de faible intensité à haute cadence. Le nouveau régime d'interaction qui en découle est basé sur un effet d'accumulation thermique hautement efficace résultant de la cadence GHz au sein de la rafale. Il permet de modifier, voire ablater, les matériaux même pour des intensités inférieures au seuil d'ablation. Il permet en outre de diminuer les effets de propagation non linéaires dans les matériaux diélectriques et de maximiser le dépôt d'énergie au voisinage du point focal.

II. Démarches utilisées :

1. Stations d'usinage :

Ces travaux ont été menés en collaboration étroite avec deux partenaires industriels, l'entreprise Amplitude et le centre technologique ALPhANOV. Dans ce cadre de la collaboration avec Amplitude, l'entreprise met à disposition du CELIA une source laser femtoseconde prototype développé sur une base Tangor 100 pouvant opérer en mode mono-impulsion répétitives, en mode rafale MHZ ou en mode rafale GHz (Figure 1).

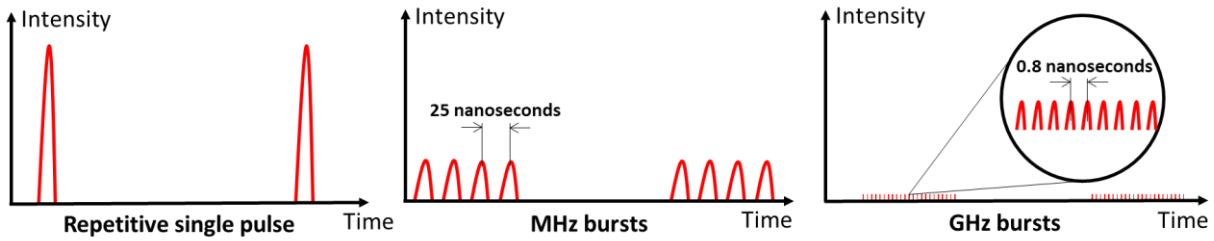

Figure 1. Représentation des trois régimes accessibles via notre laser.

Le premier mode correspond à des mono-impulsions successives, dans ce cas, l'intensité laser est contenue dans des impulsions très énergétiques ayant une faible cadence, typiquement jusqu'à quelques MHz. Le mode rafale MHz consiste à répartir l'énergie de chaque impulsion en une rafale de plusieurs impulsions de plus faible intensité avec une cadence intra-rafale MHz. Le mode rafale GHz est similaire au précédent avec une cadence intra-rafale GHz. Autour de ce système laser, nous avons développé deux stations de micro-usinage laser, la première avec une focalisation de faisceau Gaussien pour l'ablation et le perçage (Figure 2 (a)), et-la seconde avec une focalisation type faisceau de Bessel pour la découpe de verre (Figure 2(b)). La première station utilise une tête de focalisation fixe équipée de deux miroirs dichroïques, une lumière blanche et une caméra ce qui permet la visualisation de l'échantillon par le dessus. La seconde station est équipée d'un module de découpe de verre par faisceau

de Bessel. Ce dernier est une figure d'interférences produite à partir d'une lentille conique dite axicon. Ce faisceau de Bessel primaire est réduit via un système optique 4f pour obtenir un faisceau de Bessel secondaire suffisamment intense pour générer de l'absorption non-linéaire dans les diélectriques sur un diamètre de quelques microns et une longueur de plusieurs centaines de microns.

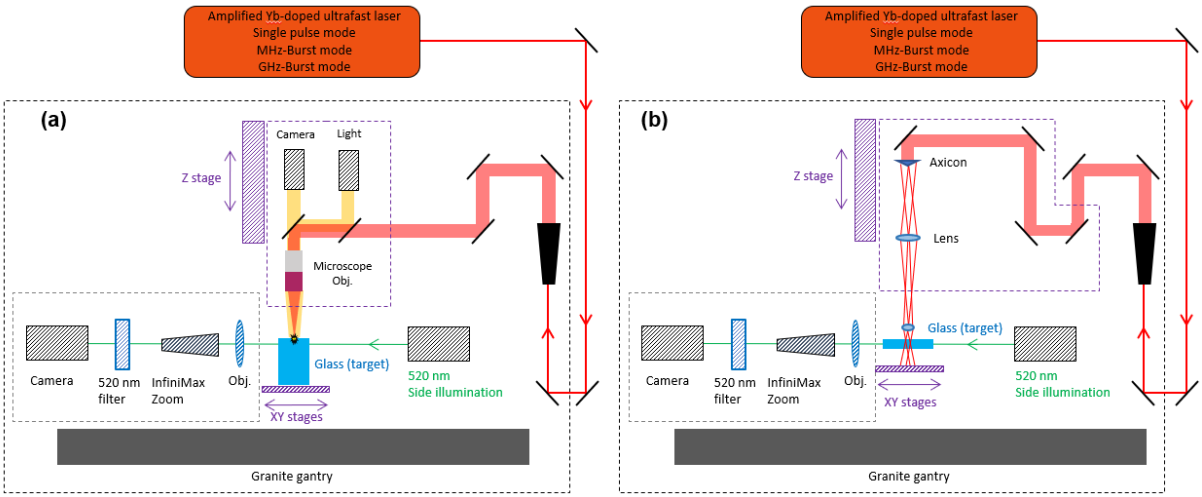

Figure 2. Schémas des stations d'usinage par faisceau Gaussien (a) et Bessel (b).

Sur ces schémas on peut voir que nos deux stations sont assez similaires, toutes deux sont équipées d'un système de visualisation latérale composé d'une diode à 520 nm, d'un microscope à longue distance de travail (InfiniMax), d'un filtre à 520 nm pour ne pas être aveuglé par la longueur d'onde d'usinage et d'une caméra Basler. L'échantillon, quant à lui, est monté sur une platine XY motorisée résolue au micromètre. Ces deux stations, ainsi que la commande laser sont contrôlés par le logiciel DMCpro couplé à un contrôleur XPS Newport.

2. Expérience pompe-sonde :

L'un des principaux objectifs de ce travail de thèse fut la compréhension de la dynamique des procédés laser en mode rafale GHz. Pour ce faire, nous avons mis en place une expérience dite pompe-sonde. Le défi dans le développement de cette expérience est de synchroniser l'arrivée d'une rafale GHz pompe sur la cible avec l'arrivée d'une impulsion simple sonde de manière transverse qui va illuminer le procédé. Pour ce faire, nous avons décidé de synchroniser 2 lasers qui sont à notre disposition comme représenté en Figure 3. Sur cette figure on peut constater l'utilisation de 3 générateurs de délais électroniques (Aérodiode, modèle Tombak), ceux-ci nous permettent de contrôler les modulateurs acousto-optiques présent dans les différents lasers ainsi que le déclenchement de la caméra. Ce montage, couplé à une ligne à retard optique, nous permet de sonder le phénomène avec un délai entre la pompe et la sonde variable entre 250 fs et 5 ms. La Figure 4 représente les délais 0 ns, 25 ns ainsi que 50 ns pour les trois régimes existants, la pompe est représentée en noir et la sonde en rouge.

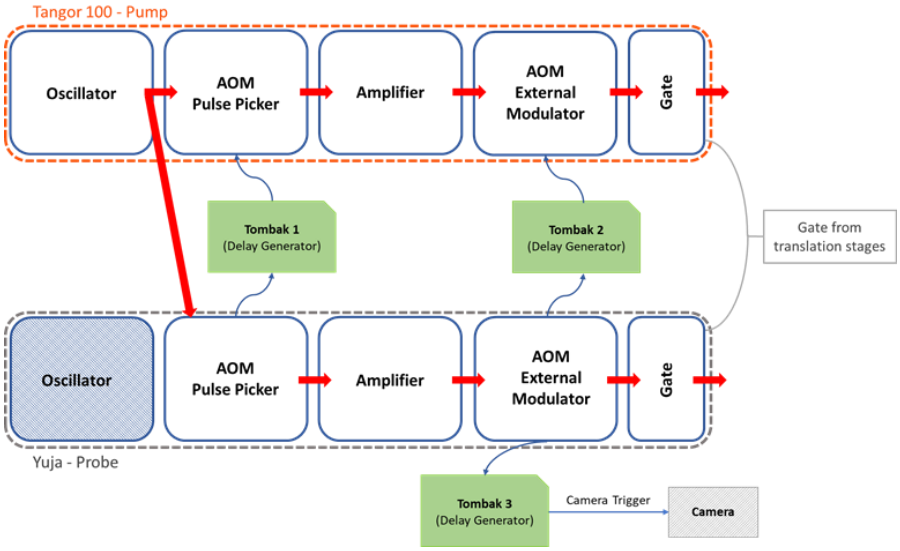

Figure 3. Schémas de principe de la synchronisation des lasers.

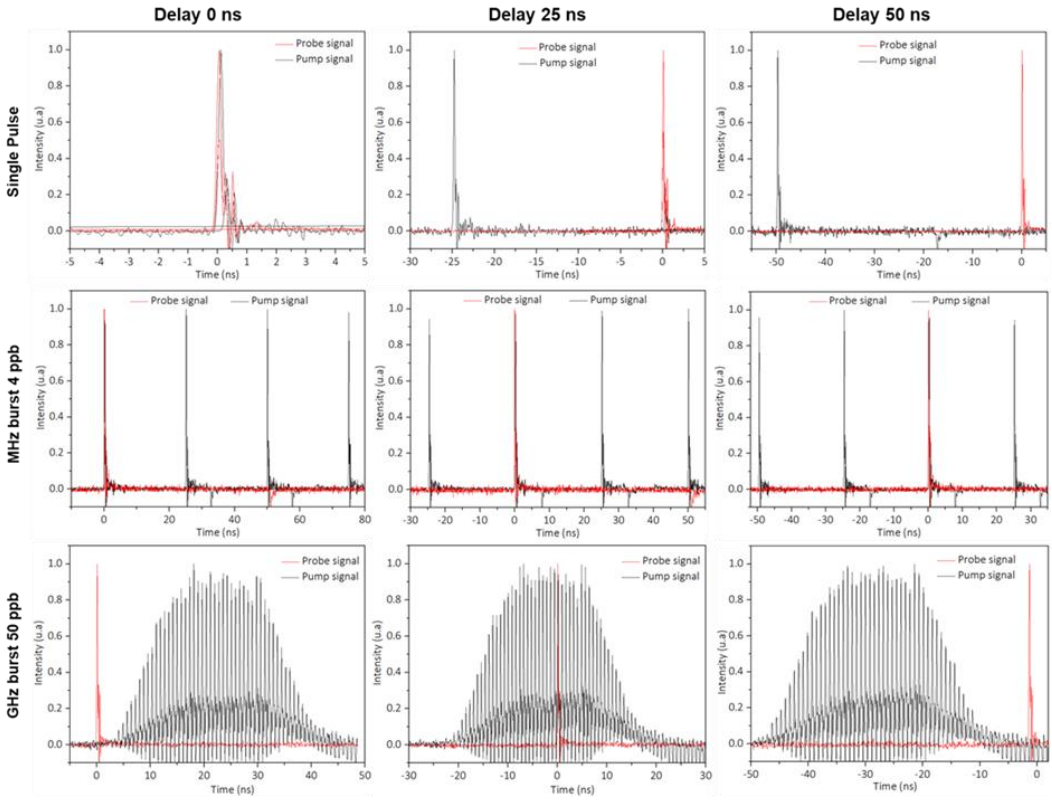

Figure 4. Oscillogrammes correspondants aux délais 0 ns, 25 ns et 50 ns pour les régimes mono-impulsions (haut), rafale MHz (milieu) et rafale GHz (bas).

Pour cette expérience pompe-sonde, c'est la caméra qui dicte le taux de répétition de la pompe et de la sonde pour l'usinage. En effet, l'objectif de cette expérience étant d'acquérir un maximum d'informations sur le procédé nous sommes donc limités par le taux d'acquisition maximal de la caméra. Pour cette expérience, le choix de la caméra est capital. Il existe deux modes d'acquisition d'image pour les cameras Basler, la première est appelée *rolling shutter* (shutter roulant) la seconde *global reset release* (réinitialisation globale), celles-ci sont représentées en Figure 5.

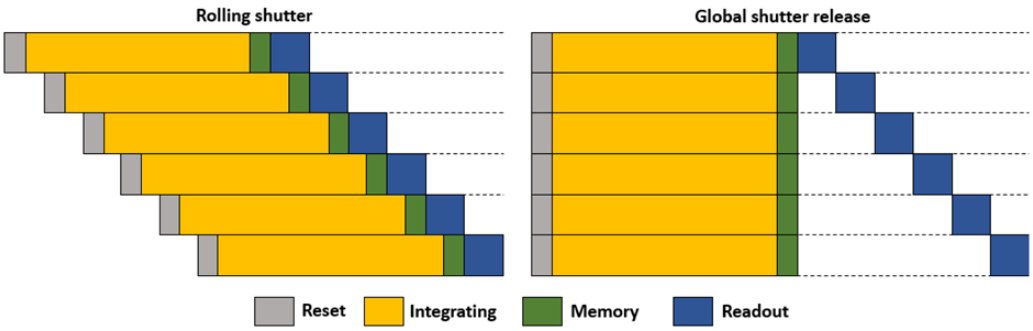

Figure 5. Représentation graphique des deux processus d'acquisition des caméras.

Dans le premier cas, l'intégration se fait bande par bande. Cela signifie qu'il y a un délai entre l'acquisition de la première et de la dernière bande ce qui n'est pas acceptable pour une telle expérience. Notre caméra de visualisation latérale (Basler, modèle acA1440-220uc) est donc basée sur la seconde option et avec un taux d'acquisition maximum de 227 Hz.

III. Résultats expérimentaux :

1. Etude de perçage de verres :

Dans un premier temps nous avons souhaité étudier le régime GHz en particulier. Nous avons commencé par étudier l'influence du nombre de rafales envoyées à l'échantillon ainsi que l'énergie de la rafale dans le sodalime et la silice fondue. La Figure 6 correspond à l'image microscope des trous obtenus avec un temps de perçage entre 20 ms et 100 ms. La cadence des rafales est fixée à 1 kHz et la fluence de celles-ci est de 52 J/cm² pour le sodalime et 136 J/cm² pour la silice fondue qui présente un seuil d'ablation plus élevé. Le diamètre du point focal est de 8.5 µm et celui-ci est positionné à la surface de l'échantillon tout au long du perçage.

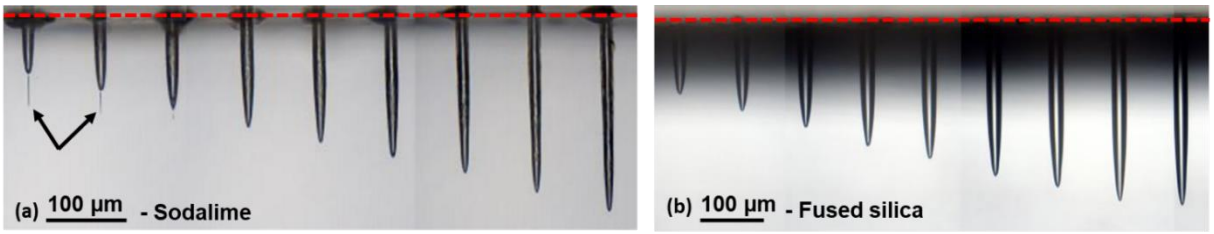

Figure 6. Images au microscope des trous obtenus dans le sodalime avec une fluence par rafale de 52 J/cm² (a) et dans la silice fondue avec une fluence par rafale de 136 J/cm².

Sur cette image, on peut observer des trous d'une excellente qualité, notamment dans la silice fondue qui ne présente aucune fissuration et des parois parfaitement lisses. Les trous présentent une forme cylindrique avec une pointe conique. La représentation graphique de l'évolution de la profondeur en fonction du nombre de rafales pour des fluence entre 136 J/cm² et 339 J/cm² est donnée en Figure 7. Sur ces graphiques, nous pouvons voir que, pour un faible nombre de rafales, la profondeur semble suivre une évolution linéaire, ce que nous avons déjà observé dans la Figure 6. Ensuite, la profondeur atteint un palier au-delà duquel elle n'augmente plus, même pour un nombre plus élevé de rafales envoyées. Sur cette figure, on peut noter que les tout premiers points, correspondant à un faible nombre de rafales, ne sont pas affichés car il n'y avait pas de perçage visible en-dessous d'une vingtaine de rafales. Cette valeur seuil diminue avec l'augmentation de la fluence ; par exemple elle varie de 10

rafales pour une fluence de 171 J/cm² à 1 rafale pour une fluence de 369 J/cm² dans le sodalime.

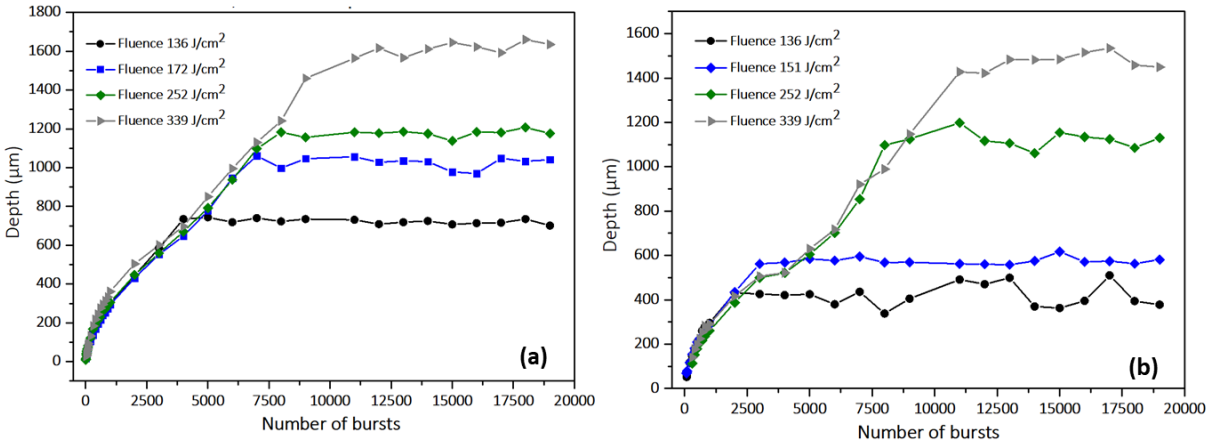

Figure 7. Représentation graphique de l'évolution de la profondeur des trous en fonction du nombre de rafales envoyées à l'échantillon de sodalime (a) et de silice fondue (b).

On peut également remarquer que la plus basse fluence de 136 J/cm² affichée en Figure 7 correspond à une fluence par impulsion de 2,7 J/cm², car il y a 50 impulsions par rafales, ce qui est inférieur au seuil d'ablation pour une seule impulsion pour les deux matériaux (autour de 2,9 J/cm² pour le sodalime et 3,6 J/cm² pour la silice fondue). La capacité de percer à une fluence inférieure au seuil d'ablation, défini pour une impulsion unique, résulte d'un effet cumulatif bénéfique au sein de la rafale GHz. L'incertitude des mesures en vue latérale avec le microscope (± 2,2 µm + 0,02L, avec L en mm) n'est pas représentée sur ces graphiques. La Figure 8 représente l'évolution de la profondeur du trou en fonction du nombre de rafales envoyées à une fluence fixe de 151 J/cm² et un taux de répétition de 1 kHz dans le sodalime.

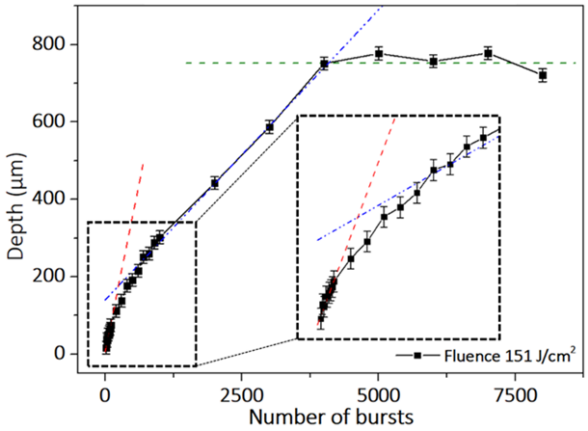

Figure 8. Représentation graphique de l'évolution de la profondeur des trous en fonction du nombre de rafales envoyées à l'échantillon de sodalime pour une fluence de 151 J/cm². Le carré en pointillé représente un zoom du début du graphique.

L'incertitude sur la profondeur (± 20 µm) résulte de la rugosité de la surface et de la précision de la position de focalisation. L'encart de la Figure 8 montre un zoom sur l'évolution de la profondeur du trou pour un petit nombre de rafales et permet de mieux comprendre le mécanisme de perçage. Ce graphique révèle trois étapes dans la formation du trou, indiquées par trois droites et schématiquement illustrées dans la Figure 9.

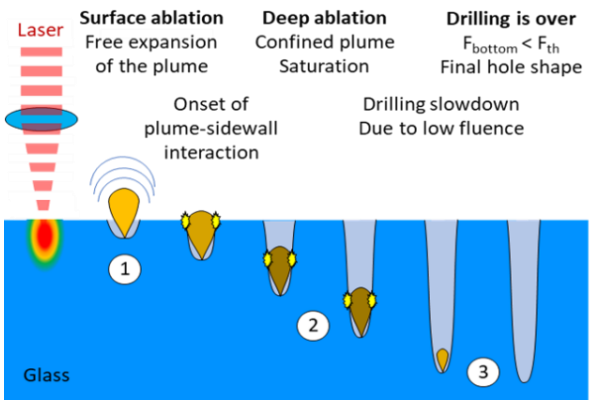

Figure 9. Représentation des trois étapes de perçages en mode rafale GHz.

La première étape correspond à l'ablation de surface (droite rouge sur la Fig. 8, étape 1 sur la Fig. 9). Le panache d'ablation peut s'étendre librement dans l'air ambiant au-dessus de la cible. La deuxième étape correspond à l'ablation profonde (droite bleue sur la Fig. 8, étape 2 sur la Fig. 9). Le panache d'ablation est ici confiné par les parois internes du trou en formation. Notre hypothèse, soutenue par travaux antérieurs rapportés dans la littérature, est que la propagation du faisceau laser à l'intérieur du trou par réflexions sous incidence rasante sur les parois internes et à une diffusion multiple. Cependant, à chaque réflexion, une partie de l'énergie est perdue par réfraction, et des pertes supplémentaires sont également causées par la diffusion multidirectionnelle. Par conséquent, l'énergie disponible pour le perçage diminue avec l'augmentation de la profondeur et la profondeur finit par saturer. Dans la troisième étape (droite horizontale verte sur la Fig. 8, étape 3 sur la Fig. 9), le processus de perçage est terminé car la valeur de fluence effective à la pointe du trou est inférieure au seuil d'ablation. L'intersection entre les droites rouge et bleu correspond à la transition entre l'ablation de surface et l'ablation profonde (170 µm dans le sodalime) tandis que l'intersection entre les droites bleue et verte correspond à la fin du perçage (745 µm dans la sodalime).
Notons que des études similaires ont été réalisées étudiant notamment l'effet de la répartition de l'énergie dans la rafale. En effet, notre système laser nous permet d'avoir accès à différentes formes de rafales représentées en Figure 10.

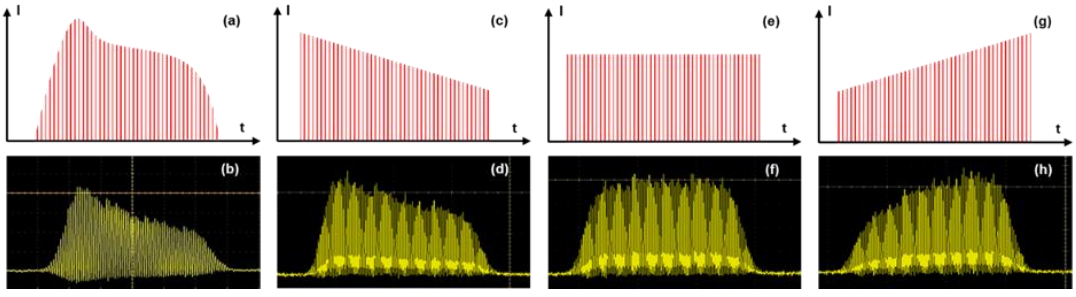

Figure 10. Représentation graphiques des formes de rafales à notre disposition (a,c,e,g) et les oscillogrammes correspondants (b,d,f,h).

Lors de cette étude nous avons notamment pu déterminer que la forme de la rafale n'a que très peu d'influence sur le perçage ; cependant la rafale plate, dans laquelle l'énergie est répartie de manière homogène entre les impulsions, constitue le meilleur compromis entre qualité de perçage et profondeur.

2. Comparaison des trois régimes :

Lors de ce travail de thèse nous avons également eu l'opportunité de réaliser une étude comparative entre les trois régimes décrits en Figure 1. Pour ce faire nous avons fixé l'énergie des rafales ainsi que leur taux de répétition. L'énergie par rafale, ou par impulsion en régime mono-impulsion, est fixée à 140 µJ et la cadence à 1 kHz. La Figure 11 montre les trous obtenus pour un temps de perçage de 200 ms sur les images (a) à (e) et 1 s de (f) à (k). Sur cette figure, nous observons que le régime mono-impulsion et le régime de rafale MHz avec 2 impulsions par rafale produisent des parois internes et des morphologies de trous similaires. En effet, sur la Fig. 11 (f) et (g), les parois internes des trous apparaissent rugueuses et les trous sont coniques. De plus, ces deux configurations laser sont les seules à afficher un collet à la surface, témoignant d'une énergie par impulsion trop élevée sur le matériau, ce qui peut entraîner des modifications de ses propriétés et éventuellement une qualité de surface réduite. Pour les rafales MHz avec 4 impulsions par rafale, la qualité des trous semble changer. Les parois internes sont clairement plus lisses mais fissurées. Il est possible que, pour ce régime, chaque impulsion au sein de la rafale soit encore trop énergétique. Notons que la morphologie des trous en régime de rafale MHz avec 8 impulsions est très similaire et n'est pas montrée ici. De plus, on peut remarquer que les trous sont encore coniques mais tendent vers la morphologie de trous obtenue en régime rafale GHz. Pour tous les temps de perçage, le mode de rafale GHz produit des trous plus cylindriques que les deux régimes précédents et une meilleure qualité de surface.

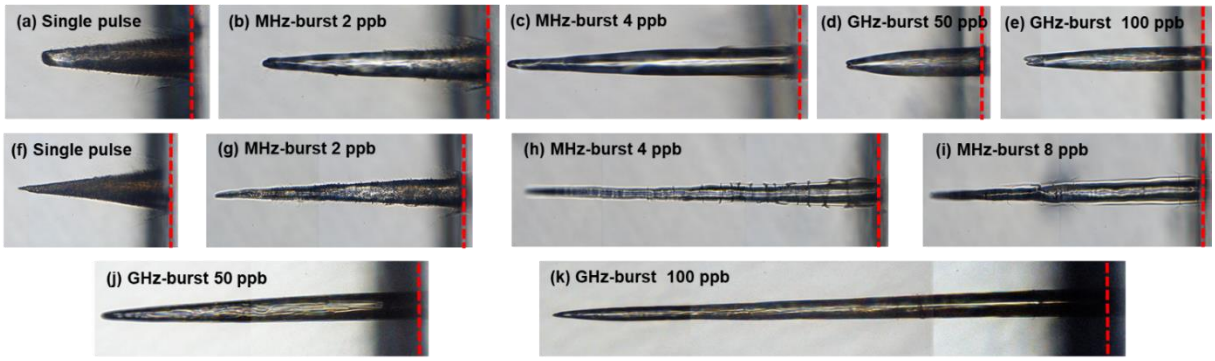

Figure 11. Image microscope des trous obtenus pour les trois configurations pour un temps de perçage de 200 ms (a,b,c,d,e) et un temps de perçage de 1 s (f,g,h,i,j,k) avec une énergie par rafale de 140 µJ et une cadence de 1 kHz.

Ces observations soutiennent l'idée que l'interaction en rafale MHz est dominée par l'intensité laser, où l'intensité optimale est un compromis entre l'absorption non linéaire et les effets cumulatifs, tandis que le régime de rafale GHz est principalement dominé par l'accumulation de chaleur. À l'inverse, dans le régime de rafale MHz, l'effet coopératif entre les impulsions au sein de la rafale a un impact moindre puisque le délai entre les impulsions est beaucoup plus long que le temps moyen de relaxation thermique du matériau.

De plus, malgré le fait que pour un temps de perçage de 200 ms, les trous dans ce régime sont moins profonds que ceux en mode de rafale MHz, pour un temps de perçage de 1 s, la tendance est inversée. Le trou obtenu avec une rafale GHz de 100 impulsions à une profondeur de 600 µm comparé aux 385 µm du régime de rafale MHz avec 4 impulsions. En outre, il faut noter l'excellente qualité des trous percés en mode de rafale GHz, et que la forme

cylindrique est conservée même pour des perçages profonds. Notons qu'une étude comparative de perçage menée dans le silicium a révélé que le régime MHz serait le plus adapté pour ce matériau en particulier.

3. Expérience pompe-sonde :

3.1. Comparaison des trois régimes

Dans cette sous-section, nous présentons les résultats obtenus en ombroscopie pompe-sonde sur des trous borgnes percés avec les trois régimes. La Figure 12 montre les résultats obtenus pour un délai de 25 ns entre la pompe et la sonde dans les trois régimes avec un nombre de rafales (ou de mono-impulsion) entre 1 et 120.

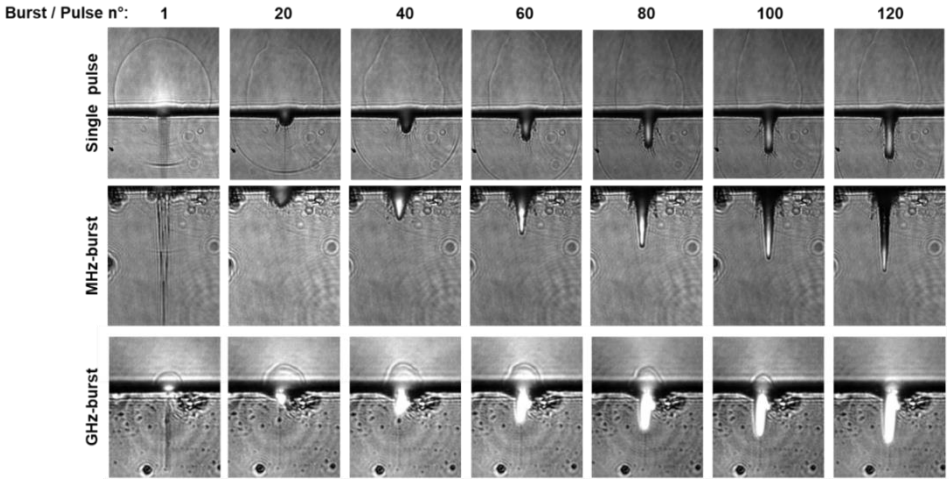

Figure 12. Imagerie pompe-sonde d'un trou borgnes percé à 200 Hz avec un délai pompe-sonde de 25 ns. La rangée supérieure montre le perçage en mono-impulsion, celle du milieu le régime rafale MHz à 4 impulsions et celle du bas le régime rafale GHz à 50 impulsions.

Sur cette figure on peut observer que le mécanisme de perçage est assez similaire pour les deux premiers régimes. Il est intéressant de constater ici que les ailettes à l'entrée du trou que l'on a pu observer pour ces deux régimes résultent de l'accumulation de plusieurs impulsions (ou plusieurs rafales) et non d'une seule comme nous le soupçonnions. Dans le cas de l'interaction en régime mono-impulsion, une onde de choc intense, se propageant depuis la surface vers le cœur du matériau, peut être observée. Celle-ci résulte du fait que les impulsions dans ce régime sont très intenses. En régime rafale MHz on peut également observer une onde de choc mais de bien plus faible intensité. Ceci est probablement dû au fait que les impulsions dans la rafale ont une intensité moindre. Notons que chaque impulsion dans la rafale donne lieu à une onde de choc de moindre intensité. Enfin, le régime rafale GHz qui ne produit aucune onde de choc visible tant les impulsions ont une faible intensité. En ce qui concerne le comportement de la plume de matière ablatée, nous avons pu constater que la même évolution est observée dans les trois régimes.

3.2 Perçage de trous traversants

Dans cette sous-section, nous présentons les résultats d'une expérience d'ombroscopie pompe-sonde sur un trou traversant dans un échantillon biseauté de sodalime. L'objectif était d'étudier la dynamique du panache d'ablation pendant le processus de perçage et de révéler

son rôle dans le processus de perçage car nous supposons que le panache d'ablation confiné est responsable de l'agrandissement du trou. Nous avons percé des trous traversants dans un échantillon biseauté avec plusieurs délais. Dans la Figure 13, nous montrons le perçage avec un délai de 50 ns, ce qui signifie que l'impulsion de sonde arrive environ 12 ns après la dernière impulsion de la rafale pompe. Cette valeur de délai a été choisie volontairement afin d'observer à la fois l'éjection de matière et la luminescence du panache tout au long du processus de perçage. Dans cette étude, nous avons percé un échantillon biseauté avec une fluence de rafale de 300 J/cm² et une fréquence de répétition de rafale de 1 kHz.

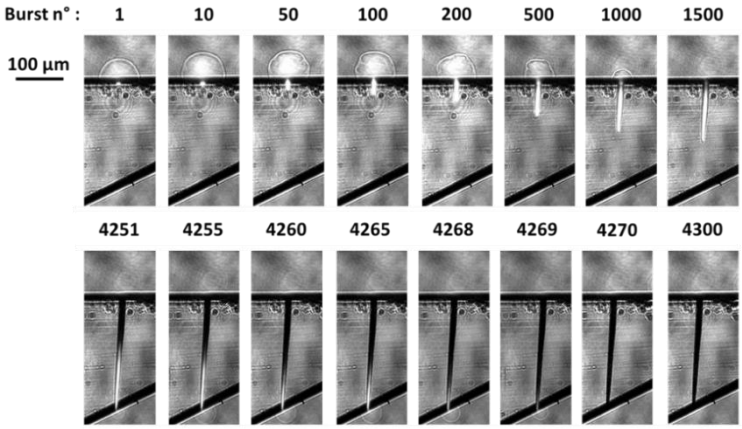

Figure 13. Imagerie pompe-sonde d'un trou traversant percé à 200 Hz avec un délai pompe-sonde de 50 ns. La rangée supérieure montre le début du perçage tandis que la rangée inférieure montre la fin. Le nombre d'impulsions est donné pour chaque image.

La rangée supérieure de cette figure montre le début du perçage. Nous pouvons observer que le panache est d'abord éjecté en amont de l'échantillon puis il va être confiné dans le trou comme observé dans la sous-section précédente. La partie qui nous intéresse ici concerne la fin du perçage pour les rafales de 4251 à 4300. L'image correspondant à la rafale 4251 (c'est-à-dire un temps de perçage de 21,2 s) est la toute première image avec un trou traversant. En effet, comme on peut l'observer ici, cette image montre une éjection de matière en face arrière de l'échantillon. Cette structure en bulle est assez similaire à celle observée en face avant au début du perçage. Une fois que le trou est traversant, le panache fuit par le trou de sortie et sa luminescence diminue dans le trou. Notez que la fuite est assez rapide car en moins de 20 rafales, le panache n'est plus visible. A la rafale 4270, tout le panache s'est échappé du trou. Un point intéressant ici est que si nous continuons à appliquer des rafales après la fuite du panache, aucune interaction ne peut être observée et il n'y a aucune évolution de la géométrie globale du trou, comme illustré sur cette figure pour la rafale 4300. Ainsi, dès que le panache quitte le trou, la géométrie finale du trou et le diamètre de sortie sont fixés. Cette observation confirme notre première supposition selon laquelle le panache d'ablation joue un rôle majeur dans le perçage par percussion en régime de rafale GHz. Cette limitation pourrait être surmontée en utilisant une couche sacrificielle sur la face arrière de l'échantillon principal comme montré dans la Figure 14 pour le perçage matriciel dans un échantillon de sodalime de 1 mm d'épaisseur. En effet, le défi ici est de maintenir le panache d'ablation contenu dans le trou au-delà de la face arrière de l'échantillon.

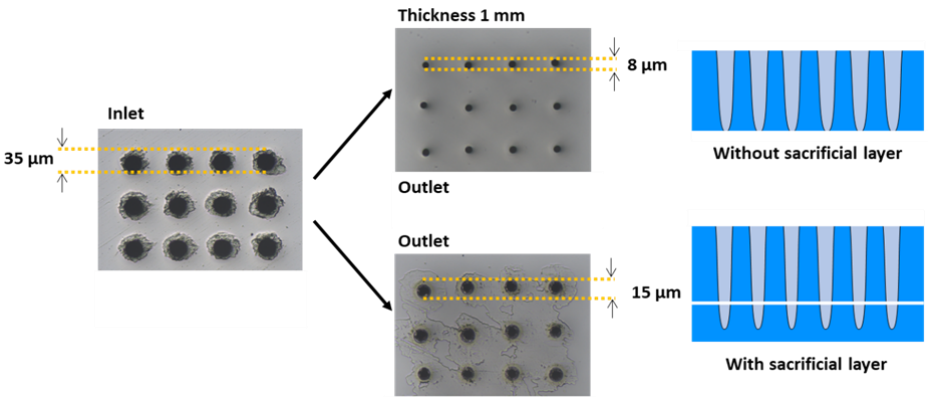

Figure 14. Représentation de la solution technique pour augmenter le diamètre de sortie à l'aide d'une couche sacrificielle.

Pour ce faire, il est nécessaire d'ajouter de la matière sous la face arrière de l'échantillon à traiter. Sur la Figure 14, le diamètre de sortie est d'environ 15 µm avec une couche sacrificielle (verre sodalime) alors qu'il est de 8 µm sans. Ces observations nous mènent à croire que le perçage dit « *bottom-up* » pourrait ne pas être possible en régime de rafale GHz. En effet, nous avons identifié que le rôle du panache est crucial dans le perçage en rafale GHz et que l'élargissement du trou s'arrête dès que le panache est éjecté du trou. Cependant, dans le perçage *bottom-up*, le panache serait instantanément éjecté par la face arrière de l'échantillon, et ainsi l'élargissement du trou s'arrêterait immédiatement. Cette supposition nécessiterait des preuves expérimentales.

4. Découpe de verres par faisceau de Bessel :

Lors de ce travail de thèse nous avons utilisé le faisceau de Bessel afin de couper des échantillons de verres. Le procédé de découpe est représenté en Figure 15.

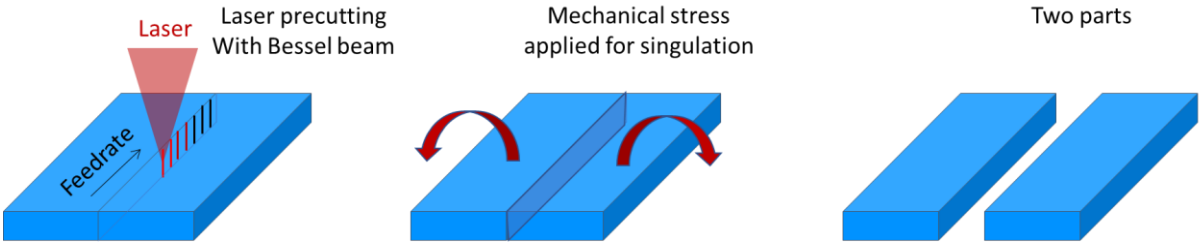

Figure 15. Représentation schématique du procédé de découpe de verre par faisceau de Bessel.

La première étape consiste à créer un plan de prédécoupe en déplaçant de faisceau de Bessel dans l'échantillon, puis, en appliquant une contrainte mécanique, on peut séparer les pièces. Cette étude porte sur la qualité de découpe, c'est-à-dire la rugosité de la surface coupée. Afin de mettre le régime rafale GHz en perspectives, nous l'avons comparé au régimes rafale MHz qui fait office d'état de l'art en ce qui concerne la découpe. Nous avons été en mesure de découper des échantillons de sodalime de 1 mm d'épaisseur et nous avons identifié les zones de fonctionnement des deux régimes comme représenté en Figure 16. Sur ces schémas, nous avons identifié 4 zones de fonctionnement de découpe pour les deux régimes. La première en vert correspond à la zone de découpe optimale, la seconde en orange une zone de découpe présentant une rugosité plus importante, en rouge une zone pour laquelle la découpe n'est pas possible par manque d'énergie ou par un recouvrement insuffisant entre Bessels

successifs et finalement en gris lorsque l'énergie ou le recouvrement est trop important et on entre dans un régime de découpe thermique incontrôlé.

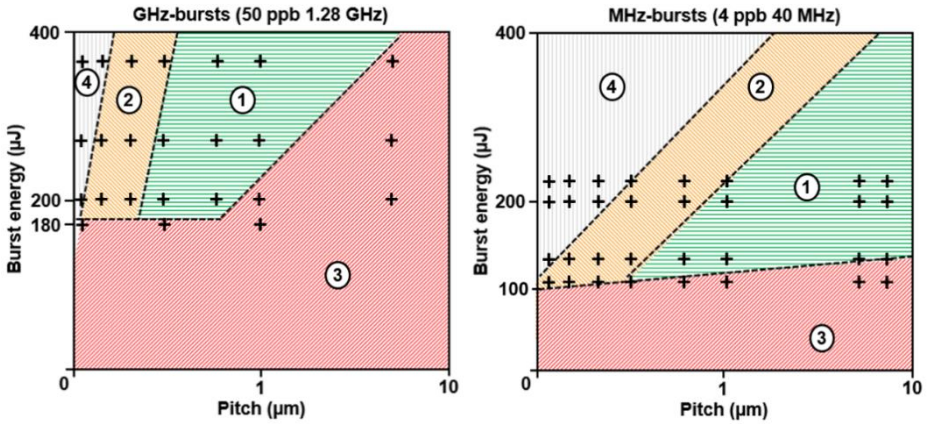

Figure 16. Représentation schématique des fenêtres opératoires du procédé de découpe pour les régimes rafale GHz (gauche) et MHz (droite).

Dans ce dernier cas, le plan de découpe ne suit plus la trajectoire du faisceau de Bessel mais la zone affectée thermiquement. Cette étude a révélé que la qualité de découpe était meilleure en régime rafale GHz. Cependant, ce résultat est contrebalancé par le fait que la longueur effective du Bessel est réduite de par la faible intensité des impulsions.

IV. Conclusion :

Lors de ces trois années de thèse nous avons pu étudier le nouveau régime d'interaction laser-matière que permettent les rafales GHz. Au travers de nombreuses études de perçages ou de découpe, nous avons pu attester du grand potentiel que présente ce nouveau régime. A travers nos études comparatives, nous avons été en mesure de montrer que, tant par la qualité de l'usinage que par les rendements ou même la capacité à produire de très haut facteur de forme, le régime rafale GHz présente bien des avantages au regard des régimes existant. Ces travaux de thèse avaient notamment pour but d'apporter une étude expérimentale approfondie de ce nouveau régime afin de pouvoir dégager un consensus dans la communauté au regard de son apport pour l'industrie. Nous avons clairement montré l'apport du régime GHz ainsi que des premières pistes de compréhension de ce nouveau régime. Une perspective majeure serait le développement d'un modèle théorique capable de simuler l'interaction d'un matériau avec une rafale GHz.

Acknowledgements

Alrighty! It's time for some acknowledgements! If you were somehow involved in this PhD, prepare to be acknowledged.

Before going chronologically, I wanted to start with my supervisors as they hold quite an important place in this work. It was quite risky for me to take this PhD grant in Bordeaux. The point was that I was going to join a quite small research team (2 permanent researchers) that I did not meet before May 2021. It is fair to say now that I have been incredibly lucky to end up here. For 3 years, I have had the chance to work alongside two exceptional people. Inka, you have been of unconditional support professionally as well as personally. I don't think I met someone as dedicated to her work as you have been, your rigor coupled with your experience has made you the perfect PhD supervisor and it was a true honour to grow as a person and a scientist alongside someone of your calibre. One of the things I will take away is that I am at the climax of my productivity on Fridays from 5.00 pm to 7.00 pm. Now it is up to good old John to be acknowledged! You told me once (amongst countless anecdotes) that you have 4 brains and you were willing to dedicate one to my work. Honestly looking back, I think you have even more brains than you claim the credit for. Hopefully this is the last manuscript I will make you read. You truly are the master in the experimental room, and once I got enough endurance to follow you around, there was no thing you would not teach me. Your tendency to touch everything when you came to help me, forcing me to realign everything, only perfected my mastery of the setups and I think you did it on purpose. In September 2021 I started working here with you 2 thinking that 3 years was quite a long time, not so sure about that now. I know we will keep working together but this time as colleagues! Already excited about this!

Now let's get back to the very beginning. First, I was born, thanks to my parents Christian and Carole Balage. Of course, my family had a major role in the success of this work. My whole family literally brought me here by teaching me the value of work and to be persevering. I think now I can say it, I was not such a hard worker in my early days of school (to the great dismay of my mother) but my parents always trusted and supported me even if it meant that I would move away from my home region. I guess I am also very thankful for them not to put pressure on me to take over the family farm. Also, a big thank to my big sister Emilie Balage, not so many people can say that they really have a fusional relationship with their siblings but I think I can. She has always been there for me in quite a supportive way and now by the end of my PhD I will have a nephew to cherish, calling me Dr. Tonton (I deserve the title). I can't really go through the acknowledgements without mentioning Nicolas and Anne-Sophie (aka Tatou), I love your way of having fun and always pushing me to find the worst gift ever. I really have a huge family and we all are very close together, I will not thank them one by one but let's just say that I benefited from a very supporting environment which was not easy for them as they are not scientists but they took the time to try and understand my work and I feel very lucky about that. Sorry guys, I'm definitely going to be unbearable now that I'm going to be a Doctor.

Throughout my years of education, I made a lot of friends which also supported me a great deal. The major group of friends come from high school and my two years university degree (DUT). Maxime, Romaric and Lucas with whom we form “Les 4 fantastiques” no less than that, I put you in the friend section but you already are family, through a painstaking process of hazing! Yes, one shall be worthy of joining my family. Frédéric, Paul, Lucas and Hugo with whom we form “Les physiciens”, again, no less than that. We created this group in the very first year of DUT clearly not expecting one of us to become a physicist and here I am. During such trying times, it is always very important to let go of the pressure and have fun and you all were such great night out companions. Special dedication to Fredo which is also going through a PhD! So proud to be friend with a guy studying clouds. I don’t think we were the brightest students around in DUT but man did we have fun.

Now my master years with two of the nicest and brightest people I know, Manu and Léa. Manu you stayed for your PhD in Clermont, and you already passed so I should call you Dr. Chereau. Such an interesting man that I had the chance to work with. Léa, you passed the AGREG in Lyon which is already such an accomplishment, I was very impressed! However, I think maybe your biggest success was to endure hours of lessons with Manu and I always joking around. I don’t think I would have gone through with my master without you guys, we lifted each other up for two years and it really was a lot of fun to learn physics with you around.

Now we get to my PhD years in Bordeaux. Things started a bit complicated, socially speaking, in a new town with no acquaintance. But it got better quite fast during the teaching training that I had to follow for 3 days. There I met “Les cognitivistes”, a bunch of PhD student all willing to teach during their PhD. I will single out Mathias with whom I particularly sympathized. A lot of fun going to play squash like 2 times a week and going to watch UBB games at Chaban-Delmas. I think we will stop the squash because you are starting to win a bit too often now!

After about a year I was joined by Théo Guilberteau in the experimental room, first as an intern and then he joined ALPhANOV as a PhD student in august 2023. I supervised a certain number of interns during these three years but I have got to say that you were the brightest one. I think I taught you basically everything I learned and now you just have to try and enjoy your PhD. Early in 2023 we were also joined by Manon Lafargue, also doing a PhD but in Amplitude. This last year of PhD has been quite fun with you two around. You also got to play squash with Mathias and I, which was quite challenging. The development of the pump-probe setup will forever be one of the greatest achievements of my PhD. I thank you both for your help and I wish you all the best for your PhD. I will see you around!

Of course, I am forgetting a lot of people that were supportive, this accomplishment is also theirs. I hope you will enjoy reading this manuscript as much as I enjoyed these three years.

Foreword

This PhD thesis was financially supported by the French Ministry of Higher Education, Research and Innovation (MESRI). This work was realized in the CELIA laboratory and in a close collaboration with Amplitude and ALPhANOV. This collaboration has then been officialized in August 2023 within the frame of a three-partite Labcom named TRICORN (CELIA, Amplitude and ALPhANOV).

The CELIA laboratory is a joint research unit located in Talence, with oversight from the University of Bordeaux, the CEA, and the CNRS. Its scientific activities focus on the following themes: (i) high repetition rate and high intensity femtosecond lasers, studies in intense laser optics; (ii) Ultra-intense fields, ionic collisions, and X-ray sources through plasmas; (iii) XUV harmonics and applications in the study of ultrafast processes, attosecond pulses; (iv) Laser-plasma interaction, physics of hot and dense plasmas, inertial confinement fusion, laboratory astrophysics; (v) Laser-material interaction, direct femtosecond laser writing, multi-material laser processes in ns/ps/fs regimes, laser and plasma spectroscopy.

This PhD grant was obtained as a part of the reconstruction of the research group SLAM (Short-pulse lasers: Applications and Materials). Indeed, as of 2021, Professor Inka Manek-Hönninger and Doctor John Lopez were granted an experimental room inside the building of the CELIA laboratory to centralize their research activity. A significant part of this work has been to create, from scratch, a healthy and well-equipped research environment with limited resources. This challenging but rewarding task has been a fantastic opportunity in terms of experience, responsibility, autonomy and control of the research environment.

Table of contents

Table of Figures

Introduction

Miniaturizing the components of all devices has become one of the challenges of the micro-electronics industry. Nowadays, 3D structures allow to get to the next step of miniaturizing but it requires a high density of interconnections between the logical unit and the memory unit. This density of interconnections is achieved by interposers as represented in blue in Figure 0. Up till now, these thin layers are made of silicon drilled by deep reactive ion etching and then the holes are metallized. However, the industry is considering switching for glass interposers which are less expensive and easier to process [1].

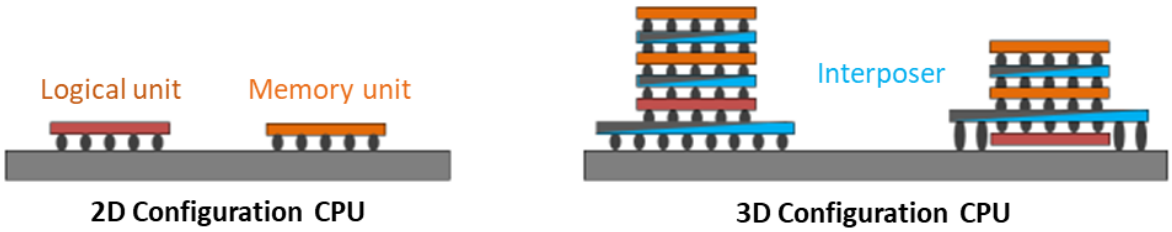

Figure 0. 2D and 3D configurations for microelectronics components.

Glass interposers present much interest as glass has a better flatness than silicon and it is naturally insulating. This latter property means that for thin layers it will not require any treatment and it will reduce leakage currents. The drilling methods used on silicon wafers cannot be used in glass as its properties are very different. For applications such as dynamic random-access memory (DRAM), micro electro-mechanical systems (MEMS), chip dicing or even flexible electronics, the most used technique is deep reactive ion etching (DRIE). By this method up to a few hundreds of micrometres in silicon with etching rates as high as 20 µm/min can be reached. To get to high aspect ratios or complex structures, DRIE is also used with a hybrid soft/hard mask [2]. Many techniques can be used to drill glass such as: chemical drilling, mechanical drilling, laser assisted chemical etching, water assisted laser drilling and others [1]. In terms of processing speed, laser assisted chemical etching appears to be the best method. However, it is highly polluting so other alternatives would be preferable. The integration of glass in microelectronics marks a junction of materials science and technology, opening avenues for innovation in miniaturization and precision engineering. Beyond its conventional role as a transparent medium, glass has emerged as a crucial component in the fabrication of microelectronic devices. Its unique properties, including excellent thermal stability, electrical insulation, and optical transparency, make glass an ideal substrate for the intricate world of microelectronics. Glass is also easy to produce as very thin, unlike silicon where thinning is costly and time-consuming (≈30% of the preparation cost). In this particular field, glass plays multiple roles, from providing a stable platform for the fabrication of integrated circuits to serving as a substrate for emerging technologies such as flexible electronics and wearable devices. The use of glass in microelectronics underlines its transformative impact on the miniaturization of electronic components, enabling advancements in diverse fields, from consumer electronics to healthcare and beyond.

Recent technological advances in the realm of industrial ultrashort lasers have facilitated an increase in both average power—now reaching 1 kW—and repetition rates—extending up to several MHz.

Many applications of ultrashort laser-based material processing have emerged in the literature, such as index change [3], 3D data storage [4–7], waveguides and diffraction gratings writing [8–11], bottom-up drilling [12], as well as zero-kerf and dust-free glass cutting [13] to mention just a few. Thanks to the ultra-short interaction time, femtosecond lasers allow for a highly localized and intense energy deposition [14,15]. However, the throughput may not meet industrial requirements due to the small amount of material being processed during the interaction with each single pulse. An interesting strategy for increasing the productivity of femtosecond laser processing is spatial beam shaping. For instance, Bessel beam shaping has been studied for glass cutting [16–18], as well as nano-hole drilling [19], in-volume nanoscale modifications [20], and high-aspect-ratio drilling [21]. This technical solution allows for an elongated, very localized, and homogenous energy deposition. Gaussian beams are also used for high-aspect-ratio drilling with elongated spatial beam shaping, for instance by using a spatial light modulator [22].

In order to facilitate the integration of femtosecond lasers in the industry, it is necessary to increase the efficiency of those processes. Of course, the first step is to optimise the process itself by tuning the laser parameters to match the characteristics of the materials. The main goal, to increase the efficiency, can be achieved mainly in two ways. Either one can parallelize the process, by dividing a femtosecond laser beam in several sub-beams in order to machine at different locations at the same time (for example a 100 W laser beam into ten 10 W laser beams could increase the productivity by a factor of 10). The other way is to optimise the energy deposition and for example the ablation efficiency. This PhD grant has been entirely dedicated to the second strategy by investigating this new light-matter interaction regime, the GHz-burst mode.

In 2016, Professor Ömer Ilday's team in Turkey demonstrated the efficiency of micro-machining using femtosecond laser pulses in GHz-burst mode [23,24]. This novel laser operation mode replaces each individual high energy pulse with a burst of a high number of low energy pulses, wherein the delay between successive pulses is on the same order of magnitude, or even less, than the thermal relaxation time in the material. Consequently, the energy deposition occurs cumulatively within each burst exclusively.

This unprecedented laser-material interaction regime fosters the emergence of transient phenomena or permanent modifications resulting from a thermal process. It also brings the benefits associated with the brief duration of femtosecond pulses, such as low energy per pulse (~µJ), an ultra-short interaction time, and the capacity to modify the surface or volume of transparent dielectric materials through nonlinear absorption [25]. GHz-burst mode processing of dielectric transparent materials is the main topic of this PhD work. Indeed, the burst mode is expected to minimize the undesirable effects of nonlinear propagation upstream of the focal point, increasing the confinement of the interaction near the focal point in dielectrics.

The first chapter of this manuscript is dedicated to the theoretical background as well as the state of the art. The goal here is to introduce all the physics concepts that are needed for a good understanding of this work. Additionally, this chapter provides a comprehensive state of

the art on laser processing in order to put this work in perspective. One will easily understand that the state of the art in GHz-burst processing remained quite small due to a lack of laser sources up till the very recent years with emerging companies.
In the second chapter, I provide an extensive list of the materials and methods we used during the three years. The experimental setups designed and implemented for the different studies regarding the GHz-burst regime are detailed along with the metrology equipment and analysis methods.
The third chapter concerns the most detailed study that was led all along those three years. We performed an extensive percussion drilling study with GHz-bursts which gave excellent results. We took care of designing comparative studies on several regimes in order to be able to put the GHz-burst regime into perspective with respect to the existing regimes. We were also able to investigate several burst configurations for example burst length and burst shape. This means that we were able to choose the number of pulses per burst at a fixed repetition rate as well as the energy repartition within the burst. We reveal the existence of a particular drilling dynamics in GHz-burst mode as well as certain drilling limitations. The pinnacle of this work is reached with the pump-probe shadowgraphy experiment designed to bring a whole different level of understanding of the process.
In a fourth chapter, we extended the study to other materials at our disposal, especially silicon but also crystalline materials such as sapphire and CaF_2. We reveal the impact of the GHz-burst regime on percussion drilling of such materials. We provide a comparative study on percussion drilling of silicon with the existing regimes just as in Chapter 3. The last part of this chapter is dedicated to a particular experiment we implemented on silicon with an appropriate wavelength regarding the spectral transparency of silicon. The goal here was to investigate the GHz-burst regime for in-volume modifications of silicon. This setup has been included in a recent project regarding in-volume modifications of silicon using bursts of femtosecond pulses in collaboration with the group of Stefan Nolte in Jena. This experiment was also designed to familiarize ourselves with this new wavelength as well as the challenges of in-volume modifications of silicon.
The last chapter of this manuscript completes the burst mode studies. During these three years, we implemented a Bessel beam glass cutting module. By this means, and quite similarly to the previous chapters, we have been able to compare the different regimes available for glass cutting. In this chapter we depict the glass cutting process in GHz-burst regime, which has never been investigated before to the best of our knowledge. We provide an experimental study of the cutting quality, which will be defined then, as a function of the burst-to-burst pitch (i.e. the Bessel-to-Bessel spacing) for the two regimes investigated. We reveal that the GHz-burst mode provides a better surface quality but is a bit more complicated to implement. In addition, we propose a graphical representation of the process windows in both regimes.
Finally, a summary of the whole PhD work is given in a conclusion part along as well as some discussion regarding future experiments. It is important to understand, before reading this manuscript, that the results presented in this document, and more generally the work realised these last three years, were exclusively experimental.

Chapter 1: Theoretical background & state of the art

In this chapter, we will introduce the basics in physics needed to get through this manuscript as well as the state of the art regarding femtosecond laser processing. We will discuss the properties of gap materials as well as their interaction with pulsed lasers especially the timescale of the phenomena taking place right after the interaction. The latter are represented in Figure 1.1 with the corresponding timescale spreading from 10^{-15} seconds to 10^{-5} seconds [25]. However, the physical phenomena and what comes with them is highly affected by the parameters of the laser pulse (duration, wavelength or intensity) as well as the material parameters (bandgap, thermal conductivity). Therefore, this presentation of the phenomena can only be seen as a qualitative explanation.

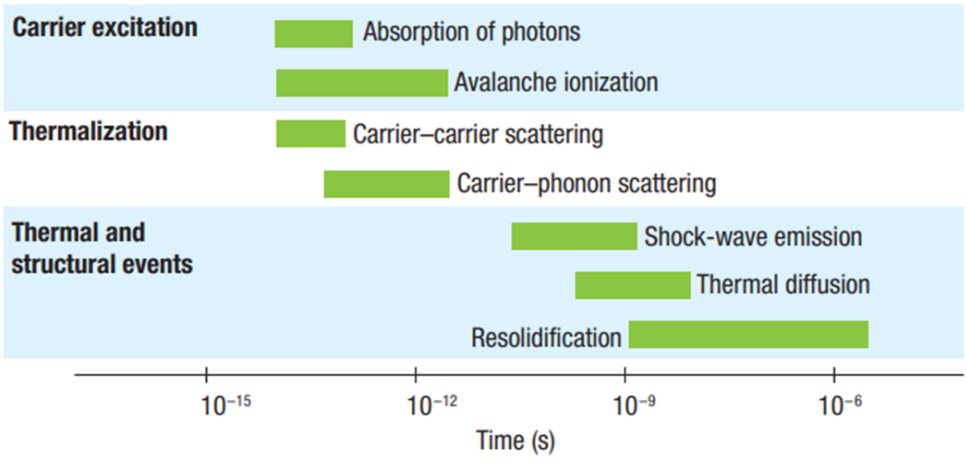

Figure 1.1. Physical phenomena attached to the interaction of a femtosecond laser pulse and their corresponding timescale [25].

The absorption begins in the very first femtosecond (10^{-15} s) of the pulse. One may notice that, although the pulse duration is a few hundreds of femtoseconds, the material continues to undergo changes up to a few microseconds after the laser pulse. The mechanisms of absorption that occur during the interaction are divided in two categories. The first category is the photoionization, including multiphotonic absorption and quantum tunnelling effect, whereas the second one is impact ionization. After the absorption follows thermalization with a relaxation of the free carriers by impact with other electrons (electron-electron collisions) or with the lattice (electron-ion or electron-phonon collisions). Indeed, the lattice can vibrate and spread the energy, these vibrations can be quantized and the quantum of this vibration is the phonon. The electron-electron thermalization takes place within a few hundreds of femtoseconds after the pulse. For longer times, in a range from 1 picosecond (10^{-12} s) to tens of picoseconds, occurs a transfer of the energy acquired by the electrons to the phonons via collisions, the transfer timescale is material-dependent [26]. Shockwaves and acoustic waves can appear due to the rapid temperature change of the bulk leading to a high temperature gradient. Depending on the laser parameters and focusing conditions, the relaxation of the material will produce (i) an appearance of residual stresses, (ii) a variation in density and refractive index due to chemical element migration, and for higher laser intensity (iii) a melting located upstream and/or around the focal point, or (iv) the appearance of a physical defect such as a crack, a void or a bubble.

This chapter is divided in three parts. The first section is dedicated to *gap materials*, we will briefly present these materials with their specificities and properties that are interesting for this work. The second part focuses on the *electron dynamics* and the different processes during the light-matter interaction relevant for the understanding of this work. Then, finally, the last section introduces the notion of *femtosecond laser processing.*

1. Gap materials

The matter around us is composed of atoms themselves composed of a core (protons and neutrons) and electrons orbiting this core. An isolated atom presents discrete energy levels, electrons can only occupy states defined by quantum mechanics. Those levels are filled with electrons starting from the levels closer to the core and ending on the periphery. In a solid, the proximity between atoms coupled with the interaction between the electrons induces a degeneration of the levels. In a bulk with a very large number of atoms, the discrete levels shift towards a continuum leaving a band-like structure represented in Figure 1.2 [27].

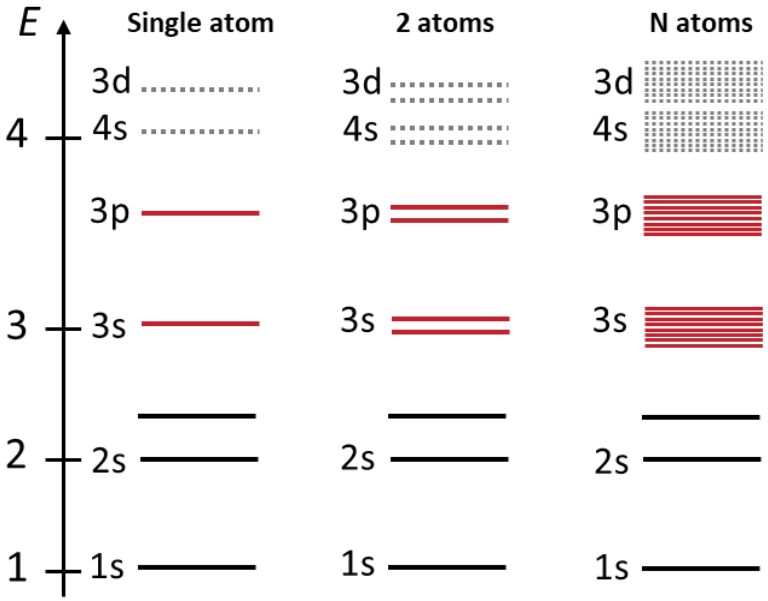

Figure 1.2. Evolution of the energy levels from one single atom to N atoms.

This representation can be simplified by using a three-band configuration, the valence band being the last band occupied by electrons for atoms at rest, the conduction band corresponding to the first unoccupied band and the bandgap between them. This simplified representation allows us to clearly define three types of materials depending on the bandgap represented in Figure 1.3. These types of materials are generally defined by the value of their gap energy $\mathbf{E_G=E_C-E_V}$, with E_c the energy of the first level of the conduction band and E_v the energy of the last level of the valence band. The Fermi level represented by the black dashed line represents the highest energy level reachable by the electrons for a temperature of 0 K. The particularity of the conductors is that there is an overlap between the valence band and the conduction band. These materials don't have enough electrons to fill their last electronic layer. An unfilled electronic layer means that the electrons on this layer are less linked to the atom and can participate in the conduction of the material. The first category to present a gap between the valence band and the conduction band is the semi-conductor. Their last

electronic layer is filled and no electrons are in the conduction band. To send an electron in the conduction band there must be an energy income at least equal to the bandgap energy. The last category corresponds to the insulators. Just as the semi-conductors they present a gap between the valence band and the conduction band. The only difference between these two types of materials is the value of the bandgap. For semi-conductors the bandgap energy is nearby **1 eV**, for insulators it is usually between **3 eV** and **12 eV**.

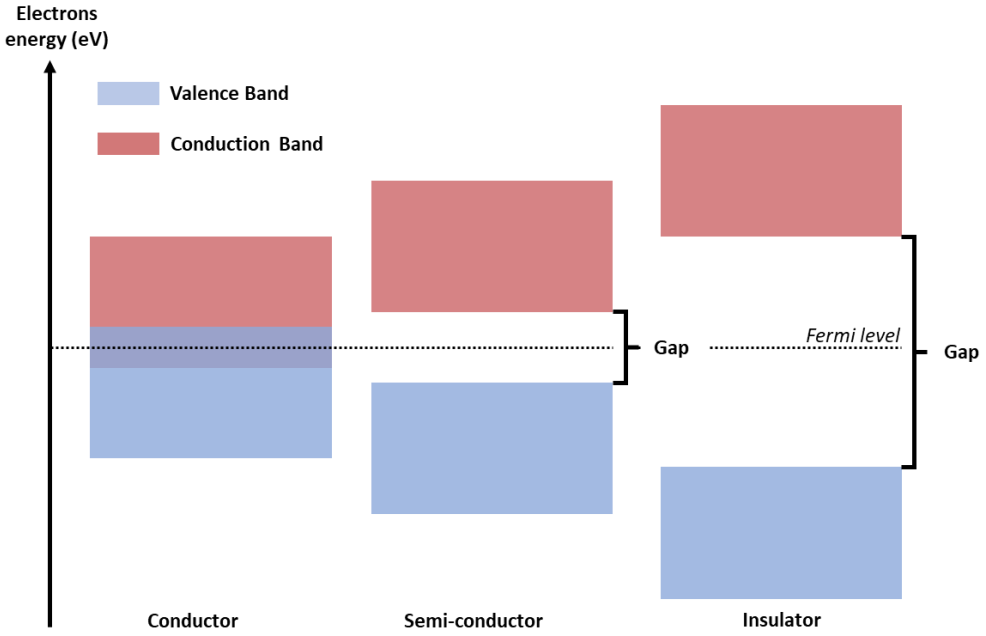

Figure 1.3. Blueprint of the band organization for the three types of materials, conductor, semi-conductor and insulator.

Note that complementary levels might appear due to impurities in the materials even within the bandgap. Therefore, the value of the bandgap and the properties of the materials are very dependent on its purity.

Most of the electronic components rely on all three types of materials. The conductors are used for the transportation of the current as well as temperature conductivity, the dielectrics (insulators) to insulate and the semi-conductors are the very base of the detectors, transistors or laser diodes etc. The following table summarizes the values of the bandgap of some of the materials investigated in this study.

	Sodalime	**Fused silica [28,29]**	**Sapphire [30,31]**	**CaF_2 [32]**	**Silicon [21]**
Bandgap (eV)	3.9	7.5-9	8.8-9.9	12	1.12

Table 1.1. Bandgap energy of the different materials studied in this manuscript.

In these 5 materials, we can see two types of glass (Sodalime and Fused silica) and three crystals. The glasses are transparent dielectrics as well as sapphire and CaF_2 which is easier for visualizing the process directly with a lateral visualization system. Calcium fluoride and sapphire are crystals just like silicon but they are transparent in the visible range. These two materials were used to get a first idea on the behaviour of the interaction of the laser with crystals. Indeed, the range of transparency for silicon is for wavelengths above 1.1 µm.

Therefore, classical visible cameras cannot be used to see through silicon for observing the process dynamics.

2. Electron dynamics

The mechanisms of absorption also rely on two phenomena, linear and non-linear absorption. The former corresponds to conductors, the electrons can linearly absorb the energy of the incoming photons to get to a higher level of energy. The latter is linked to the band-like structure of the materials and can be explained using the representation used on Figure 1.3. In this case, there exists a gap between the energy level of the electron at rest and the first accessible excited level. Therefore, the incoming photon needs an energy at least equal to the gap in order to promote the electron from the valence band to the conduction band. If the energy of the photon is not high enough and if the laser intensity is not high enough to provoke non-linear effects, the material is transparent, meaning that the photon cannot interact at all with the material. This section is dedicated to the photoionization and impact ionization, which constitute the two main categories of absorption phenomena as cited in the previous section. Moreover, the material will tend to relax through electronic relaxation which will be described as well.

2.1 Photoionization

The photoionization corresponds to the use of light's energy in order to ionize the matter. Linear absorption occurs when a single photon energy is enough for the electron to overcome the bandgap. On the other hand, non-linear photoionization relies on two mechanisms, the multiphotonic ionization and quantum tunnelling ionization. As most of the non-linear effects, photoionization depends mostly on the intensity of the pulse as well as on the wavelength of the laser. Of course, for laser processing, the properties of the materials are crucial, especially the bandgap energy.

2.1.1 Multiphotonic ionization

When dealing with non-linear absorption, the intensity is a key parameter as it is linked with the number of photons propagating per unit of time and space. The energy of a photon is given by $E=\hbar\omega$, with $\hbar$ the reduced Planck constant and ω the optical pulsation of the laser. In our case for photons at 1030 nm, the energy is about 1.2 eV. Let us take the example of fused silica with a bandgap energy of 9 eV. For this material, the linear absorption is not possible as 1.2 eV < 9 eV. It would take at least 8 photons at 1.2 eV to get an electron from the valence band through the bandgap. For simultaneous multiphotonic absorption to be significant, the intensity needs to be at least 10^{12} W/cm² [33]. This particular phenomenon, mostly takes place at the focal point of a laser and allows for a transparent material to be locally absorbent. This mechanism is illustrated in Figure 1.4 along with the quantum tunnelling. The probability for an electron to get through the bandgap is directly proportional to the laser intensity **I**. Indeed, the absorption rate can be determined using equation (1).

$$W_{IMP}(I) = \sigma_n I^N \quad (1)$$

In this equation, σ_n stands for the generalized cross section and N is the number of photons [34].

2.1.2 Quantum tunnelling

The quantum tunnelling effect is illustrated on Figure 1.4 on the right (tunnel ionization). This particular phenomenon is provoked by the electric field of the incident laser beam. When the latter is powerful enough, it will be able to deform the conduction band, and thus lower the bandgap, transiently. This modification can be consequent enough so that the probability of an electron going through the bandgap is no longer negligible. Of course, the electric field being alternate, this deformation follows the oscillation [35,36]. Just as in the previous section, the ionization by quantum tunnelling is highly dependent on the intensity of the laser as it depends directly on the intensity of the electric field.
Models were developed to estimate the photoionization rate depending on the laser parameters such as the wavelength as well as the intensity. These models consider both phenomena in order to determine the quantity of free carriers created by the energy deposition of the laser and its electric field.

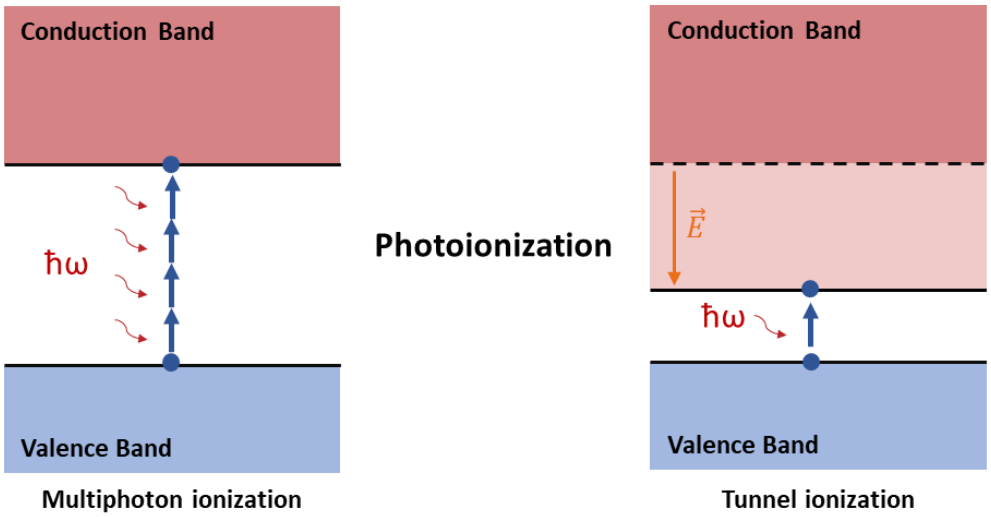

Figure 1.4. Schematic representation of two mechanisms involved in photoionization.

2.2 Electronic heating and electronic avalanche

The mechanisms corresponding to electron heating and electronic avalanche are depicted in Figure 1.5. These phenomena rely on the electrons that are already in the conduction band due to photoionization. Once they are *free*, they can absorb energy via several mechanisms to reach higher energy levels inside the conduction band. Indeed, once the bandgap has been overcome, the free carriers can absorb linearly energy from the photons of the laser irradiation, through collision mechanisms [37] and also by inverted Bremsstrahlung [38]. The latter takes place in the local electric field generated by an ion, the free electron can be accelerated by absorbing a photon of the laser beam. For inverted Bremsstrahlung to be significant, there must be a lot of free carriers, therefore, it generally takes place later on the interaction process once enough electrons have been promoted to the conduction band. This delayed occurrence enables the necessary accumulation of free carriers, ensuring a more consistent and pronounced manifestation of the phenomenon in the material.

Figure 1.5 represents the phenomena that occur leading to electronic avalanche. The very first one, involving the laser beam and the free carriers generated by photoionization, is heating. The free carriers linearly absorb energy from the photons. Indeed, the bandgap being already overcome, the electrons can absorb energy of any amount. Once a free electron has reached an energy level whose energy E responds to the inequality $E\text{-}E_C > E_G$, the electron, via collisions, can transfer this energy surplus to an electron on the valence band (I) getting it in the conduction band (II), this phenomenon is called impact ionization [39]. Therefore, by this chain of mechanisms, the population of free carriers in the conduction band is doubled. For an important number of free carriers going through the same steps, we can introduce the term electronic avalanche as the number of free carriers will increase exponentially.

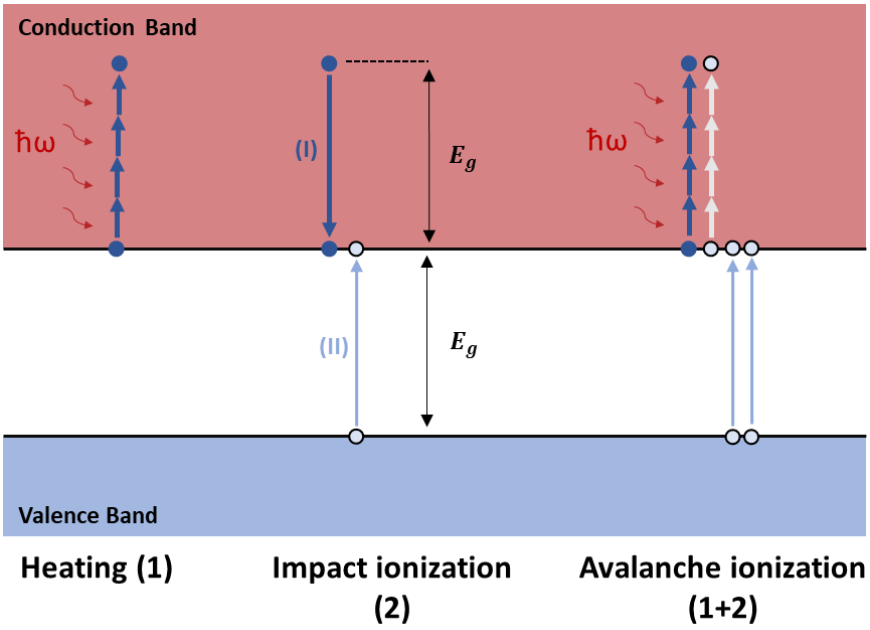

Figure 1.5. Schematic representation of the avalanche ionization. The first step is the heating of the free electrons through inverse Bremsstrahlung, the second is impact ionization leading to an exponential increase of the free carrier population (1→2→4→8…).

Once again, the parameters of the laser pulse are decisive for electron heating, especially the wavelength, the pulse duration as well as the intensity. Indeed, the wavelength determines the energy of each photon and, thus, determines the number of photons needed to be lifted to the required energy level. The pulse duration also impacts greatly the electronic avalanche. Indeed, contrary to photoionization, these processes require electrons in the conduction band to start with. Therefore, some time is required prior to this phenomenon, the pulse duration needs to be long enough so that these phenomena can occur. Figure 1.6 taken from [33] shows the rate of the different phenomena as a function of the pulse duration and pulse intensity. In this graph, $\mathbf{t_{MRE}}$ corresponds to the transition time between photoionization and impact ionization. The impact ionization rate can be determined by the following formula:

$$W_{II}(I) = \alpha\, n_e(t) I(t) \tag{2}$$

With $n_e(t)$ the free electrons density, I(t) the laser intensity and α the impact ionization coefficient. The latter can be estimated using the Drude model and needs to be calculated for each material. A pump-probe experimental study led by Lebugle et al. [40] revealed that the maximal electron density, for a wavelength of 1025 nm and pulses of 500 fs in fused silica, is

around 0.5 ps after the pump pulse. It is worth noting that the Keldysh parameter indicates which of the mechanisms, multi-photon ionization or impact ionization, is predominant [41]. In the case of dielectrics, quantum tunnelling is only significant for pulse durations below 100 fs.

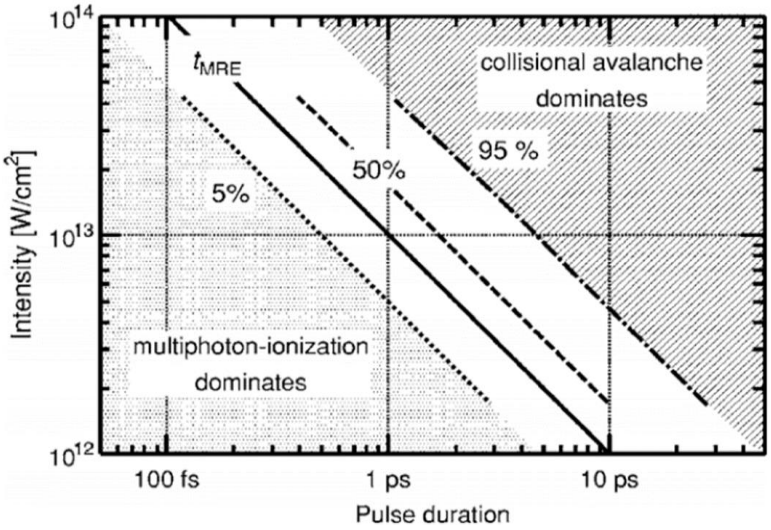

Figure 1.6. Comparison of the rate of multiphoton ionization and impact ionization as a function of the pulse duration and the pulse intensity. The model used is the multiple rate equation and it was plotted using a bandgap of 9 eV and a photon energy of 2.48 eV [33].

2.3 Electronic relaxation

Along with the ionization, generating free carriers inside the conduction band, electronic relaxation appears with an increasing number of electrons in the conduction band. Indeed, via multiple processes, an electron from the conduction band can get back to the valence band by losing energy [42]. More precisely, collisions can occur such as electron-photon (e-γ), electron-ion (e-i), electron-electron (e-e) and electron-neutral (e-n). One can define the collision frequency by summing up all the contributions as follows:

$$\nu_C = \nu_{e-\gamma} + \nu_{e-i} + \nu_{e-e} + \nu_{e-n} \tag{3}$$

The frequency of collisions highly depends on the electronic temperature as well as the number of electrons in the conduction band. One of the collision mechanisms will then predominate the others. For example, for electronic temperatures lower than the Fermi temperature, it is the electron-phonon collisions that prevails, meaning that the energy losses allowing for the electrons to get back to the valence band are mainly due to interactions with the lattice. When the temperature gets higher than the Fermi temperature, both the electron-electron and the electron-ion collisions predominate.

The electron-electron collisions are divided in two categories. On the one hand, the electrons of the conduction band can collide with the electrons in the valence band participating in an increase of the population of the free carriers (electronic avalanche). On the other hand, the electrons in the conduction band can collide between themselves participating in the thermalization of the free carriers gaz.

Electron-phonon collisions occur within the crystalline structure of solid materials at extremely high frequencies, typically in the range of 10^{14} to 10^{15} collisions per second [39,42,44]. These interactions are crucial for electronic cooling, where energy is transferred

from the electrons to the lattice, helping to dissipate excess electron energy and cool the system. This process facilitates thermalization, achieving thermal equilibrium between electrons and ions.

Following laser-matter interaction, free electrons in the conduction band can recombine with holes in the valence band. These recombinations, influenced by material properties, can evolve with continuing laser irradiation. Radiative recombination emits photons, with the energy of the photons corresponding to the energy gap between the electron's initial level and the valence band. Non-radiative recombination, on the other hand, releases energy in the form of phonons. The efficiency and nature of these recombinations are determined by the specific characteristics of the material, such as its band gap and presence of impurities or defects.

The presence of impurities inside the material or after the laser-matter interactions, can generate intermediate energy levels inside the bandgap. Furthermore, in bandgap materials, a pseudo particle can appear, the *self-trapped exciton* [45]. By Coulomb interaction, the hole (positively charged) and the electron (negatively charged) are linked creating another level of energy. An electron, trapped in these intermediate levels has a lifetime up to two times higher than a free electron in the conduction band [46]. The recombination rate is given by the following equation:

$$W_R(t) = -\frac{N_e(t)}{\tau_{STE}} \tag{4}$$

In this equation, N_e corresponds to the number of free carriers in the conduction band and τ_{STE} is the lifetime of a Self-Trapped Exciton.
Inside a material, during the interaction with a laser, the ionization and the recombination take place at the same time, the intensity of the laser and the absorption of the material has to be high enough to compensate these recombinations.

2.4 Electron density in the conduction band

Thanks to the previous sections, the electron density in the conduction band can be estimated using models that consider every process [47]. The electron density is a crucial parameter as it also acts on the absorption of the material. Indeed, for a low density of electrons in the conduction band, the absorption relies only on non-linear mechanisms while for an important population of free electrons, there is linear absorption which is much more efficient. The easiest model called Multiple Rate Equation, is described in the following equation:

$$\frac{dn_e}{dt} = W_{IMP} + W_{II} + W_R = \sigma_n I^N + \alpha\, n_e I - \frac{n_e}{\tau_{STE}} \tag{5}$$

This equation regroups all the terms we introduced in the sections preceding this one. Of course, like every model, the validity stands for adapted parameters and it requires adjustments for each configuration. One may notice that the intensity is the most important term of this equation as it represents a crucial parameter for non-linear absorption.

3. Femtosecond laser-induced ablation and bulk modification

When a gap material is exposed to a laser beam and non-linear absorption takes place, an energy absorption capable of modifying the material can be reached. This energy absorption leads to an increase of the population of free electrons in the conduction band. These mechanisms of absorption take place during the irradiation in our case during the pulse of about 500 fs. From the very beginning of the interaction one can distinguish three steps. The first step is the excitation of the electrons through photoionization and impact ionization [46,47], the second one is the heating of the lattice via electron-phonon collisions, and the last step is heat diffusion through the material [25,42].
The increase of the electron population in the conduction band induces a significant change in the dielectric function of the material, thereby causing modifications of the refractive indices that, in turn, influence the skin depth according to the Drude model. This phenomenon leads to energy deposition, either on the surface, following the Gamaly model, or in the volume. The temperature increase, likely due to the interaction with phonons, initiates a sequence of events, including decomposition, degassing, and eventually the formation of voids. The temperature gradient generates rapid heating and cooling causing thermal expansion, the creation of residual stress, and potentially the formation of cracks. The chain reaction continues with processes such as ablation, involving Coulomb explosion, phase explosion, or spallation. The diffusion of elemental species towards hot or cold spots results in local variations of the chemical composition and/or density, leading to changes in the real part of the complex refractive index [48,49]. This cascade of events culminates in the creation of defects, color centers, and variations in the imaginary part of the refractive index. These effects are particularly used for the formation of nanogratings. Note that in the case of bulk modifications, the volume in which the energy is deposited is much bigger than for surface treatment. Indeed, it was shown that the absorption volume exhibits a large comet upstream the focal point, especially for ultrashort pulses [50-53].
This complex sequence highlights the diversity of transformations induced by femtosecond lasers in materials, providing rich perspectives in applications and understanding the underlying physical processes.
These processes highly depend on the couple laser-material. Therefore, the laser process can be enhanced by carefully fitting the laser parameters (wavelength, pulse duration, energy of the pulse, repetition rate, polarisation) to those of the material. The temporal shape of the laser is also a very important parameter and will be discussed in section 3.3. Indeed, controlling the spatial shape and the temporal shape of the pulses helps improving the energy deposition, especially in the case of ultrashort pulses.

3.1 Coulomb explosion and phase explosion

After the absorption of the laser energy by the material, the matter ejection can take two forms, the Coulomb explosion and/or the phase explosion. Note that these two phenomena can happen simultaneously [54,55]. Let us have a look at both of them:

- For the very first nanometres of the materials, on the first atomic layers, it is the Coulomb explosion that prevails. Indeed, as depicted in Figure 1.7 (a), after the absorption of the energy, the most energetic electrons from the first atomic layers can

escape in the air leaving positive ions in the bulk. Electrostatic forces are then put in place, repulsive between these ions of same charge, and attractive between the electron cloud and the ions in the bulk. For an important population of ions created within the bulk, these forces are consequent enough to break the lattice and the matter will be ejected. The resulting craters usually have a depth of several nanometres. There is almost no residual heat since the thermal load is gone with the ejected matter.

- In the deep atomic layers, the energetic electrons are stuck in the lattice and cannot escape in the air, the heat is "trapped" deep into the matter. Thus, they contribute in heating the lattice as depicted in Figure 1.7 (b). Eventually, for enough energy absorbed, the lattice can reach the melting temperature or even the boiling temperature. In this case, the matter is ejected in droplets of melted matter or gas. This phenomenon, takes place within the skin depth and the resulting craters for phase explosion can reach up to several hundreds of nanometres [56,57].

One may notice that for the phase explosion droplets of different sizes are ejected. These droplets can land on the surface of the materials afterwards polluting it. This could demand a subsequent cleaning step after the laser processing.

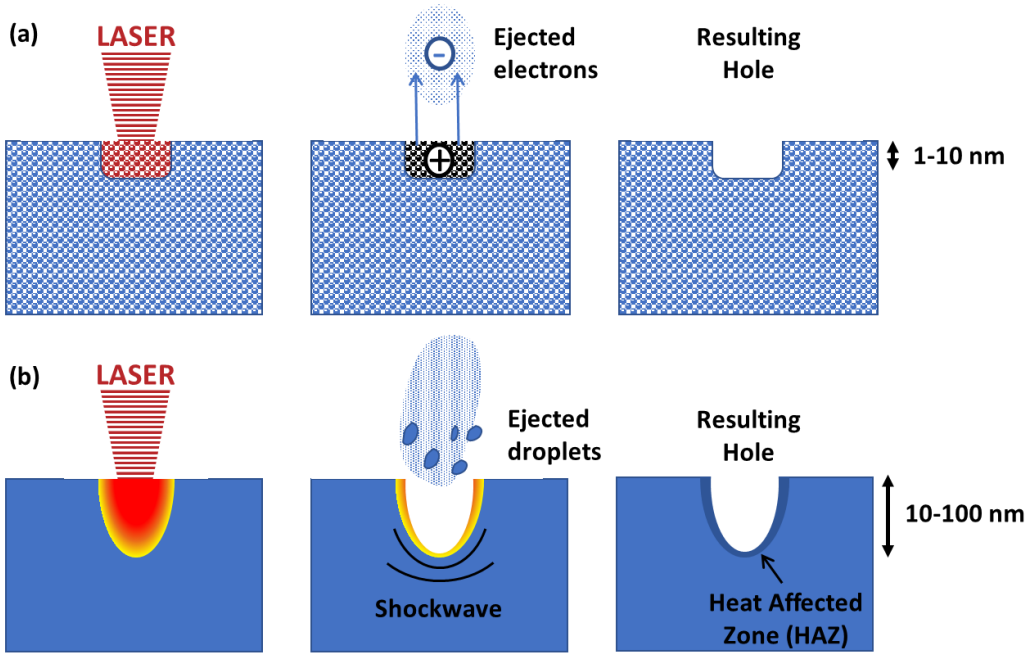

Figure 1.7. Schematic representation of the Coulomb explosion (a) and the phase explosion (b).

Note that the shockwave results from the reaction of the material to the matter ejection. After the matter ejection, some residual heat can remain near the ablation crater affecting the properties of the material in the Heat Affected Zone (HAZ). In many laser processes, the main goal is to reduce the HAZ as much as possible mainly for two reasons. The first reason is to reduce the damages around the processed area. Indeed, this could lead to a more efficient use of resources as it would increase the quantity of elements that can be produced within a given space. The second reason is that limiting the HAZ increases the precision of the process itself. Additionally, there is a final phenomenon that can result in the removal of material

through femtosecond pulses, known as spallation [58]. Essentially, the expulsion of material creates a recoil effect within the material (due to the conservation of momentum), leading to the propagation of a shockwave in the irradiated material, moving from the surface to the rear face of the sample. The rebound of this shockwave towards the irradiated surface may induce a fracture of the solid layer, and thus provoking the expulsion of material fragments; this phenomenon is referred to as spallation.
Of course, in reality, the interaction between a femtosecond laser pulse and a dielectric involves more processes. An extensive study of these mechanisms can be found in [59].

3.2 Femtosecond laser processing

Let us consider top-down processing in the femtosecond regime and compare it to nanosecond laser processing. In the former, the energy deposition remains contained in a volume close to the ablated volume due to the timescale. The heat diffusion does not have the time to get involved so the material is not damaged as displayed in Figure 1.8 taken from [60].

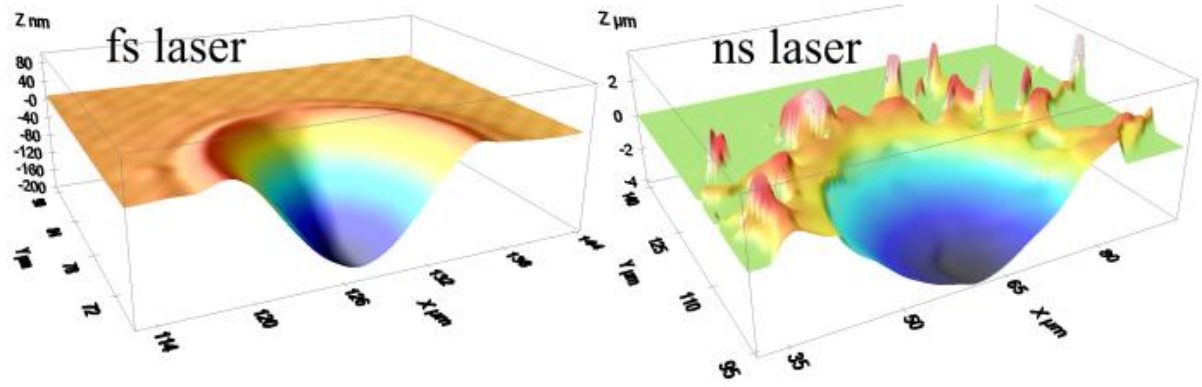

Figure 1.8. Comparison of the ablation crater for femtosecond laser and nanosecond laser for comparable fluences on a silicon sample [60].

These profilometer measurements depict the differences between femtosecond laser processing and nanosecond laser processing. One may notice that despite the general quality of the crater, droplets in the case of nanosecond processing also pollute the surrounding. Additionally, nanosecond laser processing exhibits burr and over-thickness which significantly lowers the processing quality. Although the thermal containment is one of the biggest advantages in the use of femtosecond lasers, it is also one of the points that keep the industry from applying them. Indeed, the low volumes of ablated matter (one may be careful while reading the two pictures in Figure 1.8, the scale bars are not the same) lowers the efficiency of femtosecond laser processing which is a crucial point for industry. Two solutions are mainly studied to develop the femtosecond laser technology in the industry to increase the throughput. The first one is an increase of the average power of the lasers in order to parallelize the processes. It consists in dividing the laser beam by means of a Space Light Modulator (SLM) or a Diffractive Optical Element (DOE) for multi-beam processing [61-64]. In the case of line engraving or surface structuring, a galvo scanner is generally used to exploit the laser beam. Depending on the average laser power, it is possible to divide the beam in thousands of beams multiplying by a thousand the efficiency. The other solution consists in

increasing the efficiency of the processes itself. The first step in this case is to apprehend the process. It is crucial to understand that laser processing is all about compromising. As a consequence, the yield of femtosecond laser processing is highly linked to processing strategies (On-the-fly, iterative, interlaced…) [65]. One should always consider the couple *laser & material* before trying to optimize a process meaning that the laser parameters should always be chosen with respect to the properties of the materials and the desired process.

3.2.1 Femtosecond laser processing of dielectrics

Femtosecond laser micromachining stands at the forefront of precision material processing, offering unprecedented capabilities at the micro- and nano-scale. This subsection provides an insight of the current state-of-the-art in femtosecond laser micromachining of transparent dielectrics. This technique exploits in-volume energy deposition thanks to multiphoton and nonlinear mechanisms, enabling the fabrication of intricate structures in a variety of materials. Moreover, three-dimensional microfabrication has become a reality through multi-photon absorption, offering unprecedented freedom in designing complex geometries. Nonlinear propagation processes, such as filamentation and self-focusing, have opened avenues for novel micromachining applications especially on transparent materials, which allow for an absorption on the surface but also in the bulk, including the creation of waveguides and other optical elements [66]. A non-exhaustive list of laser processes is represented in Figure 1.9.

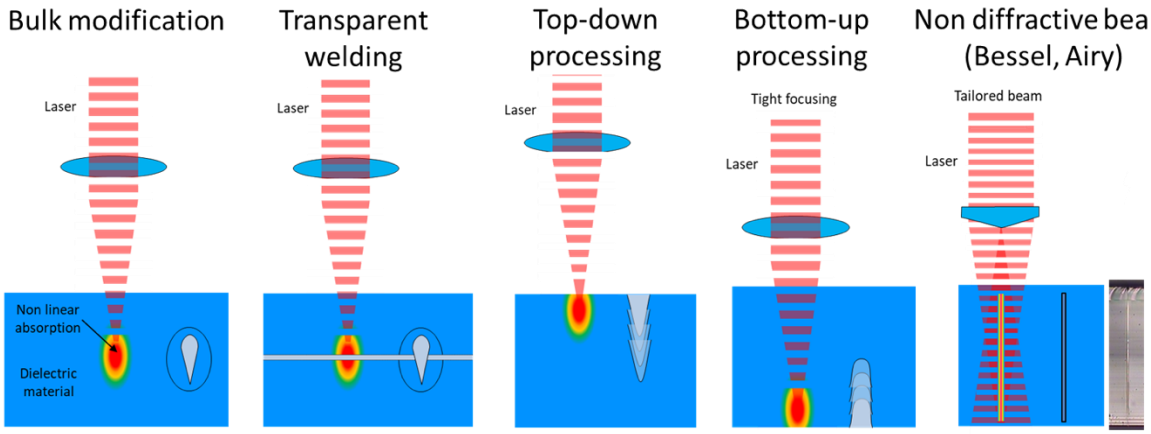

Figure 1.9. Schematic representation of a few femtosecond laser processes.

Numerous applications have been explored in the literature regarding bulk modifications, including alterations in the refractive index [3], 3D data storage [5-7,10] or fabrication of waveguides and diffraction gratings [8,9,11,50,66]. Intra-volume 2D marking involves inscribing patterns inside a three-dimensional material. Approaches to 4D (concept developed by Lionel Canioni) and 5D (pioneering work by Peter Kazansky) data storage introduce a temporal dimension into information writing and reading, offering advanced capabilities for data preservation and retrieval.

Transparent welding using femtosecond laser technology represents a cutting-edge approach in precision manufacturing and materials processing [5-13,19,51,52,67,68]. Unlike traditional welding methods, which often rely on mechanical fasteners or adhesives that can detract from the aesthetics and integrity of the material, transparent laser welding uses focused laser beams to create nearly invisible bonds. This method works by targeting a region close to the

interface between two components (at least one transparent), where the laser's energy is absorbed and converted into heat, melting the materials locally and allowing them to fuse without affecting the surrounding areas. This precise control over the welding process results in minimal thermal distortion and high-quality welds. The applications of transparent laser welding are vast and growing, particularly in industries where clarity and precision are crucial. In the medical field, for instance, this technology is used to manufacture sophisticated medical devices and instruments that require sterile, contaminant-free assemblies. In consumer electronics, transparent laser welding enables the creation of sleek, durable screens and casings for smartphones. Furthermore, this technique is environmentally friendly, as it reduces the need for additional materials like adhesives, thereby minimizing waste.

Top-down processing of transparent materials using femtosecond laser technology has emerged as a powerful method in precision microfabrication [11]. This approach involves the controlled removal or structuring of material from the surface down to the desired depth with ultra-short laser pulses [69,70]. This technique can provide either deep ablation such as drillings but it can also be limited to surface structuring in order to get new properties from a material (hydrophobicity, bacteriophobic, anti-icing, anti-fogging...) or for design purposes [71,72]. Surface structuring involves creating micro- and nano-scale patterns and textures, enabling precise manipulation of the physical and optical properties of materials. Laser-assisted chemical etching provides a precise method for sculpting complex patterns with high resolution.

Bottom-up processing of transparent materials using femtosecond laser technology represents a transformative approach in precision microfabrication [13,73,74]. In this innovative method, ultra-short laser pulses induce controlled modifications at the microscopic and nanoscopic scales, enabling the creation of complex structures from the rear surface up. This technique presents many benefits, for example, in bottom-up drilling we can expect a clean surface as the ejected matter is falling down from the sample. Moreover, this method could help creating taper-free or cylindrical holes without chemical treatment contrarily to top-down drilling.

3.2.2 Spatial beam shaping

Bessel beams, characterized by their central intensity core and ring-shaped structure, enable unique light propagation properties that can be harnessed for complex modifications in transparent materials [12]. This advanced technique involves the use of ultra-short femtosecond laser pulses to create non-diffractive Bessel beams, allowing for extended focal lengths and minimal energy dispersion. This method offers advantages such as reduced spherical aberration and enhanced depth of focus. Indeed, while a classical Gaussian beam depth of focus is usually limited to a few tens of micrometres, the Bessel beam shows an even intensity profile up to a few millimetres in length, experts in the field speak of a *nano-needle of light*. The use of a non-diffractive Bessel beam for microcutting offers the advantage of a dust-free and zero-kerf micromachining process. Such a Bessel beam can be produced by an axicon or a spatial light modulator and allows for an elongated and highly localized energy deposition over several millimetres thanks to its interferential character [18]. Indeed, this latter approach is already used for materials cutting [17,20,74,75], bulk modifications [19,76],

nanoholes drilling, or for high-aspect ratio drilling [21,77-79]. This spatial beam shaping technique can be used to enhance the energy deposition in a decisive way for glass cutting. The principle is then to produce an intense elongated and uniform bulk modification for micro crack appearance along the glass thickness with every Bessel beam.
While femtosecond laser micromachining has achieved remarkable advances, challenges persist. Scalability for mass production, optimization for diverse materials, and the development of in-line monitoring and feedback systems are areas requiring further attention.

3.3 Burst processing

In this section, we will discuss the temporal beam shaping called *bursts*. The latter refers to a pulse train with a high repetition rate (i.e. a low pulse-to-pulse delay). This regime allows for new degrees of freedom, pulse number, pulse duration, pulse repetition rate or energy distribution. By this means, the use of burst regimes in laser processing presents several advantages listed below:

- Improved ablation efficiency: Bursts can enhance material removal rates, especially in materials that are difficult to ablate with single pulses. The rapid succession of pulses can cause cumulative effects that improve the ablation efficiency.
- Reduced Heat Affected Zone (HAZ): The short interval between the pulses within a burst allows for effective material removal while minimizing heat diffusion into the surrounding material. This leads to a reduced HAZ and better precision in processing.
- Customization: The parameters of the burst, such as the number of pulses within a burst, the duration of each pulse, and the interval between pulses, can be customized to suit specific material properties and processing goals.

Overall, bursts in laser processing provide a versatile tool for improving processing efficiency and precision, enabling advanced manufacturing and material processing techniques.

3.3.1 The double-pulse regime

One can consider the so-called *double-pulse* process. The scientific literature has extensively covered the topic of double-pulse ultrafast laser irradiation on dielectric materials [80-97]. Various experiments have been documented in several materials such as fused silica, quartz, sapphire, and borosilicate glass. The principle involves the utilization of the first pulse to elevate electrons into the conduction band through multiphoton absorption. Afterwards, the second pulse induces the heating of free electrons through linear absorption and the inverse Bremsstrahlung mechanism, leading to material ablation. Factors such as intensity, pulse duration, and wavelength influence the occurrence of electron avalanches. In fused silica, for instance, the mean lifetime of free electrons in the conduction band is approximately 150 fs, resulting in a potential change in energy deposition when the second pulse arrives before electron relaxation. Existing studies suggest a modest positive impact on the optical breakdown threshold or removal rate for short pulse-to-pulse delays (0 to 600 fs). Stuart et al. recommend maintaining the intensity of the first pulse below the threshold. The distribution

of energy between the two pulses as well as the polarization significantly influence the ablated volume [60,80].

On metals, the double-pulse regime has been intensively investigated both experimentally and theoretically [81-96]. In 2021, a review paper on laser ablation on metals with single pulse, double-pulse and bursts has been published [97]. The latter shows the crucial parameters as well as the limitations of the double-pulse method on metals. It appears that, not only the energy repartition between the two pulses but also the pulse-to-pulse delay plays an essential role on the optimization of the ablation process. As detailed in this review, the ablation process can be apprehended in terms of shockwaves and rarefaction waves, a high energy single pulse generates an intense shockwave and thus an intense rarefaction wave which leads to the ablation process. Now, for the double-pulse regime with a combined energy comparable to that of the single pulse, the first pulse generates a weaker rarefaction wave which may not be intense enough to provoke ablation. Therefore, it is up to the second pulse to arrive at the right time to amplify this wave to ablate the material with a comparable ablated volume as the one obtained with a single pulse. In addition, the second pulse must arrive soon enough so that the ablation plume resulting from the first pulse has not taken off from the front surface of the material. This plume could linearly absorb the second pulse leading to a shielding phenomenon. The nature of the shielding (free electron, plasma or particle), will depend on the pulse-to-pulse delay [98]. In this case and for other inappropriate delays, the ablated volume can be much lower than that obtained with a single pulse with a comparable energy.

An extensive study was recently published with double-pulses in fused silica [99]. The latter investigates the removal rate in double-pulse regime for pulses with different wavelengths, by adjusting the pulse-to-pulse delay as well as the energy repartition. The authors worked with pulses at 515 nm and 1030 nm and investigated delays from -10 ps (the red pulse arrives before the green one) to 10 ps (the green pulse arrives before the red one). As a reference, they compared their results to the removal rate obtained with single pulses with the corresponding wavelengths. The take home message of this study is that the pulse-to-pulse delay is a key parameter regarding the ablated volume. They showed that a cooperative effect is indeed possible but only for short pulse-to-pulse delays. However, no matter the parameters investigated in this study, the ablated volume resulting from the double-pulse regime was lower than that of the corresponding single pulse, ruling out the double-pulse regime for increasing the yield.

3.3.2 MHz-burst mode processing

Another method consists in using bursts of multiple pulses at a MHz repetition rate so as to benefit from cumulative effects within the burst. Interestingly, this regime revealed an alternating behaviour of the maximum energy specific ablation rate ($\Delta V/\Delta E_{max}$) with high values for odd numbers of pulses in the burst and low values for even numbers of pulses [100]. This was interpreted as follows: the second pulse is fully or partially shielded but its energy clears the ablation plume such that the third pulse can be absorbed by the surface. The third pulse again generates an ablation plume, and the fourth pulse is therefore shielded again. The fourth pulse again clears the plume of the third pulse so that the fifth pulse can again contribute to the ablation process and so on [101].

Recently, a comprehensive investigation delved into the behaviour of stainless steel with pulses at a wavelength of 1030 nm, featuring pulse durations of 270 fs, 1 ps, and 10 ps for single pulses and bursts of up to 9 pulses, with a pulse-to-pulse delay of 15.4 ns. The findings revealed that the deposited energy in a specific volume, at peak fluences of 0.5 J/cm², 1.5 J/cm², and 2.5 J/cm², were highly dependent on the pulse duration. Interestingly, these volumes followed consistent trends as the number of pulses per burst increased. Depending on the pulse duration and peak fluence, distinct regimes were identified where the formation of a melt film resulted in smooth surfaces [102]. Comparable smoothing effects were previously documented for steel, cobalt and titanium alloys [103,104]. Interestingly, unlike copper or brass, no smoothing effect was observed, and the surfaces began to oxidize only when machined with MHz bursts. In contrast to double-pulses, the theoretical understanding of MHz-burst ablation remains unclear, necessitating further investigations with varied intra-burst delays to unveil the underlying physical mechanisms at play.

Laser processing of glass using MHz-burst modes has emerged as a highly effective technique for enhancing processing efficiency and quality. Another remarkable benefit of the MHz-burst mode is the minimization of thermal damage. The short intervals between the pulses concentrate the heat in a localized area, thereby reducing heat diffusion and minimizing the heat-affected zone (HAZ). This controlled energy input reduces the risk of thermal damage such as cracking, which is especially important when processing brittle materials like glass [12]. The localized heating effect also ensures that the structural integrity of the glass is maintained, which is critical in applications demanding high precision. This mode also allows for controlled surface texturing, which can modify the optical, mechanical, or adhesive properties of the glass to meet specific application requirements.

MHz-burst processing of glass features many advantages. It produces high-quality cuts and edges with minimal micro-cracking, making it highly suitable for applications in electronics and optics where edge quality is essential. For example, in the manufacturing of display panels, semiconductor wafers, and optical components, the precise and clean cuts enabled by MHz-burst processing are invaluable. This technology ensures that the delicate glass substrates used in these applications are not compromised by thermal stress or mechanical damage, thereby maintaining their functionality and performance.

Despite its advantages, MHz-burst mode processing of glass also presents some challenges. Effective thermal management remains critical to prevent overheating and to ensure the desired outcomes. Additionally, optimizing processing parameters such as pulse energy, burst duration, and repetition rate is essential for achieving the best results for each type of glass and application.

In summary, laser processing using MHz-bursts offers substantial benefits in terms of efficiency, precision, and quality. It addresses specific challenges associated with traditional laser processing, making it a valuable technique for advanced manufacturing applications across various industries, including electronics, optics, and medical devices. The ability to customize pulse parameters and to control the energy distribution precisely makes the MHz-burst mode a versatile and powerful tool in modern laser processing technology, especially for the intricate and delicate demands of glass processing.

3.3.3 GHz-burst mode processing

In 2016, Kerse et *al.* [23] already considered a new regime that they called *ablation cooling*. They started with the idea that a consequent part of the energy brought by the laser pulse is ejected with the ablated matter, leaving a *cold* and unaffected material. However, in classical ablation processes, this phenomenon is in competition with the heat diffusion. They stated that, "*The condition for being in the ablation-cooling regime is for the time delay between laser pulses to be small enough that the part of the material to be ablated does not cool substantially between successive pulses. If this condition is satisfied, heat extraction due to ablation becomes comparable to thermal diffusion from the processing region to the surrounding regions of the target material*." The authors gave the idea of using a pulse repetition rate within the burst in the order of magnitude of the GHz so that the heat diffusion can be neglected between two pulses. Based on this model of ablation they extracted three key points:

- A GHz repetition rate would optimize the usage of the energy of each pulse as there would be less heat diffusion within the material.
- The decrease of the energy lost in the material by heat diffusion allows for a reduction of the thermal effects on the surrounding material and a diminution of the heat affected zone.
- At fixed pulse fluence, an increase of the pulse repetition rate will increase the shielding effects. However, a diminution of the pulse energy and an increase of the number of pulses per burst allows for keeping a high ablation efficiency.

To validate their theory, they developed a custom laser producing bursts at 1.6 GHz and with a tunable burst length. Their own ablation experiment on silicon appeared to confirm those points as well as an increase of the ablation efficiency for pulses of about a third of the initial energy and a decrease of the thermal damages in the material. This very first experimental evidence of the existence of such a light-matter interaction regime led the way to nearly 10 years of development of GHz-burst sources.

3.3.3.1 Silicon processing with GHz-bursts of femtosecond pulses

Two years later, another study confirmed their hypothesis with experimental results on silicon with a custom laser source with bursts at 1.6 GHz [24]. They were able to ablate silicon and copper with pulses ten times below the ablation threshold with ablation rates surpassing the ones of repetitive single pulse regimes (1.8 mm^3/min/W in GHz burst mode versus 0.5 mm^3/min/W in repetitive single pulse mode). To follow up on this study, another one was realized by our group investigating the influence of the pulse number and the pulse repetition rate within the burst [105]. This study revealed an optimum combination of parameters, 200 pulses per burst at 0.88 GHz to obtain an even higher ablation rate of 2.5 mm^3/min/W. A more extensive study on GHz-burst mode ablation of silicon with a number of pulses per burst adjusted from 50 to 3200, a pulse repetition rate from 0.88 GHz to 3.5 GHz and a burst fluence from 8 J/cm^2 and 80 J/cm^2 was also published more recently [106]. This study relates that there is a burst duration threshold beyond which GHz-burst machining becomes beneficial for increasing the ablation rate compared to the MHz-burst mode or even repetitive single pulses. In these two last studies from our group, the authors proposed a model based on a

phenomenological approach for the temperature evolution within the material during the burst which is represented in Figure 1.10.

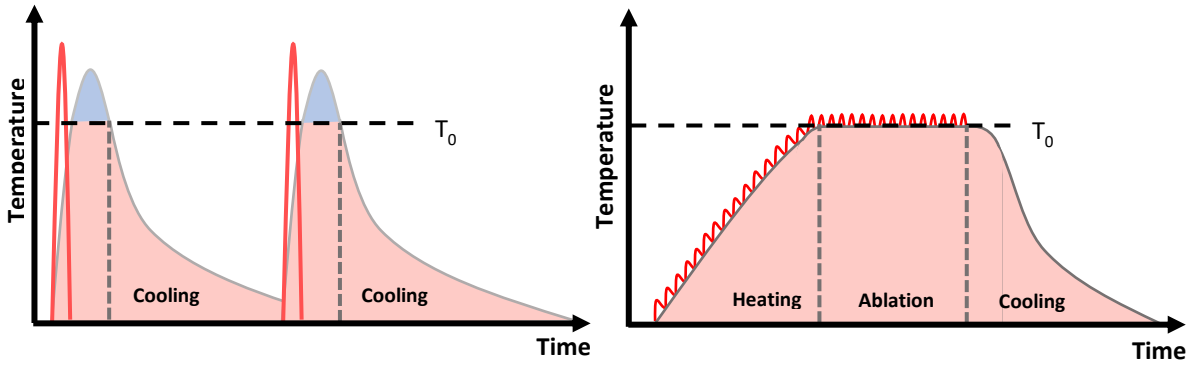

Figure 1.10. Schematic representation of the ablation process with single pulses and with a GHz-burst.

In the single pulse configuration, we can observe that a part of the energy is lost during the cooling step corresponding to heat diffusion. Another disadvantage is the inefficient usage of the energy. Indeed, each individual pulse has to heat the material up to T_0, the sublimation temperature, again and again. Any excess of energy, if absorbed, will only participate in an increase of the kinetic energy of the ejected matter. Therefore, there is an optimal value of fluence, close to the ablation threshold, for which the ablation is most efficient [107-109].
In the GHz-burst configuration, the heat diffusion between two pulses is negligible, the pulse N+1 will interact with a surface already warmed up by the pulse N and so on. In these conditions, less energy is required to ablate already hot material, the pulse train at a GHz repetition rate can ablate at a pulse fluence much lower than the ablation threshold. The usage of GHz-bursts appears as a good solution for minimizing the energy losses by thermal diffusion in the bulk [105,106].

3.3.3.2 Metals processing with GHz-bursts of femtosecond pulses

On metals, we can find a more exhaustive literature regarding the GHz-burst regime [100,101,106,110]. Basically, these four papers all provide the same observations as the studies realised on silicon. It appears that once again the pulse repetition rate and the burst duration are crucial parameters to benefit from the GHz-burst regime. Especially, here as on metals, the absorption of the laser is linear. Thus, the absorption of the energy is less dependent on the pulse energy.
Other studies show a lower ablation efficiency for GHz-bursts than for multiple single pulses, depending on the burst parameters, such as laser fluence and number of pulses per burst [111,112]. In these contributions, the authors attest to an important screening effect induced by the timescales involved in the GHz-burst regime (around 30 ns). However, in these experiments, bursts containing a very restricted number of pulses with rather high energy were applied. Therefore, in these studies the use of GHz-bursts showed less efficiency, and was even partly detrimental to the ablation quality. Thus, in such cases, the utility of the burst mode is very limited, as the energy repartition of the pulses within the burst is not optimized, and the beneficial accumulative effect cannot be exploited.
Milling and scribing applications were also studied with the GHz-burst regime on metals [106,110,113,114]. In reference [115], it was noted that a reduction in the removal rate was observed for stainless steel (>15%) and copper (>5%) when employing bursts with a pulse

delay of 1 ns (equivalent to a pulse repetition rate of 1 GHz) and varying energy distributions. Another study by Bonamis et al. highlighted a quite similar pulse delay of 1.13 ns (corresponding to a pulse repetition rate of 0.88 GHz), revealing that under specific conditions (high fluence and pulse overlap exceeding 70%), grooves were replenished with molten material [106]. This phenomenon was also observed in line scribing with a single pulse operation at a relatively high pulse repetition rate of 4.1 MHz [116].
Recently, a team of researchers carried out a study on copper milling by a femtosecond laser in GHz-burst mode [117]. It appeared that for milling experiments, the GHz-burst mode delivered contrasted results. Indeed, they observed an increase of the ablation efficiency but a decrease in the milling quality in terms of surface roughness. Those results are debatable by the quality of the parameters chosen to lead this experiment. Indeed, the pulse energy within the burst was probably too high to reach a sufficient quality.
For drilling experiments, there have been some studies indicating that the maximum energy-specific volume ($\Delta V/\Delta E_{max}$) can increase by a factor 3.5 in copper, this increase can get as high as 4.6 times in steel and for aluminum, it can reach a factor up to 5.8 when using the GHz-burst regime as opposed to single pulses [110]. This clearly confirms the hypothesis proposed in [23]. It was shown that the maximum energy-specific volumes attainable, employing a burst with 200 pulses at an intra-burst repetition rate of 1.76 GHz, are comparable to those achieved when using a laser with a pulse duration of 100 ns for percussion drilling of copper, aluminium, and stainless steel [106, 118].

3.3.3.2 Dielectrics processing with GHz-bursts of femtosecond pulses

On dielectrics, only a few studies were published. The very first use of pulse trains dates back to 1999 where *Hermann* et *al*. proposed the use of MHz-bursts of picosecond pulses to prevent fused silica from displaying microcracks during the drilling process [118]. We had to wait until 2020 to witness the first report of ablation experiments on dielectrics such as fused silica, borosilicate glass, sapphire and diamond [119]. In fused silica for example, a heat dissipation time in a range from 1 ns to 10 ns has been estimated, a pulse-to-pulse delay of 1 ns (corresponding to a repetition rate of 1 GHz) seems appropriated to obtain thermal accumulation [120]. In this scenario, the adjustable parameters were the number of pulses per burst and the pulse-to-pulse delay within a GHz-burst. These parameters govern both the peak power of the individual pulses and the total duration of the energy delivery. In the same year, an extensive study on several materials such as metals and glasses supported these excellent results [113]. In this particular study, they investigated the specific removal rate. Although the results were disappointing in metals following their previous study [121], in glasses they obtained promising results with bursts with a maximum pulse number of 25 pulses and a pulse repetition rate of 5.4 GHz. A year later, a team reported on milling applications on fused silica with bursts at 2.17 GHz [122]. This study revealed that the ablation efficiency could be enhanced by means of GHz-bursts. The maximum ablation efficiency in fused silica obtained with bursts of ten pulses was around 3 mm^3/min / W compared to 0.41 mm^3/min / W in single pulse regime. They revealed the existence of two ablation regimes, a gentle and a coarse ablation regime while for higher burst numbers, the material removal is dominated by breaking out the surface rather than ablation. However, by applying a pulse number of five they increased the ablation efficiency by a factor of 3.5 while keeping an adequate surface.

4. Conclusion

GHz-burst processing has shown significant promise for ablation of materials, such as glasses, metals and semiconductors. Research indicates that increasing the number of pulses within a burst can improve the ablation efficiency, though it may also increase the risk of damaging the processed area. Recent advancements focus on this new mechanism based on cumulative energy deposition and controlled thermal ablation, which aims to enhance the ablation efficiency while minimizing thermal damage. This approach leverages the high repetition rates of GHz-bursts to achieve precise, high-quality material removal with reduced heat-affected zones.

In this first chapter, I presented some essential theoretical concepts crucial for comprehending this manuscript. The focus was on various material types, with particular attention given to the materials directly relevant to this study, the gap materials. Additionally, I introduced the dynamics of electrons, recognizing their pivotal role in the interaction between gap materials and lasers.

I also presented an overview of the different types of laser processes that constitute the state of the art on which was based this work.

As can be seen in this chapter, only a few studies were realized regarding the use of the GHz-burst mode as a tool for enhancing laser processing. Moreover, most of them were realized on metals and silicon. The goal of this PhD work is to investigate the capabilities of the GHz-burst mode by means of several laser processes that are already mastered in the single pulse regime and/or in MHz-burst mode.

This chapter highlights the fact that the GHz-burst mode is subject to debate in the scientific community. Although a great potential for industrial applications has been foreseen in a recent review [123], some studies reveal that the GHz-burst mode could turn out detrimental for some applications. We suspect, based on previous work and literature, that these studies provided negative results due to a mismatch of parameters, meaning that they used bursts with too few pulses with too high energy. The objective here will then be to investigate processes that had not yet been studied such as percussion drilling or glass cutting in order to reveal the real potential of this new regime and try to understand the physics driving it. We aim to provide a significant contribution to the state-of-the art of GHz-burst processing thanks to our close collaboration with Amplitude.

Chapter 2: Material & methods

In this chapter, I will introduce the technical aspect of our experiments as well as the experimental setups that were implemented during this work. Indeed, this project started from scratch with an empty optical table at the beginning of this PhD. Therefore, we had to design, implement and set all the equipment that was needed during these 3 years. I will start this chapter by presenting the laser system that was developed by Amplitude and allowed us to investigate several laser parameters and especially the rather new GHz-burst regime with a large band of adjustments at our disposal. I will then get to the twin micromachining workstations we used for the drilling and the ablation-free cutting as well as the third workstation dedicated to pump-probe shadowgraphy. The twin workstations as well as the laser gate were controlled by means of an XPS-Q8 controller from MKS Instruments and the DMC PRO software that will be detailed in this chapter. I will also introduce the measuring equipment and the methods that we used to characterize the setups. The last part of this chapter will be dedicated to the different samples and different materials we chose to investigate.

1. Laser systems

The laser system we used is a prototype developed by Amplitude on the base of a Tangor 100. The later was customized to fit our demands. We were able to study three distinct regimes, the repetitive single pulse regime, the MHz-burst regime, and the GHz-burst regime, which are represented in Figure 2.1.

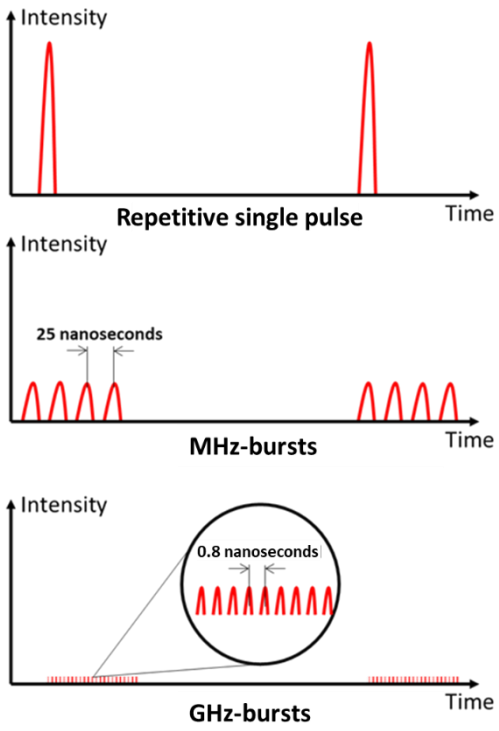

Figure 2.1: Schematic view of the energy reparation for the three regimes available with our laser.

In the repetitive single pulse (RSP) regime, the laser delivers pulses at 1030 nm with a pulse duration of 480 fs, a pulse energy up to 300 µJ and a repetition rate up to 2 MHz. In MHz-burst

regime, the laser delivers bursts of 2 to 24 pulses at 40 MHz with a pulse duration of 480 fs and an energy per burst up to 300 µJ. The repetition rate in this regime can get up to 400 kHz. Finally, the GHz-burst regime, in this case the laser system can deliver bursts from 50 pulses per burst (ppb) up to 800 ppb with a pulse repetition rate of 1.28 GHz and an optimized pulse duration of 530 fs. By adjusting the compressor of the Tangor we were also able to change the pulse duration within the burst in a range from 530 fs to 2.5 ps. In GHz-burst regime, the burst repetition rate is limited to 200 kHz. In all three regimes, the average power delivered by the laser is 100 W. Note that our laser system allows us to switch very easily from one configuration to another by following a simple procedure without changing the alignment. We only needed to switch the laser off and change the program on the arbitrary wave generator (AWG). These programs were edited by Amplitude, the only step left was to change the pulse picker repetition rate. The lowest value, corresponding to the highest energy per burst, is set to 200 kHz for the GHz-burst regime and 400 kHz for the other regimes. Lower pulse picker repetition rate could induce damages in the laser system. This enabled us to provide valid comparative studies as will be discussed later on.
Additionally, in GHz-burst mode, we have the possibility to change the energy repartition within the burst. This function allows us to have access to 4 types of bursts represented in Figure 2.2 (a,c,e,g) and Figure 2.2 (b,d,f,h) for the corresponding oscillograms for bursts of 100 pulses.

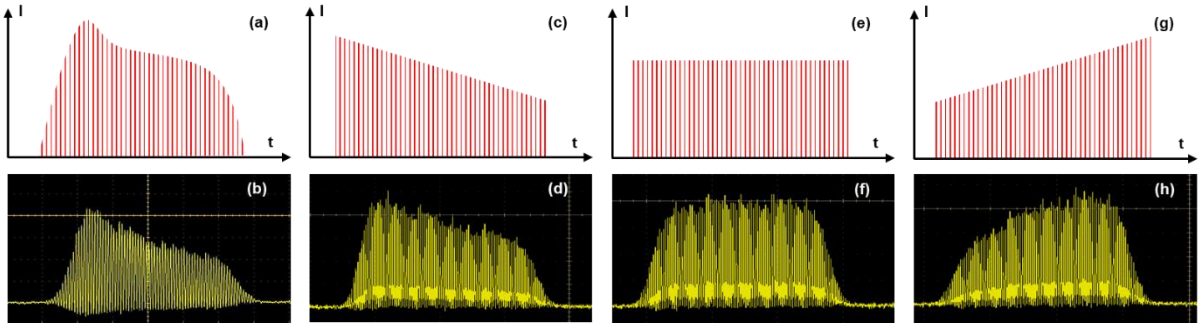

Figure 2.2: Schematic representation and measured shape of a classical burst (a,b), of a decreasing burst (c,d), of a flat burst (e,f), and of an increasing burst (g,h) for bursts of 100 pulses.

We chose these burst shapes for the following reasons. The very first burst configuration is called the *classical* burst shape. The latter is gain depleted, the shape of the burst is not processed by an arbitrary wave generator coupled to the first acousto-optic modulator. The *decreasing* burst shape was chosen in order to determine if higher energy pulses in the beginning of the burst would optimize the heating process of the material and thus the process. The *increasing* burst shape was also implemented to determine if lower pulses in the beginning of the burst could increase the overall quality of the process by slowly heating the material and keeping a reasonable ablation rate, with the high energy pulses at the end of the burst. The *flat* burst was investigated as a compromise between the two first configurations. Changing the laser configuration (regime or burst shape) doesn't affect neither the optical path nor the beam alignment from the laser to the sample. Therefore, for the comparative studies, for example, we can choose to work at a fixed burst energy and only change the number of pulses per burst (i.e the energy repartition within the burst).

The output of the laser is a Gaussian beam with a diameter of around 3 mm. The beam profile acquired with a beam analyzer (DAT-WinCamD LCM4) is depicted in Figure 2.3. The laser beam is then brought to the micromachining workstations by means of mirrors. The total transmission up to the workstations is nearly 90 %.

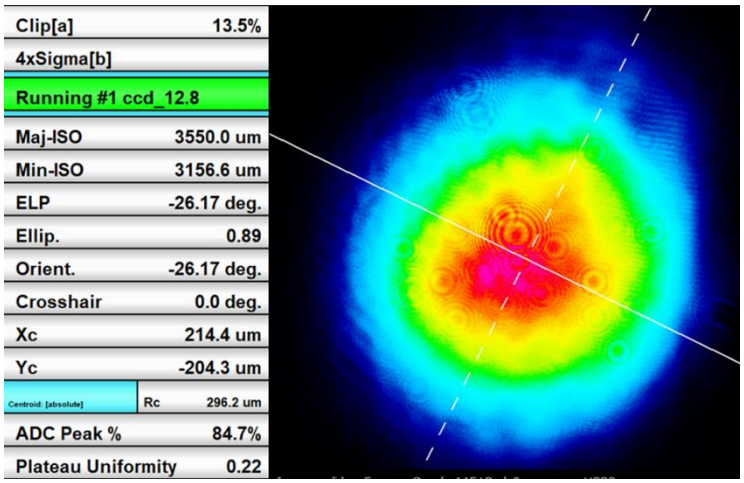

Figure 2.3: Beam profile acquired directly at the output of the laser system with the WinCam.

2. Micromachining workstations

This section is dedicated to the two workstations. From a practical point of view, the two workstations are twin stations whose design was inspired from another workstation that was implemented in a previous research project (ASTGV 2017-2021). The goal on these workstations was to implement a process (drilling, cutting, in-volume modification …) and as many diagnostics as possible to acquire un understanding of these processes. The workstations are based on a granite gantry designed by ALPhANOV and manufactured by Microplan. The laser beam is injected from the rear side and then goes to the front side through holes done in the granite structure by Microplan. The laser beam is then routed towards the processing module that is either Gaussian or Bessel beam and will be detailed below. Directly at the output of the laser, we installed a mechanical shutter for safety. The laser beam is then directed towards the workstations via mirrors.

2.1 Gaussian beam

For the drilling experiments, we used a microscope objective (Mitutoyo NIR APO 5x) with a maximal numerical aperture of 0.14 to focalize the laser beam. In order to benefit from the whole numerical aperture, we implemented a beam expander on the optical path so that we can adjust the beam size at the injection of the objective. This also enables us to study the effect of the numerical aperture of the different processes. We used a beam analyzer (DAT-WinCamD LCM4) to ensure that the beam was collimated after the beam expander.
In Figure 2.4, we display the experimental setup used for the drilling experiments. The part squared in dashed purple is the Seiwa focusing head. The latter is equipped with two dichroic mirrors, one letting the laser go through and reflecting the white light, and the other one reflecting the laser and half of the white light. A front CMOS camera (Basler acA1920-25mu, 1/3.7'' sensor, resolution of 1920 × 1080p, pixel size 2.2 µm × 2.2 µm, 25i/s, rolling shutter)

from top view allows for visualizing through the microscope objective and verifying the position of the laser focus at the front surface of the different glass samples. The microscope objective mount on the Seiwa focusing head presents a barrel of four rings that needs to be set so that there is no Z offset. Moreover, one needs to set carefully the Z position of the front camera with an adjustment ring. Indeed, to automatize the processes it is much more comfortable when the white light and the laser share the same focus position. The focusing head is mounted on a Z-motorized stage (VP25X, MKS Instruments, step-by-step motor) whereas the sample is fixed on a motorized XY-monolithic stage (One-XY60, MKS Instruments, brushless motor with encoder).

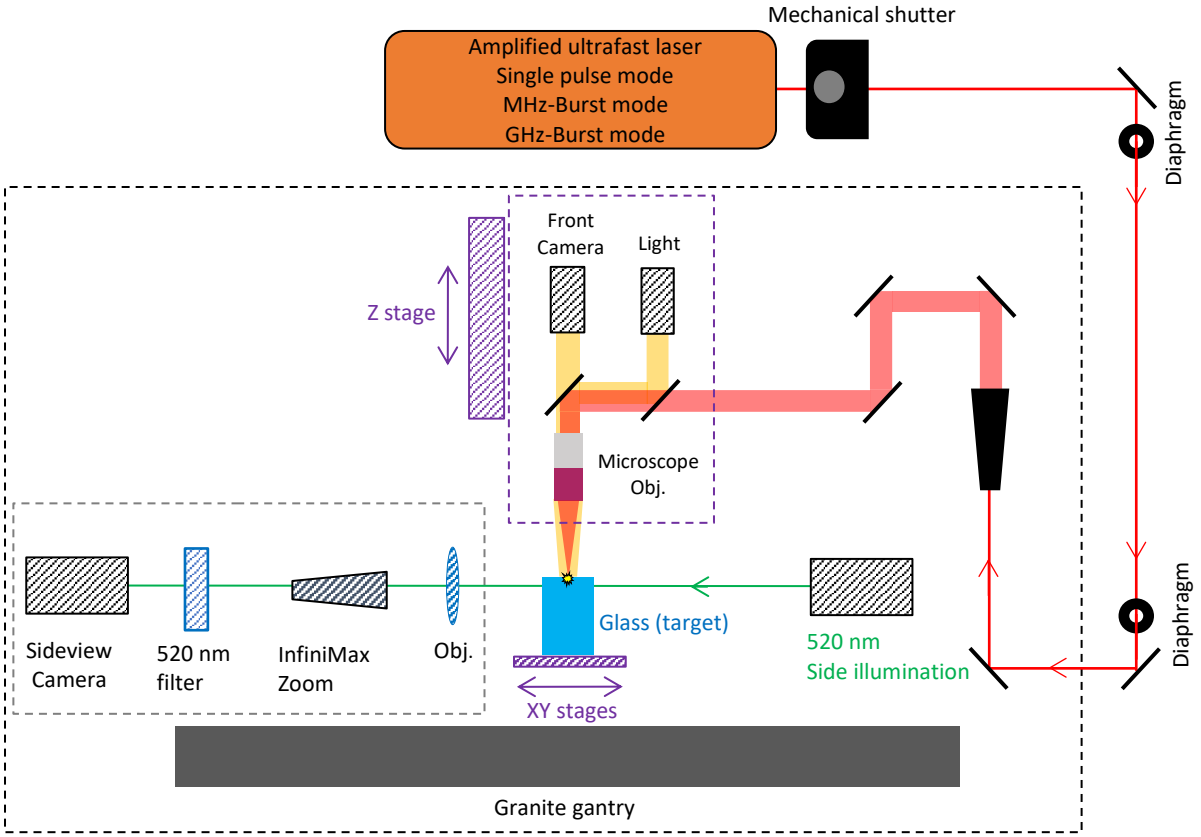

Figure 2.4: Blueprint of the experimental setup used for the drilling experiment.

On this figure, one may also notice a second camera. The latter takes part in the side view visualization system that is implemented in order to visualize directly through the samples during the processes. This system is equipped with a light emitting diode that emits at 520 nm. The imaging system is composed of an InfinyMax long distance microscope (InfiniMax KX with MX Objectives detailed in Table 2.1 in which FOV stands for Field of View in millimetres, WD for Working Distance in millimetres, DOF for Depth of Field in millimetres and NA for Numerical Aperture) with a 520-nm bandpass filter in order to visualize directly horizontally through the samples and not being blinded by the processing laser wavelength.

The XYZ-stages and the laser gate are controlled by the DMC PRO software (Direct Machining Control) coupled with an XPS-Q8 controller (MKS Instruments/NEWPORT XPS-Q8). The software allows us to take control of the whole system, translation stages, laser gate, cameras, or powermeter as well as different equipment that we implemented in the software with the help of the DMC team. Just as the rest of the equipment, the software had to be set

accordingly to our needs. We worked with the developing team to implement every device we used. In this software, we have the possibility to automatize different drilling programs, it is also equipped with the function *find focus*, meaning that during series of drillings, the laser focus can be adjusted before each single hole drilling during a drilling experiment series, reducing the uncertainty of the sample positioning. This increases the need to have the same focus point between the white light and the laser as this function is based on the sharpness of the image acquired with the front view camera.

	MX-1	MX-2	MX-3	MX-4	MX-5	MX-6
FOV (mm)	10	7.9	6.4	5.5	4.5	2.2
WD (mm)	315	250	174	169	134	65
DOF (mm)	0.24	0.15	0.08	0.07	0.043	0.023
NA	0.05	0.06	0.09	0.09	0.11	0.15

Table 2.1: Specifications of the MX objectives from Infinity. FOV stands for Field Of View, WD stands for Working Distance, DOF stands for Depth Of Field and NA stands for Numerical Aperture.

For the drilling experiments in silicon, we had to change the visualization system. Indeed, silicon is opaque to wavelengths < 1100 nm. Therefore, we used a LED at 1300 nm coupled with an Infrared camera InGaAs-based (WiDy SenS 320, NIT). This system allows to visualize directly through the silicon sample.

2.2 Bessel beam

The Bessel beam shaping module is mounted on the second granite gantry of the twin machining stations. In this case, the beam expander is used to directly change the final length of the Bessel beam itself as will be explained in Chapter 4. The entire workstation is depicted in Figure 2.5. Note that only the part that is mounted on the Z stage has changed with respect to Figure 2.4. Technically speaking, we use an axicon of 170 ° with a setup inspired from [13]. The axicon generates a primary Bessel beam with high dimensions and a low effective intensity. Such characteristics are not likely to generate non-linear absorption. Thus, we reduce the dimensions and concentrate the energy by means of a telescope-like system with two lenses. This particular experimental setup is highly dependent on the quality of the alignment. A comprehensive alignment protocol has been developed as well as a characterization method. Both these steps will be described in Chapter 5 for the cutting experiments. In this setup, one can notice that there is no front view camera. The adjustment of the position of the sample regarding the Bessel beam is done directly with the side view imaging system, but it is less critical.

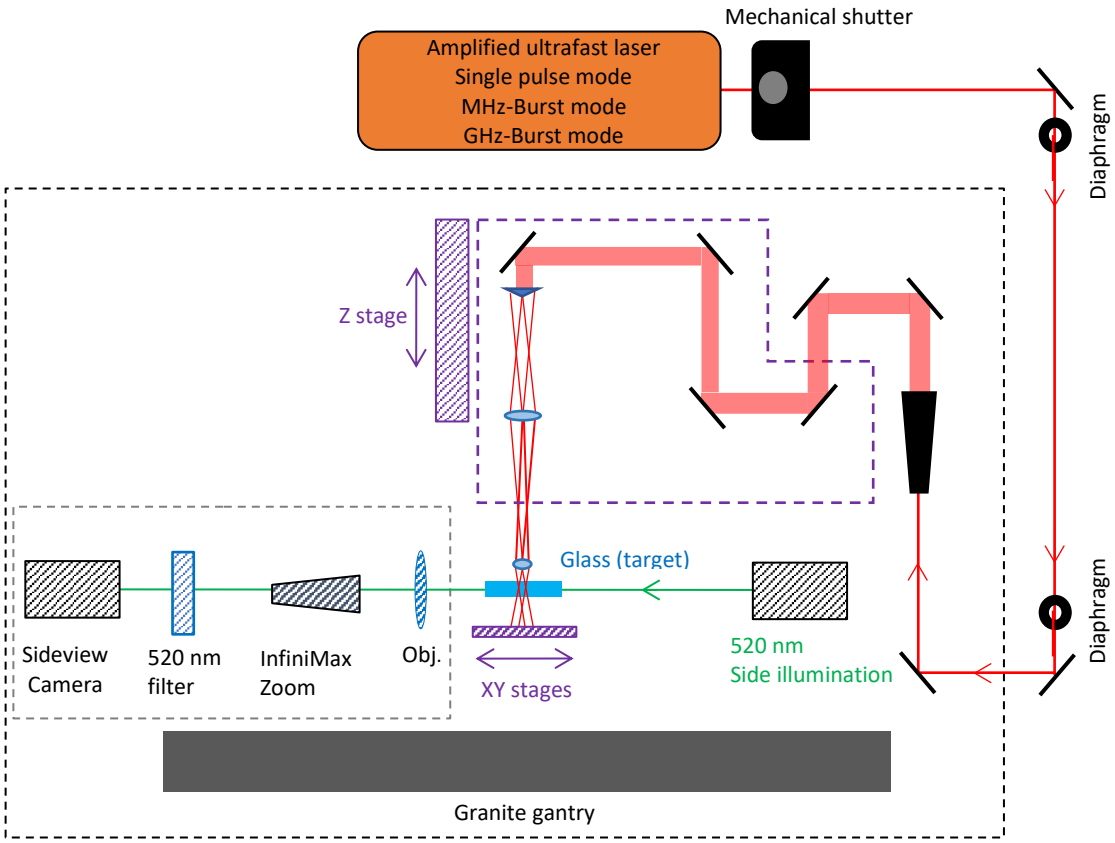

Figure 2.5: Blueprint of the experimental setup used for the cutting experiment.

2.3 Pump-probe shadowgraphy experiment

The pump-probe shadowgraphy setup was developed in the late days of this work but it represents the pinnacle of this PhD work. The principle of this experiment is based on previous work of our team [124,125]. This particular setup revealed several challenges. The very first one results from the laser itself. Indeed, in the framework of this PhD work, we needed to implement a pump-probe experiment with a GHz-burst pump and a synchronized single pulse probe. The point is that, technically speaking, the typical way to implement a pump-probe experiment is to use the same laser as a pump and a probe in order to prevent clock deviations from different oscillators. However, since we want the pump to be in a GHz-burst regime, we need to use a second laser source as a probe or we would have lost the time resolution, rendering useless the pump-probe experiment. Indeed, if the probe was a burst, the camera would have the time resolution of the whole burst duration (≈ 38 ns for a burst of 50 pulses at 1.28 GHz) instead of a single pulse (≈ 500 fs). Moreover, in a classical pump-probe experiment with a single laser, the delays are generally implemented with optical delay lines which is limiting the delay range to a few tens of nanoseconds (9.9 ns ≈ 3 m of propagation).
To successfully implement such an experiment, we needed to perfectly synchronize two lasers so that the burst emitted from the pump can arrive on the sample at the same time as the probe (or with a perfectly mastered fixed delay). In this optic, we decided to use the model of the Yuja (Yuja prototype, Amplitude) that is at our disposal. In order for the lasers to have the same clock (no jitter), we injected a portion of the oscillator of the Tangor into the Yuja. The Tangor was set as the pump and the Yuja as the probe. The model of the Yuja is only used as

an amplifier, composed of two amplification stages and a compressor, for the signal coming from the Tangor's oscillator. The point was that, to inject the oscillator of the Tangor into the Yuja, we used an optical fibre of 11 m. We then had to compensate the delay afterwards, both electronically and optically. The general architecture of both lasers is basically the same, after the 40 MHz oscillator comes first an Acousto Optic Modulator (AOM) called the *pulse picker* (PP) which has a maximal repetition rate of 2 MHz. The pulses selected are then amplified and a second AOM is positioned at the end of the laser right before the gate. This second AOM is called the *external modulator* (ModExt) and its repetition rate can go up to the value of the PP. The challenge here was to synchronize the pulse pickers and the external modulators of both laser systems to ensure a perfect synchronization of the system. In addition, we also had to synchronize the camera in order to acquire images at the right time. The principle of this method is schematized on Figure 2.6.

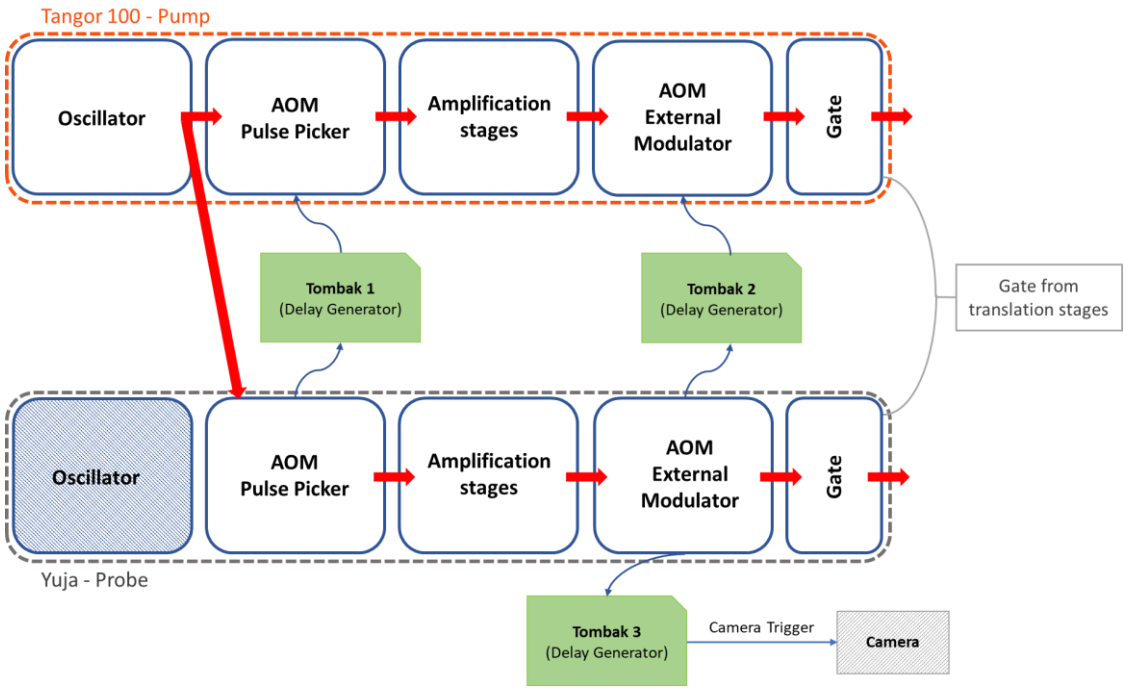

Figure 2.6: Blueprint of the experimental setup used for the pump-probe experiment.

One may notice that we used the signals taken from the Yuja, which acts as the master laser. Ideally, we would have chosen the Tangor to be the master, but the point here is that there is no input on the Yuja prototype to control the PP and the ModExt. As can be seen here, the core oscillator of the Yuja is shortcut and the portion coming from the Tangor oscillator is injected instead. This was the easiest way to synchronise the laser systems, otherwise, it would not have been possible as oscillation would start independently after each interruption of lasing. In addition, the software of the Yuja was much more difficult to shortcut as it did not allow for an external pulse picker signal nor an external modulator signal as it is a first prototype version. In order to ensure a perfect mastery over the delays and the synchronisation of the different stages of the lasers, we used two hardware delay generators (Tombak, Aerodiode). The first one controls the pulse picker, one should be very careful when setting this Tombak and set it with the amplifiers shut off so as to prevent any material damages. The delay on this Tombak can be adjusted in steps of 25 ns which corresponds to the period of the oscillator of the Tangor (40 MHz). The second Tombak controls the external

modulator located right after the amplifiers. This one can be set by steps corresponding to the period of the pulse picker (5 µs for a PP repetition rate of 200 kHz). All these settings were realized by means of two identical photodiodes (Alphalas, UPD-35-IR2-P) and a 4 GHz - oscilloscope (Waverunner 9404, Teledyne Lecroy) to check that the arrival of the pump corresponds to the arrival of the probe. The remaining delay between the pump and the probe, up to 25 ns if the PP and the ModExt are set, can be compensated by optical delay lines. We designed two optical delay lines, one for the pump in order to compensate the electronic delay resulting from the PP, and one for the probe so that we can study a large range of time delay after the interaction of the pump with the matter. For the pump optical delay line, we used a simple back and forth system with mirrors but the one for the probe is a bit more complex and is represented in Figure 2.7.

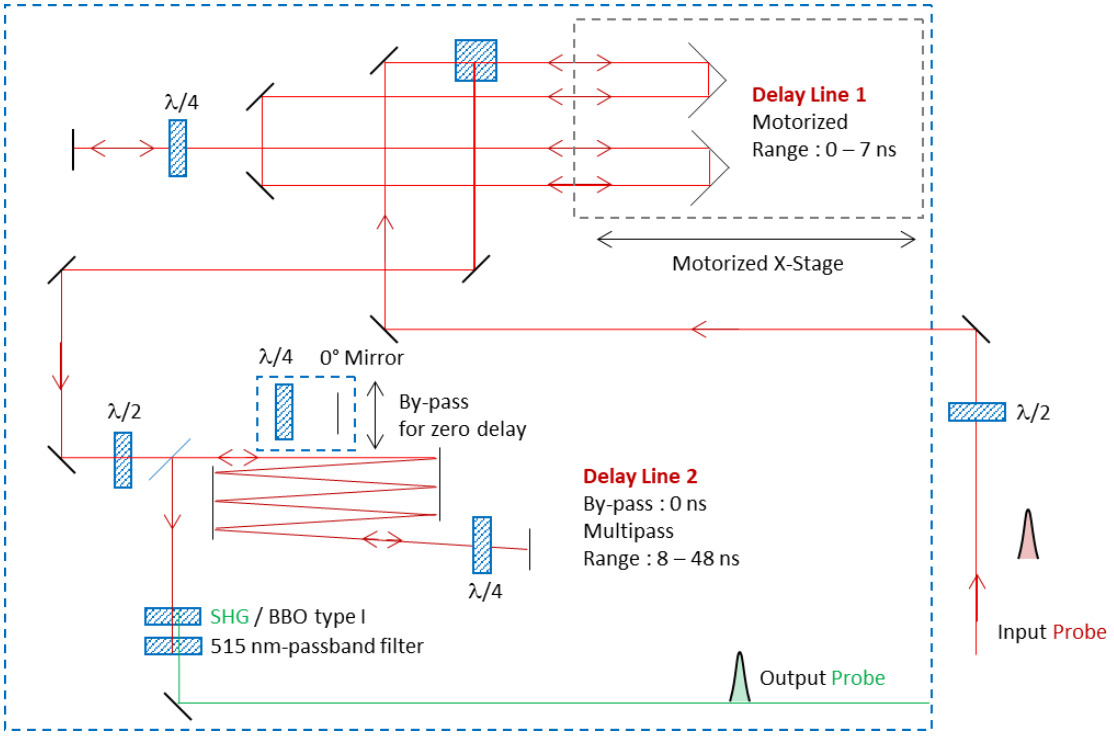

Figure 2.7: Blueprint of the experimental setup used for the 2-stage delay line of the probe [124].

In order to access a large range of delay, we used a 2-stage delay line. The first stage with a motorized stage for a delay ranging from 0 ns to 8 ns. The second stage based on back and forth with two rectangular tilted mirrors allowing us to reach to 48 ns delay. Note that since we control the pulse picker, to go even further in the delay, we can jump to the next pulse of the oscillator and induce a delay of additional 25 ns. Thanks to this system, we have virtually access to whatever delay we want since the pulse picker allows for 25 ns steps and our optical delay line has a range superior to 25 ns. The full setup is depicted in Figure 2.8 with the workstation. In addition, since we have a perfect mastery over the external modulator, we can easily get to an even higher step. For example, with a pulse picker at 400 kHz, the pulse-to-pulse delay gets as high as 2.5 µs. On Figure 2.8, we did not represent the synchronization of the lasers that was depicted in Figure 2.6 nor the delay lines for the pump for the sake of clarity. One may notice on Figure 2.8 that we use two bandpass filters at 515 nm in order to not being blinded by the processing wavelength nor the plume during the interaction. In addition to that, the camera parameters such as the gain can be appropriately adjusted in

order to amplify as less as possible the signal coming from the plume. The trick here is to amplify as much as possible the signal (the laser intensity) coming from the probe. By this means, we can reduce the gain of the camera on the Pylon software (Basler) so that the luminescence of the plume is less amplified.

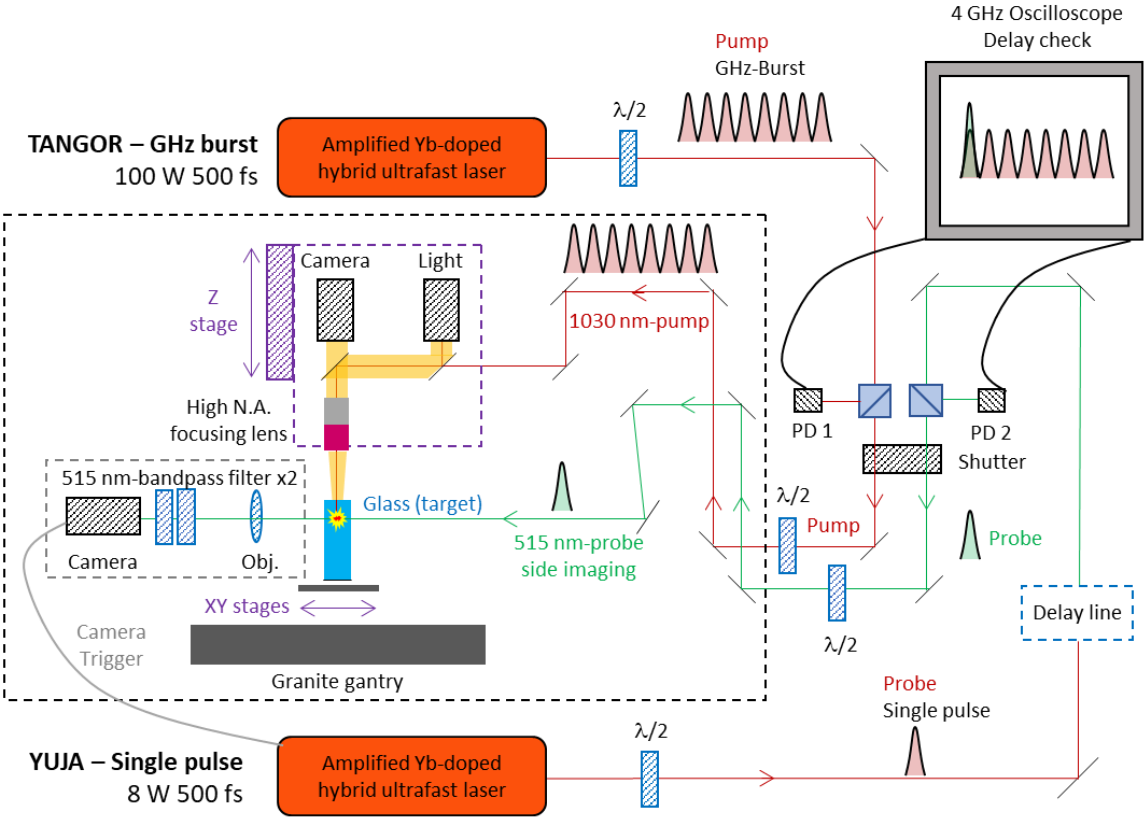

Figure 2.8: Blueprint of the experimental setup used for the pump-probe shadowgraphy experiment.

Regarding the camera, another challenge emerged concerning the actual acquisition process. It turned out that the two acquisition possibilities, *rolling shutter* and *global shutter release* are significantly different and must be well understood for the pump probe experiment to be successful. The schematic of these two acquisition processes is represented on Figure 2.9.

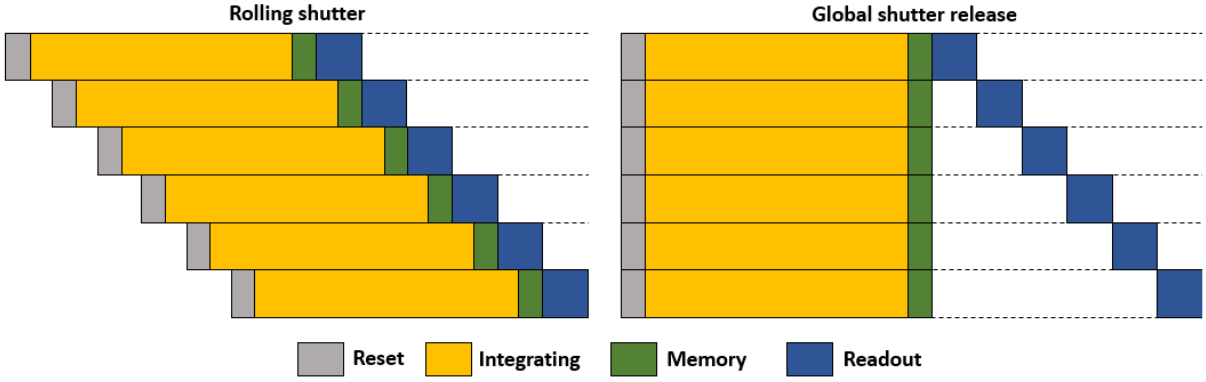

Figure 2.9: Blueprint of the two acquisition options available on cameras.

This figure shows the dynamics behind the image acquisition with a CMOS camera. As can be seen here, the rolling shutter option raises a problem. Indeed, the point here is that there is a delay between the acquisition of the first line and the second and so on. Thus, this type of

acquisition process cannot be used for the pump-probe setup. On the other hand, the global shutter release allows for a simultaneous integration of the whole buffer meaning that there is no delay between subsequent lines. In our case, it is absolutely necessary to use the global shutter. The camera we chose for this task is also a Basler (CMOS 1/2.9" 1440x1080p 220i/s) which has an acquisition rate close to 200. The exposure time was deduced to be 4.979 ms and we set a trigger delay of 0.021 ms on the Pylon software.

In pump-probe shadowgraphy, the *zero* delay needs to be defined. In our case, we chose to measure the delay with the photodiodes and an oscilloscope at the entrance of the micromachining workstation, and to correct the delay value considering the difference in optical path between this location and the target for both pump and probe. The uncertainty on the absolute zero delay is about 0.33 ns (1 cm). We define the absolute zero delay when the probe pulse reaches the sample at the same time as the first pulse of the pump burst as depicted below in Figure 2.10 with the corresponding oscillogram.

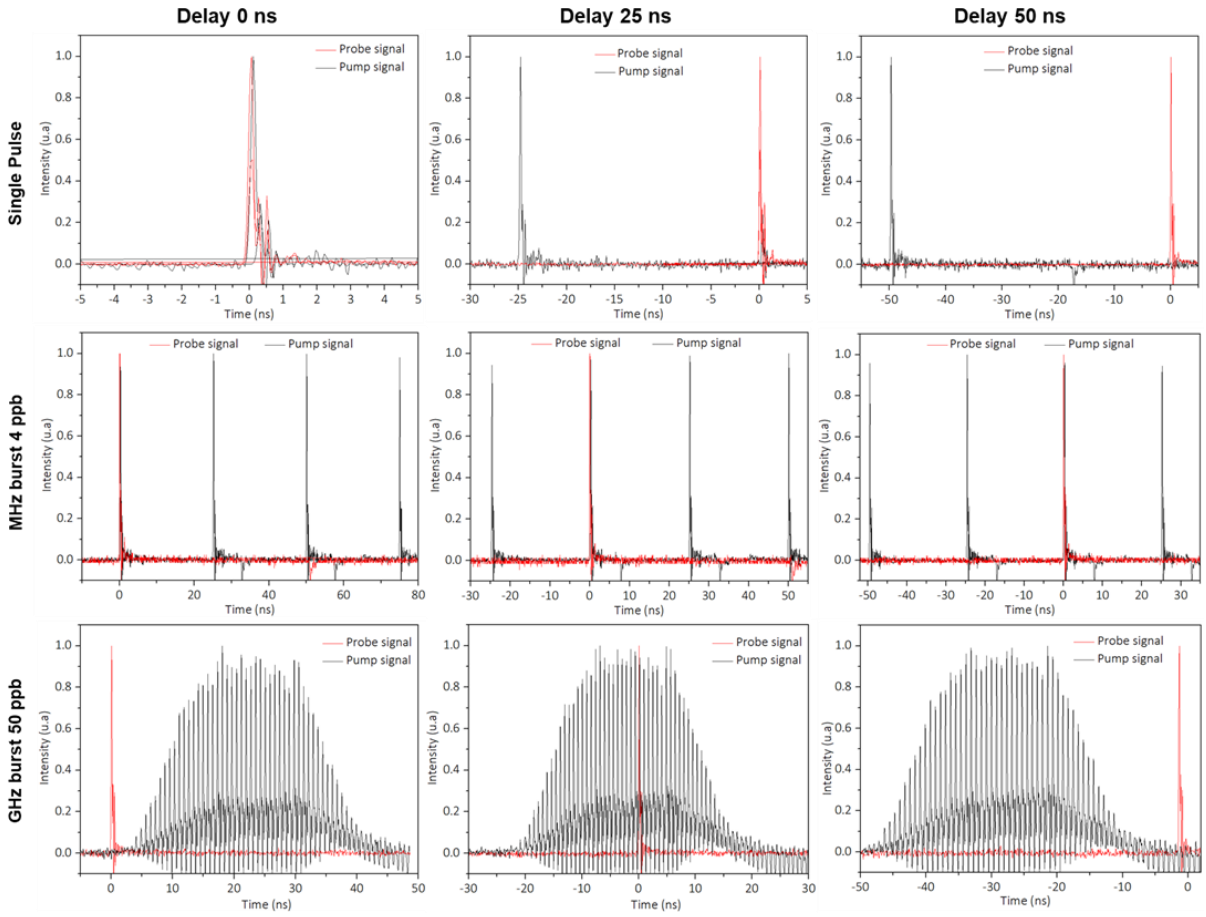

Figure 2.10: Oscillograms corresponding to delays 0 ns, 25 ns, and 50 ns, respectively, for the single pulse regime (top row), the MHz-burst regime with 4 pulses per burst (middle row) and the GHz-burst regime with 50 pulses per burst (bottom row).

This figure also contains the oscillograms corresponding to the delays of 25 ns and 50 ns between the pump and the probe signals acquired with the photodiodes. Note that on these graphs, the reference is the single pulse probe signal which is, by default, placed at zero on the scalebar. The delay measurement is then based on this reference. This choice was made due to the fact that the trigger for the acquisition with the oscilloscope was much more stable

when set on a single pulse. In addition to the delay measurement and setting, one can also clearly observe that the photodiodes and the oscilloscope can be used to check the number of pulses per burst in GHz-burst mode as well as the energy repartition. In this setup, the precision over the variation of the pump-probe delay results from the precision of the translation stage in the probe path which is ≈10 µm. This spatial precision corresponds to roughly 270 fs (4 round trips = 80 µm) which is an excellent resolution.

Note that the repetition rate of the laser for these pump-probe experiments has to be limited according to the camera specifications. Therefore, for pump-probe experiments, the repetition rate of the laser needs to be set to 200 Hz, which is the highest acquisition rate of the camera we use, so that we can see the impact of each burst.

On the other hand, for experiments that require a high number of bursts such as drilling experiments, the Pylon software allows us to reduce the number of pictures taken. We have the possibility to take 1 picture every 1000 bursts or so. Additionally, with the software we can make videos of the process or we can reconstruct the movie for a high number of pictures taken.

2.4 Experimental setup for 1700 nm

Bulk and backside processing of silicon remains a major issue in industry. One of the challenges is to work with appropriate wavelengths. With that in mind, we invested in an optical parametric amplifier (OPA) module from Amplitude to get to a wavelength superior to 1100 nm, in the spectral transparency domain of silicon. Thanks to this system, we have access to a wavelength of 1700 nm by injecting our Tangor in the OPA module. The initial idea was to inject GHz-bursts into the OPA to get GHz-bursts at 1700 nm. Combining a wavelength in the transparency domain of silicon with the GHz-burst regime could pave the way for silicon processing. However, the GHz-burst is not appropriate for such a frequency conversion. During the installation of the OPA, we observed that the GHz-burst regime at 1030 nm from the Tangor processes the crystal and thus prevents from frequency conversion. Therefore, the OPA is finally injected with the pump operating in the MHz-burst regime with 4 pulses per burst. The OPA has a yield of 10% to 15% and delivers bursts of 4 pulses at 40 MHz. To study the impact of the GHz-burst regime, we implemented delay lines to go from 4 pulses at 40 MHz up to 128 pulses at 1.28 GHz. The blueprint of the delay lines is depicted in Figure 2.11. In this setup, we use 10 polarizing beamsplitter cubes and 5 halfwave plates to control the energy repartition within the burst. Supplementary mirrors can be used here to cut arms of this setup. By this means, we have access to intermediate values between 4 pulses per burst and 128. Thanks to these mirrors, we can choose 8 pulses at 80 MHz, 16 pulses at 160 MHz, 32 pulses at 320 MHz, and 64 pulses at 640 MHz as well. However, these 6 configurations are the only ones that are accessible; we cannot investigate other numbers of pulses per burst nor other repetition rates.

First of all, the whole setup has to be aligned. This part is very challenging. Indeed, the really tricky part here is not to control the pulse-to-pulse delay but rather to obtain a perfect spatial overlap of all the laser beams resulting from the delay lines. Note that the overlap has to be aligned on the whole trajectory and not only at a single point. To ensure a perfect alignment,

each cube is mounted on small kinematic mounts. The point here is that, in addition to the setup needing some robustness, it also has to be compact to fit on less than half an optical table. Therefore, we choose 12.5 mm polarizing cubes with the corresponding mounts, which are nearly stuck together so that the cube-to-cube spacing matches the roof mirrors. To counteract the natural divergence of the 1700 nm beam, which is crucial here due to the long total optical path, we use a beam expander X 1 at the output of the OPA to ensure that the 2.5 mm beam expands as little as possible. The spatial overlapping of the 6 beams is controlled thanks to our beam profiler from Femtoeasy (SWIR 13.10).

After these painstaking and time-consuming steps of alignment, it is necessary to ensure the energy repartition within the burst. To do so, we use a powermeter and ensure the energy repartition in each branch of the setup.

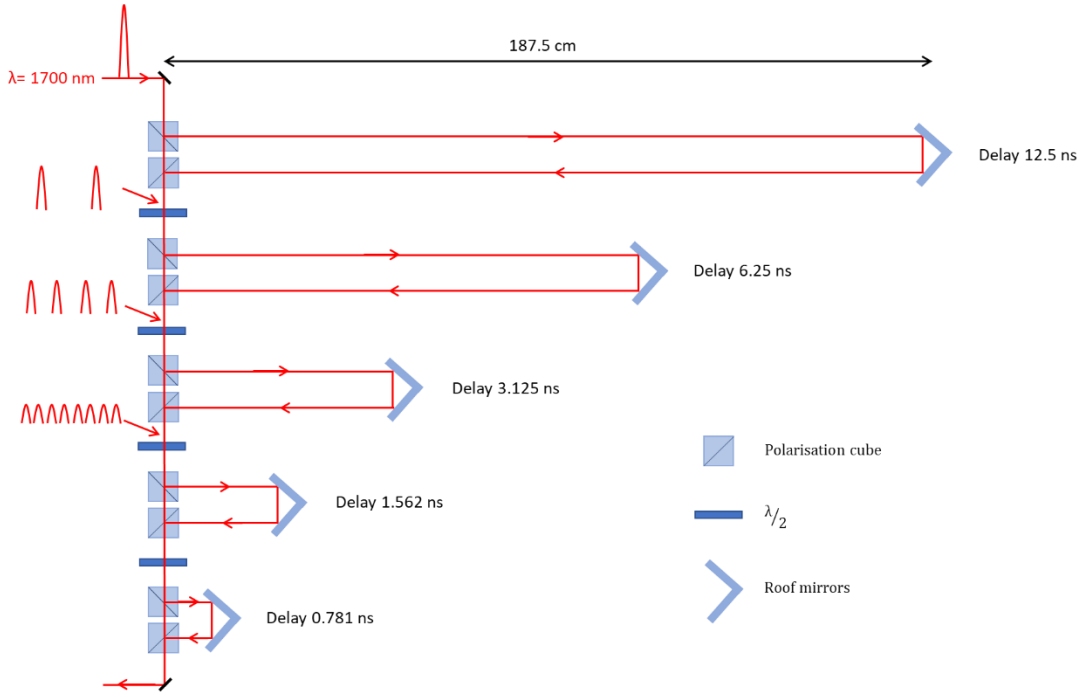

Figure 2.11: Delay lines used to get from bursts of 4 pulses at 40 MHz up to bursts of 128 pules at 1.28 GHz.

This particular setup is designed to investigate the interaction of silicon with GHz-bursts of femtosecond pulses at 1700 nm for in-volume modifications. Silicon is a very difficult material, first of all due to its very high refraction index. Therefore, to achieve in-volume modifications, it is necessary to use high numerical apertures. To do so, we use a set of microscope objectives from Mitutoyo, which will be presented in Chapter 4. Another challenge here is that such objectives have a low entrance pupil. Therefore, the beam size has to be adapted upstream to use the full numerical aperture. The point here is that it is very difficult to implement a beam expander after the delay lines due to working with 6 overlapping beams. As a consequence, the beam size has to be carefully set upstream of the cubes so that it matches the entrance pupil of the objectives at the very end of the experimental setup.

The output energy of the OPA is around 30 µJ per burst, meaning that each pulse has an energy of about 7.5 µJ. This value is quite low, but this could play in our favor as low-energy pulses are favorable for in-volume modifications in silicon as will be detailed later. Unfortunately, we

are not able to measure the pulse duration due to a lack of material, but we suppose that the pulse duration does not change much in the OPA, so we consider it to be around 500 fs.

3. Measuring equipment

In this section, we will introduce the different measuring equipment used for our experiments. This section is divided in two parts, first, we will present the measuring equipment used as a characterization tool (beam power, beam shape, pulse duration…). Then, in a second part, we will present the equipment used to characterize the samples.

3.1 Characterization tools

Beam characterization in laser processing is critical, especially in microprocessing. It is absolutely crucial to know each parameter such as the pulse energy, the pulse duration, the beam size or the energy repartition within the burst. In addition, for spatial beam shaping we need to analyse the spatial energy repartition.

- **Average power:** The average power measurements were realised using a powermeter, type Maestro from Gentec (UP19K-50F-W5-D0). Note that the pulse energy in either of the laser regimes can directly be deducted from the average power.
- **Pulse duration:** The pulse duration was directly measured using an autocorrelator from FemtoEasy (ROC).
- **Beam profile:** The beam profile was measured using a CMOS camera (DAT-WinCamD LCM4) with a sensor of 11.4 mm * 11.4 mm and pixels of 5.5 µm. This camera directly gives us the profile of the beam as can be seen in Figure 2.3. For experiments at 1700 nm we used our InGaAs based beam profiler from Femtoeasy (SWIR 13.10).
- **Burst duration and shape:** The burst duration and shape (energy repartition) was determined using an ultrafast photodiode (Alphalas, UPD-35-IR2-P, Rise time 35 ps) and an oscilloscope (Teledyne Lecroy, Waverunner 9404).
- **Intensity profile (Bessel beam):** To measure the energy repartition in the Z direction of the Bessel beam, we implemented an automatized acquisition with a translation stage and a beam analyzer.
- **Spot size:** The measurement of the beam spot sizes was a bit less direct. Indeed, in order to obtain a valid measure with a WinCamD-XHR beam analyzer, at least 10 pixels must be covered. However, with microscope objectives, we can obtain spots with diameters lower than 10 µm and the lowest pixel dimension at our disposal was 3.3 µm. The spot size was measured with a homemade calibrated magnification system as represented in Figure 2.12. This system was calibrated using a Mitutoyo reference sample. By using an objective 10X we obtain a magnification of a factor 10.

All this equipment allowed to produce robust results with reliable data. Before every publishable experiment we took care of characterizing as much as possible the laser system to prevent from deviations from the specifications given by the manufacturer. These characterizations also helped us to keep a clean setup and prevent any transmission losses that could occur during the use of high energies. Table 2.2 here below shows the spot size measurements realized for different beam diameters upstream the 5 X objective along with

the corresponding transmission of the whole setup. In this table, we added two different formulas for theoretical spot size calculation.

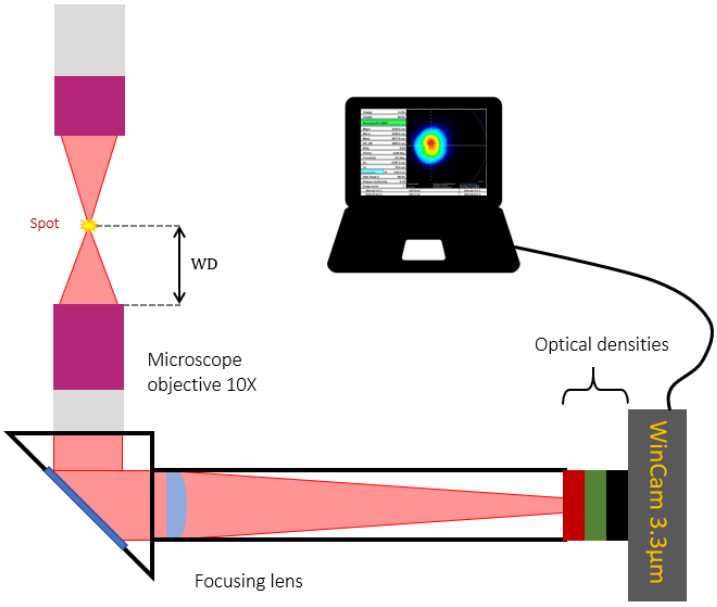

Figure 2.12: Schematic representation of the spot size measurement using our homemade calibrated measuring system.

The first formula corresponds to a diffraction calculation, the latter corresponds to large beams with a beam size quite close to the entrance pupil of the objectives, resulting in diffraction. The second one corresponds to a perfect gaussian beam which should be applied for lower beam size resulting in almost no diffraction.

$$Formula\ 1 = \frac{2.44.\lambda.f}{D} \tag{6}$$

$$Formula\ 2 = \frac{1.27.\lambda.f.M^2}{D} \tag{7}$$

Beam size (mm)	N. A	Spot size (µm)	Formula 1 (µm)	Formula 2 (µm)	T (%)
4.3	0.054	9.1	23.4	14.6	81
8.2	0.102	7.7	12.3	7.7	76
9.7	0.120	7.6	10.4	6.5	71
9.9	0.123	7.45	10.1	6.3	69
10.7	0.132	7.3	9.4	5.9	67
12	0.139	7.3	9	5.6	61

Table 2.2: Spot size measurement with the 5 X objective along with the corresponding beam size, numerical aperture and transmission of the setup.

As was expected, when the beam size upstream the objective is much lower than the entrance pupil, formula 2 corresponding to the perfect Gaussian focalisation is close to the measured value and even equal for a beam size of 8.2 mm. When increasing the beam size, the diffraction formula (formula 1) comes closer to the measured value. However, one can easily observe from this table that it is absolutely necessary to measure the real spot size as it differs from the formulas.

3.2 Sample characterization

Most of the experiments in this manuscript were realized on different types of glasses which will be introduced in section 4 of this chapter. The glass samples were much easier to characterize as a simple microscope can do most of the measurements. However, we also investigated silicon. In this case the measurements were a bit trickier as I will discuss here.

- **Hole depth:** The hole depth measurements in the case of glass samples were realized post-mortem on an optical measuring microscope (Mitutoyo, MF-B1010D) equipped with optical encoders with an accuracy of ±2.2 µm + 0.02L, with L the measured dimension in mm. This microscope, equipped with 20X or 50X objectives, also provides a good vision of the inner walls' quality.
- **Surface roughness and topography measurement:** Both topography and surface roughness (Sa) measurements of the sidewalls (i.e. the cutting planes) were performed using a confocal profilometer (ZEISS, Smart Proof 5) equipped with a 20X objective with a numerical aperture of 0.7. For samples exceeding a thickness of 500 µm, the sidewalls are wider than the measurement field of the confocal microscope, so the surface roughness Sa was estimated as an average on several measurements covering the full sidewall. The access to the profilometer was granted by Alphanov in the frame of the LabCom TRICORN.
- **Hole depth (Silicon):** In the case of silicon, the optical microscope cannot be used. Therefore, in order to estimate the depth of the hole, we used the side view imaging system as a home-made microscope coupled with the ImageJ software. By knowing the distance between the holes (by controlling it on DMC PRO software), we can estimate the depth of the holes.

4. Materials of interest

The major part of our studies was realized on **sodalime glass** which is among the most prevalent alkaline glasses, constituting approximately 80% of commercially available glass. It is composed of about 70% SiO_2 (silica), 15% Na_2O (soda), and 9% CaO (lime) However, this material is quite cheap and often displays composition variations. This glass is easy to work with due to a relatively low softening temperature (~750 °C) [126], exhibits good chemical stability, has moderate hardness, but is sensitive to thermal shocks due to its relatively high coefficient of expansion. It finds wide applications in the manufacturing of flat glass products such as windows and mirrors, as well as in the production of bottles and containers, representing 90 % of the total glass production.

We also worked on **fused silica**. Fused silica is a colorless glass composed of silicon dioxide (SiO_2), the sole constituent of the glass. Fused silica is synthesized and non-crystalline. Fused silica undergoes a heat treatment at 2000°C to reduce impurities and defects, significantly enhancing its purity. Noteworthy for its exceptional resistance to chemical agents (excluding HF and alkalis), low coefficient of expansion providing excellent resistance to thermal shock, high softening point (1665°C) [126], and outstanding optical qualities (refractive index, n=1.458), including high transparency in the ultraviolet range (for $\lambda<250$ nm). While it boasts excellent dielectric properties, its high cost limits its applications in electronics. Fused silica finds prominent use in optical and UV materials, serves as a fundamental matrix in optical

fibers, microstructured photonic fibers, or termination elements (endcaps), and is employed as protective glass in optoelectronics (e.g., UV-sensitive CCD sensors) and as a substrate in microfluidics.

Some experiments have been done on **alkali-free borosilicate** glass such as **AF32** from Schott since it is a widely used glass in consumer electronics industry (display and cover glass). This type of glass is also of interest due to the fact that its thermal expansion coefficient is quite close to that of silicon.

We extended the studies to three crystalline materials, **calcium fluoride (CaF_2), sapphire (aluminum oxide, Al_2O_3) and monocrystalline silicon**. CaF_2 and sapphire are two materials that play integral roles in diverse industrial applications (optical components, photography, defense…), owing to their unique and advantageous properties. CaF_2, recognized for its exceptional optical characteristics (wide transparency range, low refractive index, high laser damage threshold…), finds application in lenses, windows, and optical components, particularly in the ultraviolet and infrared spectra.

Sapphire, with its transparency spanning from ultraviolet to mid-infrared, is extensively utilized in optical components and laser systems. It serves as a substrate for gallium nitride in the semiconductor industry, plays a vital role in watch crystals, and finds applications in mechanical components due to its high hardness and wear resistance. Sapphire is also used as a cover-glass in luxury watchmaking for its scratch resistance and mechanical strength, in opto-electronics for the same reasons, and sometimes for its high thermal conductivity (40 times that of glass on average). The distinct properties of CaF_2 and sapphire make them indispensable in a wide array of industrial sectors, from electronics and metallurgy to optics and mechanical engineering.

Silicon, a fundamental element with remarkable properties, serves as the backbone in numerous industrial applications. At the heart of the electronics industry, silicon's crystalline structure and semiconductor properties make it the very base of integrated circuits and microelectronics. Silicon wafers, precisely engineered and processed, become the substrate for the creation of intricate circuits that power an extensive array of electronic devices, from computers and smartphones to embedded systems. The relentless pursuit of miniaturization and enhanced performance in the semiconductor industry pushes the boundaries of silicon's capabilities. Beyond microelectronics, silicon is a key part in the fast-growing field of photovoltaics, driving advancements in solar energy. Silicon solar cells, harnessing the photovoltaic effect, convert sunlight into electricity, contributing significantly to renewable energy solutions. Silicon's abundance and reliability make it a preferred material in the fabrication of solar panels, encouraging the transition towards sustainable power sources. Moreover, silicon plays a crucial role in power electronics, facilitating the development of devices for efficient energy conversion and transmission. In addition, compound semiconductors derived from silicon are gaining prominence in power electronics, offering advantages such as higher efficiency and improved performance in electric vehicles, renewable energy systems, and smart grids.

Micromachining of these materials is very interesting due to their broad range of applications across multiple industries. The precision and versatility offered by laser micro-machining contribute to advancements in technology and the development of compact, high-performance devices.

Chapter 3: Dielectrics percussion drilling

The primary goal of this drilling study is to comprehend the dynamics of percussion drilling with femtosecond lasers in GHz-burst mode and investigate its possible applications and limits. The later, by combining a pulse duration of the order of magnitude of the femtosecond and a burst duration in the range of nanoseconds, brings the possibility of combining excellent processing precision (fs) and high ablation rate (ns). Furthermore, one should notice that the pulse-to-pulse delay within the burst (0.8 ns in our case with a pulse repetition rate of 1.28 GHz) is quite close to the heat diffusion time in dielectrics (1-10 ns in fused silica) [120]. Therefore, one can expect a cumulative energy deposition. Additionally, this chapter aims to provide a comparative study between the repetitive single pulse regime (RSP), the MHz-burst regime, and the GHz-burst regime.

During this study, the major part of the drillings has been done with a rather low repetition rate. This was determined as a consequence of a prior study that revealed that some materials are sensitive to burst-to-burst heat accumulation and cannot handle high burst repetition rates as can be observed in Figure 3.1 for sodalime [124]. On this Figure, we display microscope images of holes drilled in sodalime with bursts of 50 pulses at 1 GHz at a burst fluence of 112 J/cm² and burst repetition rates ranging from 5 Hz to 200 kHz with a spot size of 7.3 µm and a numerical aperture of 0.14. The drilling time was adjusted so that the same number of bursts is applied to the sample for all the repetition rates. Ref. [124] was in preparation at the very beginning of this work (October 2021) and has been one of the bases on which the drilling study was led.

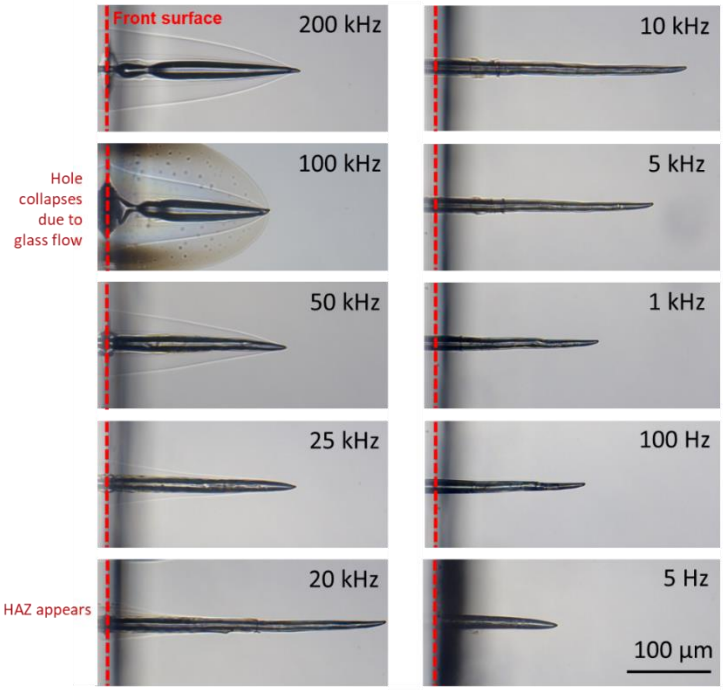

Figure 3.1: Microscope images of the holes drilled in sodalime with 1000 bursts of 50 pulses at a repetition rate of 1 GHz, a burst fluence of 51 J/cm² and a burst repetition rate ranging from 5 Hz to 200 kHz [124].

Increasing the burst repetition rate leads to burst-to-burst heat accumulation and temperature raise. This pre-heating has a beneficial effect on the drilling process and on the

hole length below 20 kHz, but it gives detrimental effects such as a heat affected zone (HAZ) appearance and shorter holes above 20 kHz. At repetition rates beyond 100 kHz, the temperature reaches the softening point (approximately 700 °C for sodalime) and then the glass undergoes deformation due to its own weight during drilling, leading to hole refilling approximately 50 µm below the surface. Some bubbles resulting from thermal decomposition of the glass are also trapped in the heat affected zone. If part of the energy is spent in the HAZ, this part is not available for drilling, and therefore, the holes are shorter when detrimental effects appear. Furthermore, the burst repetition rate beyond which these unwanted modifications appear is highly material- and fluence- dependent. The limit is about 10-20 kHz for sodalime, 50 kHz for AF32, 100 kHz for fused silica and 200 kHz for sapphire at a burst fluence of 100 J/cm². Moreover, in sodalime, the limit is about 20 kHz at 112 J/cm², 10 kHz at 220 J/cm² and 5 kHz at 330 J/cm².

1. GHz-burst mode percussion drilling

1.1 Influence of the burst number

We studied the evolution of the hole depth as a function of the number of bursts applied to the sample, and thus, with the increase of the drilling time. The repetition rate was fixed at 1 kHz, this value was chosen to avoid any visible HAZ at the entrance of the hole, and the drilling time was increased from 20 ms to 100 ms in steps of 10 ms. The fluence was 52 J/cm² in the case of sodalime and 136 J/cm² in fused silica. The spot size here is 7.3 µm with a numerical aperture of 0.14 and the focus is fixed on the surface of the sample during the whole drilling experiment. The resulting holes in sodalime and fused silica are shown in Figure 3.2.

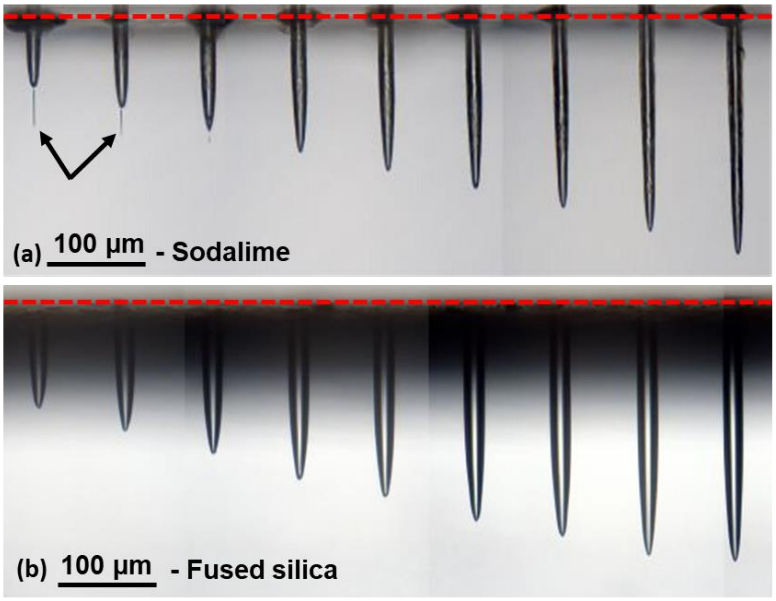

Figure 3.2: Microscope images of the holes drilled at a burst repetition rate of 1 kHz, with bursts of 50 pulses at 1 GHz and drilling times from 20 ms to 100 ms, in sodalime with a burst fluence of 52 J/cm² (a), and in fused silica with a burst fluence of 136 J/cm² (b) [124].

This figure depicts that the morphology of the holes is quite similar for both materials, the holes are cylindrical and there seems to be a linear evolution of the depth as a function of the number of bursts (20 bursts to 100 bursts). Drilling fused silica requires a higher fluence than

sodalime as its bandgap is higher (3.9 eV for sodalime [128] and 9.0 eV for fused silica [129]) resulting in a higher ablation threshold (3.6 J/cm² for fused silica, 2.9 J/cm² for sodalime [130]). Furthermore, fused silica has a lower thermal expansion coefficient which provides a better resistance to thermal dilatation and resulting shear stress [126].

One may notice, in Figure 3.2 (a), waveguide-like modifications indicated by the two black arrows. These modifications were created by the very first bursts and attest of a higher sensibility of sodalime. Regarding the morphology of the holes, we observe that it is very different from single pulse drilling as depicted in Figure 3.3 in sodalime. Indeed, the single pulse technology produces holes with a conical shape and very uneven inner walls. These pictures were obtained for the same fluence of 105 J/cm², drilling time of 1s and repetition rate of 1 kHz but for a GHz-burst of 50 pulses and single pulses. The energy of a single pulse has been divided in 50 pulses within the burst. This will be discussed in details in the comparative section.

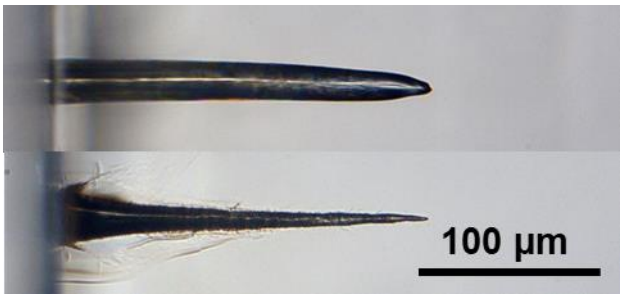

Figure 3.3: Hole drilled with GHz burst technology (top) and with single pulse technology (bottom) for the same fluences.

On Figure 3.4, we display the evolution of the hole depth as a function of the number of bursts received by the sample. The burst fluences were chosen in a range from 136 J/cm² to 339 J/cm². The whole experiment was controlled and automatized using DMC PRO. In these graphs we can see that, for a low number of bursts, the depth seems to follow a linear evolution, which we already observe in Figure 3.2. In a second time, the depth reaches a step for which the depth will no longer increase even for a higher number of bursts sent. On this figure, one may notice that the very firsts points with a low number of bursts are not displayed as there was no visible drilling up to a number of about 20 bursts. This value decreases for increasing fluence, for instance to 10 bursts at 171 J/cm² and down to 1 burst at 369 J/cm² in sodalime. One may also notice that the lowest burst fluence of 136 J/cm² shown in Figure 3.3 corresponds to a pulse fluence of 2.7 J/cm² as there are 50 pulses per burst, which is lower than the single-pulse ablation threshold for both materials. Processing at a fluence value below the single-pulse ablation threshold is characteristic for the GHz-burst regime and proves the outstanding accumulative character of the interaction process [102,103,125]. The uncertainty of the side-view measures with the microscope (± 2.2 µm + 0.02L, with L in mm) is neglected as it is more than an order of magnitude lower than the spreading due to the front surface, which has an average surface roughness (Sa) of 0.8 µm, and a peak-to-valley surface roughness (Sz) of 20 µm (measured with a Zeiss profilometer, objective 20x/NA 0.70).

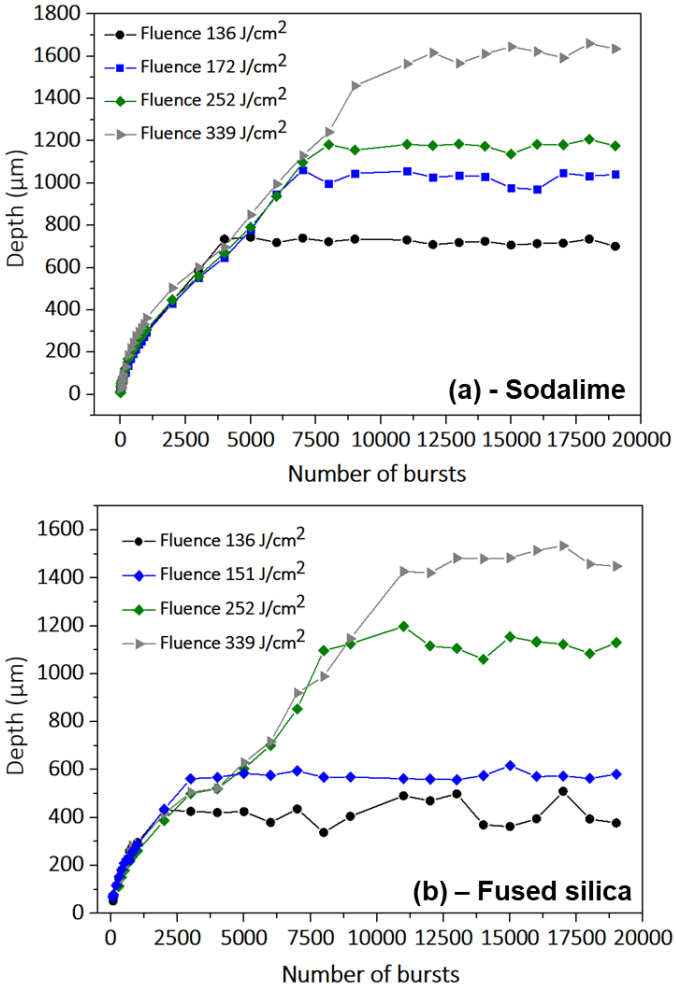

Figure 3.4: Evolution of the depth of the hole as a function of the number of bursts in sodalime (a) and in fused silica (b) at various burst fluences ranging from 136 J/cm² to 339 J/cm². The interburst repetition rate is fixed at 1 kHz, the number of pulses per burst is 50 and the burst repetition rate at 1 GHz for bursts of 50 ns.

Figure 3.5 represents the evolution of the hole depth as a function of the number of bursts sent at a fixed fluence of 151 J/cm² and an inter-burst repetition rate of 1 kHz in sodalime. The error bars (± 20 µm) on this graph origin from the front surface roughness and the accuracy of the focus position. The insert in Figure 3.5 shows a zoom on the evolution of the hole depth for small burst numbers and gives a closer look on the drilling mechanism. This graph reveals three stages in the hole formation which are indicated with three linear fits and are schematically illustrated in Figure 3.5. The first stage corresponds to surface ablation (red linear fit on Fig. 3.5, stage 1 on Fig. 3.6). The ablation plume can expand freely in the ambient air above the target. The drilling rate is high. The second stage corresponds to deep ablation (blue linear fit on Fig. 3.5, stage 2 on Fig. 3.6). The ablation plume is confined by the inner walls leading to a decrease in ablation efficiency. The drilling rate is lower compared to surface ablation (0.70 µm/burst for surface ablation versus 0.15 µm/burst for deep ablation). The drilling rate is almost constant during each of the first two stages. This hypothesis is supported by assuming a beam propagation inside the hole, according to previous work reported in literature, where the laser beam is subject to reflection under grazing incidence on the inner walls and multiple scattering [131-133].

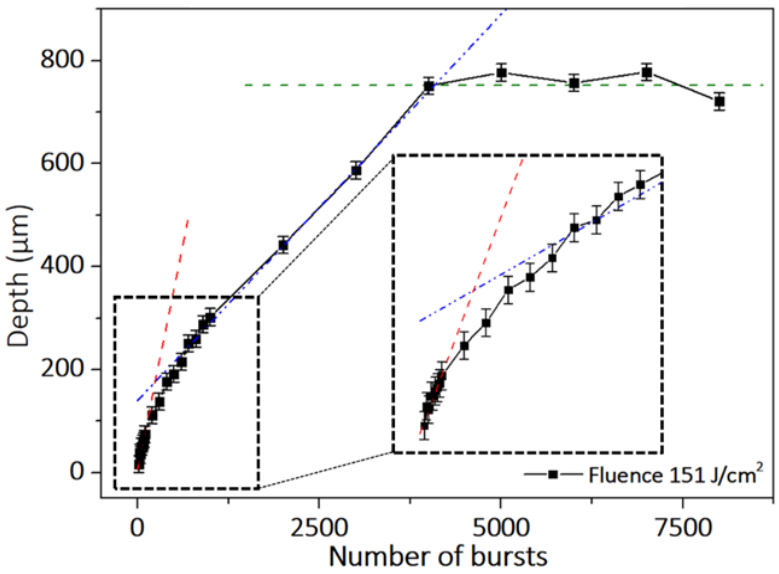

Figure 3.5: Evolution of the hole depth as a function of the number of bursts applied to the sample for a burst fluence of 151 J/cm², a burst repetition rate of 1 kHz, and a burst repetition rate of 1 GHz. The square in dashed black is a zoom of the first part of the graph.

However, at each reflection, a part of the energy is lost by refraction, and supplementary losses are also caused by multi-directional scattering. Therefore, the available energy for drilling decreases with increasing depth and the depth finally saturates as has been observed in polymers [132,133]. In the third stage (green linear horizontal fit on Fig. 3.5, stage 3 on Fig. 3.6) the drilling process is over as the effective fluence value at the tip of the hole is below the ablation threshold.

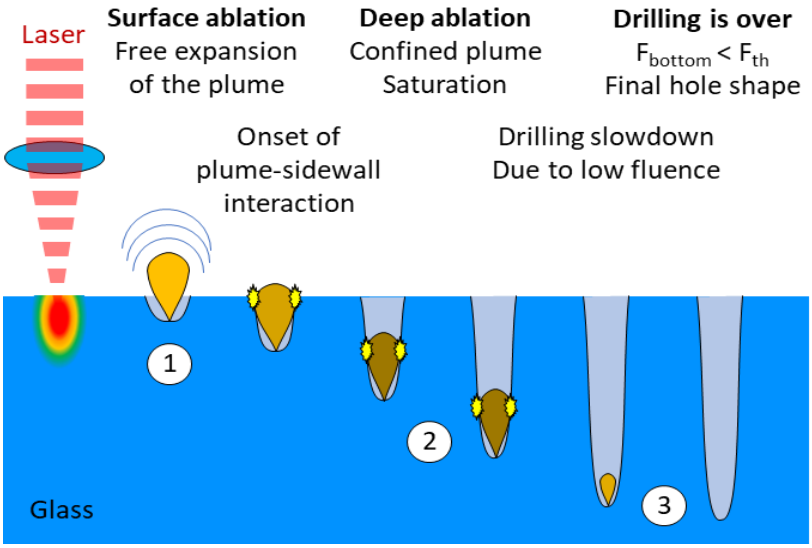

Figure 3.6: Schematic view of the three stages in the hole formation. Surface ablation with free expansion of the plume in the ambient air (1). Deep ablation and plume confinement due to plume-inner walls interaction (2). The confinement induces a saturation of the drilling rate. Termination of the drilling when the fluence reaching the tip of the hole is below the ablation threshold (3).

The intersection between the red and blue fits corresponds to the transition between surface and deep ablation (170 µm in sodalime) whereas the intersection between the blue and green fits corresponds to the termination of the drilling (745 µm in sodalime). Thanks to the linear

fits visible in Figure 3.5, we were able to estimate the drilling rates for the two drilling stages (the green linear fit rate is not considered as there is no more drilling). We summarized the values in the following table for the two glasses and for burst fluences ranging from 136 J/cm² to 369 J/cm². In both materials, we kept the burst repetition rate at a value of 1 kHz.

	Sodalime		Fused silica	
Fluence (J/cm²)	**Surface ablation rate (µm/Burst)**	**Confined ablation rate (µm/Burst)**	**Surface ablation rate (µm/Burst)**	**Confined ablation rate (µm/Burst)**
136	0.50	0.14	0.30	0.13
151	0.70	0.15	0.33	0.14
172	0.80	0.12	0.36	0.11
252	1.20	0.13	0.30	0.12
339	0.70	0.13	0.30	0.12
369	1.60	0.14	0.35	0.11

Table 3.1: Surface ablation rate and confined ablation rate for different burst fluences in sodalime and fused silica at a burst repetition rate 1 kHz for flat bursts of 50 pulses at 1 GHz.

This table was obtained for experiments with flat bursts of 50 pulses. It displays that the surface ablation rate is much higher in the case of sodalime. This can be explained by the fact that the ablation threshold is higher for fused silica as mentioned above [130]. One may also see that the values remain rather constant over the increasing of the burst fluence for fused silica. Regarding the confined ablation rate, we can observe that it seems to be rather similar for the two materials and constant over the increasing of the burst fluence, so the confinement has a real impact on the drilling rate. This table confirms that, even for pulse fluences lower than the ablation threshold of the two materials, we still observe drillings. This characteristic is very specific to GHz-burst ablation.

1.1.1 Hole depth and diameter

In this section, we studied the hole diameter with the same kind of study as for the depth. The burst repetition rate was kept at 1 kHz and we studied the evolution of the hole depth as a function of the number of bursts for fluences ranging from 136 J/cm² to 369 J/cm². The spot size is 7.3 µm with a corresponding numerical aperture of 0.14 as for the previous study. The resulting graph is depicted in Figure 3.7. The diameters were measured with the measurement microscope. In sodalime, we realized the measure at 10 to 20 µm under the surface. For fused silica, the measurements were done under the shadow part that appears near the surface as we can see in Figure 3.2. The uncertainty on the diameter corresponds to the accuracy of the microscope which is not represented on the graphs for the sake of clarity. On the beginning of the drilling, for a low number of bursts, the diameter increases rapidly with the increase of the number of bursts. On a second time, it reaches a saturation whose value increases with the burst fluence. The results for the maximum depth, diameter and aspect ratio of the holes in sodalime and fused silica for a burst repetition rate of 1 kHz are summarized in Table 3.2. We observe that both the diameter and the depth increase with the fluence.

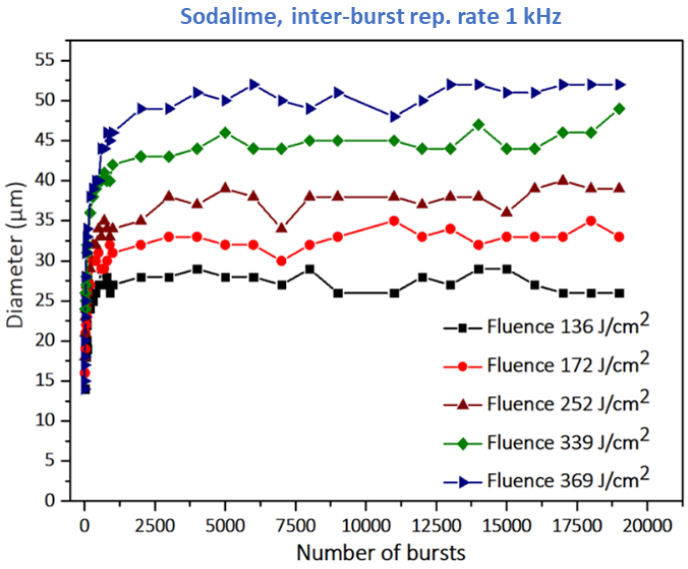

Figure 3.7. Evolution of the hole diameter as a function of the number of bursts in sodalime for fluences between 136 J/cm² and 369 J/cm².

One should notice that the diameters are different in sodalime and fused silica while the spot size remains the same. This can be explained by heat diffusion. Heat diffusion in fused silica is higher in fused silica than in sodalime (1.81 W/m/K in fused silica [128] and 1.42 W/m/K in sodalime [129]), this means that the heat diffuses faster in fused silica leading to an interaction volume close to the spot volume. However, in sodalime, there is a more important heat accumulation surrounding the spot. The aspect ratios obtained in these experiments were up to 37 for sodalime. However, the quality of the inner hole surface became rather poor with increasing fluence in sodalime. Figure 3.4 attests that fused silica seems to follow the same tendency as sodalime regarding the evolution of the maximum depth with an increasing fluence. Moreover, for this material, the maximum aspect ratio obtained in this experiment is 41 and the quality of the inner surface does not change with the fluence nor with the number of bursts applied on the sample.

	Sodalime			**Fused silica**		
Burst fluence (J/cm²)	**Maximum diameter (µm)**	**Maximum depth (µm)**	**Aspect ratio**	**Maximum diameter (µm)**	**Maximum depth (µm)**	**Aspect ratio**
136	27	744	28	21	510	24
172	33	1061	32	26	895	34
252	38	1207	32	32	1198	37
339	45	1660	37	38	1539	41
369	52	1520	30	44	1620	37

Table 3.2. Maximum diameter, maximum depth and aspect ratios for different burst fluences in sodalime and fused silica at a burst repetition rate 1 kHz for flat bursts of 50 pulses.

1.1.2 Hole quality

To get a closer look on the inner walls, we used a 20X microscope objective which gives us the image shown in Figure 3.8 (a). Figure 3.8 (a) depicts the holes obtained in sodalime for drilling times of 800, 900, and 1000 ms for a burst fluence of 270 J/cm². The spot size is 7.3 µm with a corresponding numerical aperture of 0.14. Figures 3.8 (b) and (c) show images taken for

drilling parameters set to a burst fluence of 270 J/cm² and for drilling times from 1 s to 15 s (from the left to the right) in sodalime and fused silica, respectively. The images framed in red are a zoom of the entrance part of the two holes for a drilling time of 7 s. We observe a very different quality of the inner walls for the two materials (Figure 3.8 (b) and (c)).

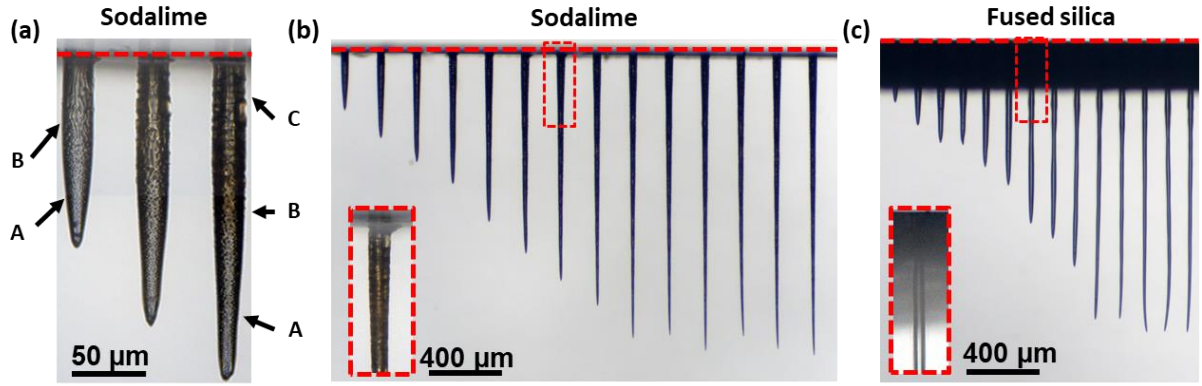

Figure 3.8. Evolution of the inner surface of the holes in sodalime at a burst fluence of 270 J/cm² for drilling times of 800 ms, 900 ms, and 1000 ms (a). Microscope images of the holes for burst fluences of 270 J/cm² and a zoom of the entry point for a drilling time of 7 s in sodalime (b) and fused silica (c), respectively [127].

In sodalime, the inner walls are structured (Figure 3.8 (a)), whereas in fused silica the inner surface remains smooth all along the hole. In sodalime, we distinguish three zones, at the tip the surface is bumpy (A), further up the hole in a transition zone, the surface appears rippled (B). Finally, the inner walls feature a groove-liked structure (C). These surface patterns remind of surface structuring of metals [134] and silicon [135]. Moreover, the inner texture of the hole depends on the drilling time as only the drilling time, and thus the burst number, increases from the first hole in Figure 3.8 (a) (left: 800 ms) to the third hole (right: 1000 ms). The difference of the inner surface quality induces different scattering losses of the beam during the drilling process in these two materials. The glossy surface of fused silica (Figure 3.8 (c)) allows for low-loss reflections and therefore a more efficient beam transmission towards the tip of the hole increasing its depth. This results in a compensation for the larger energy amount needed for drilling due to the higher ablation threshold of this material and the hole depth obtained on fused silica can be compared to the one on sodalime despite its higher ablation threshold.

1.2 Influence of the burst duration

We studied the evolution of the hole depth as a function of the number of bursts applied to the samples of sodalime and fused silica in a range from 1 burst to 10 000 bursts. The resulting holes for the two materials, using a classical burst shape with 300 bursts, 400 bursts, and 500 bursts, respectively, are depicted in Figure 3.9, for a burst fluence of 300 J/cm², different numbers (30, 70, 100, and 130) of pulses per burst (ppb) at a burst repetition rate of 1 kHz, and a pulse repetition rate of 1.28 GHz within the burst. The spot size is here again 7.3 µm with a corresponding numerical aperture of 0.14. The holes on these images present all an excellent quality without exception. Moreover, one can clearly observe a very different morphology of the holes obtained with standard repetitive single pulse femtosecond technology [124]. Indeed, the holes here are cylindrical for both materials and the inner

surface is very smooth, even glossy in fused silica. In addition, one may notice the absence of a heat-affected zone surrounding the holes. In sodalime, we distinguish some structures of the inner walls, but the tip remains smooth. These images attest that the number of pulses per burst seems to have no impact on the general morphology of the holes. However, in a range from 300 to 500 we can observe that for longer bursts, the depth seems to increase, which validates the results found in Ref. [119].

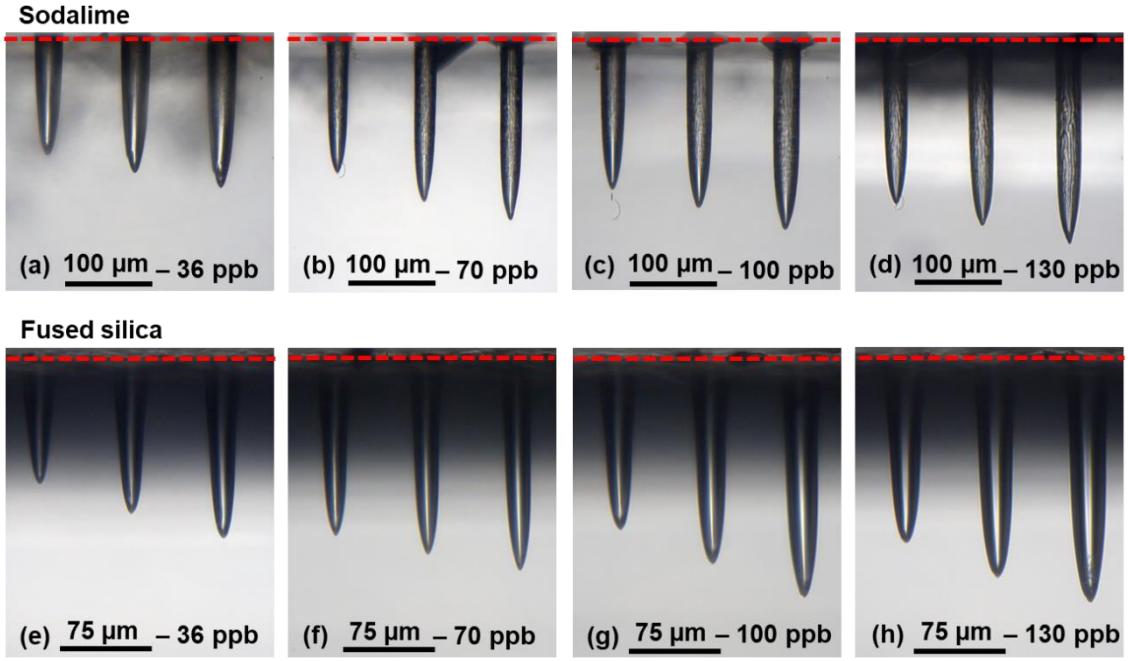

Figure 3.9. Microscope images of the holes drilled with a classical burst shape and a burst fluence of 300 J/cm² in sodalime for 300 bursts, 400 bursts, and 500 bursts with 36 ppb (a), 70 ppb (b), 100 ppb (c) and 130 ppb (d), and for fused silica for bursts of 36 ppb (e), 70 ppb (f), 100 ppb (g) and 130 ppb (h) [136].

This observation attests that for bursts with more pulses, the accumulative regime is enhanced and the energy usage is optimized as it is on metals and silicon [105,106,110]. The graphs corresponding to the evolution of the hole depth on the full range of drilling time are represented in Figure 3.10. The uncertainty on the depth measurements is not displayed on this graph as the values were negligible (lower than ± 5 µm). Figure 3.10 shows that the behaviour of the two materials regarding the number of bursts is quite similar leading to comparable hole depths as published in [127]. Moreover, from these graphs, we identify for all configurations the same three distinct stages of the drilling process: (1) surface ablation, (2) confined ablation, and (3) ablation termination where the drilling depth saturates, as explained in Ref. [127].

Figure 3.10 clearly shows that, for both the classical and the flat burst shapes, the number of pulses per burst as well as the energy repartition within the burst have a direct impact on the drilling rate and on the maximum achievable hole depth. Indeed, the zooms on Figure 3.10 show an increase of the drilling rate for higher numbers of pulses per burst, as observed for milling on metals and silicon [105,106,110]. However, the hole depth saturates at lower values for increasing numbers of pulses per burst. Furthermore, we observe that the drilling process is more efficient for the flat burst shape compared to the classical burst shape. Indeed, the

ablation depth during the first two drilling stages is higher for a flat burst shape having 50 ppb than that was produced using a classical burst shape having 70 ppb. The ablation depth at the saturation is also higher than that was produced with a classical burst shape having 36 ppb.

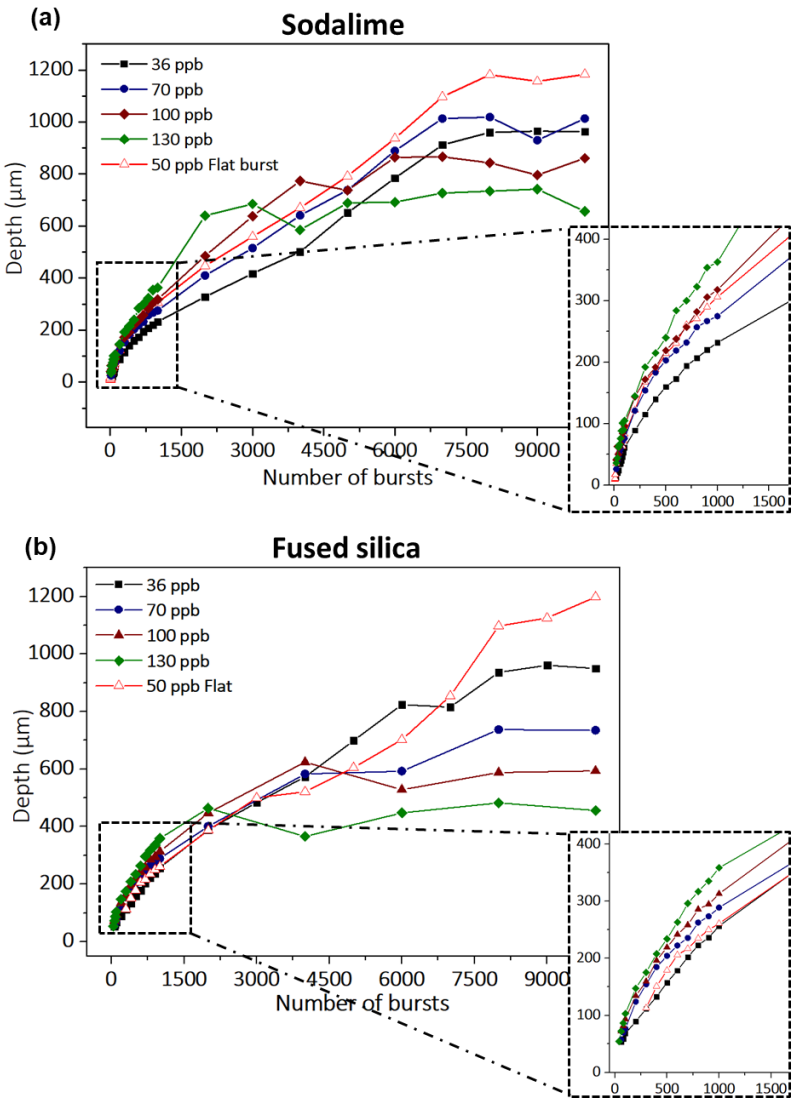

Figure 3.10. Evolution of the hole depth as a function of the number of bursts up to 10000 bursts with a burst fluence of 300 J/cm² for sodalime (a) and fused silica (b). The inserts on the right bottom corner are a zoom of the very first part of the graphs delimited by a rectangle of black dashed lines [136].

The drilling rates and the maximum hole depth extracted from the depth measurements (slope) for a burst fluence of 300 J/cm² are summarized in Table 3.3 with Rate 1 corresponding to surface ablation and Rate 2 corresponding to confined ablation before saturation. The confined ablation rate is significantly lower than the surface ablation rate, probably attesting a screening effect while the laser-matter interaction is confined, this observation confirms the tendency observed in table 3.1. The surface ablation rate doubles in sodalime when the number of pulses per burst increases from 30 to 160. Regarding fused silica, the same tendency in drilling rate increase is observed, and an interesting point can be seen at 160 pulses per burst. For this particular configuration, there was no clear drilling visible as the individual pulse energy within the burst might not be high enough due to the higher ablation

threshold of fused silica and despite the accumulative regime. Experiments with higher burst energies (i.e higher energy per pulse) confirmed this hypothesis.

	Sodalime			Fused Silica		
Burst	**Rate 1 (µm/burst)**	**Rate 2 (µm/burst)**	**Maximum depth (µm)**	**Rate 1 (µm/burst)**	**Rate 2 (µm/burst)**	**Maximum depth (µm)**
36 ppb	0.65	0.11	950	0.23	0.11	1000
70 ppb	0.7	0.12	1000	0.48	0.10	800
100 ppb	0.9	0.16	820	0.6	0.12	600
130 ppb	1.2	0.28	690	0.78	0.27	420
160 ppb	1.3	0.35	550	/	/	/
50 ppb Flat	0.5	0.12	1190	0.3	0.12	1180

Table 3.3: Drilling rates and maximum achievable depth in sodalime and fused silica for a burst fluence of 300 J/cm² for the classical burst shape (36 ppb to 160 ppb) and the flat burst shape with 50 pulses per burst.

In a second time, we chose to investigate only flat bursts as they appear to be the better compromise between ablation rate and saturation depth of the hole. We investigated the evolution of the hole depth as a function of the number of bursts applied to the sample for a fixed burst fluence and a number of pulses per burst ranging from 50 to 400. The resulting graphs are depicted in Figure 3.11 for a burst fluence of 246 J/cm².

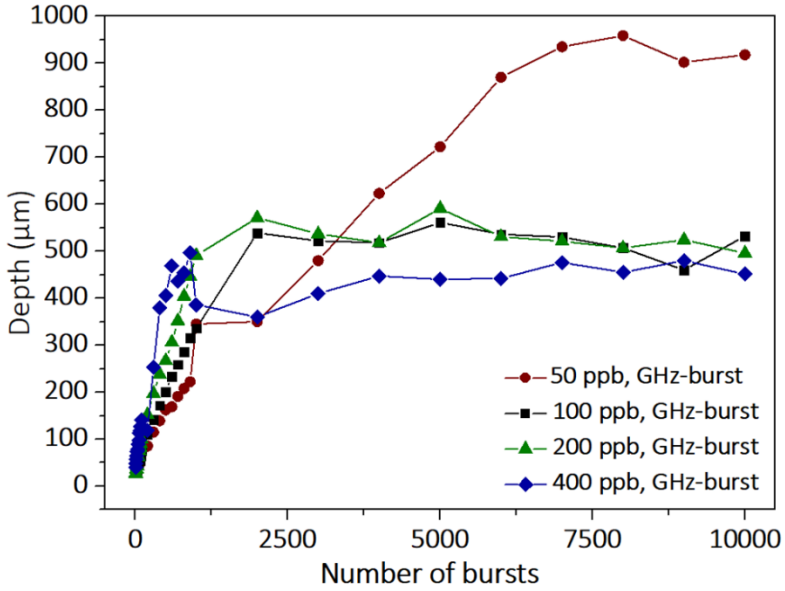

Figure 3.11: Evolution of the depth as a function of the number of bursts applied to the sample of sodalime for a burst fluence of 246 J/cm², a burst repetition rate of 1 kHz and a pulse repetition rate of 1 GHz. The pulse number within the burst is ranging from 50 to 400.

In this study, the burst fluence is similar for all cases meaning that for a 400-pulse burst, the pulse energy is 8 times lower than that of the 50-pulse burst. In this figure, one can clearly deduce that the 50-pulse burst is optimal regarding the saturation depth by nearly a factor 2 in comparison with the other configurations. For this second part, the drilling rates and the

maximum hole depth extracted from the depth measurements (slope) for a burst fluence of 246 J/cm² are summarized in Table 3.3 with Rate 1 corresponding to surface ablation and Rate 2 corresponding to confined ablation before saturation.

	Sodalime			Fused Silica		
Burst	**Rate 1 (µm/burst)**	**Rate 2 (µm/burst)**	**Maximum depth (µm)**	**Rate 1 (µm/burst)**	**Rate 2 (µm/burst)**	**Maximum depth (µm)**
50 ppb flat	0.7	0.125	900	0.23	0.11	1000
100 ppb flat	1.1	0.22	550	0.48	0.10	800
200 ppb flat	2	0.48	490	0.6	0.12	600
400 ppb flat	2.2	0.8	450	0.78	0.27	420

Table 3.4: Drilling rates and maximum achievable depth in sodalime and fused silica for a burst fluence of 246 J/cm² for the flat burst shape with 50, 100, 200 and 400 pulses per burst.

As depicted in Figure 3.11, the ablation rate per burst rises with an increase in the number of pulses per burst. The slope of the initial two stages increases from 0.7 µm/burst for the surface ablation rate at 50 ppb to 2.5 µm/burst at 400 ppb. This observation agrees with the studies reported in the literature [23,96,111,114]. However, the maximum depth decreases by nearly a factor 2 compared to GHz-bursts with 50 ppb. This observation suggests an optimal value for the number of ppb to attain the highest hole depth, highlighting that a compromise needs to be found. Indeed, the process could benefit from a longer burst which would allow for a longer beneficial heat accumulation. However, a longer burst implies lower laser intensity per pulse, leading to less effective non-linear absorption. This results in a lower effective pulse energy reaching the tip of the hole, eventually insufficient for ablation, leading to the saturation of hole depth.

One can notice that the deep ablation rate is much lower for 50 and 100 ppb than for longer bursts. This can be explained by a smaller ablation plume inducing less screening effect within the burst, as the energy is distributed among a higher number of pulses. Therefore, a much longer burst results in higher deep ablation rates. However, as mentioned earlier, the saturation depth of the hole is subject to a compromise in the number of pulses per burst, depending on the material and the laser energy. So, short bursts are suitable for deep holes whereas long bursts are preferred for high drilling rates. Therefore, we assume that the energy per pulse within the burst plays a major role in maximum hole depth. The reason could be the kinetic energy of ejected matter or the energy loss along the hole length.

1.3 Influence of the energy repartition

In this part, we present the difference between the increasing burst, the decreasing burst and the flat burst on the drilling process in sodalime. We fixed the burst energy at 200 µJ and the number of pulses per burst at 100, as the burst shaping process requires a certain amount of pulses to be relevant, for shorter bursts the burst shaping had no visible effect. The spot size is again 7.3 µm with a corresponding numerical aperture of 0.14. The resulting holes are shown in Figure 3.12. These images were taken with a 10X objective mounted on the optical microscope. In Figure 3.12 we observe once again holes with an excellent quality for the

increasing (b) and the flat (c) burst shapes. It appears that for the decreasing burst configuration, the depth increases faster than for the two other configurations. However, for this burst shape, the holes present some cracks surrounding the inner walls which is in full agreement with the observations on the cavity millings reported in [112,119,121,137].

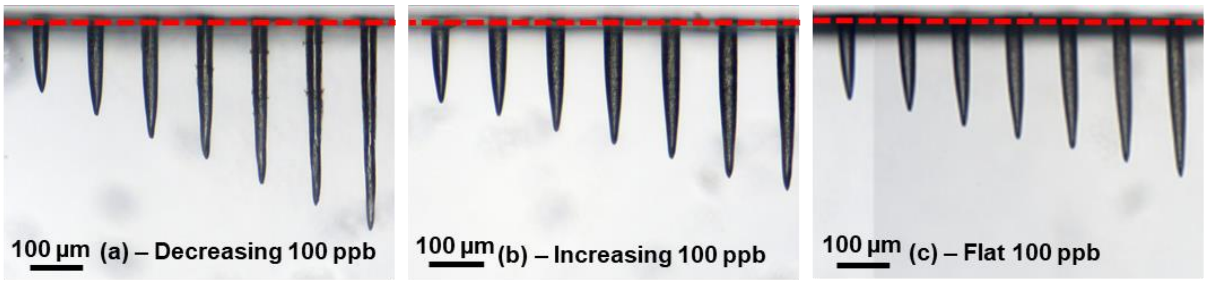

Figure 3.12. Microscope images of the holes drilled in sodalime with 100 pulses GHz-bursts of 200 µJ with a number of bursts in a range from 200 to 800 for a decreasing burst shape (a), for an increasing burst shape (b) and for a flat burst shape (c) [136].

The graphical representation of the depth as a function of the number of bursts applied on the sample for the three configurations is depicted in Figure 3.13. This graph demonstrates that the burst shape obviously has a clear impact on the drilling dynamics. The drilling rate for decreasing bursts is much higher than for the two other configurations. However, we also observe that the saturation depth is lower. The drilling rates extracted from this graph as well as the average saturation depths for each configuration are summarized in Table 3.5.

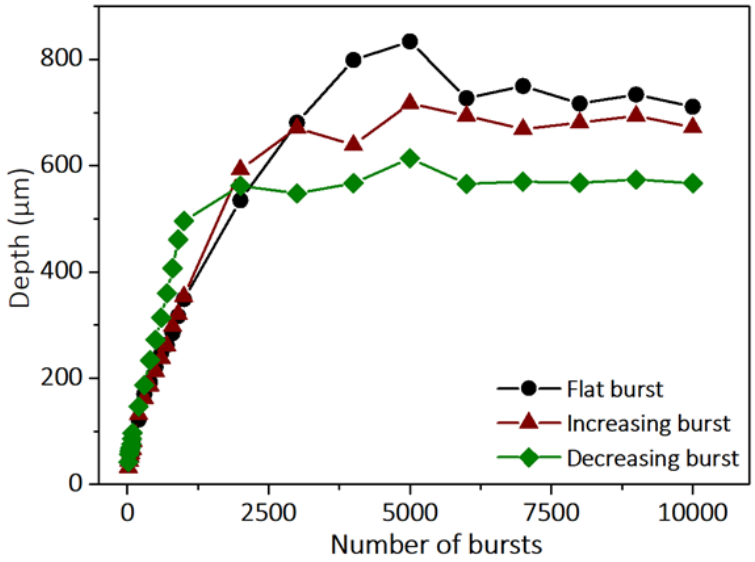

Figure 3.13. Evolution of the hole depth in sodalime as a function of the number of bursts applied on the sample for the three burst shapes with bursts of 100 pulses and a burst fluence of 350 J/cm² [136].

Laser parameters	Rate 1 (µm/burst)	Rate 2 (µm/burst)	Maximal depth (µm)
100 ppb decreasing	1.2	0.45	614
100 ppb increasing	0.6	0.25	717
100 ppb flat	0.6	0.16	780

Table 3.5. Drilling rates and maximum depth reached for decreasing, flat and increasing GHz-bursts with 100 ppb and a burst fluence of 350 J/cm² [136].

This table shows a significantly higher surface ablation rate (Rate 1) in the decreasing configuration compared to the other two configurations. This can be attributed to the higher energy carried by the initial pulses in the burst for the decreasing configuration. Consequently, rapid heating during the first pulses leads to a drilling process resembling the MHz-burst regime (see Section 2 of this chapter), resulting in an enhanced ablation rate. On the other hand, higher intensity at the beginning of the burst may induce a faster accumulation of plasma, causing an earlier drilling saturation due to an increased screening effect. Moreover, the relatively high energy of the first pulses within the burst does not allow for fully profiting from the accumulative GHz-burst regime like in ablation experiments with bursts containing a small number of high-energy pulses [96,100,110]. Furthermore, it appears that an increasing burst shape allows for deeper hole drilling. This is attributed to the gradual heating of the material by low-energy pulses, generating ablation incubation and low screening effects. High-energy pulses towards the burst's end enhance material ejection from the hole. Both configurations offer advantages, and it is noteworthy that the flat burst configuration appears to be the best compromise since it combines the benefits of both. This burst shape allows for even deeper drillings while maintaining the high-quality characteristic of the GHz-burst regime at a reasonable drilling rate. Figure 3.14 shows the images of the holes with full depth. They were obtained by stitching several images measured by the 50X microscope that has a limited field of view.

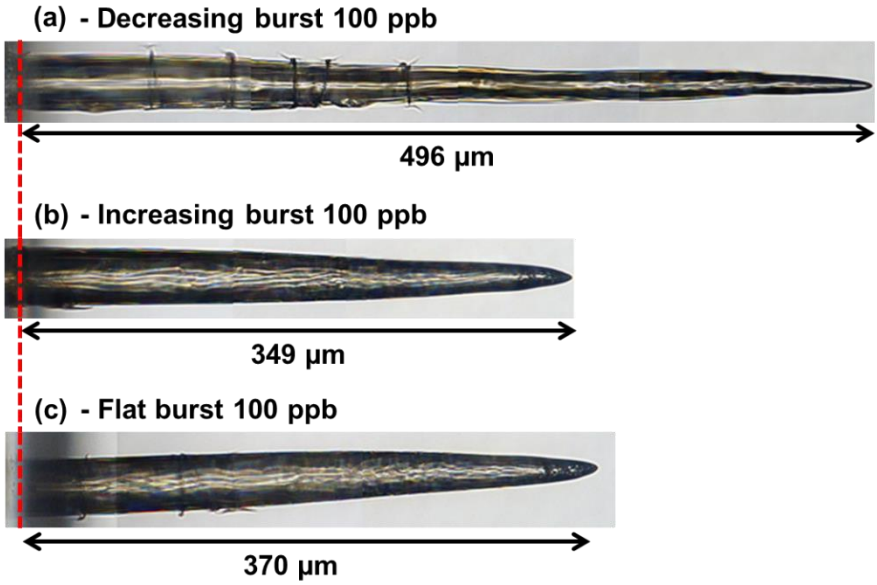

Figure 3.14. Microscope image of the holes drilled in sodalime for a drilling time of 1 s with bursts of 100 pulses at burst fluence of 350 J/cm² and a decreasing burst shape (a), an increasing burst shape (b) and a flat burst shape (c) [136].

These images confirm that, with a drilling time of 1 s (i.e 1000 bursts applied), the hole quality depends on the burst shape configuration despite applying comparable burst energies. In the case of a decreasing burst shape, the hole is much deeper than for the two other configurations. However, we can clearly see multiple cracks appearing and the overall morphology is heading towards MHz-burst drilling [137-139] as will be described in Section 2

of this chapter. This indicates that a higher energy from the first few pulses may initiate the creation of the cracks.
Regarding the two other burst shapes, the hole morphology and depth are very similar. Note that the increasing burst shape seems to produce less cracks and, thus, the best hole quality, probably because the very first pulses carry and deposit a low amount of energy.

1.4 Towards high aspect ratio

In order to reach even higher aspect ratios than that was obtained in the previous sections (37 in sodalime and 41 in fused silica), a compromise had to be found between the repetition rate, which has to be low enough so that there won't be a heat affected zone, the fluence, which has to be high enough so that, despite the depth of the hole, the energy reaching the tip will be enough to produce ablation, and the numerical aperture [131,132]. Indeed, the latter appeared to be a crucial point for the drilling as it must not be too low so that the energy will not be spread on a too large surface. However, it should not be too high so that the beam keeps under grazing incidence and, thus, limiting refraction losses during the reflections on the inner walls as represented on Figure 3.15. Ideally, the hole in formation should act as a waveguide in order to guide the laser beam down to the bottom of the hole. To validate this hypothesis, a study on the influence of the numerical aperture was led. We investigated 5 different numerical apertures with the 5X objective by changing the beam diameter by means of a beam expander. Of course, by changing the numerical aperture and keeping the same objective, care as to be taken regarding the fluence. Indeed, changing the numerical aperture while keeping the same working distance induces a spot diameter change, and thus a fluence change.

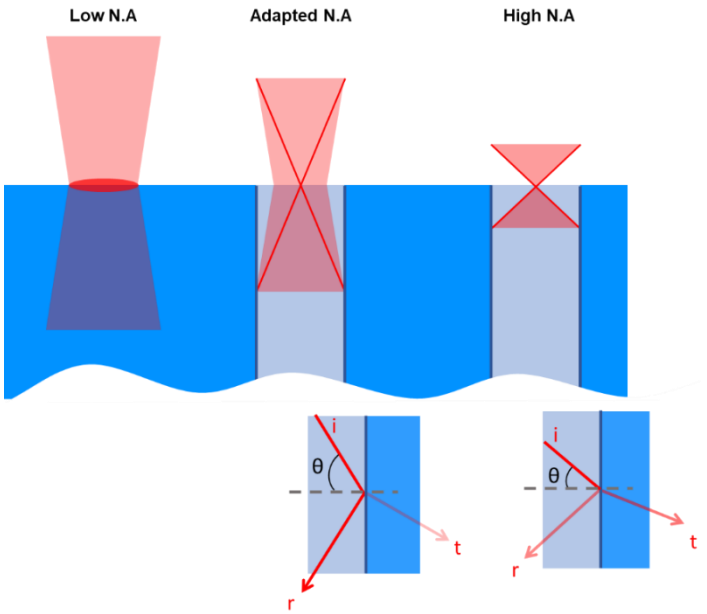

Figure 3.15. Representation of the influence of the numerical aperture on the transmission of the energy towards the tip of the hole.

In order to compensate this phenomenon, we adapted the burst energy to lead a valid study with a fixed fluence. Figure 3.16 displays the evolution of the depth as a function of the number of bursts applied to the sample in the repetitive single pulse regime. This graph attests

that the hole depth is highly affected by the numerical aperture even for the repetitive single pulse regime. The ablation rate as well as the saturation depth for all the numerical apertures (see Table 2.2) are summarized on Table 3.6.

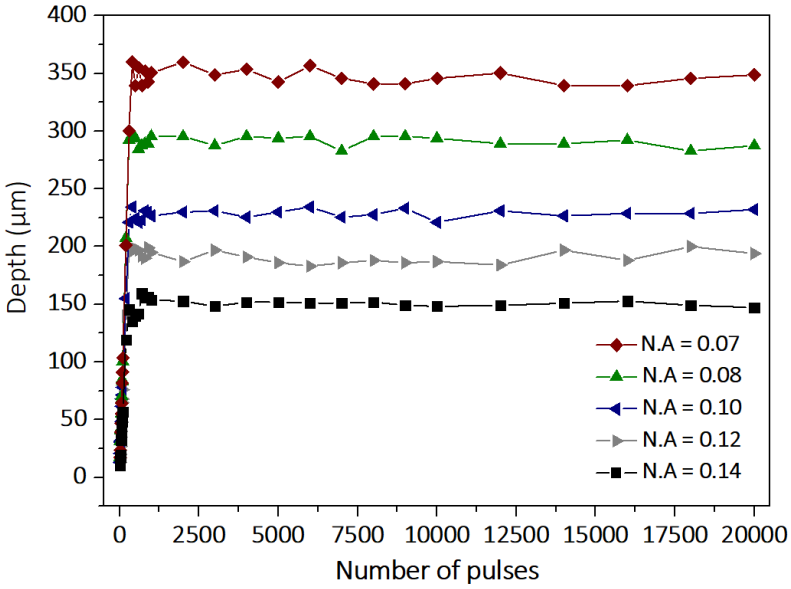

Figure 3.16. Evolution of the hole depth in sodalime as a function of the number of pulses applied on the sample for 5 numerical apertures in repetitive single pulse regime for a pulse fluence of 110 J/cm². The repetition rate is 1 kHz.

Numerical aperture	Rate (µm/burst)	Maximal depth (µm)
0.14	0.6	150
0.12	0.7	200
0.10	0.8	225
0.08	1.1	300
0.07	1.0	350

Table 3.6. Drilling rates and maximum depth reached for numerical apertures ranging from 0.07 to 0.14 with a pulse fluence of 110 J/cm².

This table shows that the depth is increased by a factor of more than 2 when the numerical aperture is divided by two. One may notice on this table that the ablation rate is also significantly affected by the numerical aperture.

Figure 3.17 shows the evolution of the depth as a function of the number of bursts applied to the sample in GHz-burst regime with 50 ppb and a burst fluence of 292 J/cm². As was expected, the numerical aperture has a significant effect on the resulting saturation hole depth for a fixed fluence. In this case, we observe a variation up to 35 %. This graph also shows that the numerical aperture appears to have no significant impact on the surface ablation rate, unlike its effect on the deep ablation rate. Both these drilling rates as well as the corresponding saturation depth are summarized on Table 3.7 for the 5 numerical apertures investigated.

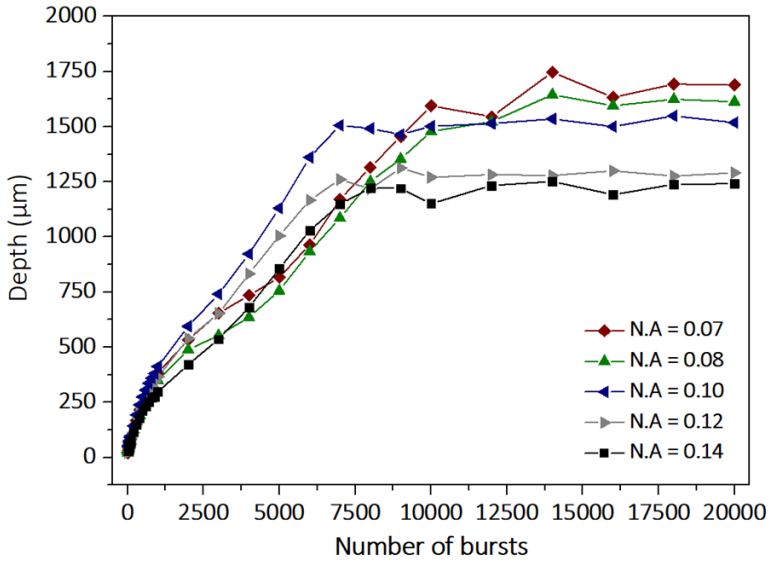

Figure 3.17. Evolution of the hole depth in sodalime as a function of the number of bursts applied on the sample for the 5 numerical apertures with bursts of 50 pulses and a burst fluence of 292 J/cm². The pulse repetition rate is 1.28 GHz and the burst repetition rate is 1 kHz.

Numerical aperture	Rate 1 (µm/burst)	Rate 2 (µm/burst)	Maximal depth (µm)
0.14	0.6	0.125	1150
0.12	0.6	0.130	1250
0.10	0.6	0.180	1500
0.08	0.6	0.200	1600
0.07	0.6	0.200	1650

Table 3.7. Drilling rates and maximum depth reached for numerical apertures ranging from 0.07 to 0.14 with a burst fluence of 292 J/cm².

This table confirms that the numerical aperture has no effect on the surface ablation rate. Indeed, so far only the burst duration and the burst fluence had a real effect on this ablation rate. However, they have a relevant effect on the deep ablation rate. It appears that the lower the numerical aperture, the higher is the deep ablation rate, as shown in Figure 3.15. Moreover, the lower the numerical aperture, the higher the beam reflection towards the tip of the hole. On the other hand, a too low numerical aperture could lead to lose focusing a thus no drilling would be observed.

In order to obtain extreme aspect ratios, the numerical aperture was reduced from 0.14 to 0.10 to maximize reflections under grazing incidence. Furthermore, we chose to keep the repetition rate at 1 kHz and to work with the highest burst fluence available with our setup. The resulting holes are depicted in Figure 3.18 for drilling times ranging from 16 s to 18 s (left to right). For this experiment, the hole diameter is about 50 µm in sodalime and 22 µm in fused silica, for depths of 1520 µm and 1602 µm, respectively, leading to aspect ratios of 30 and 73, respectively. One can see that the depths in sodalime and in fused silica are comparable while the ablation threshold is higher in fused silica. This can be explained by the fact that the inner walls in fused silica are very smooth all along the hole whereas in sodalime the walls quality is much more uneven, rough and deteriorated. In our hypothesis of multiple reflections and scattering, the quality of the inner walls plays a major part. Indeed, the walls

in fused silica are smooth and probably present a much higher reflection coefficient than in sodalime.

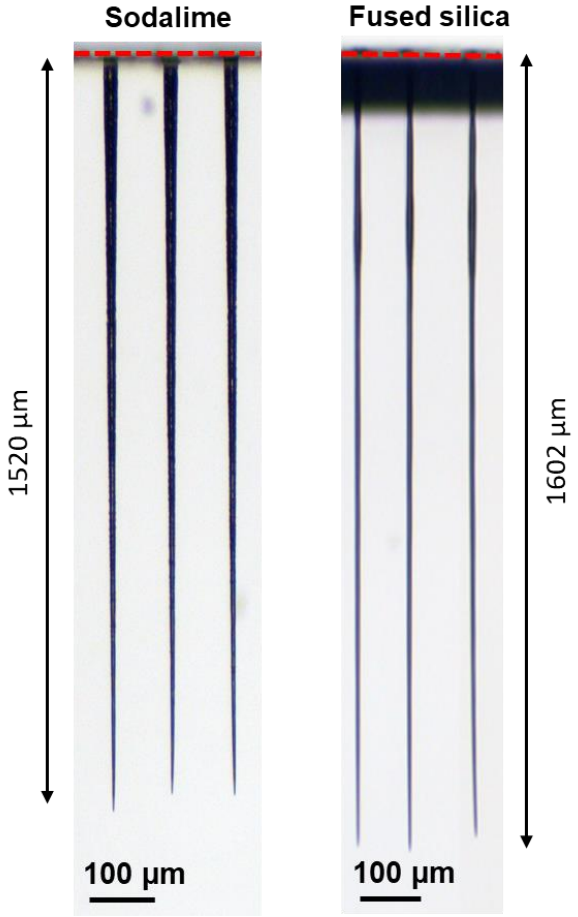

Figure 3.18. High-aspect ratio holes for a burst repetition rate of 1 kHz with bursts of 50 pulses at an intra-burst repetition rate of 1 GHz and with a burst fluence of 369 J/cm2 for drilling times in a range from 16 s to 18 s in sodalime (right) and in fused silica (left) [127].

This is the reason why we measure similar lengths in sodalime and in fused silica (Figure 3.10). By optimizing the parameters of the laser as well as the focusing parameters, we were able to reach even higher aspect ratios. Since the burst repetition rate has been identified as a critical parameter to get high aspect ratios, we have chosen to work on fused silica, a material that can stand higher values of repetition rate (up to 100 kHz) without detrimental side-effects or hole collapse [124]. Moreover, fused silica is a standard material in many applications. Note that the beam focus stays at the sample surface and neither the sample nor the beam focus are moved. GHz-burst drilling was performed with bursts of 250 µJ burst energy and 70 ppb at 20 kHz, 50 kHz and 100 kHz, respectively. In this case, the spot size was 7.7 µm and the numerical aperture was still set to 0.10. The resulting holes after a drilling time of 5 s are depicted in Figure 3.19. Note that we voluntarily chose a relatively long drilling time with respect to the repetition rates to ensure that the drilling process stops from itself (saturation) and not from a too short drilling time.

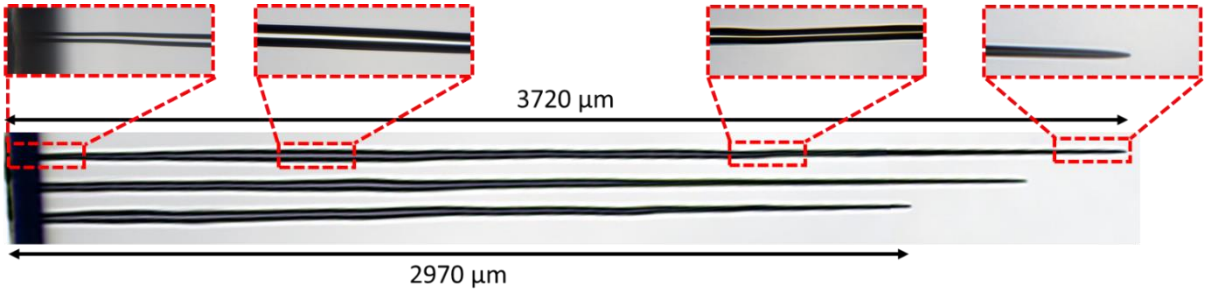

Figure 3.19. Holes drilled in fused silica in GHz-burst mode with bursts of 250 µJ and a number of 70 ppb at repetition rates of 100 kHz, 50 kHz and 20 kHz (from the top to the bottom), respectively, and a drilling time of 5 s. The red rectangles are zooms taken with a 50X objective on the microscope [138].

On this figure, we observe extremely deep holes with an excellent quality. The diameters at the entry of the holes were measured just after the shadows arising from the surface. From the top to the bottom, the diameters are 25 µm, 30 µm and 34 µm, respectively, and the corresponding depths are 3.72 mm, 3.40 mm and 2.97 mm, respectively. These values correspond to an aspect ratio as high as 150 for the deepest hole, which is the highest aspect ratio reported so far with femtosecond GHz-burst drilling. The zooms taken at different depths of the hole attest that the inner walls keep an excellent quality, they are glossy and crack-free all along the hole. Moreover, one can notice that there is no heat affected zone whatsoever despite the relatively high burst repetition rate and burst energy.

2. Comparison of repetitive single pulse, MHz-burst and GHz-burst regimes

In this section, I present a comparative analysis of various temporal beam shaping strategies, specifically focusing on the standard regime of repetitive single femtosecond pulses. This standard regime is compared with the MHz-burst and GHz-burst regimes, each containing varying numbers of pulses per burst. The study explores the evolution of hole depth and morphology in sodalime glass, with a particular emphasis on increasing the number of bursts for the burst regimes or the number of pulses for the repetitive single pulse (RSP) regime.

2.1 Hole depth

The variation in the number of bursts or pulses (for RSP) ranges from 1 to 10 000 for all investigated regimes, maintaining a consistent single pulse and burst repetition rate of 1 kHz. The spot size is 7.3 µm with a corresponding numerical aperture of 0.14. The single pulse and burst energies are set at 140 µJ, making the single pulse mode equivalent to repetitive pulses of 140 µJ each, while the MHz- and GHz-burst modes correspond to bursts containing N pulses, each carrying an energy of 140/N µJ.

Figure 3.20 shows microscope images of the holes obtained for different regimes: the repetitive single pulse regime (a), the MHz burst regime with 2 and 8 ppb (b and c), and the GHz-burst regime with 200 ppb (d). The drilling times are ranging from 70 ms to 700 ms, which correspond to 70 bursts (pulses) to 700 bursts (pulses). The resulting hole depth varies across the different regimes: 34 µm to 197 µm in the repetitive single pulse regime, 49 µm to 274 µm in the MHz-burst regime (2 ppb), 68 µm to 308 µm for MHz-bursts (8 ppb), and 32 µm to 280 µm for the GHz-bursts with 200 ppb. The images highlight distinct hole morphologies and depths for the three regimes. The single pulse regime produces highly tapered holes with a

wide entrance diameter and a rough inner surface. Saturation in depth occurs after 300 ms. Transitioning to MHz-bursts (2 ppb) results in a higher saturation depth of about 280 µm, with smoother inner walls compared to repetitive single pulses. Longer MHz-bursts (8 ppb) display smoother inner walls, likely due to lower individual pulse intensity and the onset of a beneficial heat accumulation effect. However, we still observe an important number of cracks along the hole. The GHz-burst regime demonstrates superior hole quality, exhibiting a more cylindrical hole geometry and a lower occurrence of cracks, particularly noticeable for long drilling times.

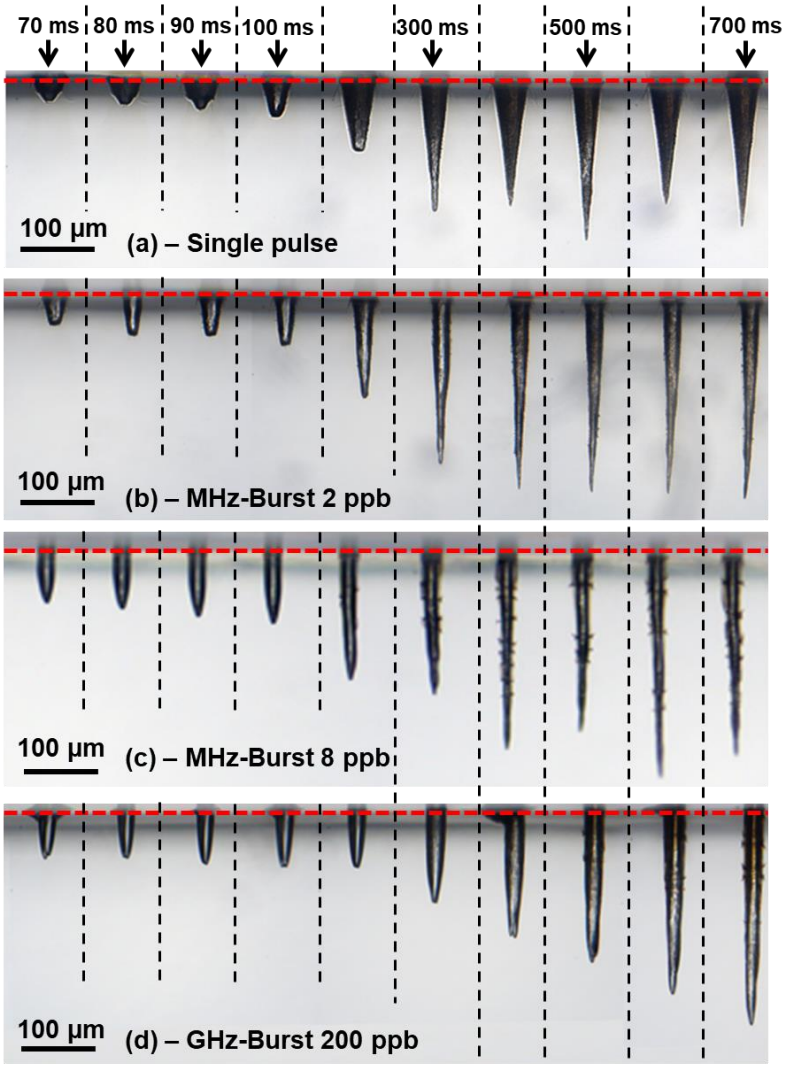

Figure 3.20. Microscope images of the holes drilled in sodalime with a drilling time ranging from 70 ms to 700 ms with repetitive single pulses of 140 µJ (a), with 140 µJ-MHz bursts of 2 ppb (b) and 8 ppb (c), and with 140 µJ-GHz bursts of 200 ppb (d). The red dashed line indicates the sample surface [138].

The graphical representation of the hole depth as a function of the number of bursts (pulses in RSP), and thus drilling time, on the full range of this study (1 ms to 10 s) is depicted in Figure 3.21. As all these experiments were carried out at a pulse or burst repetition rate of 1 kHz, a drilling time of 1 s corresponds to 1000 bursts (pulses) applied to the sample. The black dots correspond to the single-pulse regime, the red and green triangles correspond to the MHz-burst mode with 4 ppb and 8 ppb, respectively, and the red and grey squares correspond to the GHz-burst mode with 50 pulses per bursts and 100 pulses per burst, respectively. No error

bars are visible on these graphs as the uncertainty on the depth measurements is negligible (lower than ±5 µm).

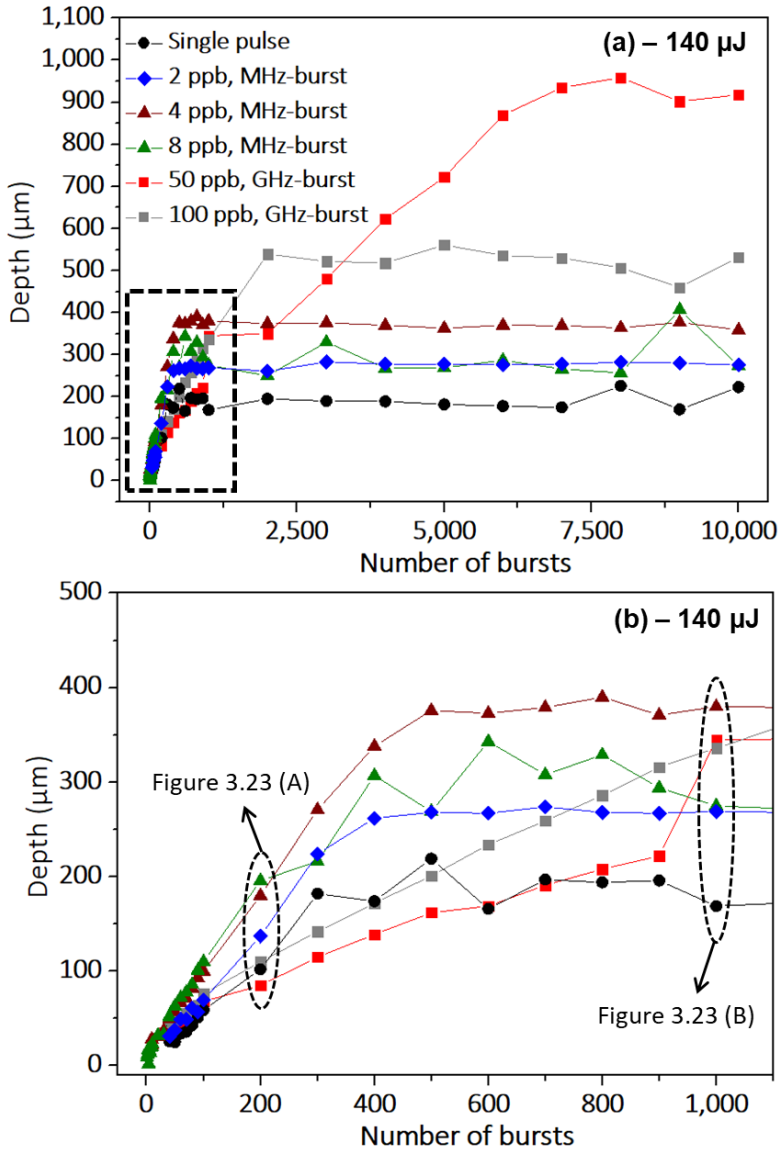

Figure 3.21. Evolution of the hole depth as a function of the number of bursts (pulses) applied to the sample in sodalime for single pulse regime, MHz-burst regime with 4 and 8 ppb at 40 MHz and GHz-burst regime for 50 and 100 ppb at 1.28 GHz (a). Zoom on the evolution of the depth as a function of the number of bursts (pulses) for the beginning of the graph as indicated by the dashed rectangle (b). The burst (pulse) energy is fixed at 140 µJ and the burst (pulse) repetition rate is fixed at 1 kHz [138].

The graphs reveal distinct behaviours among the three regimes concerning the evolution of depth as a function of the number of pulses/bursts. Regarding the maximum achievable hole depth, indicated by the saturation points on the graphs, the GHz-burst regime saturates at a significantly higher depth value. Specifically, for a GHz-burst with 50 pulses per burst (ppb), the maximum depth is up to five times greater than the one obtained with repetitive single pulses. Notably, longer drilling times are associated with higher hole depths. A similar trend is observed for the MHz-burst regime where the depth at 4 ppb is greater than at 8 ppb, suggesting an optimum number of pulses per burst or laser intensity. This hypothesis is confirmed by Figure 3.22.

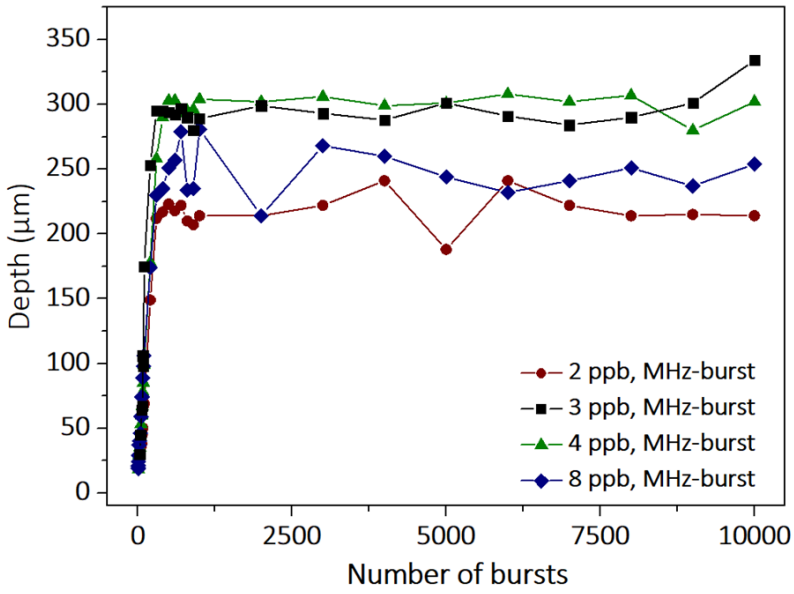

Figure 3.22. Evolution of the hole depth as a function of the number of bursts applied to the sodalime sample for the MHz-burst regime with 2, 3, 4 and 8 ppb at 40 MHz repetition rate for a burst energy of 96 µJ. The burst repetition rate is 1 kHz.

In the repetitive single pulse regime and the MHz-burst regime, the behaviour differs slightly from what was observed in section 1 with GHz-bursts. It displays only two stages: a linear increase in depth with the number of pulses or bursts, followed by saturation where the drilling process stops. It is reasonable to assume that the saturation stage results from similar phenomena as in the GHz-burst mode, involving losses in beam propagation towards the hole tip, resulting in insufficient energy for ablation. However, in the initial part of the graph, for a low number of pulses/bursts, the surface ablation process is likely skipped due to the high energy of the pulses. The high intensity of the pulses results in a high ablation rate meaning that the confined ablation appears sooner. Both of these graphs validate the hypothesis that there exists an optimal number of pulses per burst (ppb) that maximizes the achievable hole depth. In the case of MHz-bursts, it appears that, for sodalime, the optimal number of pulses per burst is around 4, whereas, in the GHz-burst regime, the optimal value was notably 50 ppb as can be seen in Figure 3.10. Interestingly, within the MHz-burst mode, the number of ppb seems to have a limited impact on the ablation rate, as indicated by the slope of the graph representing the drilling process before saturation. In this regime, each pulse within the burst carries an energy surpassing the ablation threshold of sodalime [126, 130]. Consequently, increasing the number of pulses per burst while maintaining a constant total energy does not increase the ablation rate. This is because the pulse-to-pulse delay within the MHz-burst is significantly longer than the heat diffusion time of the material [96] so there is a moderate cooperating effect between subsequent pulses. The varied ablation rates and average depths of saturation for all the parameters explored in this study are summarized in Table 3.6. In this table, Rate 1 corresponds to the surface ablation rate, and Rate 2 to the deep ablation rate with respect to the GHz-burst regime drilling process. The presented table reveals that the single pulse regime exhibits a relatively low deep ablation rate, nearly two times lower than the ablation rate observed in the MHz-burst regime. Furthermore, the maximum average depth of saturation for comparable energy is much lower than that achievable in the MHz-burst regime (by a factor of 2 for 5 ppb) and in the GHz-burst regime (by a factor of 4.5 for 50

ppb). As deduced from the graphs, the ablation rate in the MHz-burst regime remains rather constant over an increasing number of pulses and is much higher than in the single pulse regime. This is due to the pulse-to-pulse delay that is longer than the mean heat diffusion time, therefore there is only a moderate cooperative effect between subsequent pulses in the single or MHz-burst regimes, contrarily to the GHz-burst one.

Regarding the depth, an optimum number of pulses per burst, in this case, is 5 ppb, allowing for deeper drillings.

	SPR	**MHz burst mode**							**GHz burst mode (flat bursts)**			
Nb pulse	1	2	3	4	5	6	7	8	50	100	200	400
Rate 1 (µm/burst)	/	/	/	/	/	/	/	/	0.7	1.1	2	2.5
Rate 2 (µm/burst)	0.55	0.75	0.75	0.8	1	0.95	1	1	0.125	0.22	0.48	0.8
Avg. depth (µm)	200	280	334	390	400	350	320	300	900	550	490	450

Table 3.7 Drilling rates and average saturation depths in sodalime for a burst (pulse for SPR) energy of 140 µJ for the single pulse regime, the MHz-burst regime for 2 to 8 ppb and in GHz-burst regime for 50 to 400 ppb.

Note that in the single pulse and in the MHz-burst regime, higher ablation rates lead to deeper holes. In contrast, in the GHz-burst regime smaller ablation rates are linked to higher values of hole depth meaning that slower drilling allows for achieving deeper holes.

2.2 Hole morphology

In order to evaluate the morphology of the holes and inner walls, high-resolution images were taken using a 50X microscope objective (see Fig. 3.23). The images in this figure correspond to holes drilled with 200 bursts (pulses in RSP) for the top row (A) and with 1000 bursts (pulses in repetitive single pulse) for the bottom row (B). The observations reveal that the single pulse regime and the MHz-burst regime with 2 ppb produce similar inner walls and hole morphologies, featuring rough inner walls and tapered holes. These configurations are also the only ones displaying a collar at the surface, indicating excessively high pulse energy that may alter the material properties and result in lowered surface quality. This collar should result from the first reflection of the laser beam on the inner walls. This phenomenon is not visible for higher ppb since the pulse intensity is lower. For MHz-bursts with 4 ppb, the hole quality appears to change, with smoother but crackled inner walls. The morphology in the MHz-burst regime with 8 ppb is very similar and not shown here. Additionally, the holes maintain a conical shape but shift towards the characteristics of the GHz-burst regime. Across all drilling times, the GHz-burst mode consistently produces more cylindrical holes than the two preceding regimes and achieves a superior surface quality.

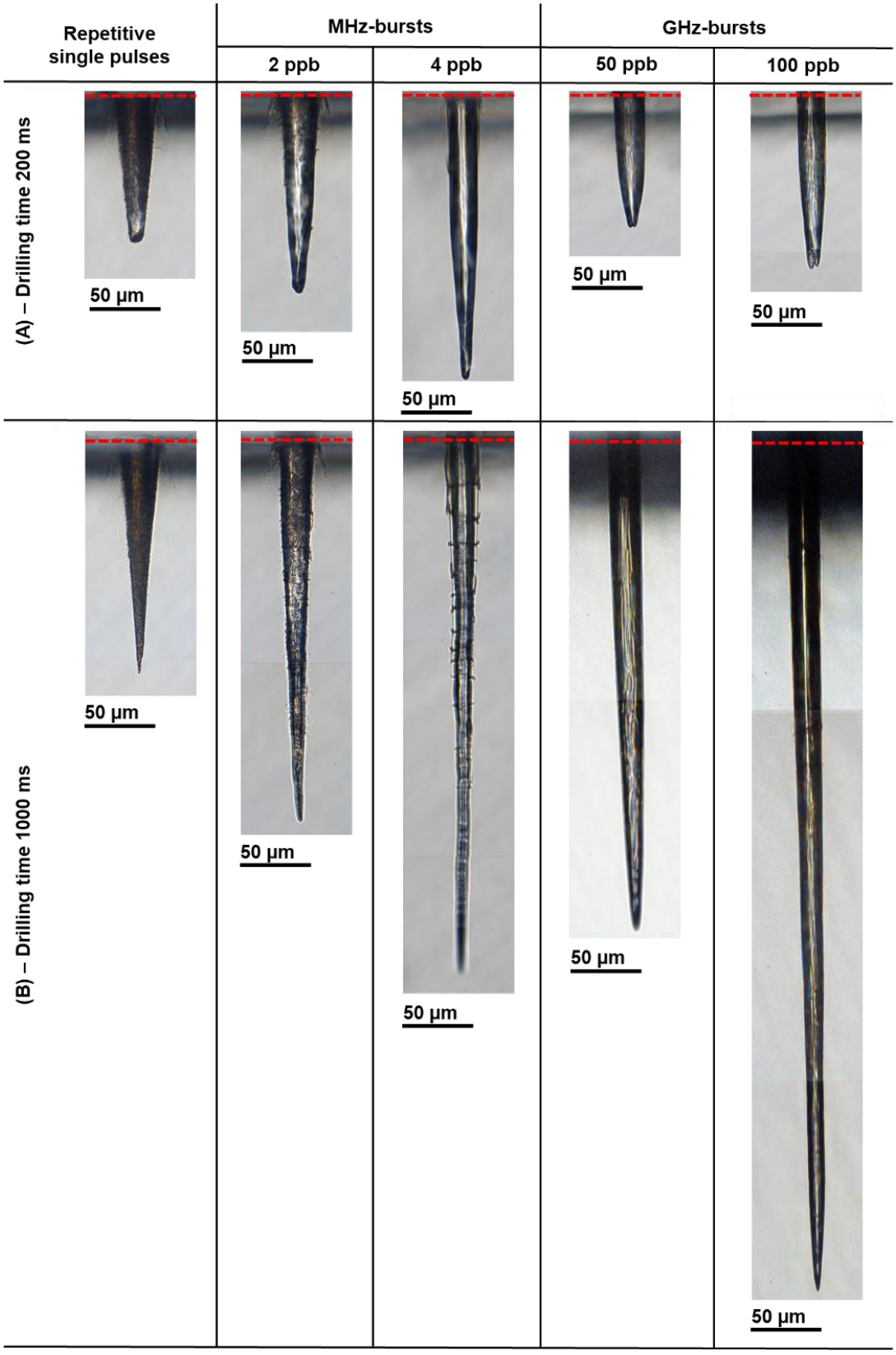

Figure 3.23. Microscope images of the holes drilled in sodalime taken with a 50X microscope objective with repetitive single pulses (a), in MHz-burst mode with 2 ppb (b) and 4 ppb (c) and in GHz-burst mode with 50 ppb (d) and 100 ppb (e). The top row (A) depicts holes for a drilling time of 200 ms corresponding to 200 bursts (pulses) and the bottom row (B) depicts holes for a drilling time of 1 s corresponding to 1000 bursts (pulses in SPR). The burst (pulse in SPR) energy and the repetition rate are fixed at 140 µJ and 1 kHz, respectively.

Moreover, despite the fact that for 200 ms drilling the holes in this regime are less deep than the ones in the MHz-burst mode, at 1 s drilling time the tendency is inverted. The hole obtained with 100 ppb has a depth of 600 µm compared to the 385 µm of the MHz-burst with 4 ppb. In addition, one should notice the excellent quality of the holes drilled in GHz-burst mode, and that the cylindrical shape is kept even for deep drillings.

3. Drilling limitations and transmission measurement

In this section, the aim is to provide an experimental confirmation of our hypothesis that the guidance of the laser beam by the hole plays a major part in the drilling process. To do so, the objective here is to drill several through holes of different depths and measure the transmission of these holes. In order to provide a large study on different depths of through holes, we decided to use bevel samples to study a full range of depths on the same sample as described in literature [133] and represented below in Figure 3.24 [140].

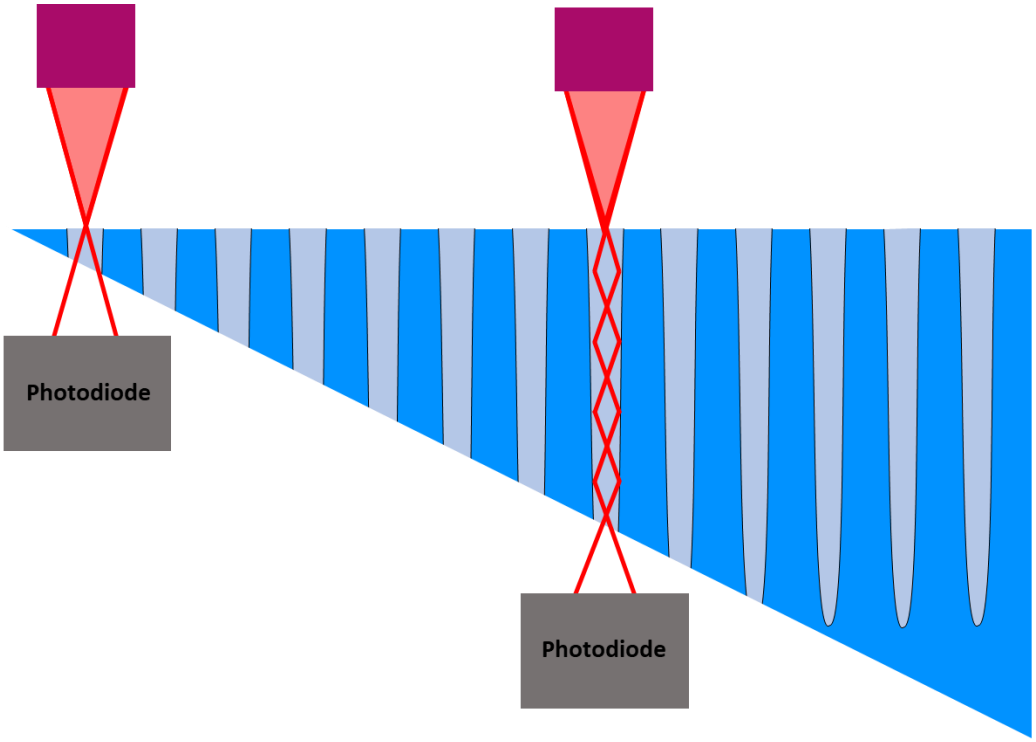

Figure 3.24. Principle of the transmission measurement by through holes.

During this experiment, two main challenges emerged, the first one is that it is necessary to put the photodiode in a place such that it does not touch the sample (whose positioning is critical) but assuring it is close enough to collect as much light signal as possible. Moreover, the second challenge was the beam placement itself. During the first trials, we observed that it was nearly impossible to measure the transmission with a GHz-burst mode laser. If the beam was misplaced of a few microns, the beam damages the inlet of the hole and thus changes the real transmission. Henceforth, the holes were drilled in GHz-burst mode but the transmission measurement was realised with the MHz-burst mode with a burst fluence lower than the ablation threshold. In this configuration, it was much easier to place the spot right at the inlet of the hole even if the sample moved a little. Indeed, in this configuration, we were able to optimize the position of the spot with a precision close to the micrometre by placing it at the

position corresponding to the maximum power on the photodiode. The photodiode we used (Gentec, PH20-GD-D0) has an upper limit of 30 mW, we estimated the uncertainty on the transmission measurement to be about 10 %. The protocol for this experiment holds in three steps:

- Pre-cutting of bevel samples by means of the Bessel beam workstation.
- Part release with a slight mechanical stress.
- Drilling of the bevel sample in GHz-burst mode. Every hole is drilled with the exact same parameters. We chose a burst repetition rate of 1 kHz and the maximum fluence so that we could drill enough holes in a single sample. The drilling time is fixed at 10 s **for all the holes**.
- Transmission measurement by switching the laser into MHz-burst mode to prevent the deformation of the inlet of the hole.

From this experiment, we expected the transmission of the holes to decrease rather linearly with the increasing depth. In addition, the hole transmission should be different from sodalime to fused silica due to the inner walls' roughness [132,133].

3.1 Drilling limitations

During the transmission experiment, we observed a rather peculiar behaviour regarding the evolution of the outlet hole diameter for through holes. It appeared that the outlet diameter of the hole was almost constant meaning that applying more bursts does not increase the outlet diameter as can be seen in Figure 3.25. Note that increasing the burst energy also did not change the outlet diameter. For these drillings, the burst repetition rate was set to 1 kHz, the burst fluence was 370 J/cm² for bursts of 50 pulses at 1.28 GHz. The spot size is 7.3 µm with a corresponding numerical aperture of 0.14. For all the holes, the drilling time was fixed at 10 s.

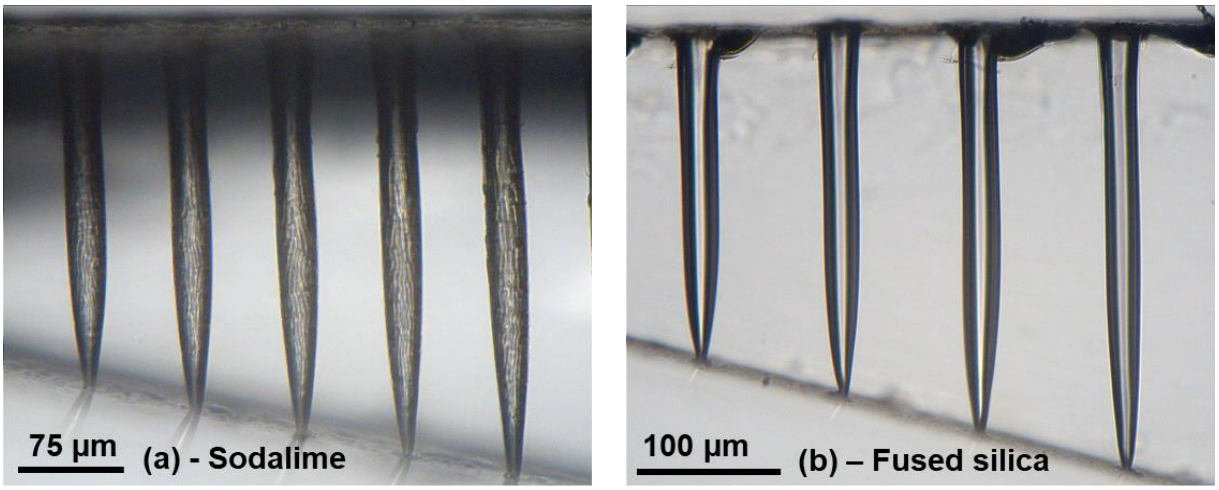

Figure 3.25. Microscope images of the holes drilled in a bevel sample of sodalime (a) and of fused silica(b).

On Figure 3.25 (a), one can observe the same hole morphology as was depicted in Figure 3.8 (a) with 3 distinct zones. At the tip the surface is bumpy, further up the hole in a transition zone, the surface appears rippled. Finally, the inner walls feature a groove-liked structure. This observation led us to believe that the plasma might be responsible for the inner walls' quality.

Note that for fused silica, the inner walls remain smooth and glossy as observed before. From these pictures one can also understand that there are some unexpected drilling limitations appearing concerning the outlet diameter. Indeed, for these drillings, the outlet diameter was always around 8 µm in sodalime and 6 µm in fused silica.

Based on this observation, we led a much larger study on bevel samples. We compared the diameters of a reference sample with blind holes and the outlet diameters of bevel samples in sodalime as represented in Figure 3.26. In this case, the drillings were done with bursts of 50 pulses at 1.28 GHz for a burst repetition rate of 1 kHz, a drilling time of 10 s and a burst fluence of 400 J/cm². In this experiment we chose a rather high burst fluence in order to have deep holes. Indeed, one of the limitations during this experiment was the cutting of the bevels. We pre-cut them in our Bessel beam workstation (see Chapter 5) and it was difficult to cut bevel samples with a low angle.

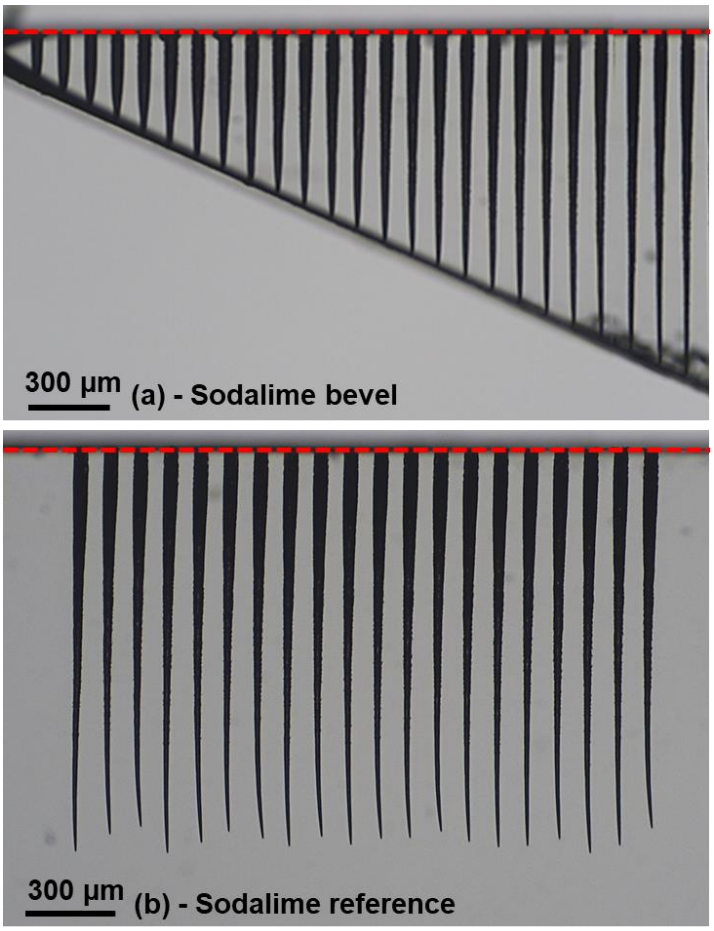

Figure 3.26. Microscope images of the holes drilled in a bevel sample of sodalime (a) and in a reference sample of sodalime (b). The holes are drilled with bursts of 50 pulses at 1.28 GHz, the burst repetition rate is 1 kHz, the burst fluence is 400 J/cm², and the drilling time is 10 s.

The first thing worth noticing here is that for fixed parameters the drilling is very reproducible as can be observed in Figure 3.26 (b) for blind holes. In addition, even for a rather high burst energy, the sodalime sample does not exhibit any heat affected zone surrounding the holes in both cases. From [124] we know that a heat affected zone appears at higher burst repetition rates. Based on these images, we measured the diameters at fixed depth on the reference

sample and compared it to the effective outlet diameter of the bevel sample as depicted in Figure 3.27 in sodalime.

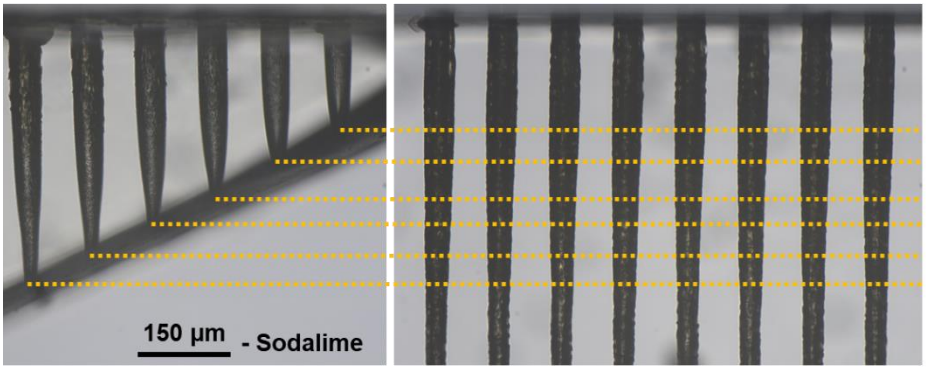

Figure 3.27. Schematic representation of the measurements realised during this study in sodalime.

The graphical representation of the diameter as a function of the depth along with pictures of the output diameters is displayed in Figure 3.28 (a) for sodalime and (b) for fused silica.

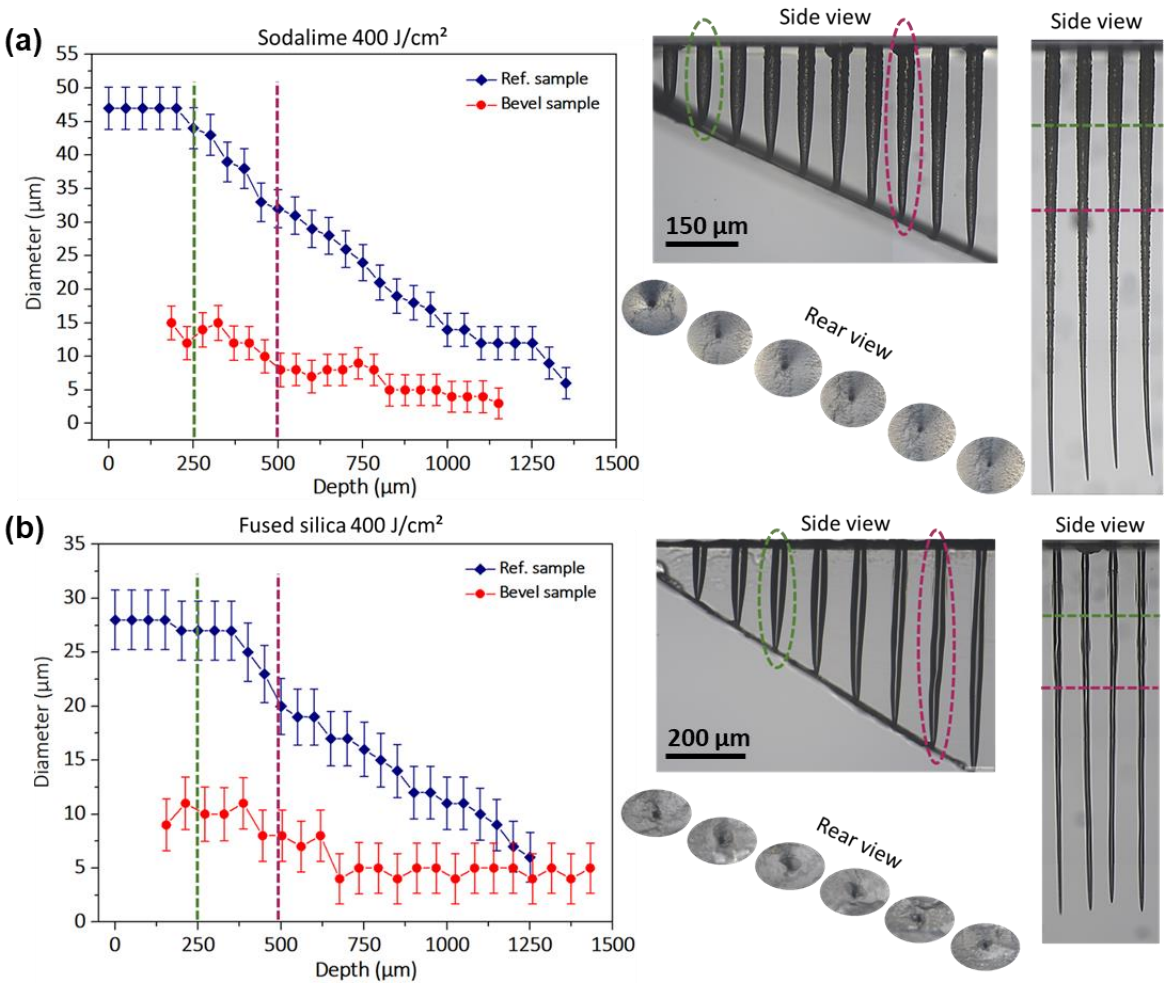

Figure 3.28. Graphical representation of the diameter as a function of the depth for both the bevel sample and the reference sample of sodalime (a) and fused silica (b).

On these graphs, we can observe that there is a significant difference between the theoretical outlet diameter, corresponding to the reference sample, and the bevel sample. This attests

that as soon as the hole is through the drilling is over no matter the number of bursts applied after. Note that for very thin samples (basically thickness < 100 µm) the outlet diameter is almost equal to the inlet diameter as was observed on Figure 10 of [124].
From several side observations of through hole drillings, it appeared that the drilling stopped as soon as the plasma leaves the hole (i.e. as soon as the hole goes through), leaving an outlet diameter around 8 µm. This observation could mean that the enlargement of the hole diameter during the drilling, leading to cylindrical holes, might come from the plasma itself.
Let us consider a comparison between the repetitive single pulse regime and the GHz-burst mode as represented in Figure 3.29. The former is based on direct laser ablation. The drilling rate is high at the bottom of the hole due to a high fluence whereas the ablation rate is low on the inner walls due to a low fluence (close to ablation threshold). Ablation of the inner walls explains the slight enlargement of the hole during the drilling process. On the contrary, in the case of GHz-bursts, the drilling mechanism at the bottom of the hole results mainly from the heat accumulation brought by the high pulse repetition rate and the elevated number of pulses per burst. The enlargement of the hole is not provoked by direct laser ablation anymore but rather by the interaction between the inner walls and the plume (which is composed by hot dense matter) either by mechanical erosion or by heat transfer. So, without the ablation plume, there is no enlargement of the hole.

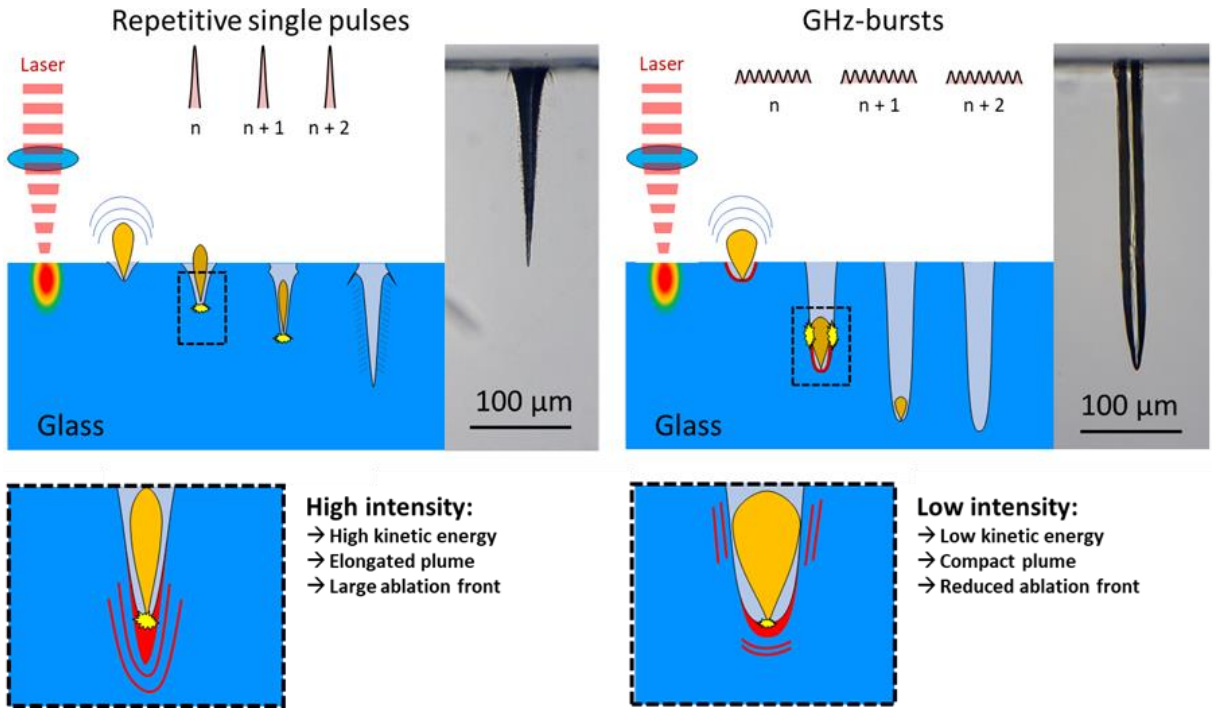

Figure 3.29. Schematic representation of the drilling process in the repetitive single pulse regime and in the GHz-burst mode.

On the basis of this observation, we defined a new protocol (P2) including four steps in order to measure the optical transmission in blind hole drilling conditions (with large outlet diameters). The new protocol is described in Figure 3.30 along with the first protocol (P1).
The first step is to pre-cut the glass sample as a bevel ①. Then, instead of cleaving the sample, we mount it on our drilling station to drill holes with the GHz-burst mode ②. The third step consists in releasing the pre-cut part by a hot air flow produced by an airgun (200 °C) that

heats the bottom part of the material. The thermal gradient induces a stress that will release the bottom part ③, leaving a drilled bevel sample ④. Using an airgun enables us to release the bottom part without moving the top part (bevel) in contrast to applying mechanical stress.

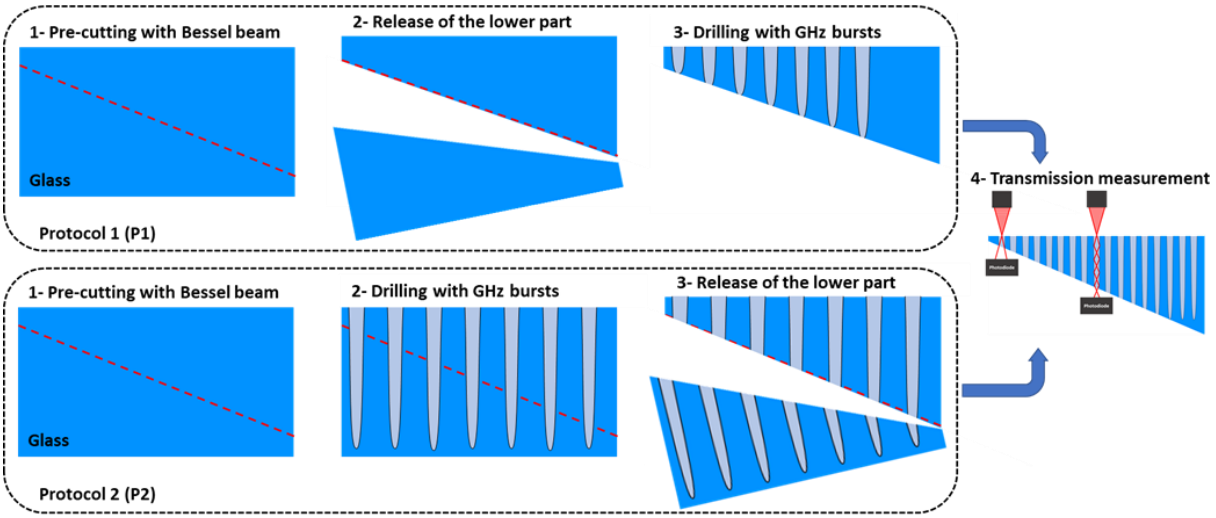

Figure 3.30. Schematic representation of the two protocols used for the transmission measurement.

With this method, we obtained the same holes as those observed in Figure 3.26 (b) except that we basically cut them in a bevel. The resulting bevel sample is displayed on Figure 3.31 along with the bevel sample taken from Figure 3.25 (a). Thanks to this method, we were able to increase significantly the outlet diameter of the hole. This confirms that the ablation plume has a major role in the drilling process and especially in the enlargement of the hole diameter. To keep the outlet diameter comparable to the expected one, it is important to keep some material underneath the desired depth.

However, by this means, we only keep the upper part of the hole meaning that we keep only the crackled part, as observed in Figure 3.8, especially when using high fluences. Note that the laser parameters are exactly the same for both drillings. Therefore, we expect to observe a decrease of the transmission properties for these holes.

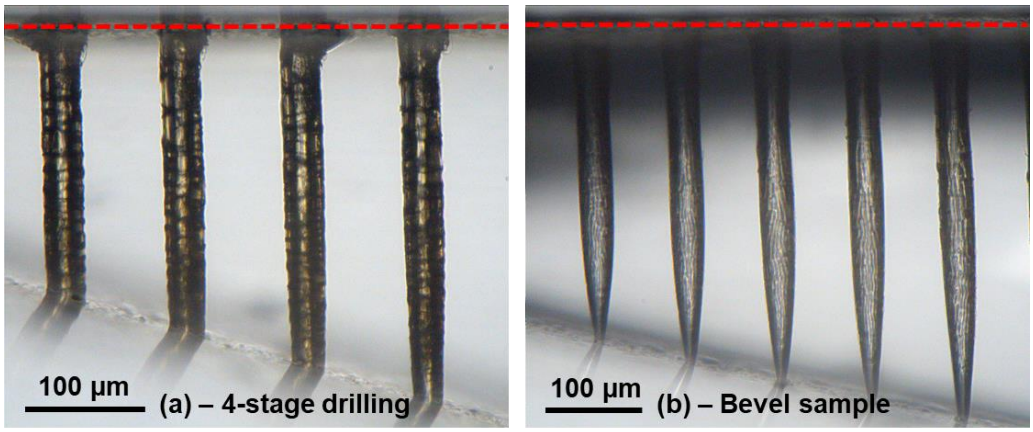

Figure 3.31. Bevel sample obtained from the 4-stage drilling process (a) and the bevel taken from Figure 3.28 (b) in sodalime.

3.2 Transmission measurement

3.2.1 Sodalime glass

Once these difficulties overcome, we were able to measure the transmission of the holes following the method depicted in Figure 3.24. The bevel samples were prepared by means of our Bessel beam cutting module. The drilling was realised with GHz-bursts of 50 pulses at 1.28 GHz with a burst repetition rate of 1 kHz, and the burst fluence was 370 J/cm². For all the holes, the drilling time was fixed at 10 s. The resulting graphs are depicted on Figure 3.32 where is displayed the evolution of the transmission as a function of the hole depth for the two investigated configurations. Note that in our case we implemented a *post-mortem* transmission measurement in MHz-burst regime. Although a *post-mortem* measurement gives us a good idea of the transmission evolution with the increasing hole depth, one should keep in mind the fact that the absorption of the laser beam along the hole could be slightly different during the drilling process since (i) the laser intensity is lower in the GHz-burst regime, (ii) the confined plume may absorb part of the incoming laser burst, and (iii) both inner walls topography and hole geometry change during the drilling process.

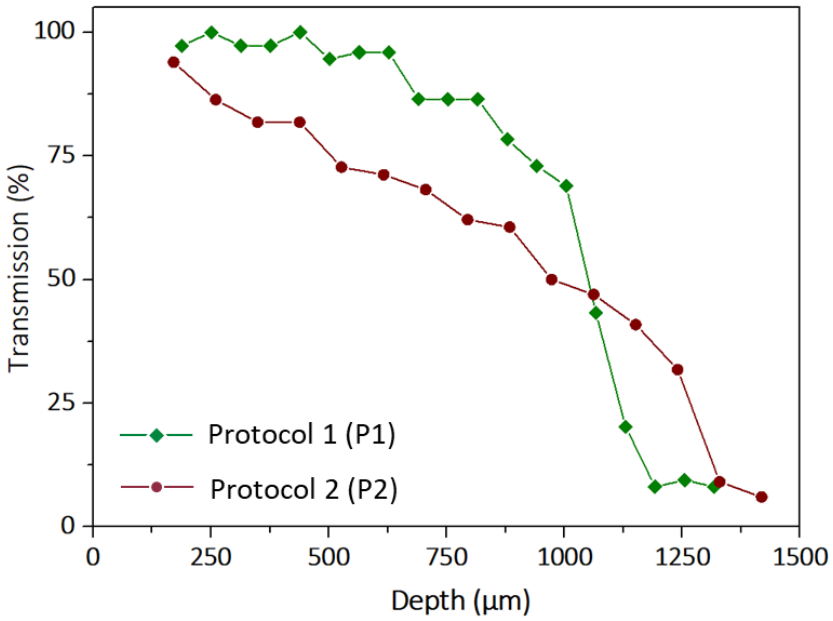

Figure 3.32. Evolution of the transmission as a function of the depth of the hole for the two configurations in sodalime.

On this graph, one can observe that the two curves are significantly different. The green curve, corresponding to protocol P1, seems to display a threshold beyond which the transmission drops significantly from nearly 75 % to 7%. Note that, as was suspected, the cracks appearing in the first few hundreds of micrometres of the hole affect significantly the transmission. The red one corresponding to protocol P2 displays a quasi-linear decrease of the transmission as a function of the depth. Note that the five last points (three greens and two red) correspond to holes that do not go through. As was expected in this case, the transmission decreases as the hole goes deeper. As can be seen in Figure 3.31, with protocol P2, all the holes are crackled while the first ones in the bevel sample (P1) are much smoother.

However, on the graph in Figure 3.32, we can observe that the transmission drops significantly on the red curve compared to the green one. This attests that the cracks appearing indeed induce a transmission drop. On Figure 3.31 (b), the cracks on the first part of the hole appear at a certain hole depth. The first holes of Protocol 1 of the bevel are very smooth all the way. This could mean that the plume also plays a part in the inner walls' quality as depicted in Figure 3.33. In the case of the first protocol, the first holes do not display cracks in the first part of the hole. Indeed, as soon as the plume escapes the hole by the outlet, the drilling is over hence there is no material redeposited on the inner walls anymore. As a consequence, the transmission remains high as the inner walls are smooth. Once the depth reaches a certain value, prior to the hole being through, the depth is already too high for the plume to fully escape, matter begins to be redeposited on the inner walls making them clearly rougher leading to a slight decrease in the transmission. This assumption can be confirmed by the fact that the smooth zone at the tip of the hole, identified on Figure 3.25, is more or less constant for a constant burst energy. The last 200 µm of the hole are always smooth due to the fact that no matter is redeposited here as the kinetic energy of the plume allows for a matter redeposition further upstream.

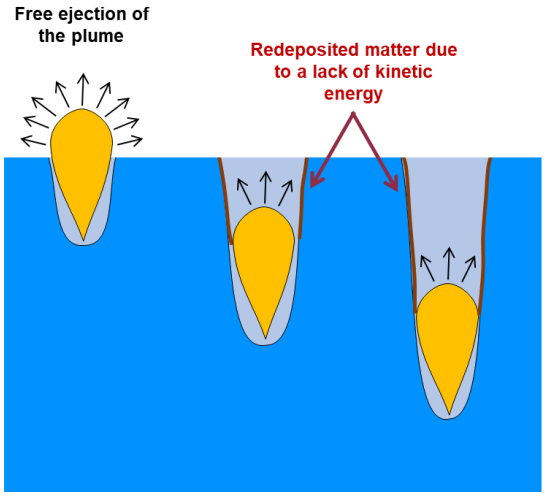

Figure 3.33. Schematic representation of the plume behaviour during the drilling.

In order to get a better sense of the phenomenon occurring here, it is important to have a look at the hole morphology as depicted on Figure 3.34 (a). This image of the bevel sample taken with the microscope allows us to observe the very same morphology as the one observed in Figure 3.8. On the graph displayed on Figure 3.34 (b), two linear fits are indicated as a visual guide for our hypothesis. The first line in dashed red corresponds to the first stage of the drilling. In this case, the plume expands freely in the air and its kinetic energy allows it to be fully ejected from the hole. In this case, the transmission of the hole is rather constant and close to 100 % up to a depth of approximatively 450 µm. For such a low depth, the number of reflections on the inner walls is probably low resulting in low refraction and scattering losses.

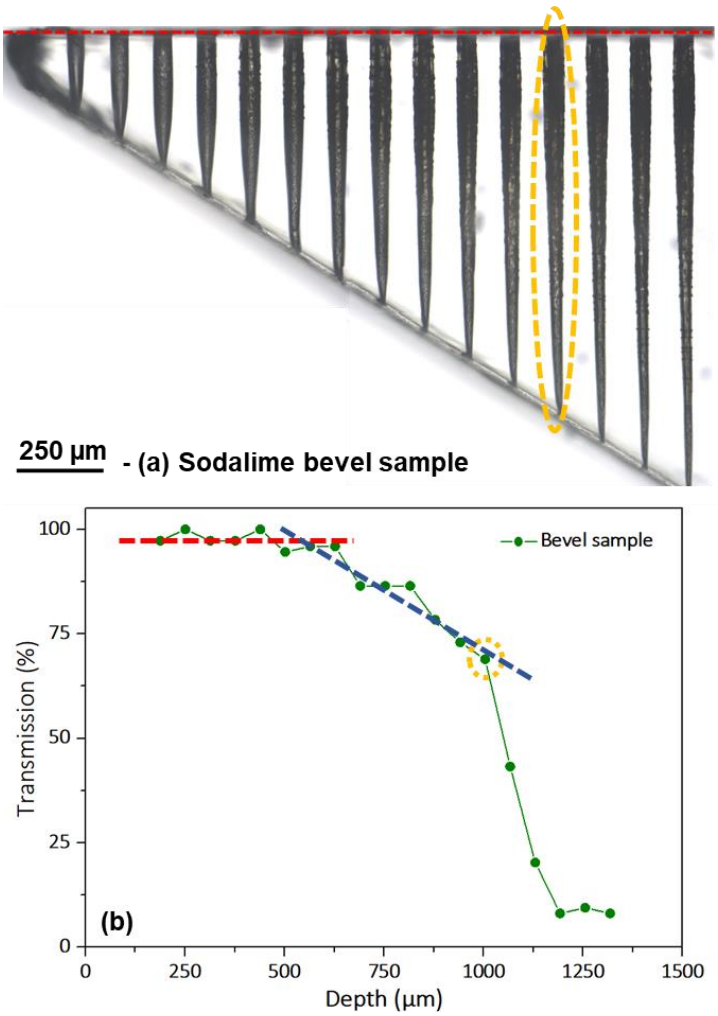

Figure 3.34. Microscope image of the holes obtained on the bevel sample of sodalime with a burst fluence of 370 J/cm² at a repetition rate of 1 kHz (a). Transmission of the hole as a function of its depth for the bevel sample (b).

When the first cracks begin to appear, in this case around the sixth hole with a corresponding depth of 500 µm, the transmission drops slightly and then it decreases almost linearly as represented by the second line in dashed blue. In this case, the transmission decreases as the hole depth increases, which is probably due to the fact that as the hole is getting deeper, the zone of redeposited matter (and thus crackled sodalime) increases, thus decreasing the transmission. Then, we get to the hole circled in yellow corresponding to the threshold beyond which the transmission drops significantly. We think that this drop in the transmission corresponds to the end of the drilling. We suspect that the energy transmission has dropped enough from scattering, multiple reflections, and conversion by drilling through ablation that the energy reaching the tip of the holes has diminished getting close to the ablation threshold.

3.2.2 Fused silica

Fused silica has a significantly different hole morphology than sodalime. The former usually does not display any cracks on the inner walls of the hole. Therefore, we expect the transmission to display a different behaviour than for sodalime. In the case of fused silica, we think that the transmission should drop linearly with the evolution of the depth as the transmission drop should only result from the increasing of the depth. The image of the bevel

sample and the corresponding transmission measurement are depicted in Figure 3.35. As can be observed in the bevel sample, the drilling is much less regular than in sodalime but the hole morphology is very smooth and even shiny. The graph in Figure 3.35 (b) shows indeed a different behaviour than that was observed in sodalime. As we expected, this graph appears to show only one decreasing step. Although the transmission is decreasing, we can clearly see that it remains very close to 100 %.

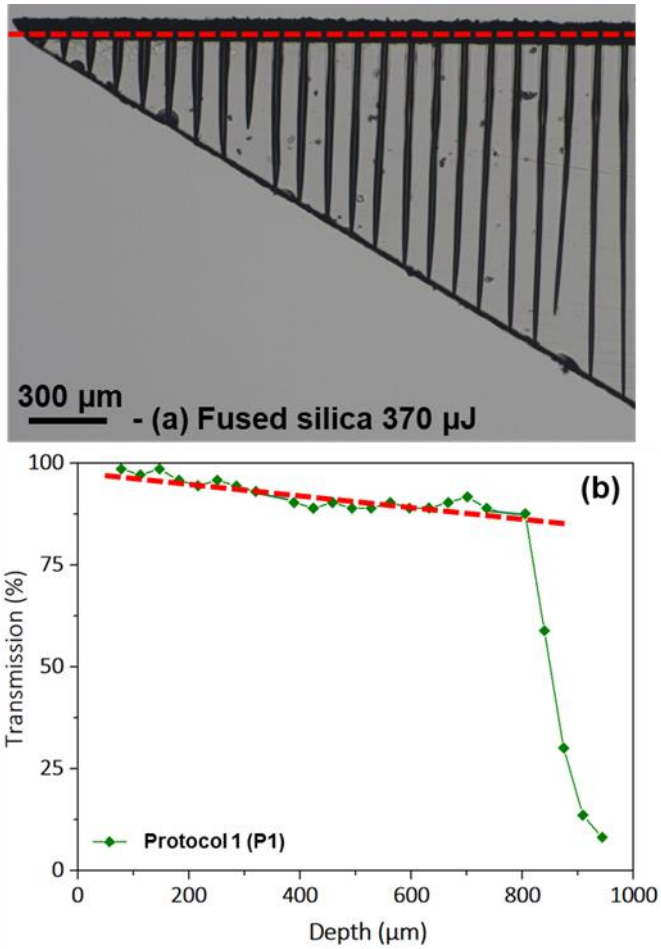

Figure 3.35. Microscope image of the holes obtained in the bevel sample of fused silica with a burst fluence of 370 J/cm² at a repetition rate of 1 kHz (a). Transmission of the hole as a function of its depth for the bevel sample (b).

As we suspected, it seems that the inner walls' quality plays a crucial part in the transmission of the energy towards the tip of the hole. Interestingly, despite the transmission dropping more slowly than in sodalime, the drilling stops a bit sooner with a corresponding transmission close to 90 %. This observation is probably due to the fact that fused silica has a higher ablation threshold than sodalime.

The observations made during this study all tend to confirm the hypothesis that the energy is guided by the inner walls towards the tip of the hole. We also revealed that the plume plays a major part in the drilling process. In order to support this hypothesis, we implemented a pump-probe imaging setup to thoroughly investigate the plume behaviour during the drilling and especially for through holes.

4. Pump-probe shadowgraphy

The pump-probe shadowgraphy was implemented in order to get a much better insight in the drilling process. In a first part, we decided to investigate the drilling process in the three different regimes with several probe delays. We were interested in the dynamics of the interaction during the burst as well as the luminescence time of the plume contained in the hole after the burst is over. The second part is dedicated to through hole drilling as we observed the limitation regarding the outlet diameter underlined in the previous section. The goal here is to provide evidence that in the GHz-burst regime, the plume plays a major part in the drilling process and especially regarding the maintaining of a rather constant diameter. Indeed, we suspect that as soon as the hole is through, the plume escapes the hole from the rear side and cannot increase the effective diameter of the hole anymore. Note that, as was explained in Chapter 2, the repetition rate here is fixed by the camera at 200 Hz.

4.1 Comparison of the three regimes

In this subsection, we show the dynamics of top-down drilling for the three different regimes thanks to our pump-probe setup. The results will be discussed in terms of quality of drilling, effect on the surrounding material as well as luminescence lifetime of the contained plume.

4.1.1 Single pulse regime

In this sub-subsection, we describe the results of the drilling studies in the repetitive single pulse regime. We investigated delays from 0 ns up to 20 µs in 300 µm thick AF 32. We chose to work on this specific material as we needed thin samples to avoid the large shadowy part that can appear near the surface of thick samples. The spot size is 7.3 µm with a corresponding numerical aperture of 0.14. In Figure 3.36, we show the drilling obtained with pulses of 200 µJ with a delay of 25 ns and a pulse number ranging from 1 to 120. We chose to display this particular delay as we can observe many interesting events (ablation plume, shockwave in the bulk) on these images.

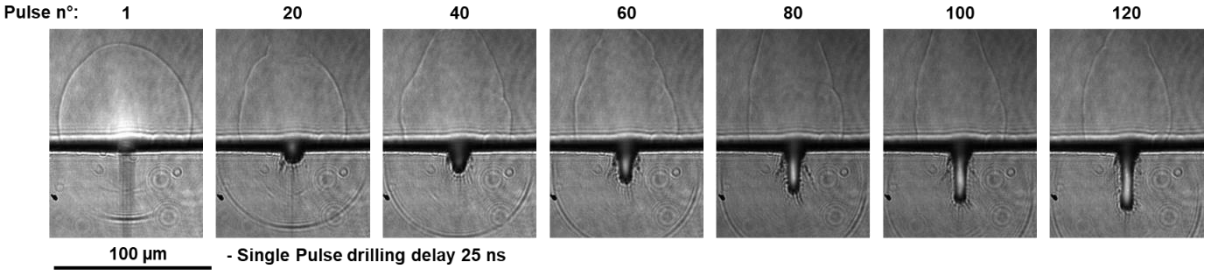

Figure 3.36. Pump-probe imaging in AF 32 in single pulse regime with pulses of 200 µJ at a repetition rate of 200 Hz from pulse number 1 to 120 and a delay between the pump and the probe of 25 ns.

As was already suggested, the very high intensity of the pulses in this regime affects the material. With this delay, the shockwave is highly visible underneath the surface for pulse number 1 up to pulse number 80, after this, the shockwave is still here but further down. Also, we have a clear vision of the plume of ejected matter and its dynamic during the drilling. The first pulse ejects matter homogeneously in all the directions as can be deducted from the hemispherical shape of the bubble-like structure above the surface. However, as the drilling

continues, the plume starts to be guided by the inner walls of the hole, which is particularly visible for pulse numbers from 60 to 120, with the ablation plume showing a preferential direction.

On the image corresponding to the first pulse applied to the sample, we can also observe a transient index change below the surface which disappears by pulse number 40. This attests once again that this regime highly impacts the surrounding material. An interesting point that can be observed here is that the collar that can be observed in high intensity regimes, does not appear right away with the very first pulse but rather with an accumulation of pulses. Interestingly, with this experimental setup, we can observe the luminescence of the ablation plume that is confined within the hole in addition to the bubble-like structure above the sample. This led us to investigate the luminescence time of this plume within the hole. Figure 3.37 shows the evolution of the hole for a fixed pulse number (50 pulses here) and an evolving delay between the pump and the probe. In this figure, the surface of the sample is not always at the same level, contrarily to Figure 3.36, as we aimed to observe the evolution of the bubble-like structure as well as the shockwave.

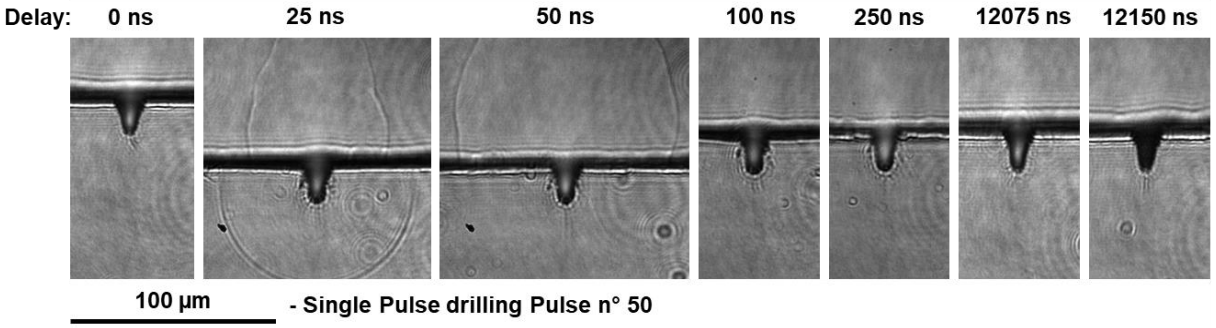

Figure 3.37. Pump-probe imaging in AF 32 in single pulse regime with pulses of 200 µJ at a repetition rate of 200 Hz with delays ranging from 0 ns to 12 150 ns for the 50th pulse applied.

This figure retraces the story of the drilling with a delay ranging from 0 ns to 12 150 ns for the fiftieth pulse applied to the sample. We chose to display only 7 delays here for the sake of clarity. However, we observed that, between delays 250 ns and 12075 ns, there was no clear change in the pictures. Indeed, as soon as the delay does not allow for visualizing the ejected matter nor the shockwave, what is left to see is only the plume luminescence. In this case, an interesting point can be seen for delays around 12 100 ns. Around this particular delay, we observed that the luminescence of the plume was discontinuous. For an even longer delay, the plume was no longer luminescent as can be seen in Figure 3.37 for the delay 12 150 ns. Note that no matter the pulse number, the luminescence delay of the plume remained 12 100 ns. Even in the single pulse regime, this luminescence time is very high. Unfortunately, we observed that the external modulator of the pump laser is not 100% efficient. As a consequence, even for a *gate close* instruction we can observe a leakage reaching the sample. This leakage has been estimated to only a few tenths of one femtojoule. Although this energy is very weak, we cannot exclude that the luminescence of the plume is fed and maintained by the leakage of the pump laser. However, as this leakage is persistent in all the regimes, we consider that the comparative study still holds.

4.1.2 MHz-burst regime

This subsection is dedicated to the pump-probe shadowgraphy of drillings in the MHz-burst regime. Just as in the previous subsection, we started with a fixed delay of 25 ns and investigated the evolution of the drilling. The corresponding images are shown in Figure 3.38. We used bursts of 4 pulses with a burst energy of 200 µJ meaning each individual pulse carries 50 µJ.

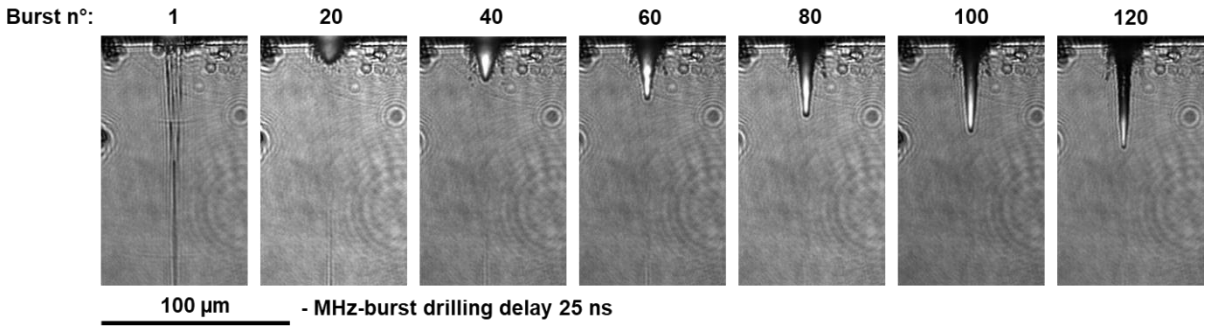

Figure 3.38. Pump-probe imaging in AF 32 in MHz-burst regime with bursts of 200 µJ at a repetition rate of 200 Hz with a delay of 25 ns and a burst number applied to the sample ranging from 1 to 120.

In Figure 3.38, we chose to display only the material as we observed that the behaviour of the bubble-like structure resulting from the ejection of the ablated plume was similar to the single pulse regime. Just as in the previous subsection, we can observe that the wings that we expected to appear took about 40 bursts to be seen which attests that it results not only from the high intensity of the pulses but also from an accumulation of bursts. Additionally, the index change that was observed in the single pulse regime can also be seen here. Note that this modification was going down the material during the drilling as can be observed from burst 1 with the modification touching the rear surface, burst 20 with the modification starting roughly 80 µm below the surface and burst 40 with the modification nearly 100 µm below the surface. Interestingly, for this configuration we did not witness any shockwave in the material. Indeed, the pulse energy is too low in burst mode, and the recoil effect, resulting from the conservation of momentum, produced by each pulse in the burst is negligible. This is the reason why the shockwave is not visible in burst mode.

Figure 3.39 shows the whole drilling story with bursts of 4 pulses and a burst energy of 200 µJ for the fiftieth burst applied to the sample.

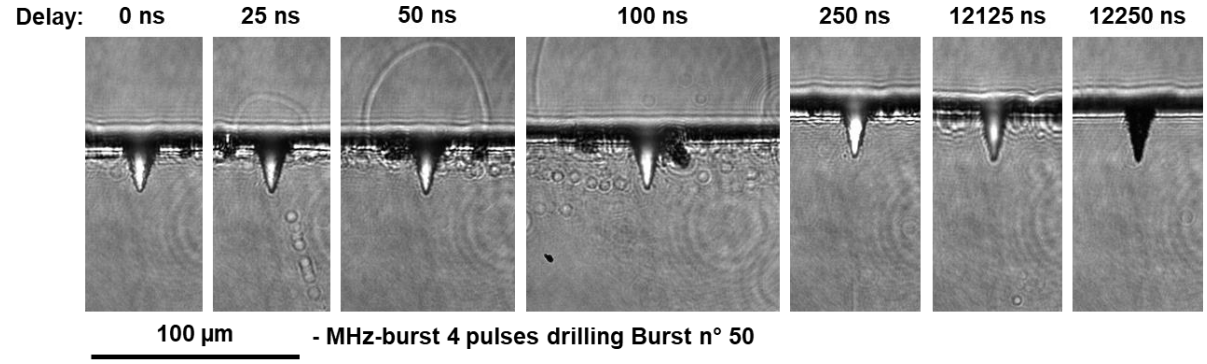

Figure 3.39. Pump-probe imaging in AF 32 in MHz-burst regime with 4 pulses per burst and bursts of 200 µJ with delays ranging from 0 ns to 12 150 ns for the 50th pulse applied.

On this figure, we observe that the drilling process is quite similar to that was observed in the single pulse regime. However, the bubble-like structure above the surface follows the same tendency but with a delay. At 25 ns, in MHz-burst regime, the plume of ejected matter is much smaller than that was observed in the single pulse regime probably due to the fact that the pulse energy is divided by 4 and thus, also the kinetic energy of the plume.
The luminescence of the plume is slightly different from the single pulse regime. It appears that the extinction of the plume is also delayed due to the use of bursts. In this case, the luminescence of the plume lasts about 12 200 ns.

4.1.3 GHz-burst regime

In this subsection, I will present the drilling dynamics in the GHz-burst regime. Figure 3.40 corresponds to the images acquired with a fixed delay of 25 ns for bursts of 200 µJ and 50 pulses. This means that each pulse carries 4 µJ which is far below the 200 µJ of the single pulse regime and even slightly lower than the ablation threshold. One should be careful, the scalebar changed for this configuration as we used a different objective resulting in a different magnification.

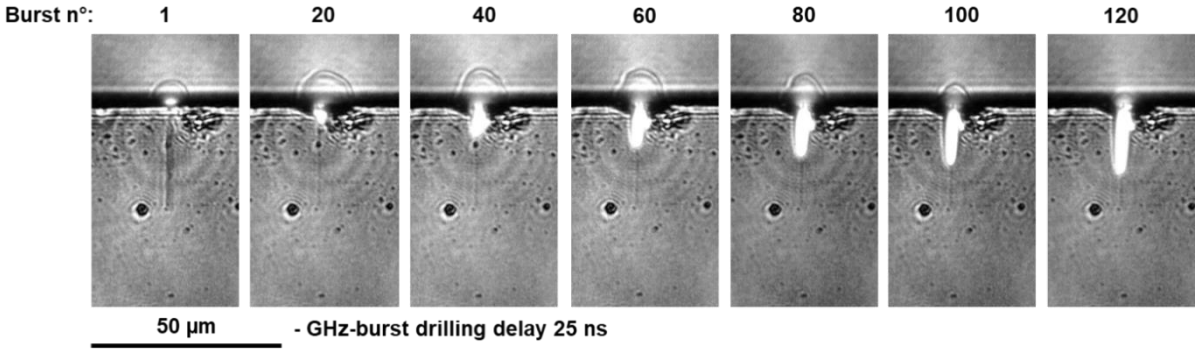

Figure 3.40. Pump-probe imaging in AF 32 in GHz-burst regime with bursts of 200 µJ at a repetition rate of 200 Hz with a delay of 25 ns and a burst number applied to the sample ranging from 1 to 120.

This series of images depicts the drilling process with a delay of 25 ns. As can be seen in Figure 2.10 in the middle graph of the bottom row, this means that the probe pulse is located nearly in the middle of the GHz-burst pump. However, we can observe that for the very first burst applied to the sample, some matter is ejected from the sample, as confirmed by the small bubble-like structure above the surface. This means that the 20 pulses of the burst arriving before the probing, are enough to provoke some ablation of the material. Note that during this study we observed that AF 32 glass required the first 13 pulses of the burst to display a clear bulk modification. We can also notice that, just as in the MHz-burst regime, we do not observe a shockwave in the material. Interestingly, we also don't observe any transient index change. The only modification that can be observed in the sample is the one resulting from the very first burst that is close to the surface and roughly 50 µm. This modification has already been observed in previous studies [124,127]. Just as in the previous subsection, we studied the whole drilling process for a fixed number of bursts applied to the sample (50 bursts here) with delays ranging from 0 ns up to the extinction of the luminescence of the plume. This series of images is depicted in Figure 3.41. This figure shows that the ejected plume follows more or less the same behaviour as that was observed in the MHz-burst mode. We can still observe a small delay with respect to the single pulse regime regarding the plume above the

sample. The major difference here comes with the luminescence of the plume within the hole. As can be seen here, the plume is luminescent up to a delay of 17 225 ns. This attests that the plume behaviour in GHz-burst is significantly different with a luminescence time up to 5 µs longer than the two other configurations.

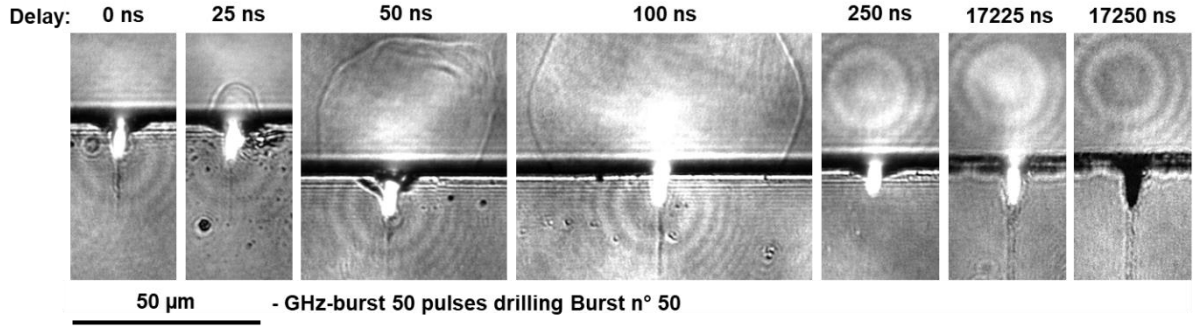

Figure 3.41. Pump-probe imaging in AF 32 in GHz-burst regime with bursts of 200 µJ at a repetition rate of 200 Hz with delays ranging from 0 ns to 17 120 ns for the 50th pulse applied.

4.2 Through hole drilling

In this section, I present the results from a pump-probe shadowgraphy experiment on a through hole in a bevel sample of sodalime. The goal was to investigate the dynamics of the ablation plume during the drilling process, and to reveal its role in the through hole drilling process as we assume that the confined ablation plume is responsible for the hole enlargement. We drilled through holes in a bevel sample with several delays. In Figure 3.42, we show the drilling with a delay of 50 ns meaning that the probe pulse arrives around 12 ns after the last pulse of the pump burst.

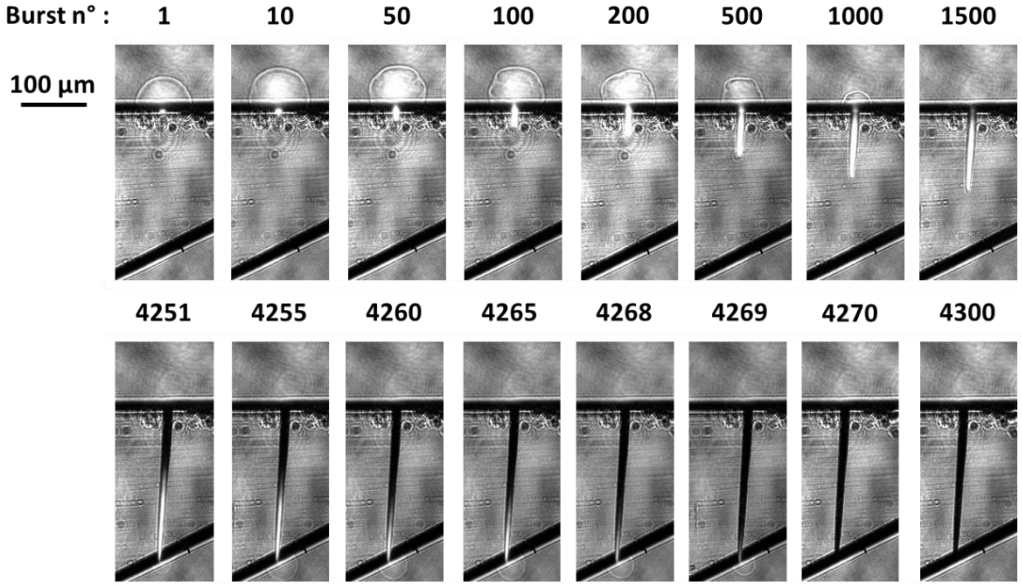

Figure 3.42. Pump-probe imaging of a through hole drilled at 200 Hz with a 50 ns-pump-probe delay. The top row shows the beginning of the drilling, meanwhile the bottom row shows the end. The pulse number is given for every picture.

This delay value was chosen on purpose in order to observe both matter ejection and plume luminescence all along the drilling process. In this study, we drilled a bevel sample with a burst fluence of 300 J/cm² and a burst repetition rate of 1 kHz. In this particular study, we chose to

record every image corresponding to every burst applied to the sample so that we would not miss anything from the whole drilling process.
The top row of this figure shows the beginning of the drilling. We can observe that the plume is ejected upstream from the sample. This figure depicts that even the very first burst ablates some material, then, for about 100 bursts, we consider that the drilling is still in the stage of surface ablation as the plume is rather constant for a fixed delay. Then, and as the drilling goes deeper, the ablation plume starts to be contained in the hole and we can observe that the plume above the front surface is reducing. The confined plume is then highly luminescent; its height is about 120 µm. By burst number 1500 (i.e drilling time of 7.5 s) the plume is fully contained inside the hole switching to confined ablation [136]. The interesting part here concerns the end of the drilling with burst numbers from 4251 to 4300. The image corresponding to burst number 4251 (i.e drilling time of 21.2 s) is the very first image with a through hole. Indeed, as can be observed here, this image shows matter ejection downstream the sample. This bubble-like structure is quite similar to that was observed on the front surface in the beginning of the drilling. Once the hole is through, the plume is leaking by the outlet hole and its luminescence decreases in the hole. Note that the leaking is quite fast as in a span of less than 20 bursts, the plume is not visible anymore. By burst number 4270, all the plume has escaped from the hole. A point worth noticing here is that if we keep applying bursts after the leakage of the plume, no interaction can be seen any more, and there is no evolution of the overall hole geometry, as depicted on this figure for burst number 4300. So, as soon as the plume leaves the hole, the final hole geometry and outlet diameter are fixed. This observation confirms our first assumption that the ablation plume plays a major part in GHz-burst percussion drilling.
This limitation could be overcome by using a sacrificial layer at the rear side of the main sample as shown in Figure 3.43. for a matrix drilling in a 1 mm thick sodalime sample. Indeed, the challenge here is to keep the ablation plume contained in the hole beyond the rear side of the sample.

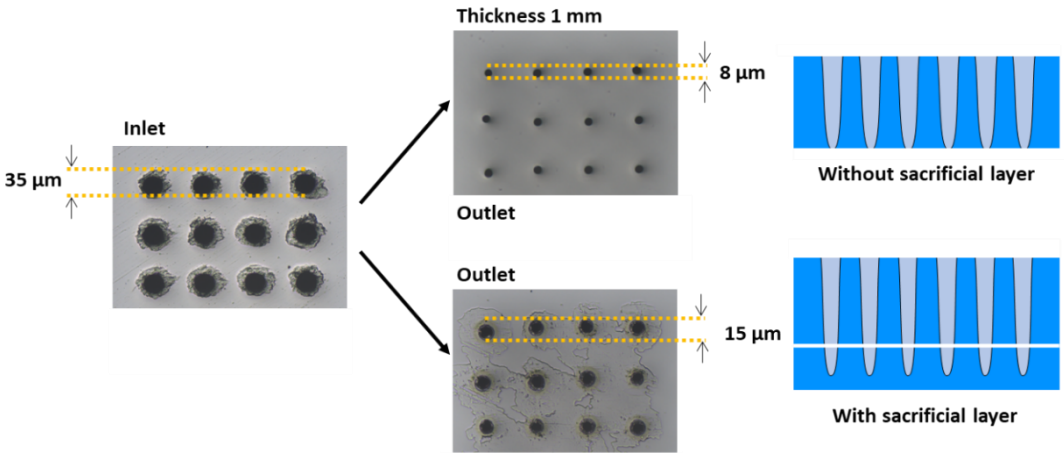

Figure 3.43. Representation of the technical solution to increase the outlet diameter by means of a sacrificial layer.

To do so, it is necessary to add some matter below the rear surface of the sample that needs to be processed. On Figure 3.43, the outlet diameter is about 15 µm with a sacrificial layer (sodalime glass) whereas it is 8 µm without. Note that the outlet diameter of 15 µm corresponds to that was expected from blind holes of 1 mm as depicted on Figure 3.28 (a).

These observations lead us to believe that bottom-up drilling might not be possible in GHz-burst regime. Indeed, we identified that the role of the plume is crucial in GHz-burst drilling and that the enlargement of the hole stops as soon as the plume is ejected from the hole. However, in bottom-up drilling, the plume would instantly be ejected from the rear side of the sample, thus the enlargement of the hole would stop immediately. This assumption would need some experimental evidence and was not investigated in the frame of this PhD.

5. Conclusion

In order to investigate the new processing regime of GHz-bursts of femtosecond pulses, a percussion drilling experiment based on focalization of a Gaussian beam has been implemented. This very first experimental chapter corresponds to the most extensive study that was led during these three years. Indeed, in the very first months of this PhD, the goal was to get familiar with the basics of laser processing by trying to obtain results similar to those obtained in a study realised a few months before the beginning of this PhD [124]. It turned out that in percussion drilling experiments, the GHz-burst immediately provided excellent results that required further studies.

We started by implementing systematic studies on different laser parameters such as burst number, burst fluence, burst duration as well as burst shape. The very first observation that was made on these drillings was that they were significantly deeper than that was observed in repetitive single pulse drillings. In addition, when plotting the depth as a function of the number of bursts applied to the sample, we identified a three-stage drilling process [127]. Indeed, on the corresponding graphs, we can clearly observe three linear stages. The first one corresponds to a low number of bursts, basically the beginning of the drilling, for which the plume expands freely in the air resulting in a low-density plume and thus a low screening effect which provides a high drilling rate. After the hole reaches a certain depth, the plume is contained inside the hole and becomes denser resulting in a higher screening effect and thus a lower drilling rate. Finally, the transmission losses and the drilling process along the hole have lowered the energy reaching the tip of the hole such that the drilling is over. At this point, the highest aspect ratio obtained in fused silica is 73 which is already an impressive result considering the focus is fixed at the font surface and there is no chemical etching. However, by adapting both the burst fluence and the numerical aperture, we have been able to reach a hole depth of nearly 4 mm with a corresponding aspect ratio of 150. From these experiments, we suspected that such high aspect ratios obtained with a fixed focus could only mean that the hole itself acted as a waveguide guiding the laser beam towards the tip of the hole so that the drilling keeps going on even for depths exceeding 1 mm.

In a second part, we provided a comparative study between the three regimes at our disposal, the repetitive single pulse, the MHz- and GHz-burst. To do so, we fixed the energy of the bursts (pulses) and investigated the evolution of the depth as a function of the number of bursts (pulses) applied. This study revealed significant differences between the three regimes regarding the possibility to reach high aspect ratios. We also observed that there were only two stages in the drilling process in the single pulse and in the MHz-burst regimes. We suppose that the first stage could be skipped due to the high intensity of the pulses in those regimes which instantly provoke deep ablation. As a consequence, the drilling rates of the three

regimes are very different. Regarding the hole quality, the repetitive single pulse regime produces very tapered holes with inner walls appearing very rough. One could also mention the wing structures appearing at the surface of the sample suggesting that the surrounding material is highly affected. We assume that these wings result from the refracted beam. They are not visible with long bursts due to the low pulse energy. In the MHz-burst regime at constant energy, it appears that the hole morphology depends on the number of pulses per burst. For a low number of pulses per bursts, the morphology is quite similar to that was observed in the repetitive single pulse regime with a conical hole and very rough inner walls. When increasing the number of pulses per burst, the morphology switches towards that was observed in GHz-burst regime. The inner walls become smoother and the wings disappear.

In the two first parts of this chapter, we proposed a hypothesis that the hole acts as a waveguide and the transmission losses would eventually stop the drilling for a lack of energy reaching the tip of the hole. To confirm this hypothesis, we decided to implement a transmission measurement on bevel samples to study a wide range of hole depths. During the said study, we identified a peculiar behaviour regarding the evolution of the outlet diameter. It appeared that the outlet diameter was rather small and constant. Microscope images of the resulting hole led us to believe that the ablation plume had a major part in the drilling process and especially regarding the enlargement of the hole. After overcoming these limitations, we designed two protocols to measure the transmission. The transmission measurements provided evidence that indeed the hole acts as a waveguide and the drilling stops when the transmission drops. In addition, it also provides evidence that redeposited matter on the inner walls appearing during the drilling can lower the transmission.

The last part of this chapter is dedicated to the pump-probe shadowgraphy study. The latter was implemented to investigate the behaviour of the plume during the drilling. It appears that our hypothesis was correct as we were able to show that as soon as the plume leaves the hole, the drilling is over and the final geometry is fixed. We also provide a comparative study of the three regimes with this setup showing that the luminescence of the plume inside the hole stops significantly sooner in the repetitive single pulse and MHz-burst regimes than in the GHz-burst regime. In addition, we observed a shockwave propagation in the material in the repetitive single pulse regime which was not the case in the burst modes probably due to the fact that the pulse energy is much lower in the latter.

This extensive study on percussion drilling on glasses with GHz-bursts of femtosecond pulses provides evidence of the potential of the GHz-burst regime for laser processing. We obtained very high aspect ratios that are inaccessible for classical regimes without any chemicals. Moreover, we provided a pump-probe shadowgraphy study of the drilling process with those three regimes which gave us a better understanding of the GHz-burst mode in the hope for a future theoretical model. One could argue that this regime is adapted only to glasses due to their heat diffusion time that is close to the pulse-to-pulse delay (1-10 ns in fused silica) [101]. In order to provide experimental results on other materials, we performed percussion drilling experiments on crystalline materials and especially on silicon, which are described in the following Chapter 4.

Chapter 4: Crystalline materials and semiconductors percussion drilling

In this chapter, a non-exhaustive percussion drilling study on crystalline materials is presented. Indeed, based on our experience on amorphous transparent materials, we were curious as to what would happen on crystalline materials, dielectrics and semiconductors. For this study, we investigated drilling of blind holes on sapphire and CaF_2 as well as on silicon. In the end, we chose to focus on silicon with a more extensive study in order to familiarize ourselves with this particular material.

1. GHz-burst mode percussion drilling

1.1 Influence of the number of bursts

1.1.1 CaF_2 and sapphire

We started by investigating the drilling process quite similarly to the previous chapter in the three materials, silicon, sapphire and CaF_2. In sapphire and CaF_2 we observed the same general tendency as in glasses as can be seen on the microscope images on Figure 4.1 for a drilling time in a range from 100 ms to 800 ms, a burst repetition rate of 1 kHz and bursts of 50 pulses at 1 GHz in CaF_2 with a burst fluence of 105 J/cm² (a), and in sapphire with a burst fluence of 255 J/cm² (b). The spot size is 8.5 µm with a numerical aperture of 0.14. One can observe that these microscope images are very similar to the ones in Fig. 3.2 in sodalime and fused silica. Indeed, the drilling process in sapphire and CaF_2 also results from non-linear absorption. Both these materials display cylindrical holes with little to no heat affected zone.

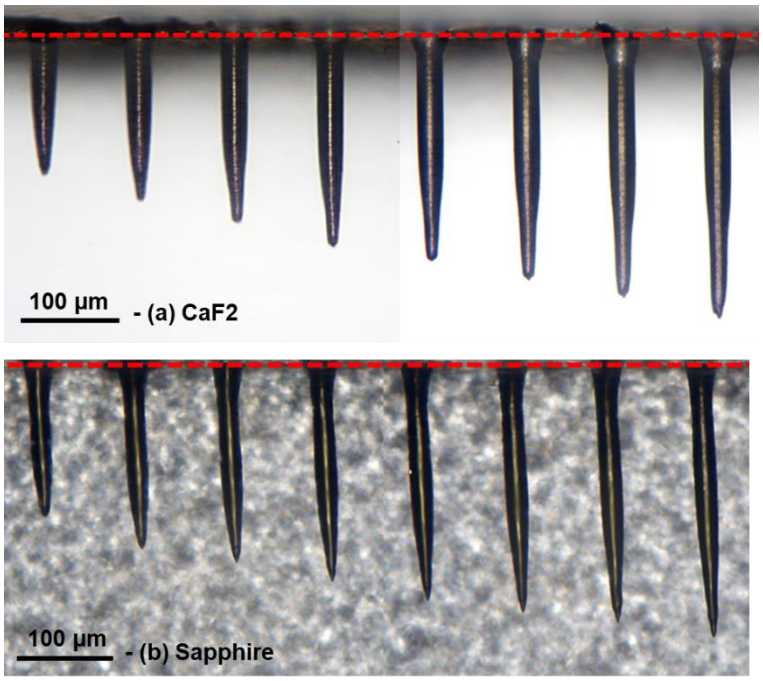

Figure 4.1: Microscope images of the holes drilled at a burst repetition rate of 1 kHz, with bursts of 50 pulses at 1 GHz and drilling times from 100 ms to 800 ms, in CaF_2 with a burst fluence of 105 J/cm² (a), and in sapphire with a burst fluence of 255 J/cm² (b).

The graphical representation of the depth as a function of the number of bursts applied is displayed on Figure 4.2 for CaF_2 for a burst fluence of 105 J/cm². Just as in the case of sodalime and fused silica, we added the linear fits of the three stages of the drilling which also appeared for these materials. In this graph, the surface ablation rate is 0.9 µm/burst and the contained ablation rate is 0.26 µm/burst.

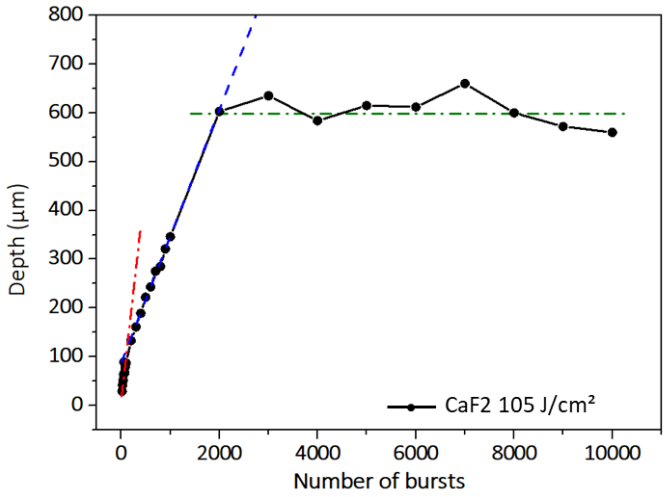

Figure 4.2: Evolution of the hole depth as a function of the number of bursts applied to the sample of CaF_2 for a burst fluence of 105 J/cm², a burst repetition rate of 1 kHz, and a burst repetition rate of 1 GHz.

During this study, we observed that the position of the focal point on CaF_2 was very critical and could reveal an interesting phenomenon that can be seen on Figure 4.3 where we display the results obtained for a focal point positioned slightly above the sample surface for the same burst energy. From Figure 4.1 to Figure 4.3, only the focus position was changed by 50 µm.

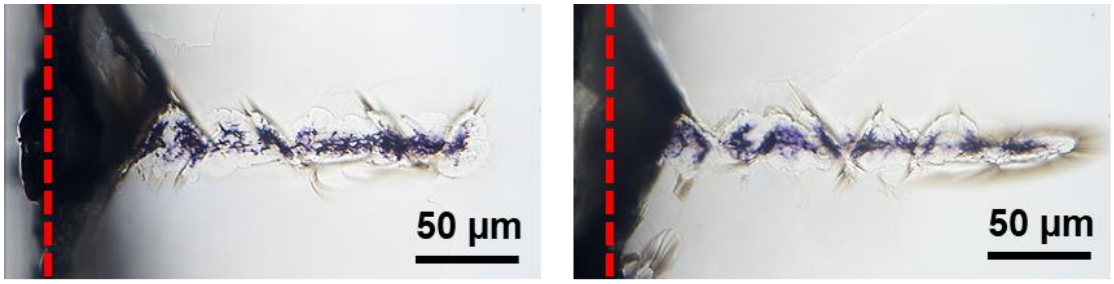

Figure 4.3. Results of the interaction between CaF_2 for a burst repetition rate of 1 kHz during 1 s, bursts of 50 ppb, a burst fluence of 105 J/cm² and a focal point 50 µm above the surface.

On these images, we can observe a cloud like structure probably due to filamentation. One can also observe cracks appearing with a particular orientation probably linked with the orientation of the lattice. Finally, a purple colour appears in the centre of the filament. This can be due to colour centres, in this case fluoridated centres. Additionally, the same phenomenon was observed for high repetition rates as depicted in Figure 4.4 with the image of a hole in CaF_2 drilled at 50 kHz for the same burst parameters for a focus at the surface of the sample.

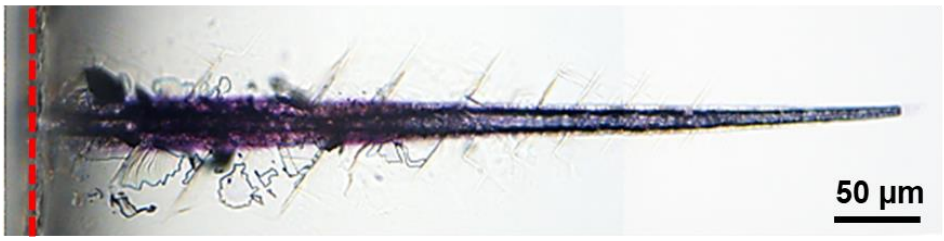

Figure 4.4. Microscope image of a hole drilled in CaF_2 with a burst repetition rate of 50 kHz, drilling time of 1 s, 50 ppb at 1 GHz and a burst fluence of 105 J/cm².

We can assume that too much heat accumulation resulting from a too low burst-to-burst delay provokes the dissociation of calcium and fluoride leading to the appearance of colour centres. This was not the case in Figure 4.1 since the burst repetition rate was much lower.

1.1.2 Silicon

On silicon, the absorption is linear for a laser beam at the wavelength of 1030 nm. We expected the behaviour to be different from the materials investigated up till this point. The infrared microscope image of holes obtained in silicon for a burst fluence of 170 J/cm², a burst repetition rate of 1 kHz and bursts of 50 pulses per burst for a drilling time ranging from 20 ms to 10 s is displayed on Figure 4.5. The spot size here is 7.3 µm and the numerical aperture is 0.14.

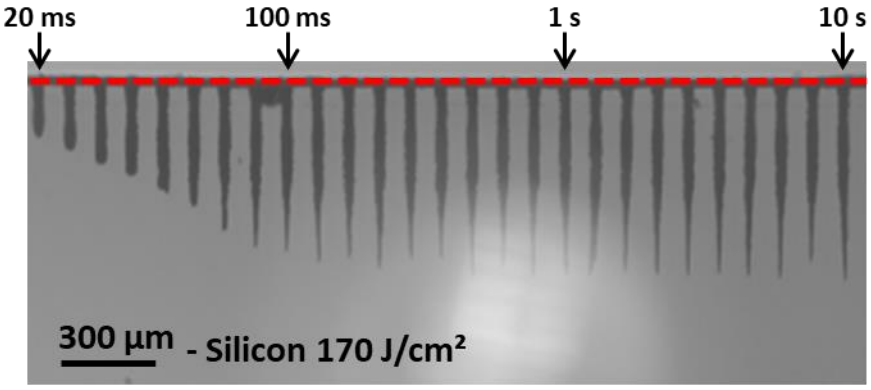

Figure 4.5. Infrared microscope image of holes drilled in silicon with a burst repetition rate of 1 kHz, a drilling time from 20 ms to 1 s, 50 ppb at 1 GHz and a burst fluence of 170 J/cm² [141].

The evolution of the depth is linear in the first part of the image before reaching saturation just as was observed previously in the dielectric materials [127]. However, the morphology is quite different to that was observed in glasses. In this case, the holes are less cylindrical and the overall uneven shape of the hole appears similar to that was observed for MHz-burst drilling in glasses [136,137]. The morphology also changes from the first holes to the last holes. In the beginning of the drilling, the holes are very cylindrical up to a certain depth where the morphology of the tip of the holes becomes much more tapered. Note that the bright halo that can be observed in the background of the image results from the 1300-nm illumination diode. The graphical representation of the hole depth as a function of the number of bursts applied to the sample for four values of fluences is represented in Figure 4.6 for the whole drilling time range. On this figure, we can observe the same tendency as was depicted in Figure 4.5, a linear increase of the depth followed by a saturation of the depth. Just as was observed on dielectrics, the depth of saturation increases with an increasing fluence.

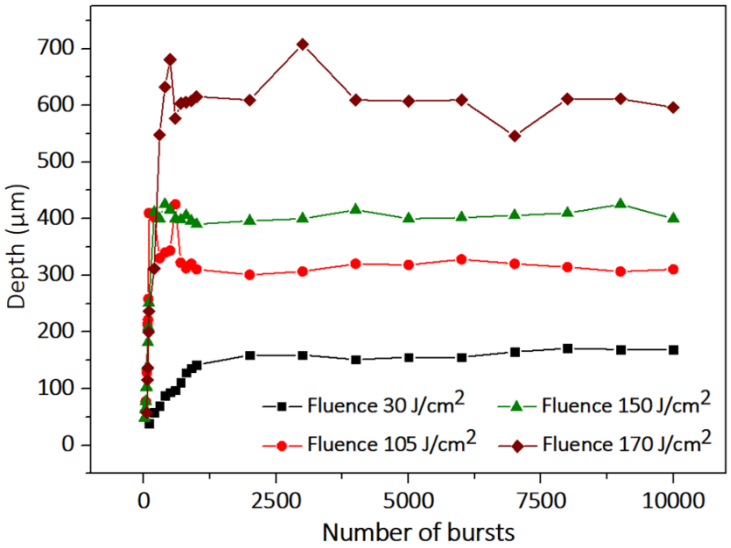

Figure 4.6. Evolution of the depth as a function of the number of bursts applied to the sample of silicon for bursts of 50 ppb, a burst repetition rate of 1 kHz, and a burst repetition rate of 1 GHz.

Contrarily to prior observations in glasses, the drilling process in silicon shown in Figure 4.6 displays only two steps while there were three on glasses. We suppose that the first stage, corresponding to a low number of bursts applied to the sample, cannot be seen with our observation system due to the shadow effect near the surface. Moreover, the absorption of the 1030 nm wavelength is linear in silicon while it relies on non-linear absorption for glasses, thus, the drilling process occurs much faster, i.e. with less bursts, in silicon than in glass. These two facts could mean that the first stage of surface ablation (identified in glasses) corresponding to the very first points of the graph is simply not visible.

During this study on silicon, we observed that, although silicon can handle higher repetition rates, it still displays different behaviours as glasses. Indeed, while increasing the burst repetition rate, we observed that after the main hole is drilled, ramifications appeared at the bottom of the hole as can be seen in Figure 4.7.

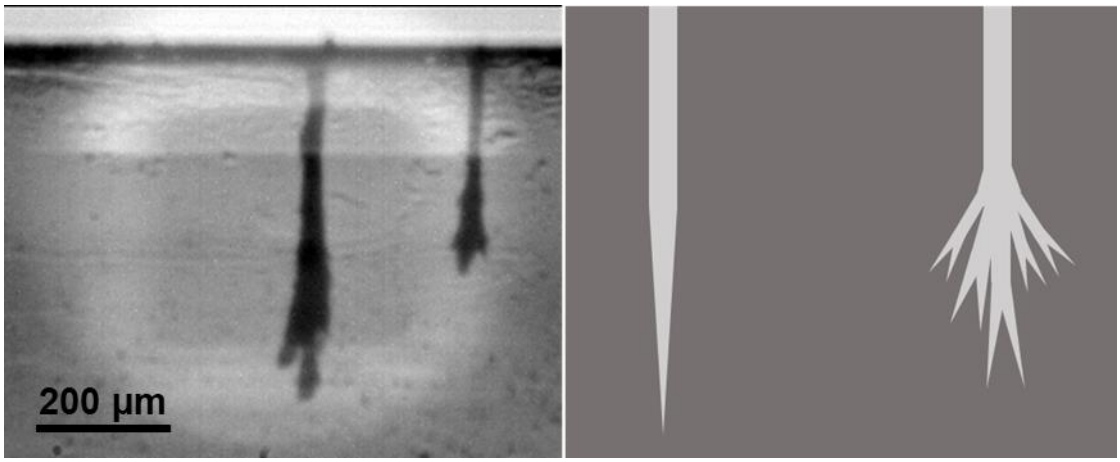

Figure 4.7. Holes obtained in a sample of silicon for bursts of 50 ppb, a burst repetition rate of 50 kHz (right) and 100 kHz (left), and a pulse repetition rate of 1 GHz (a). Schematic representation of the holes obtained in silicon for 1 kHz burst repetition rate (left) and for higher repetition rates (b).

This can be explained by the fact that the laser intensity is linearly absorbed in silicon. Thus, we can attribute the ramifications to the fact that the laser can be scattered inside the hole.

The resulting scattered sub-beams can also ablate the material creating ramifications in multiple directions.

1.2 Influence of the burst duration

This section is dedicated to the impact of the burst duration, corresponding to the number of pulses per burst, on the drilling process. We investigate the impact of this parameter in the GHz-burst regime with bursts of 50, 100, 200, and 400 pulses per burst, respectively. We keep the burst fluence constant at 450 J/cm², only the individual pulse energy within the burst is changed by adjusting the number of pulses per burst. The experimental protocol of the study, including drilling time, is the same as in the previous section. The holes obtained for three burst configurations are depicted in Figure 4.8 [141].

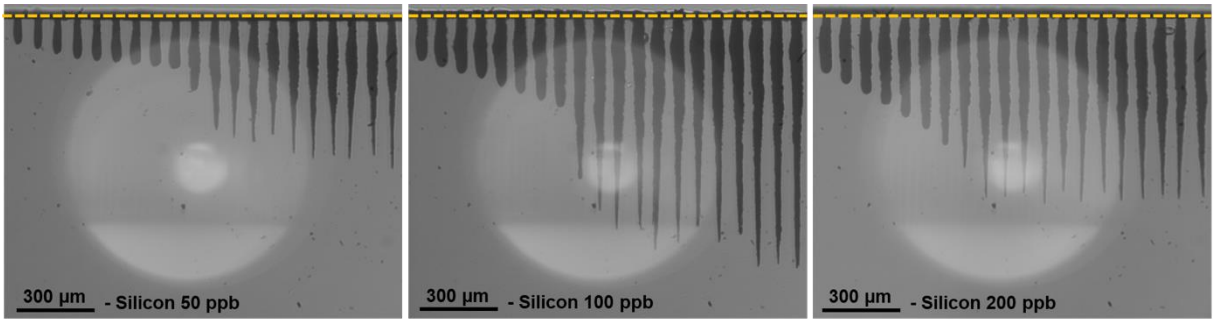

Figure 4.8. Infrared microscope images of the holes obtained in silicon for a burst fluence of 450 J/cm² with a burst repetition rate of 1 kHz and a drilling time ranging from 20 ms to 3 s for 50 ppb and from 30 ms to 4 s for 100 and 200 ppb.

As can be seen in this figure, there seems to be an optimum value of number of pulses per burst regarding both the depth of the hole as well as the overall shape. Indeed, although with 50 pulses per burst the holes are straight, we can notice a certain waviness at 100 pulses per burst. The graphical representation of the depth as a function of the number of bursts is depicted in Figure 4.9 for the whole drilling time range with the above-mentioned parameters. Additionally, we depict the graph with 400 pulses per burst. This graph confirms that there is an optimum value of burst duration for a fixed burst fluence. Indeed, on these measurements, we clearly observe that a burst containing 100 pulses per burst shows a significantly higher depth than the other configurations. This confirms that there is a compromise that needs to be found between the burst duration and the pulse energy of the individual pulses of the burst. For example, the 50 pulses per burst configuration provides twice as much energy per pulse compared to the 100 pulses burst configuration, but the burst is probably too short to benefit from accumulation [102]. Therefore, the drilling process is less efficient at 50 ppb. On the other hand, the 400 pulses per burst configuration provides a very long burst that could enhance the heat accumulation but the pulse energy is too low to provide an efficient drilling process. As has been identified in the literature [105,106,110], the ablation increases with an increasing number of pulses per burst from 1.45 µm/burst at 50 ppb up to 9.5 µm/burst for 400 ppb.

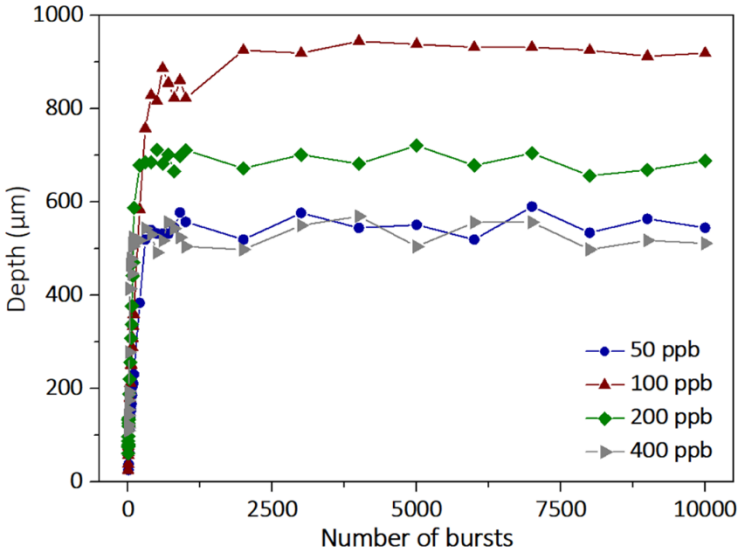

Figure 4.9. Graphical representation of the hole depth as a function of the number of bursts applied to the sample with a burst repetition rate of 1 kHz, a burst fluence of 450 J/cm² with bursts of 50, 100, 200, and 400 pulses, respectively.

A point worth noticing here is that, during this study, we were able to drill holes up to nearly 1 mm deep in silicon with a pretty regular shape. The diameter was measured around 35 µm which means we were able to obtain aspect ratios as high as 27 which is already higher than that was obtained in literature [142].

1.3 Influence of the energy repartition

In this section, we present a study of the influence of the burst shape on the drilling process. We investigated the three burst shapes introduced in the second chapter of this manuscript. The goal here is to determine if more intense pulses in the beginning of the burst can enhance the drilling process or if it is better to use high energy pulses at the end of the burst when the material has already been heated by a smoother beginning of the burst. The flat burst is also depicted in this study as a compromise between the two other burst shapes as it was shown in Chapter 3, subsection 1.3 that this burst shape produced the best results in dielectrics [136]. Just as in the previous section, we investigate the evolution of the depth as a function of the number of bursts applied to the sample. The images of the holes produced with the three burst shapes are depicted in Figure 4.10. In this Figure, we display holes obtained with a drilling time ranging from 10 ms to 10 s. The burst fluence in this case was fixed to 250 J/cm² and the burst repetition rate was kept at 1 kHz with bursts of 100 ppb. The spot size here is 7.3 µm and the numerical aperture is 0.14. On these images, we observe that the burst shape seems to produce a limited effect on the drilling process. Indeed, regarding the hole morphology, it appears that the three laser configurations produce tapered holes with much more irregular shapes than that was obtained with 50 pulses per burst on Figure 4.5. However, we can still notice a linear increase of the depth in the drilling range from 10 ms to 100 ms and then a saturation for drilling times higher than 200 ms. The graphical representation of the evolution of the depth as a function of the number of bursts applied to the sample is displayed in Figure 4.11.

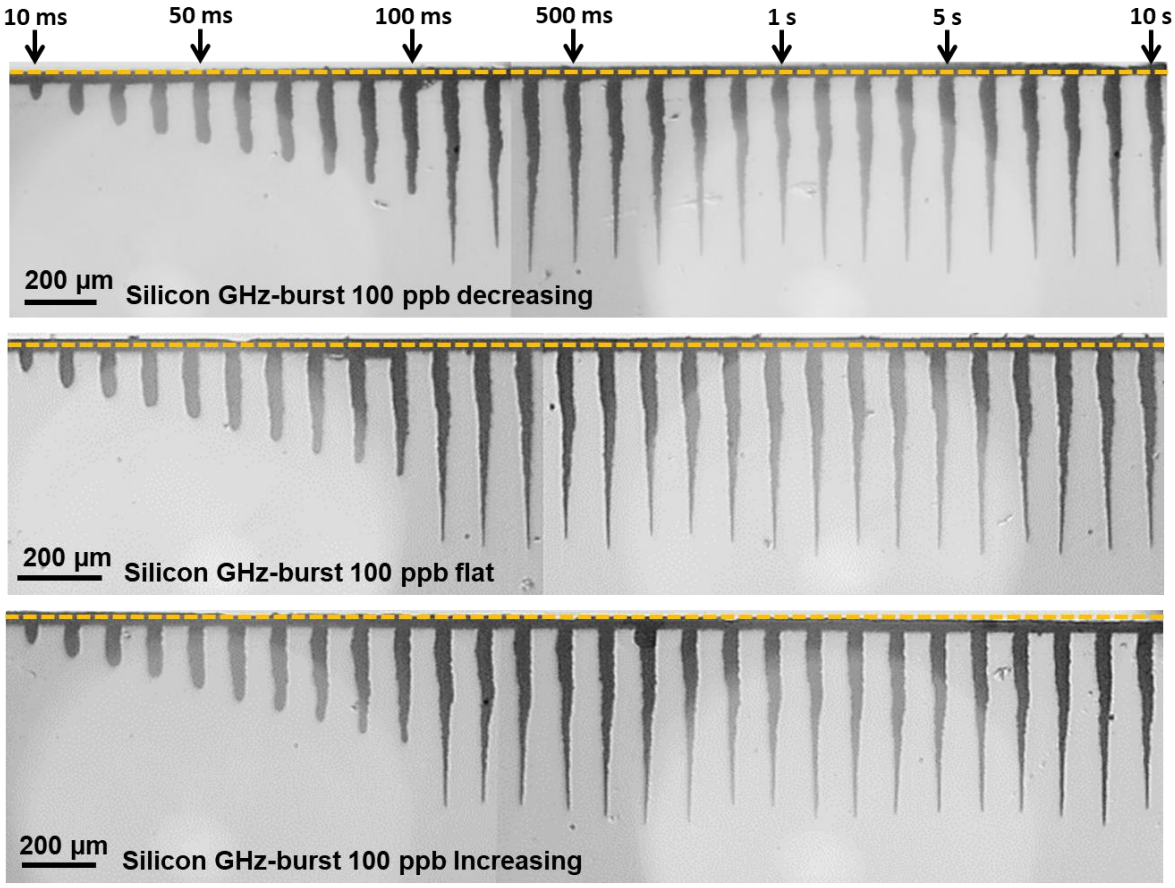

Figure 4.10. Infrared microscope images of the holes obtained in silicon with decreasing, flat or increasing burst shape, for a burst fluence of 250 J/cm² with a burst repetition rate of 1 kHz and a drilling time ranging from 10 ms to 10 s.

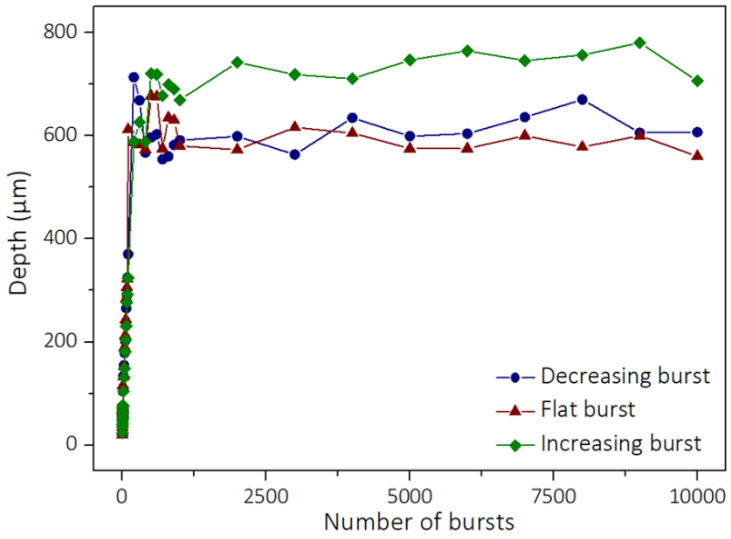

Figure 4.11. Graphical representation of the depth as a function of the number of bursts applied to the sample with a burst repetition rate of 1 kHz and a burst fluence of 250 J/cm² for the three burst shapes available, each containing 100 ppb.

In this figure, we can notice that the drilling dynamic is pretty similar for all these three burst shapes. Just as previously, the evolution of the depth displays only two stages, the first one corresponds to a linear increase of the depth as a function of the number of bursts applied to

the sample and finally a saturation of the depth as the drilling is over. In this first stage, the drilling rate is close to 60 µm/burst for all three configurations. However, in the case of silicon, it appears that the more efficient burst shape is the increasing burst shape as it displays a 20 % increase of the depth compared to the other configurations. This could be induced by the fact that the first pulses slowly heat the material while the higher energy pulses at the end of the burst eject more efficiently the ablated matter probably resulting in a lower screening effect.

2. Comparison of repetitive single pulse, MHz-burst and GHz-burst regimes

In this section, the three operating regimes, the repetitive single pulses, the MHz-burst mode, and the GHz-burst mode, are compared regarding top- down percussion drilling of silicon. Therefore, we investigated as before the evolution of the depth as a function of the number of pulses (bursts) applied to the sample in these three different regimes under comparable conditions and with exactly the same optical alignment. For the repetitive single pulse regime, we used pulses at 140 µJ which corresponds to a pulse fluence of around 200 J/cm². For the two burst regimes, we used a burst energy of 140 µJ as well, which corresponds to a pulse fluence of 50 J/cm² for MHz-bursts of 4 pulses, a pulse fluence of 25 J/cm2 for MHz-bursts of 8 pulses, and a pulse fluence of 2 J/cm² for GHz-bursts of 100 pulses. The resulting holes for the single pulse regime, the MHz-burst regime with 4 and 8 pulses per burst, respectively, and the GHz-burst for 100 pulses per burst are depicted on Figure 4.12. For the sake of clarity, we chose to display only these 4 configurations but all the laser parameters described in Chapter 2 were investigated (MHz-burst from 2 to 32 pulses per burst and GHz-burst from 50 to 400 pulses per burst). We show the holes obtained with a drilling time ranging from 60 ms to 10 s at a burst repetition rate of 1 kHz.

From this figure, we observe that the hole morphology is very different in the three regimes. First, the repetitive single pulse regime, which shows very tapered holes with a larger entrance diameter. In the beginning of the drilling, the holes are conical and show a linear increase of the depth. The saturation appears after around 7 seconds of drilling (i.e. 7000 pulses) after the two-stage of depth increase as described above. The last holes show large inlet diameters and quite irregular shapes suggesting that the material is highly affected by the high energy of the repetitive single pulses. Secondly, the MHz-burst regime, in this case the evolution of the depth seems to follow the same general trend as the repetitive single pulse regime, however, with a three-stage behaviour featuring a late saturation that appears after two distinct linear increasing stages. In this case, the morphology of the holes is very different from that was obtained in the repetitive single pulse regime. The MHz-burst regime provides very thin and very regular cylindrical holes even for the deepest ones on the right of the image. Additionally, the inlet diameters of the holes are very small probably attesting of a less affected material. Note that the configuration with 8 pulses per burst produced the best hole morphology of all the holes obtained in the MHz-burst regime. So, there is an optimum of the energy distribution within a burst to drill holes with optimum regularity and depth. Finally, we show, as a comparison, the GHz-burst regime that was already comprehensively investigated in the previous sections. The hole morphology is the same as that was shown before in the GHz-burst regime. The holes are thin with a small inlet, and the diameter is quite similar to

that was obtained with MHz-bursts. However, the morphology of the hole is different from the two other regimes.

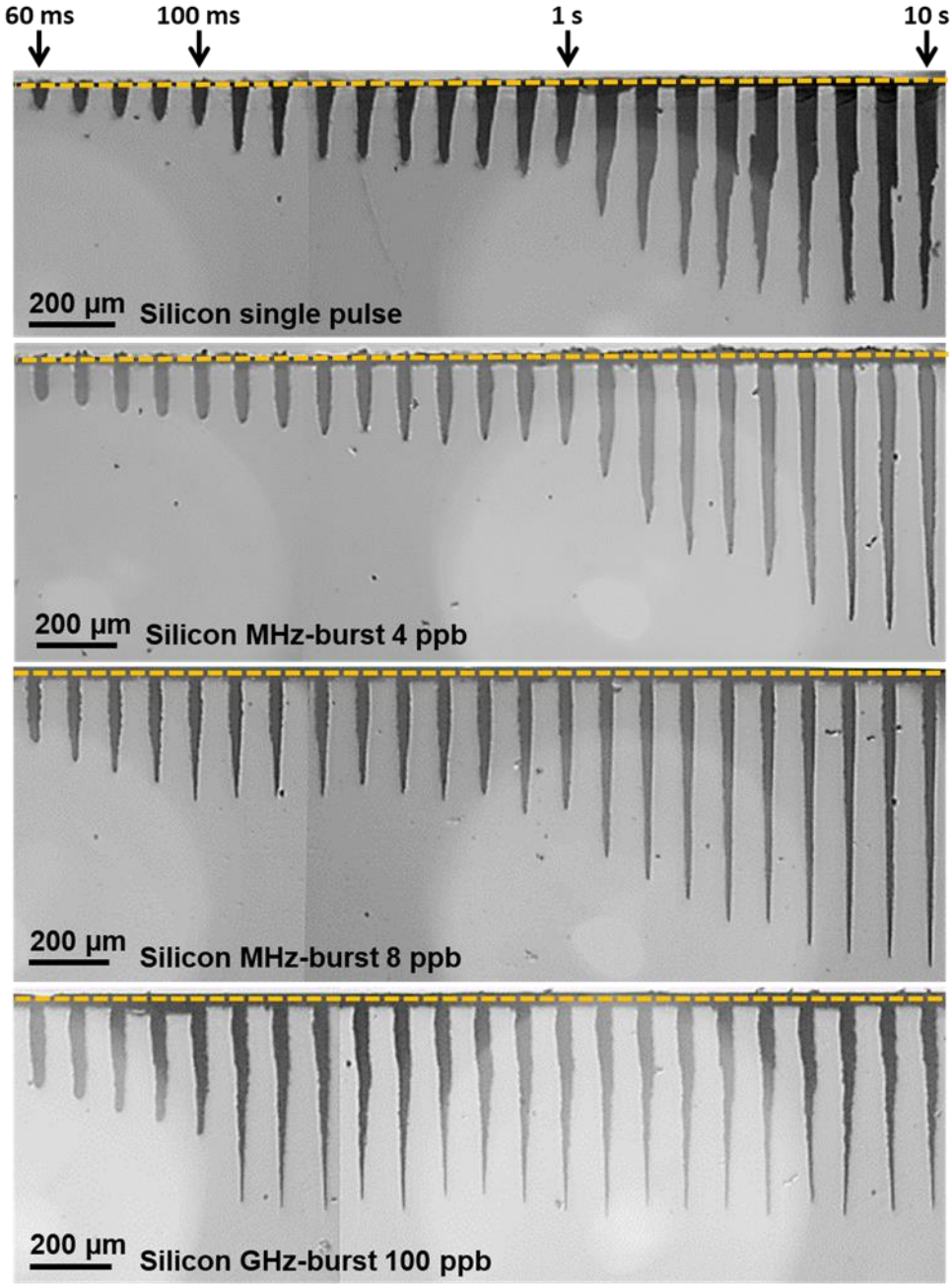

Figure 4.12. Infrared microscope images of the holes obtained in silicon for a single pulse or burst fluence of 200 J/cm² with a pulse or burst repetition rate of 1 kHz and a drilling time ranging from 60 ms to 10 s for the repetitive single pulse regime, the MHz-burst regime (4 and 8 pulses per burst) and the GHz-burst regime with 100 pulses per burst.

The GHz-burst regime provides thin holes but with an irregular shape compared to the MHz-burst regime. However, the depth saturates much sooner than for MHz-bursts, but with a very regular depth obtained afterwards. This is certainly due to the very moderate pulse energy in the GHz-burst regime.

The graphical representation of the hole depth as a function of the number of bursts (pulses in repetitive single pulse regime) is depicted in Figure 4.13. The graph displays a very different

behaviour from one configuration to another. The single pulse regime (black lozenges) shows a linear increase of the depth as a function of number of pulses applied with a low slope as can be seen in the zoom of the dashed black zone shown in the inset.

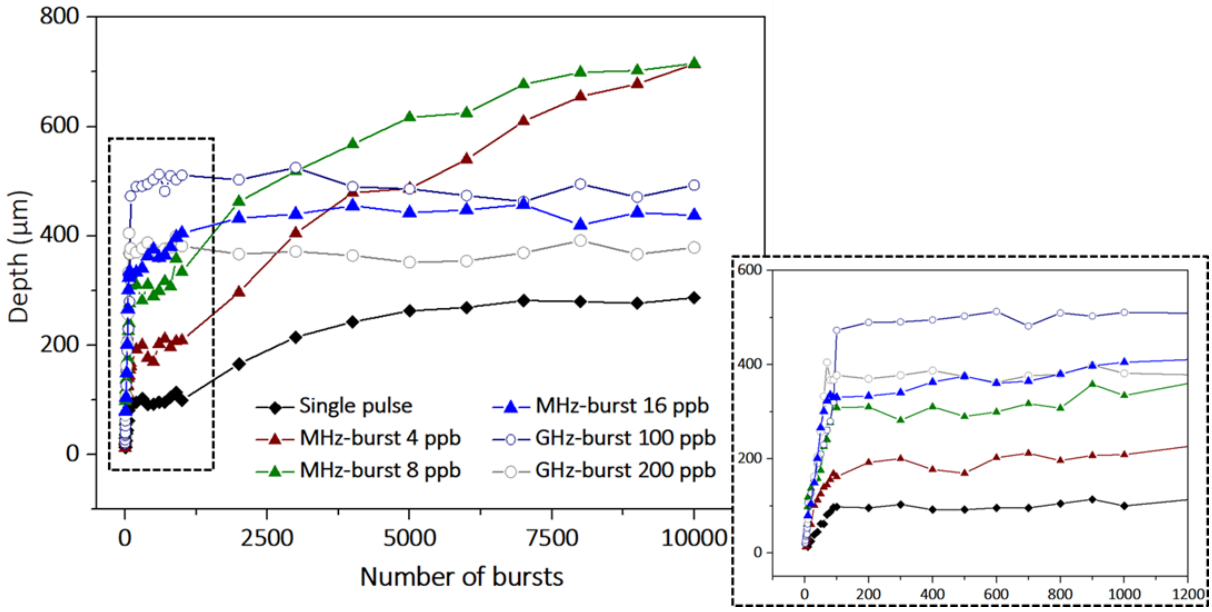

Figure 4.13. Graphical representation of the hole depth as a function of the number of bursts (pulses) applied to the sample with a burst repetition rate of 1 kHz and a burst fluence of 200 J/cm² for the repetitive single pulse, the MHz- & the GHz-burst regimes. The square in dashed black is a zoom of the beginning of the graph corresponding to the first second of drilling time.

This stage of linear increase is followed by a first stage of saturation of the depth before a non-linear increase of the depth finally reaching saturation. The same tendency can be observed in the MHz-burst regime for the three configurations (4 ppb, 8 ppb and 16 ppb) with a much higher ablation rate in the beginning of the graph. Additionally, the depth of final saturation is much higher, especially in the case of 4 and 8 ppb for the MHz-burst configurations. Note that the saturation was well reached with MHz-bursts as longer drilling times superior to 10 s did not produce holes deeper than 750 µm. These long-time drillings are not displayed here for the sake of clarity. The GHz-burst regime, on the other hand, shows a very different behaviour with only two stages. The latter shows only a linear increase of the depth followed by a saturation as was observed in the previous section. Note that the depth saturates sooner than that was observed in Figures 4.9 and 4.11. This can be explained by the fact that the burst fluence is lower here. Indeed, although we have access to these three regimes, the maximum available burst energy in the MHz-burst regime corresponds to the chosen 140 µJ. Therefore, in order to keep a valid comparison of the three regimes we chose to compare them at a constant energy of 140 µJ.

Note that the behaviour displayed by the repetitive single pulse and the MHz-burst regimes was directly observed during the drilling thanks to our transverse observation system. Then, during the drillings, we were able to directly visualize that the drilling was chopped, it displayed a phase of constant depth for some time and then the depth increases again, corresponding to the graphs depicted in Figure 4.13.

Finally, we show that the GHz-burst regime provides a much higher ablation rate (see inset of Figure 4.13) to reach a depth of several hundreds of micrometers much sooner than the other

regimes but at the expense of the hole quality. Note, the MHz-burst regime shows tremendous results with a very high hole quality and allowing for even deeper drillings, but it requires a longer drilling time. The drilling was also chopped in different phases just as was observed in the GHz-burst regime.

3. Silicon processing at 1.7 µm

In this section, I will present the results obtained with the wavelength 1700 nm. As was presented in Chapter 2 of this manuscript, the aim at long term is to be able to reach backside and in-volume modifications in silicon by switching to a longer wavelength within its spectral transparency range. In-volume laser processing with femtosecond pulses in silicon presents significant challenges due to the material's high refractive index, nonlinear absorption, thermal effects, and mechanical stress. Silicon's high refractive index complicates deep focusing [143,144], while significant reflection and refraction at the interfaces add to the difficulties [145, 146]. An exhaustive review of the challenges, especially on the non-linear effects arising during the interaction with femtosecond pulses and possible solutions, is given in [147]. These properties can lead to what is called *intensity clamping*. The latter refers to the phenomenon where the intensity of a laser pulse propagating through silicon reaches a maximum threshold beyond which it does not increase significantly, even if the input laser power is increased. To prevent intensity clamping in silicon during laser processing, several approaches can be employed. Using ultrashort femtosecond pulses with low pulse energy minimizes nonlinear effects by reducing the interaction time. Adjusting the pulse repetition rate lowers heat build-up and allows for cooling between pulses. In addition, temporal beam shaping manages peak power and could lead to promising results.

In order to study the effect of the numerical aperture (N. A) on silicon processing, we bought a set of microscope objectives from Mitutoyo which are listed below with the corresponding N. A and working distance (W. D).

Objective	**5 X**	**10 X**	**20 X**	**50 X HR**	**100 X**
N. A	0.14	0.26	0.4	0.65	0.5
W. D (mm)	37.5	30	20	10	12
Pupil (mm)	11.5	10.4	8	4	4

Table 4.1. Objectives used during this study with the corresponding numerical aperture (N. A) and working distance (W. D).

As was explained in Chapter 2, the use of these objectives is quite restrictive. Indeed, the challenge is to fit the entrance pupil of the objectives in order to benefit from the full numerical aperture. However, by a time-consuming method of alignment, it has been possible to adapt the beam size to the pupil and we were able to match the nominal numerical apertures. We led a transmission study with all the objectives at our disposal (i.e. all the numerical apertures). The experimental setup we used for the transmission measurement is depicted in Figure 4.14. The goal in this experiment was to determine the most appropriate setup (Objective and burst configuration) for potential in-volume modifications in silicon. Thanks to our setup, we were able to scan the Z position of the focal point. Note that the white

light and the top view camera in the Seiwa focusing head also allowed us to check for any surface ablation during the process. The principle of the measurement is depicted in Figure 4.14. Basically, we wanted to measure the transmission of the 1700 nm beam through the sample and identify points of interest with all the options at our disposal. In addition, any back-surface modification would be a nice result.

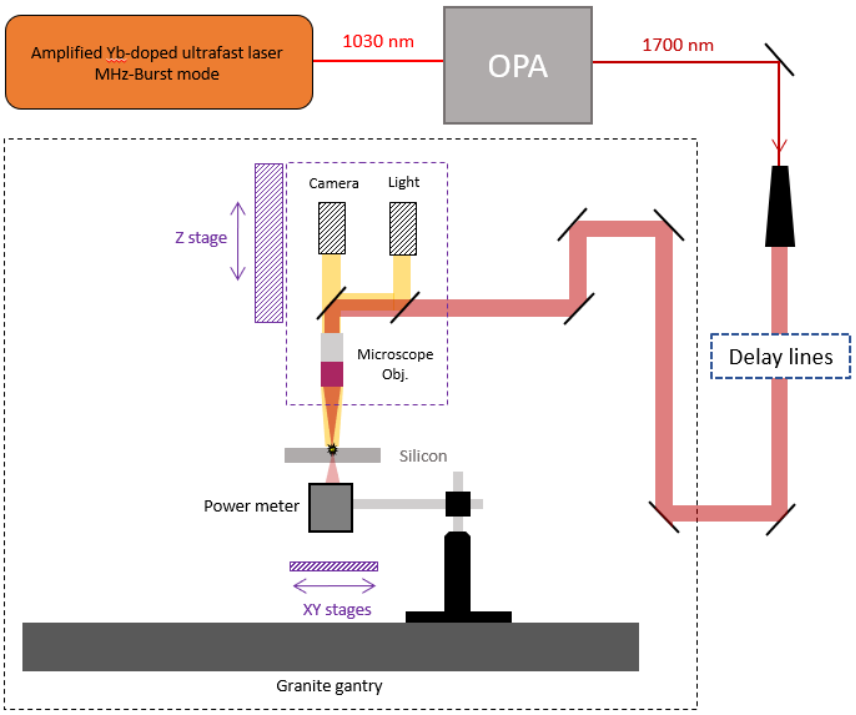

Figure 4.14. Schematic representation of the experimental setup used for the transmission measurement.

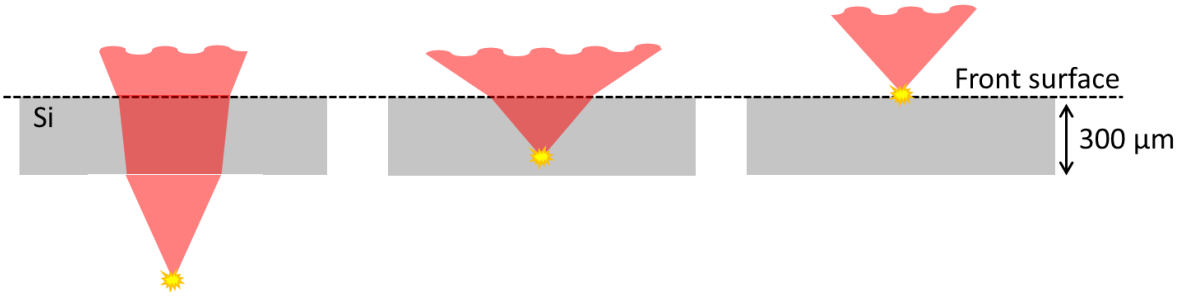

Figure 4.15. Schematic representation of the experimental method used for the transmission measurement.

We started by investigating the effect of the objectives on the absorption on silicon. To do so, we fixed the laser parameters to 64 pulses per burst at 640 MHz. We then plotted the evolution of the transmission as a function of the Z position within the 300 µm-thick silicon sample which corresponds to an optical thickness of 1050 µm. The corresponding graph is depicted in Figure 4.16, Z=0 µm corresponds to the surface of the sample, the negative values correspond to focusing within the silicon sample, i.e. below the surface. The transmission measurements were realized with a burst repetition rate of 1 kHz and the highest burst energy at our disposal which corresponds to 15 µJ per burst before the objective. Care has to be taken as the transmission of the objectives themselves is not the same.

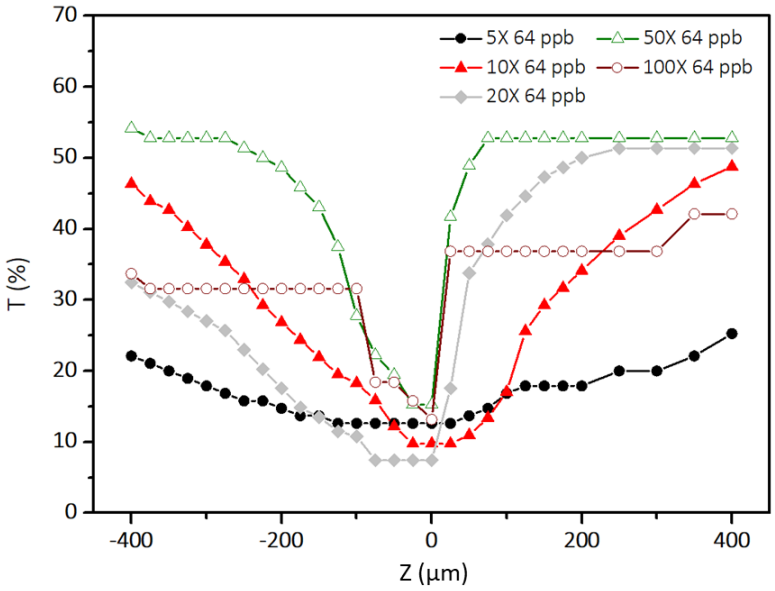

Figure 4.16. Evolution of the transmission as a function of the focus position for all the objectives at our disposal. Z=0 µm corresponds to the surface of the sample, the negative values correspond to in-volume focusing.

On this Figure, we can observe that the transmission (i.e. the absorption) is highly affected by the choice of the objective, and thus, the numerical aperture and focus size. One can clearly observe that the objective 5X shows an almost constant transmission. As a matter of fact, in this configuration, there was always surface ablation. With an increasing numerical aperture, the energy deposition zone, corresponding to the lowest point of transmission, becomes narrower. As was expected, the narrowest and steepest configurations correspond to the objectives 100X and 50X HR which have the highest numerical apertures. However, during this study we observed a significantly lower transmission of the objective 100X itself, therefore we chose to use the 50X HR for the following experiments.

Once we identified the adapted objective, we investigated the effect of the number of pulses per burst along with the repetition rate. Indeed, as was depicted in Chapter 2, the number of pulses per burst is directly linked to the pulse repetition rate due to our setup. Just as previously, we investigated the influence of the number of pulses per burst on the transmission of the beam through the sample. We kept the burst repetition rate at 1 kHz and the burst energy on-target is shown in Table 4.2 along with the corresponding pulse to pulse delay with the 50X HR objective.

Laser	**4 ppb**	**8 ppb**	**16 ppb**	**32 ppb**	**64 ppb**	**128 ppb**
Burst energy (µJ)	4.7	4.5	4.2	4.1	3	2.5
P to P delay (ns)	25	12.5	6.2	3.1	1.6	0.8

Table 4.2. Laser parameters with the corresponding maximal on-target burst energy achievable for the 50X HR objective.

In order to lead a valid comparison, the burst energy was reduced to 2.5 µJ by means of optical densities. The evolution of the transmission as a function of the Z position is depicted on Figure 4.17, Z=0 µm corresponds to the surface of the sample, the negative values correspond to in-volume focusing. On this Figure, we chose to display only four of the configurations for the sake of clarity.

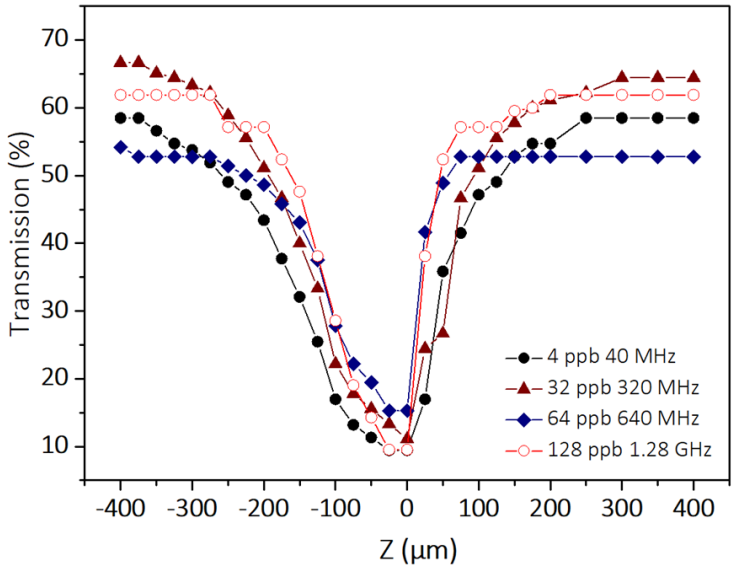

Figure 4.17. Evolution of the transmission as a function of the depth for four of the burst configurations at our disposal, Z=0 µm corresponds to the surface of the sample, the negative values correspond to in-volume focusing.

This Figure attests that, as was expected, the GHz-burst regime appears appropriate for in-volume modifications in silicon. Indeed, this graph shows that, just as the 50X HR showed a steeper and narrower transmission drop, the 128 pulses per burst at 1.28 GHz seems to be the most appropriate for in-volume modifications as it combines the narrowest and the highest transmission drop among all tested configurations. Now, let's have a closer look on this graph for the GHz configuration. Another view is proposed on Figure 4.18.

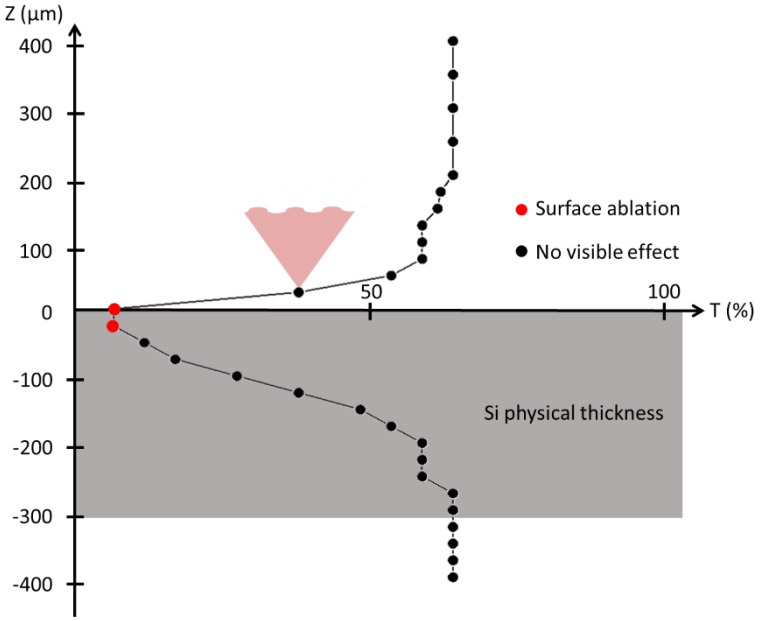

Figure 4.18. Evolution of the transmission as a function of the depth for the GHz configuration with the physical thickness of silicon sample, Z=0 µm corresponds to the surface of the sample, the negative values correspond to in-volume focusing.

This Figure brings new information regarding the transmission losses. As can be seen here, the points colored in red show surface ablation, those two points correspond to the lowest

transmission points. However, the points corresponding to a Z position of – 50 µm and – 75 µm show no surface ablation and a low transmission.

After identifying a plausible working set of parameters for potential in-volume modification of silicon, we implemented a rudimentary first test experiment in order to try and observe possible in-volume modifications in silicon. This very first approach will be discussed in the perspectives section of this work. Indeed, this preliminary experiment with the 1.7 µm wavelength brought evidence that the GHz-burst could be appropriate for achieving the coveted in-volume modification of silicon.

4. Conclusion

In this Chapter, we investigated the interaction between burst mode lasers and crystalline materials and especially silicon. We started with the nominal wavelength of the Tangor, 1030 nm. In this Chapter, we were mostly interested in silicon as it represents a major issue for microelectronics as well as for the research team so we needed to acquire as much experience on this material as possible.
For transparent materials such as CaF_2 and sapphire, a behaviour quite similar to that was observed in glasses has been observed. We identified a three-stage drilling process with the surface ablation, the confined ablation and the saturation of the drilling. Silicon on the other hand showed a different behaviour regarding the evolution of the hole depth as a function of the number of bursts (or pulses in repetitive single pulse regime). The latter showed a two-stage drilling process with first a linear increase of the depth with a high drilling rate and finally the saturation of the drilling. As we were not able to see holes with a low depth, due to our observation system, we cannot exclude that there are in fact three stages of drilling in silicon but we simply don't see it.

Just as in glasses, we investigated the impact of different parameters on the drilling process such as the burst duration (i.e. the number of pulses per bursts) and the energy repartition within the burst. This study revealed that there is an optimal number of pulses per burst to be found in silicon. In this case, we identified the optimum number of pulses per burst to be 100 with a resulting hole depth reaching nearly 1 mm for a burst fluence of 450 J/cm² which is an excellent result.
To complete this study, we compared the GHz-burst regime with two state-of-the-art regimes, the repetitive single pulse and the MHz-burst regimes, respectively. We show that the three regimes show different behaviours regarding both the evolution of the depth as well as the morphology of the holes. Interestingly, it turns out that the MHz-burst regime with 4 and 8 pulses per burst appears as the best compromise to reach high depth with very thin and regular holes. On the other hand, the GHz-burst provides a much higher ablation rate that can eventually reduce the processing time. During this study, the MHz-burst regime produced holes of 750 µm which is lower than that was observed in GHz-burst regime in the previous section with 100 pulses per burst. However, in MHz-burst mode, we were not able to reach fluences comparable to 450 J/cm². This study clearly revealed that the repetitive single pulse regime is problematic regarding both the depth of the holes as well as the quality with irregular holes and a huge entrance diameter. We provided experimental evidences that the burst regimes are perfectly suited for silicon processing at 1030 nm.

The last subsection of this chapter deals with silicon processing at 1700 nm. This study was designed as a preliminary work on silicon to start and familiarise ourselves with this particular material and this exotic wavelength. As was presented in Chapter 2, the alignment of this setup was very challenging and time consuming. Although it did not provide any result yet, we were able to address technical issues and built a better understanding of silicon processing as well as the challenges that need to be tackled.

Chapter 5: Cutting experiment

Following the excellent results for hole drillings obtained with the Gaussian beam in Chapters 3 and 4, we decided to investigate the combination of burst mode with spatial beam shaping. From a previous work from the research group [13], we know that the repetitive single pulse regime cannot be used for glass cutting, only the MHz-burst regime was successfully applied. At that time, the GHz-burst was not yet available. We figured that, as was observed for glass drilling, the GHz-burst regime could possibly bring a new degree of quality for glass cutting by combining temporal and spatial beam shaping.
The use of a non-diffractive Bessel beam for microcutting offers the advantage of a dust-free and zero-kerf micromachining process. Such a Bessel beam can be produced by an axicon or a spatial light modulator and allows for an elongated and highly localized energy deposition over several millimetres thanks to its interferential character [148]. Indeed, this latter approach is already used for materials cutting [13,17,76,149,150], bulk modifications [7,20], nanoholes drilling, or for high-aspect ratio drilling [19,21,78,79,151,152]. Furthermore, this spatial beam shaping technique can be coupled with the use of MHz-bursts in order to enhance the energy deposition in a decisive way for glass cutting [13]. The principle is then to produce an intense elongated and uniform bulk modification for micro crack appearance along the glass thickness with every Bessel beam-shaped single burst. The plane defined by subsequent micro cracks acts as pre-cutting treatment since a slight mechanical stress by hand is required to separate the pieces [20,73].

1. Experimental setup

1.1 Bessel beam generation and characterization

The spatial beam shaping setup to generate the Bessel beam inspired from [13], is represented in Figure 5.1 and uses an axicon with an apex of 170 °. The axicon creates a long and wide primary Bessel beam which is then imaged into a secondary Bessel beam using a set of lenses, mounted following a 4F setup, in order to reduce the dimensions and maximize the deposited energy in a smaller volume.

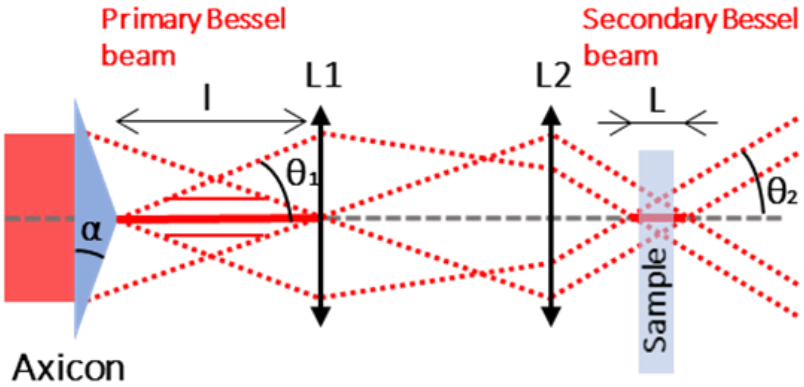

Figure 5.1. Schematic of the Bessel beam generation using an axicon and a set of lenses.

From a theoretical point of view, the parameters of the primary Bessel beam can be calculated in air with the following formulas [15,153,154]:

$$\theta_1 = (n_a - 1) \times \alpha \quad (8)$$

$$\alpha = 90 - \frac{apex}{2} \quad (9)$$

With n_a the optical index of the axicon, α the base angle of the axicon, and θ_1 the half angle of the primary Bessel beam as indicated in Figure 5.1. The length l and the central core radius r_1 of the primary Bessel beam at the zero-intensity point are given by [15,153-155]:

$$l = \frac{d}{2\theta_1} \quad (10)$$

$$r_1 = \frac{2.4 \times \lambda}{2\pi \sin(\theta_1)} \quad (11)$$

Where d is the beam diameter when entering the axicon and λ is the laser wavelength. The secondary Bessel beam parameters can be determined using the primary Bessel beam parameters and the magnification coefficient given by M= f_2/f_1 with f_1 and f_2 the focal lengths of the two lenses, respectively, in this case f_1 = 125 mm and f_2 =10 mm. The secondary Bessel beam half angle θ_2, length L and radius r_2 must be calculated in the glass sample and are given by the following formulas [15,153,154]:

$$\theta_2 = \frac{\theta_1}{M \times n_g} \quad (12)$$

$$L = \frac{Md}{2\theta_2} \quad (13)$$

$$r_2 = M \times r_1 \quad (14)$$

With n_g the refractive index of the glass sample. Note that the glass refractive index theoretically has no impact on the diameter of the secondary Bessel beam. From a practical point of view, the length of the Bessel beam can be adjusted by changing the beam diameter of the beam upstream the axicon and the radius by modifying the magnification parameter M. These formulas give the following results: the calculated primary Bessel beam half angle is $\theta_{1,\,th}$ = 2.3 °, the radius of the primary Bessel beam is $r_{1,\,th}$ = 9.8 µm, the half angle of the secondary Bessel beam is $\theta_{2,\,th}$ = 28.6 ° and the theoretical radius of the secondary Bessel beam is calculated as $r_{2,\,th}$ = 0.8 µm. However, the simple approach of geometrical optics is not suited for calculations on the order of magnitude of the wavelength, and thus, this theoretical value indicates only a lower limit [135]. Therefore, we performed careful measurements of the primary and secondary Bessel beams, respectively, a schematic drawing of the primary Bessel beam measurement is depicted on Figure 5.2.

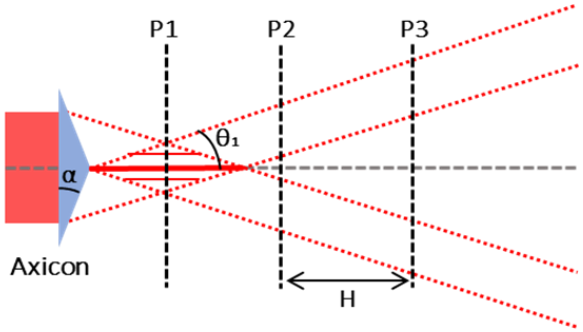

Figure 5.2. Schematic of the measurement method for the primary Bessel beam.

In this figure, P1, P2 and P3 are acquisition planes for the measurement of the primary Bessel beam radius $r_{1,exp}$ and the primary Bessel beam half angle $\theta_{1,exp}$, respectively. Figure 5.3 displays the corresponding beam analyser (WinCamD-XHR, pixel size 3.2 µm) acquisitions. Figure 5.3 (a) displays the intensity profile corresponding to P1 that we used to estimate the diameter of the primary Bessel beam. We adapted the beam size to the beam analyser resolution to ensure a reliable measurement using our homemade 10X-magnification system that has been calibrated at 2 %. Figure 5.3 (b,c) correspond to the intensity profiles acquired in planes P2 and P3 for the measurement of the angle, where the distance H between P2 and P3 was set to 1 mm.

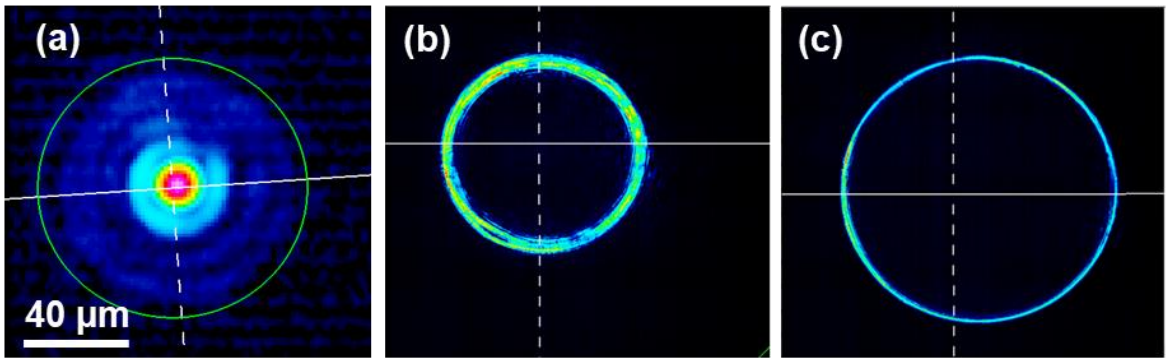

Figure 5.3. Measurement of the primary Bessel beam diameter (a). Intensity profile measured at two different planes (b,c). All measurements are made using a WinCamD beam analyzer.

From Fig. 5.3 (b,c) we can determine the half angle of the Bessel beam with the following formula by extracting the diameters of the circles:

$$\theta_{1,\mathrm{exp}} = arctan\left(\frac{D-d}{2H}\right) \quad (15)$$

With D and d the diameters of the circles, respectively, and H the distance between the two acquired planes. In our case, we obtained $\theta_{1,\,exp}$ = 2.34 ° with an uncertainty of ± 0.01 ° and a radius $r_{1,\,exp}$ = 9.00 µm with an uncertainty of ± 0.66 µm. In addition, we measured the secondary Bessel beam half angle by exactly the same method and obtained $\theta_{2,\,exp}$ = 27.26 ° with an uncertainty of ± 0.01 ° and a secondary Bessel beam radius $r_{2,\,exp}$ = 1.9 µm with an uncertainty of ± 0.66 µm. The experimental values for the primary Bessel beam half angle and radius as well as the secondary Bessel beam half angle are very close to the theoretically calculated ones. Only the secondary Bessel beam radius appears to differ but that could be explained by the fact that the dimensions are approaching the diffraction limit. Additionally, we estimated the length of the secondary Bessel beam by visualizing the modification in a glass sample as can be seen in Figure 5.4 with the luminescence during the interaction (top) and the resulting bulk modification (bottom) in a sodalime sample. The resulting length was estimated to 1.2 mm with an uncertainty of ± 0.2 mm compared to a calculated 1.8 mm. The difference here arises from the fact that the real length of the Bessel beam is probably higher than the resulting measured bulk modification, part of the Bessel beam is probably not seen as it is not intense enough to generate a visible modification.

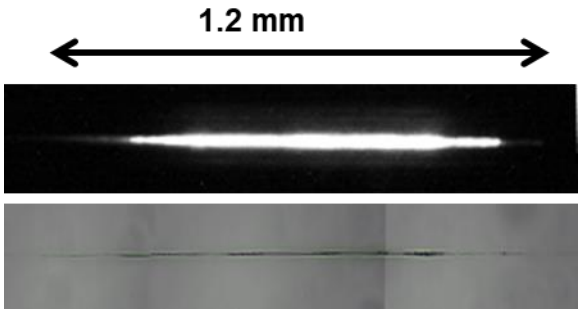

Figure 5.4. Schematic representation of the length measurement of the secondary Bessel beam.

The use of an axicon in our setup imposes a preliminary step before cutting due to imperfections in the tip of the axicon as represented in Figure 5.5. As represented here, a perfect axicon would have a perfectly pointy tip. However, during the manufacturing, such a structure cannot be obtained.

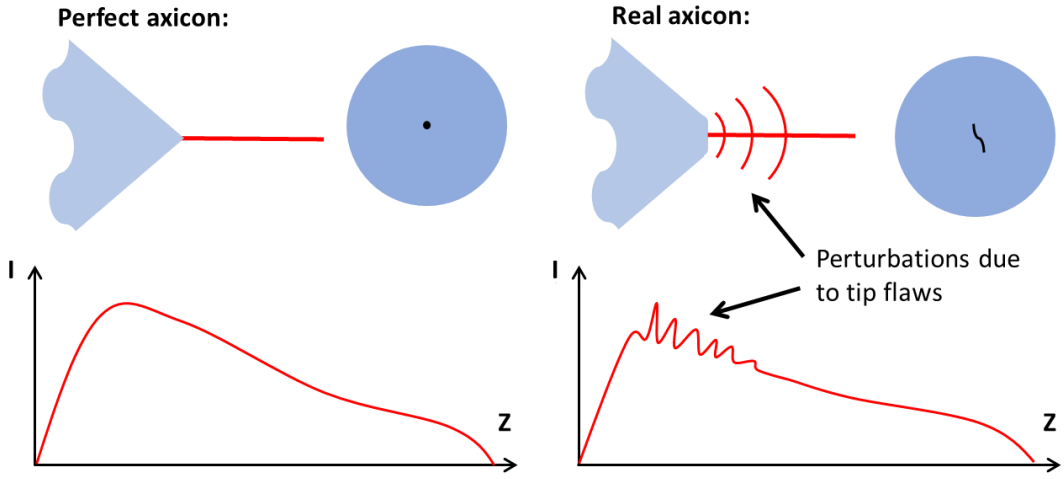

Figure 5.5. Schematic representation of a perfect, pointy axicon (left) along with a real axicon (right).

The actual axicon tip is in fact flattened (tray of about 300 µm measured with the microscope), this results in a wavefront that perturbates the reconstruction of the Bessel beam and its intensity profile as represented on the bottom right of this Figure. These perturbations will induce a crack transversely to the Bessel beam with a random orientation on the sample surface. The orientation can be controlled either by tilting the axicon itself [72] or by using a phase mask upstream the axicon [156]. In our case, we chose to implement the second configuration and to orientate the crack with a phase mask as illustrated in Figure 5.6 in a sodalime sample.

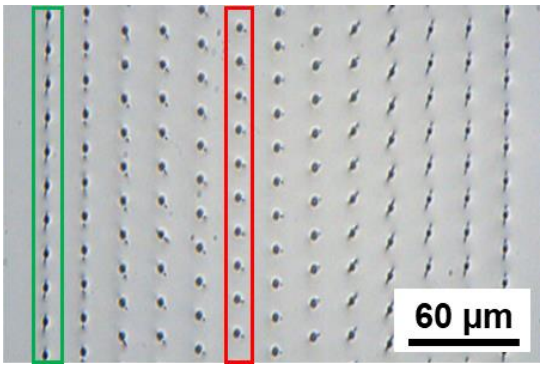

Figure 5.6. Top view microscope image of the crack orientation using a phase mask upstream the axicon with a pitch of 20 µm. The green rectangle shows the optimized orientation.

On Figure 5.6, each dot results from a single burst, and the pitch is defined as the distance between two dots. The goal here is to align the crack with the trajectory of the cut. In the case represented here, the right orientation is shown in green with vertical cracks. In red we can see the most detrimental orientation of the crack which could lead to a lowered surface quality during the cut.

1.2 Roughness and topography measurements

Both topography and surface roughness (Sa) measurements of the sidewalls (i.e. the cutting planes) were performed using a confocal profilometer (Smart Proof 5, ZEISS) equipped with a 20X objective with a numerical aperture of 0.7. The field of view of the profilometer with the 20X objective is only 500 µm, for samples exceeding a thickness of 500 µm, the surface roughness Sa was estimated as an average on several measurements covering the full sidewall. In our case, we chose to study the Sa and not the Ra, contrarily to most of the references found in literature. Nevertheless, we considered that the Sa measurement was more relevant for the whole surface quality than the Ra which is measured on a line and features typically lower values than the Sa. The Ra measurement was still realized in some cases in order to be able to compare our results to the state of the art.

1.3 Samples

The cutting experiments were carried out on samples of 1 mm-thick sodalime, on 200 µm-thick fused silica, 300 µm-thick alkali free borosilicate (AF32) glass, and 430 µm-thick sapphire. Fused silica and sapphire have a similar bandgap (about 9 eV [156]), which is higher than the one of sodalime (3-4 eV [130]). Furthermore, sapphire has a much higher thermal conductivity (about 40 W/m/K [157]),) compared to fused silica (1.81 W/m/K [128]), AF32 glass (1.5 W/m/K determined by the flying spot method [158]) and sodalime glass (1.42 W/m/K [129]).

2. Cutting results and discussion

In this subsection, the experimental results as well as the corresponding discussions are presented. This study is divided in four subsections. The first one is exclusively dedicated to the GHz-burst Bessel beam cutting with a study of the Sa as a function of the Bessel-to-Bessel pitch for several burst energies. The pitch was set by adjusting the repetition rate of the laser and the translation speed of the samples. In this first part, we wanted to investigate the GHz-burst by itself as it has never been done before. The second section is a comparative study

between Bessel beam cutting in the MHz-burst and the GHz-burst regimes for comparable burst energies and pitches. These first results reveal two main points. Firstly, we noticed that the two regimes operate with very different parameters which lead us to investigate a wider range of parameters in order to extract the processing windows of both regimes, which is the object of the third subsection. Secondly, we observed an over-exposure regime appearing for low pitches and/or high burst energies, the fourth subsection is dedicated to this regime.

2.1 GHz burst Bessel beam dielectrics cutting

This first part is dedicated to GHz-burst Bessel beam cutting of sodalime glass, fused silica and sapphire for different burst energy and pitch values. We first chose to investigate the behaviour of the GHz-burst Bessel beam cutting regime itself as it is completely unknown up to now. To do so, we studied the evolution of the surface roughness (Sa) of the cutting plane as a function of the pitch between two consecutive Bessel beams within the materials for different burst energies with bursts of 50 pulses at a repetition rate of 1.28 GHz. Figures 5.7 (b), (d) and (f) depict the results for the three materials applying four different burst energy values of 253, 294, 337, and 383 µJ, respectively. The error bars on these graphs correspond to the uncertainty on the measurements which was estimated to be ± 10 % of the surface roughness value. Indeed, for each acquisition the resolution of the profilometer depends on the scanned range as well as on the number of acquired planes. We went down to a pitch of 0.02 µm with a repetition rate of 50 kHz and a translation speed of 1 mm/s. Note that we could have gone faster with a repetition rate of 100 kHz and a translation speed of 2 mm/s, also resulting in a pitch of 0.02 µm. However, we observed that these two configurations did not give the same results. For too high repetition rates, sodalime starts to display a large heat affected zone that will be discussed in sub-section 2.4 of this chapter.
The results are similar for sodalime (b) and fused silica (d). For high pitch values, the surface roughness is rather high as the Bessel beams were too far apart from each other and the mechanical stress that had to be applied was important leading to a lowered surface quality. By diminishing the pitch, the surface quality increases (i.e decreasing Sa values) reaching a minimum value which depends on the materials itself as well as on the burst energy. Then, for too low pitches, the surface roughness increases again, evidence of a too high overlap and a thermal load that is too important for the material to support. The points corresponding to this over-exposure do not appear on this graph as the cutting plane is not uniform at all, either concave or convex, and the corresponding roughness measurements are neither reliable nor relevant. This point will be further investigated in section 2.4. In contrary to the glasses, there is no obvious trend that can be deduced from the results depicted in the graph concerning sapphire, Figure 5.7 (f). The surface morphologies corresponding to the lowest surface roughness of the cutting planes after singulation are shown in Figures 5.7 (a), (c) and (e). These results were obtained for a burst energy of 253 µJ and a pitch of 0.04 µm in sodalime, a burst energy of 294 µJ and a pitch of 0.1 µm in fused silica, and a burst energy of 337 µJ and a pitch of 0.04 µm in sapphire, respectively. The cutting quality is very good since the cutting planes are regular and smooth in both sodalime and in fused silica where the surface roughness Sa is 0.47 µm and 0.75 µm, respectively, and there is no path deviation. The cutting plane in sapphire is less uniform and exhibits a higher surface roughness (1.17 µm).

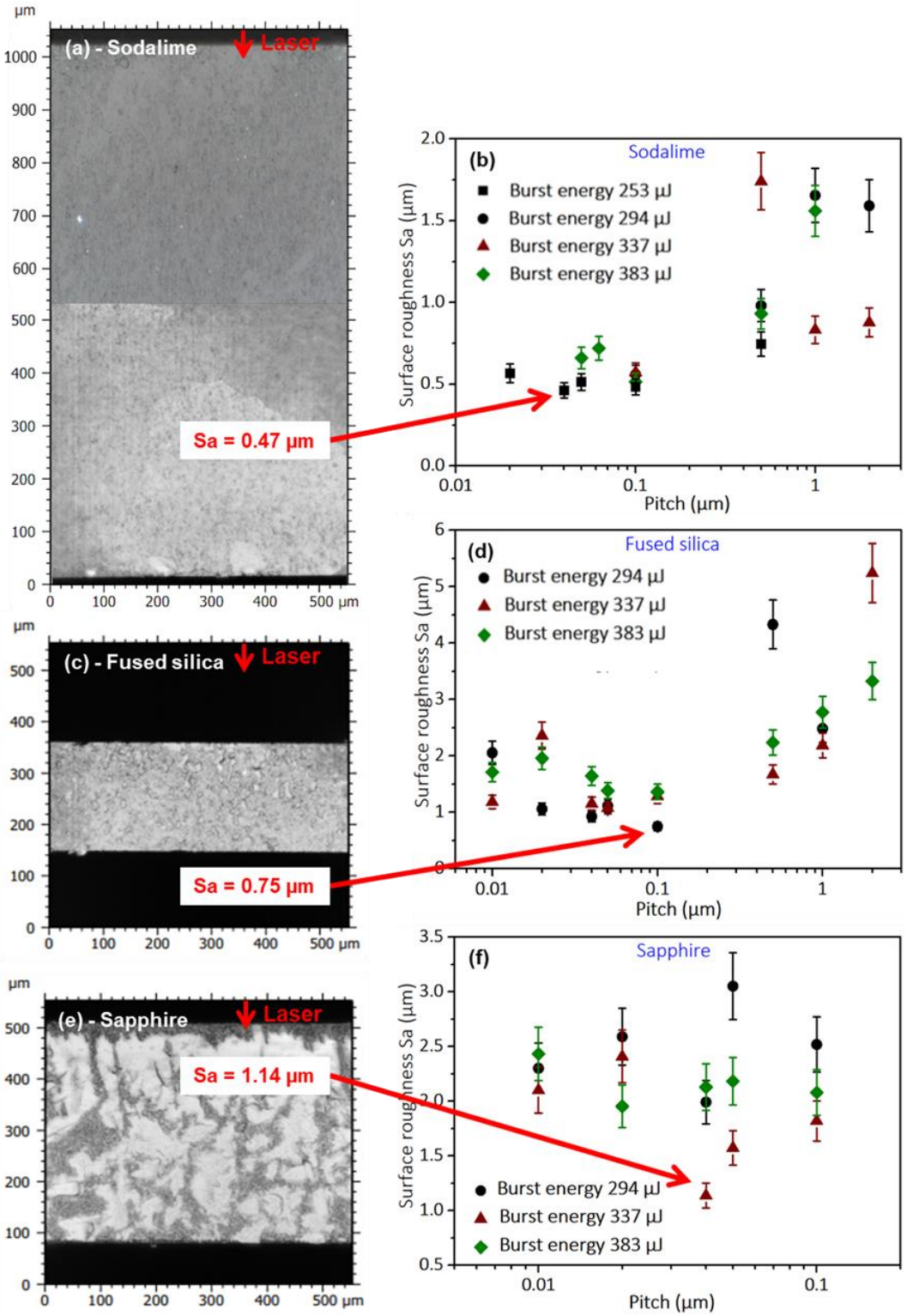

Figure 5.7. Topography measurements on sidewalls after singulation corresponding to the lowest surface roughness obtained in our study in 1 mm-thick sodalime for a burst energy of 253 µJ and a pitch of 0.04 µm for a resulting Sa of 0.47 µm (a), in 200 µm-thick fused silica for a burst energy of 294 µJ and a pitch of 0.1 µm for a resulting Sa of 0.75 µm (c) and in 430 µm-thick sapphire for a burst energy of 337 µJ and a pitch of 0.04 µm for a resulting Sa of 1.14 µm (e). Surface roughness as a function of the pitch in sodalime for burst energies in a range from 253 µJ to 383 µJ (b), in fused silica for burst energies in a range from 294 µJ to 383 µJ (d), in sapphire for burst energies in a range from 294 µJ to 383 µJ (f). Note the pitch scale differences, especially in sapphire. Laser comes from the top.

Some hilly, uncracked and glossy areas reveal that the pre-cutting has been incomplete, and thus the mechanical stress required for singulation increased for sapphire. This observation can be explained by the high bandgap value, and especially the high thermal conductivity of sapphire (about 40 times higher compared to the investigated glasses). Indeed, the cutting process in GHz-burst mode is more sensitive to the bandgap value since the low pulse energy of the individual pulses within a burst produces less non-linear absorption. This behaviour remains even for relatively high burst energies. Nevertheless, we observed no path deviation. Furthermore, we notice that there is no visible effect and no pre-cutting effect neither in fused silica nor in sapphire for the lowest burst energy value (253 µJ) whereas it is possible to pre-cut sodalime glass in these conditions. We assume that this is due to the higher bandgap value for fused silica and sapphire compared to sodalime. Moreover, in sodalime and fused silica pre-cutting can be achieved with pitches as high as 2 µm meanwhile, for sapphire, it is not the case for pitches exceeding 0.1 µm. We assume that this can be contributed to the higher thermal conductivity of sapphire compared to sodalime and fused silica, where the higher thermal conductivity prevents from pre-cutting with higher pitches. On the basis of this observation, we deduct that there is a slight heat accumulation between bursts. In the case of glasses, the material does not fully relax between two subsequent bursts. Thus, the pre-cutting process takes advantage of a low thermal conductivity value thanks to a beneficial spatial cooperative effect between subsequent bursts.

2.2 Comparison between MHz-burst and GHz-burst cutting

We performed a first comparative study between MHz-burst and GHz-burst cutting on sodalime and on AF32 glass. We kept exactly the same experimental conditions for both regimes and investigated two burst energies, 200 µJ and 215 µJ, in a pitch range from 0.005 µm to 2 µm with bursts of 4 pulses at 40 MHz repetition rate and 50 pulses at 1.28 GHz repetition rate. The energy values were chosen here as it was the highest values achievable both in MHz- and GHz-burst modes with our laser system. The graphic representation of the surface roughness as a function of the pitch and the profilometer images of the best results for the two materials, 1 mm-thick sodalime and 300 µm-thick AF32, are displayed in Figure 5.8. The images corresponding to the GHz-burst regime (on the left) in sodalime show partly a very regular and homogenous surface that has been cut by the Bessel beam and partly, we observe a cleaved plane. This observation can be explained by the fact that the pulses within the burst in this regime carry a low energy which highly reduces the effective length of the Bessel beam. Obviously, the chosen burst energies are too low to generate a long effective Bessel beam. Contrarily, for AF32, we observe regular cutting planes with low surface roughness values in the GHz-burst regime. Whereas, on the pictures on the right corresponding to MHz-burst cutting, one may notice irregularities and even bubble-like forms on AF32. These particular structures may attest of a too high burst energy for the MHz-burst regime for which each pulse within the burst carries almost 13 times more energy than the pulses within a GHz-burst. For high pitch values, the surface roughness is high, especially in the GHz-burst mode. Indeed, in this particular regime, the energy deposition is much more localized in the material, and therefore, a too high pitch (i.e. a too low overlap) does not allow for generating a continuous cutting plane but rather represents a succession of Bessel beam-induced cracks (Figure 5.5 (b)) resulting in a high surface roughness. When diminishing the

pitch, there seems to be an optimum value for which the surface roughness reaches a minimum. Then, for too low pitch values, the surface roughness increases again especially in the MHz-burst mode. Indeed, as the pulses carry much more energy, a too high overlap can lead even sooner to an over-exposure which is detrimental for the surface quality.

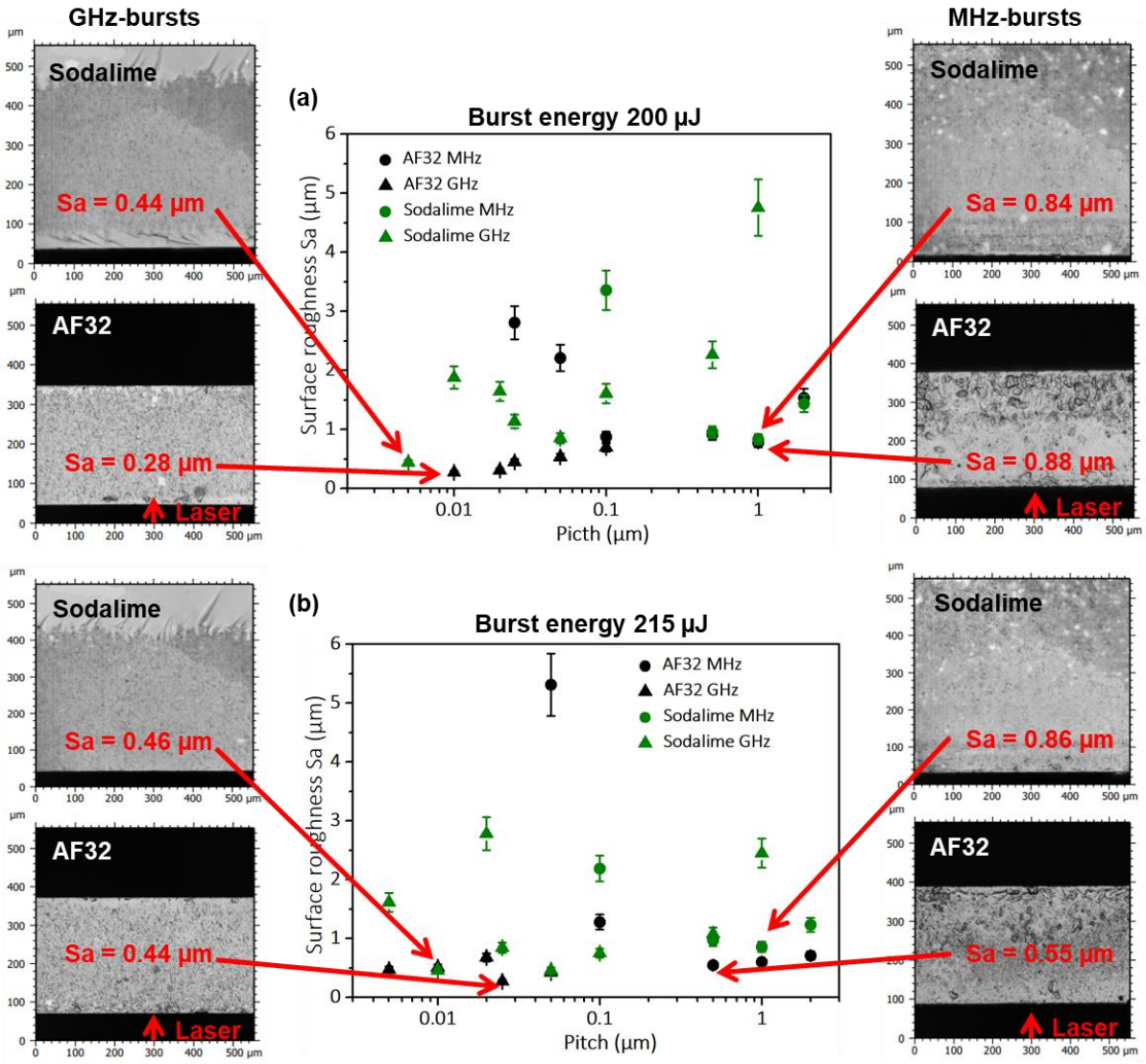

Figure 5.8. Graphic representation of the surface roughness as a function of the pitch between two consecutive Bessel beams in sodalime and AF32 for burst energies of 200 µJ (a) and 215 µJ (b). The images corresponding to the bests results obtained are displayed on the left for GHz-bursts and on the right for MHz-bursts. Laser comes from the bottom.

In Table 5.1, we summarize the best results obtained in MHz and GHz burst mode in the two materials for the two burst energies investigated. We can notice that the GHz-burst regime produced better surface quality for comparable energies especially in AF32 with an excellent Sa of 0.27 µm.

	Sodalime				AF32			
	MHz bursts		GHz bursts		MHz bursts		GHz bursts	
Burst energy (µJ)	**Pitch (µm)**	**Sa (µm)**	**Pitch (µm)**	**Sa (µm)**	**Pitch (µm)**	**Sa (µm)**	**Pitch (µm)**	**Sa (µm)**
200	1	0.84	0.005	0.46	0.1	0.88	0.01	0.27
215	1	0.86	0.01	0.46	0.5	0.55	0.025	0.28

Table 5.1: Summary of the best results obtained during this comparative study for burst energies of 200 µJ and 215 µJ for sodalime and AF32, respectively, with the corresponding pitches.

2.3 Optimization of the parameters for MHz- & GHz-burst regimes

We extended the range of processing parameters concerning burst energies and pitches to identify independently the best sets of parameters for both MHz- and GHz-burst regimes in terms of cutting quality. We varied the burst energy from 147 to 383 µJ, and the pitch from 0.005 to 10 µm. The bests results obtained in both materials for both regimes are displayed in Figure 5.9. Note that both regimes produced an excellent cutting quality with very regular cutting planes, especially in AF32 in GHz-burst mode the resulting Sa of the cutting plane is as small as 0.27 µm (Figure 5.8 d). Moreover, with the adapted burst energy it was then possible to obtain a full cutting plane over the whole sample area on 1 mm-thick sodalime even in GHz-burst mode. Figure 5.9 demonstrates that the parameters have to be chosen differently in MHz-burst and GHz-burst mode in order to obtain the best cutting plane qualities. Given that the energy is spread within 50 pulses in the GHz-burst mode, it is necessary to have a burst energy that is high enough to reach non-linear absorption along the whole glass thickness. Moreover, an important overlap is also needed to take advantage from the heat accumulation that drives the GHz-burst cutting process. Regarding the MHz-burst mode, the pulses are much more energetic, therefore a lower burst energy and less overlap can be used for cutting. However, we can see that even for the appropriate set of parameters, the best surface quality (i.e lower surface roughness) is still obtained in GHz-burst mode.

Moreover, we investigated the processing windows for GHz-burst and MHz-burst cutting for sodalime, and the results are represented in Figure 5.10. We identified four zones depending on burst energy and pitch value. Note that the proportions and the shapes of the windows represented here are indicative and might in detail depend on other experimental conditions. The black crosses in these graphs were extracted from the experimental data acquired on sodalime. For the sake of clarity, we have not represented all the experimental points as they are sometimes very close to each other.

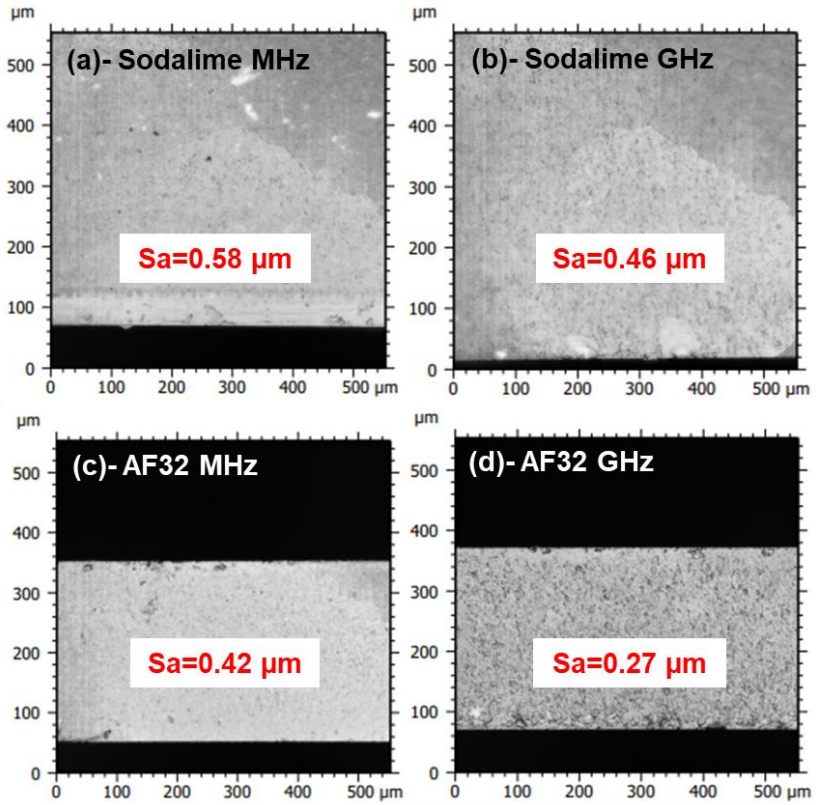

Figure 5.9. Profilometer images of the results obtained in sodalime for a pitch of 1 µm in MHz-burst mode for a burst energy of 147 µJ with a resulting Sa of 0.58 µm (a), in sodalime for a pitch of 0.04 µm in GHz-burst mode for a burst energy of 194 µJ with a resulting Sa of 0.46 µm (b), in AF32 for a pitch of 1 µm in MHz-burst mode for a burst energy of 127 µJ with a resulting Sa of 0.42 µm (c), obtained in AF32 for a pitch of 0.025 µm in GHz-burst mode for a burst energy of 194 µJ with a resulting Sa of 0.27 µm (d).

We observed a lower limit for the burst energy in both regimes, around 180 µJ in GHz-burst mode and 100 µJ in MHz-burst mode. The green zone (1) corresponds to the optimum process window producing the best cutting results in terms of cutting feasibility, uniformity and surface roughness. Its parameters are very different in the GHz-burst regime with respect to the MHz-burst regime. The former requires relatively high burst energy and a low pitch between consecutive Bessel beams while the latter requires a low burst energy but a higher pitch. The orange zone (2) represents a process window for which cutting is possible but with a lowered surface quality of the cutting plane due to a too high overlap (low pitch). The red zone (3) represents the parameters for which cutting is not feasible due to insufficient bulk modification. The mechanical stress required for singulation is too high, resulting in an uncontrolled breaking of the sample. In this range of pitches in MHz-burst mode, the third window is only visible in the lower part of the graph corresponding to very low burst energy as singulation was possible as soon as there was a visible plane. The grey zone (4) corresponds to very low pitches and/or too high burst energy leading to the thermal cutting regime which will be further discussed in the next section. Despite the fact that no mechanical stress is required in this operating window, the cutting plane no longer follows the Bessel beam trajectory which can be critical in industrial applications.

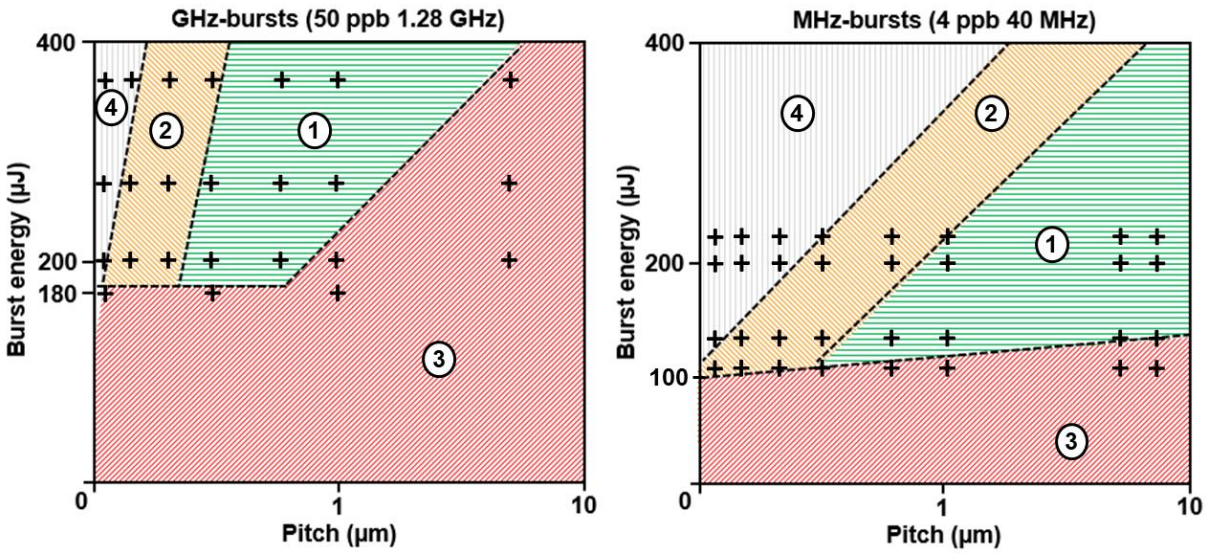

Figure 5.10. Schematic representation of the different operating windows that appeared during the cutting study. The values of burst energies, pitch and crosses correspond to experimental data in sodalime. The green zone (1) corresponds to the optimum process window, the orange zone (2) represents a process window for which cutting is possible but with a lowered surface quality of the cutting plane, the red zone (3) represents the parameters for which cutting is not feasible and the grey zone (4) corresponds to very low pitches and/or too high burst energy leading to the thermal cutting regime.

2.4 Over-exposure regime

As indicated in the former sections, for a too important overlap in both MHz- and GHz-burst configurations, depending on the burst energy, we observed that a thermal cutting regime can be reached. In this regime, applying stress to cleave the sample was not necessary and the cut part fell off itself. However, we observed that the cutting plane did not follow the trajectory defined by the Bessel beam. Indeed, for these configurations, the thermal load is too high with respect to the heat dissipation leading the material to show a large heat affected zone (HAZ) eventually reaching the softening temperature of the material [158]. The cutting plane then follows the border of the heat affected zone resulting in a path deviation both from the trajectory and from the straightness of the Bessel beam along the sample thickness as illustrated in Figure 5.11. The resulting cutting plane is curvilinear, either concave or convex, as can be seen in the 3D representation of the surface taken with the profilometer (Figure 5.11, bottom). On the top of this figure, a schematic drawing of the HAZ is depicted. On the microscope image (middle), we observe that there are points of energy concentration like on Figure 9 of Ref. [153]. Furthermore, we noticed that detrimental extended cracks appear along the Bessel beam due to heat accumulation when the burst repetition rate is too high. A similar phenomenon has been observed in drilling experiments in the GHz-burst regime [124]. Indeed, in sodalime for example, the burst repetition rate in the drilling experiments was limited to 10 kHz, while cutting with the Bessel beam is possible with repetition rates up to 50 kHz without HAZ appearing. This can be explained by the fact that the volume in which the energy is deposited is much larger for a Bessel beam than in percussion drilling using a Gaussian beam. In the case represented here, a large HAZ is displayed.

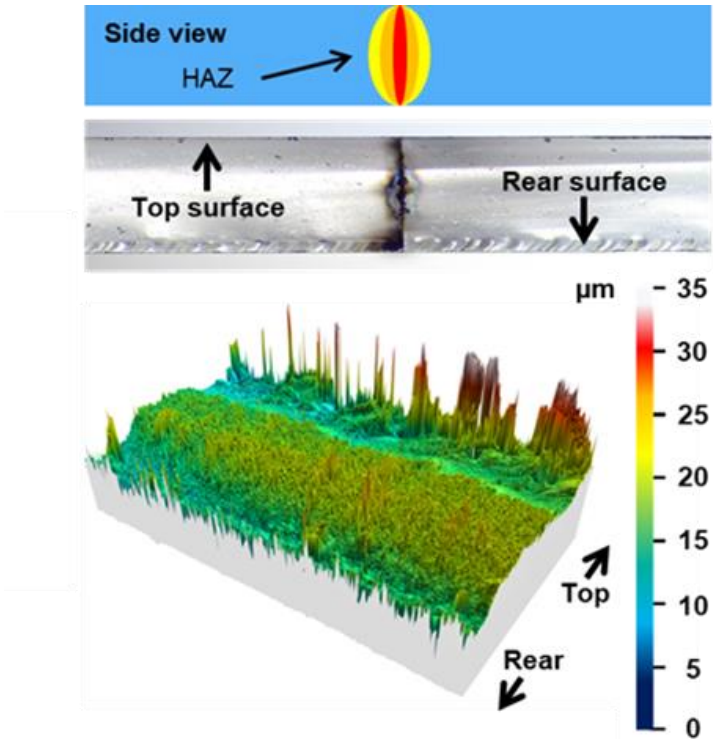

Figure 5.11. Schematic view of the HAZ appearing with high overlapping (top) with the corresponding microscope sideview image of the cutting plane (middle), and 3D representation of the surface measured with the profilometer (bottom).

2.5 Influence of the pulse duration

In this subsection, we chose to investigate the influence of the duration of the individual pulses within the burst on the cutting quality. Indeed, it was shown in a study that a picosecond pulse duration could enhance the energy deposition in single pulse regime for submicron structuring in fused silica [153]. We led a similar study as the previous one, we investigated the evolution of the surface roughness (i.e surface quality) as a function of the pitch between two consecutive Bessel beams. This time, by adjusting the compressor of the laser, we had the possibility to change the pulse duration within the burst from 530 fs up to nearly 3 ps. The graphical representation of the surface roughness as a function of the pitch for the 7 pulse durations investigated is depicted in Figure 5.12. The cutting experiments leading to this graph were realized with bursts of 400 µJ which is the highest possible burst energy at our disposal. Indeed, the study was led on 1 mm-thick sodalime samples, we needed a Bessel beam intense enough on the full length of the sample to be able to cut. It appeared that, for longer pulses, the effective length of the Bessel beam was reduced, quite similarly to that was observed at low burst energy in subsection 2.2. The maximal repetition rate here is 50 kHz and a translation speed of 2 mm/s leading to a pitch of 0.04 µm. One could understand this phenomenon in terms of peak pulse energy, when increasing the pulse duration, the pulse intensity drops inducing a reduction of the effective length of the Bessel beam. However, with bursts of 400 µJ we were able to cut 1 mm-thick sodalime in every configuration displayed here. Regarding the graph, one can see that the general behaviour identified earlier in this chapter is also followed here for the different pulse durations. Figure 5.12 shows that pulse durations in a range of a few picoseconds reach the lowest surface roughness.

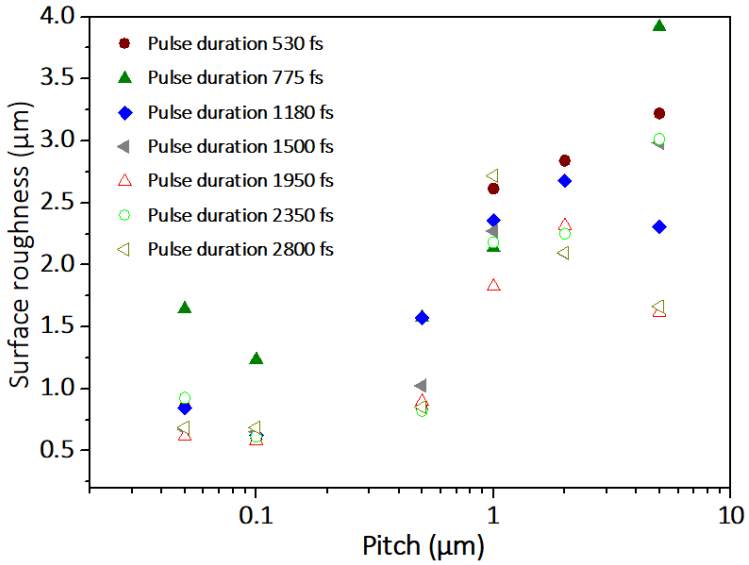

Figure 5.12. Graphical representation of the surface roughness as a function of the pitch for the 7 pulse durations investigated.

This means that indeed, the pulse duration plays a part in the energy deposition and that a pulse duration in a range of the picosecond can improve it. However, one should be careful with the burst energy needed to compensate the intensity peak losses.

3. Conclusion

In this last chapter, we investigated the femtosecond GHz-burst mode regime for glass cutting by implementing a Bessel beam shaping. To the best of our knowledge, this is the first reported study on such a combination of temporal and spatial beam shaping. Following the nice results obtained in the previous chapters, we were wondering as to the contribution of the GHz-burst regime regarding the cutting quality. The experimental protocol is quite similar in all the subsections here, we investigated the evolution of the surface quality (Sa) as a function of the pitch (i.e. the Bessel-to-Bessel spacing).

We started this study by investigating the effect of the burst energy on the cutting quality for three materials, 1 mm-thick sodalime, 200 µm-thick fused silica and 430 µm-thick sapphire. We reveal excellent cutting quality obtained in the three materials with an optimal value of pitch that needs to be found. In addition, we identified a pattern of evolution of the Sa as a function of the pitch. For an elevated pitch the Sa is high because the Bessel beams are too far apart. By diminishing the pitch, we can diminish the Sa as well, increasing the surface quality. However, if we keep diminishing the Bessel-to-Bessel distance, the Sa increases again attesting of the existence of an optimum pitch for each material. It is worth noticing that we obtained a very regular cutting plane in sodalime on the whole thickness of 1 mm, which represents already a remarkable result.

The second part of this chapter is dedicated to a comparison of the MHz-burst and the GHz-burst regimes. We wanted to implement a comparative study between these two regimes since the MHz-burst is considered as the state of the art [13]. During this investigation, we found that the MHz-burst follows the same general trend as observed with the GHz-burst, but achieves a higher optimum Sa for the materials studied. However, a significant parameter that

has been identified here is the effective length of the Bessel beam. Indeed, for comparable burst energies, the Bessel beam in GHz-burst regime appeared less elongated. We attribute this observation to the fact that the pulse energy is much lower in this regime. As a consequence, the effective length of the pre-cut planes is reduced which could reveal as detrimental beyond a certain sample thickness depending on the material.

The third part here is dedicated to the optimization of the parameters for glass cutting in both regimes so as to give a fair comparison. Indeed, we identified in the second subsection that both burst configurations show an optimum value of Sa but it appeared that the GHz-burst regime needs more energy for the Bessel beam to cut the full thickness of sodalime. We investigated the evolution of the Sa as a function of the pitch in sodalime for a much larger range of burst energies in order to try and plot the operating windows of each regime for glass cutting. We provided experimental evidence that the GHz-burst regime requires much higher burst energy and overlap than the MHz-burst regime but produces better surface quality.

The fourth part deals with a regime of overexposure that we observed in both regimes. The later results either from a too high overlap or a too high burst energy. The material, at this point, starts to display a large heat affected zone which could result in a path deviation from both the cutting trajectory and from the Bessel beam itself.
The last part provides a study of the cutting quality as a function of the pulse duration. It was expected that the pulse duration would have a significant effect on the surface roughness as it could improve the energy deposition. We showed that indeed, the pulse duration plays a part in the cutting quality but at the expense of the effective length of the Bessel beam.
In the end, we provided a qualitative study on glass cutting using a Bessel beam shaping coupled with different temporal beam shapings. This study revealed that a better cutting quality can be obtained in GHz-burst regime. However, for thick samples, one should consider using MHz-bursts of femtosecond pulses as the effective length of the Bessel beam is increased.

Conclusion

This work was led during three years in the CELIA laboratory at the University of Bordeaux. We worked in close collaboration with industrial partners, especially Amplitude and ALPhANOV. This collaboration is now part of a common laboratory in Bordeaux which gives an administrative framework for already strong exchanges between the three entities (CELIA, Amplitude and ALPhANOV). This particular environment was very favourable to the success of this work. The chosen subject was very large in order to be able to investigate every track we wanted on this new regime. Indeed, the GHz-burst regime was quite new at the beginning of this work and the goal here was to investigate as many tracks as possible.

In the first chapter, we introduced the theoretical concepts that were necessary to understand this manuscript and more generally laser-matter interaction. Several phenomena were described driving the absorption of a laser beam by a gap material such as multiphoton absorption as well as quantum tunnelling. Once the incoming beam has been absorbed, we introduced the microscopic as well as the macroscopic reaction of the material via coulomb explosion and phase explosion, respectively. We dedicated a full subsection to femtosecond laser processing of dielectrics as this manuscript is mainly focused on dielectrics. Finally, we provide a comprehensive state of the art of femtosecond laser processing with different beam shaping techniques such as temporal beam shaping with the burst mode (MHz or GHz) which is thoroughly investigated in this manuscript.

The second chapter provides a detailed list of the different equipment that were implemented and used during these three years. We implemented mainly two workstations, a Gaussian beam focalization setup and a Bessel beam generation setup. Both these workstations are mounted on granite gantries in order to increase the stability and to be able to implement in-situ diagnostics. Indeed, our opinion on the matter is that to understand and optimize correctly a process, it is absolutely necessary to have as many diagnostics as possible. The main diagnostics that was used here was the sideview imaging system. The latter allowed to visualize the drilling and cutting processes in real time transversely. This allowed us to get to a first step of hypothesis regarding the laser-matter interaction in the GHz-burst regime. Finally, on the third workstation at our disposal, we implemented a pump-probe shadowgraphy setup. The later was particularly tricky to implement as it required a perfect synchronization of two lasers, a GHz-burst pump and a single pulse probe. In the end, we had to couple an optical delay line to two electronic delay lines to reach delays up to 5 ms with a precision of a few hundred femtoseconds. This setup also uses the sideview imaging system and allowed us to get a much better sense of the phenomena occurring during the interaction as well as to investigate the differences between the three regimes (repetitive single pulses, MHz- and GHz-burst). Alongside these workstations, we worked on an exotic wavelength designed to process silicon in volume in GHz-burst regime. Due to experimental obstacles, we had to develop a GHz-burst generation setup by means of delay lines and polarization cubes. This particular setup and wavelength required a whole new set of measuring equipment for beam characterization and delay line alignment.

The third chapter is the very first dealing with experimental results. In this chapter we provided an extensive study on percussion drilling with the femtosecond laser either in single pulse, MHz- or GHz-burst regimes. We started by investigating the GHz-burst on its own and the influence of the different parameters we had access to. We obtained excellent results on percussion drilling with already very high aspect ratios and cylindrical holes. We depicted a three-stage drilling process which we detailed as follows. First, surface ablation occurs, the ablation plume is freely ejected in the air resulting in a low density and thus a low screening effect. The second drilling stage appears as the drilling goes on, once a certain depth is reached, the plume starts to interact with the inner walls of the hole. The plume becomes denser and the screening effect increases. This will result in a lower drilling rate than that was observed in the very first stage. Finally, a depth saturation occurs when the drilling is over. At this point, we considered the end of the drilling to be caused by a lack of energy reaching the tip of the hole due to transmission losses along the hole. We interpreted that the laser beam was guided by the hole itself, and thus, that the numerical aperture had to have a contribution in the transmission. Therefore, in order to obtain even higher aspect ratios, we tried to investigate the effect of the numerical and to optimize it. By this means, we were able to reach aspect ratios as high as 150 in fused silica for an impressive hole depth of nearly 4 mm.
Then, in a second time, we wanted to compare the drilling process in the three regimes at our disposal with the laser system, the repetitive single pulse, the MHz- and GHz-burst regimes. Thanks to this laser system, a valid and robust comparative study was led. We showed that the drilling results are very different from one configuration to another. The single pulse regime is already quite known, it produces very conical holes with very rough inner walls. In addition, there are usually small wings appearing close to the surface resulting from the high pulse energy and attesting that the material is highly affected. This is also the case for MHz-burst percussion drilling with a low number of pulses per burst. Indeed, it appeared that for a low number of pulses per burst, the hole morphology in MHz-burst mode is quite similar to that was observed in repetitive single pulse but it tends towards the GHz-burst regime when increasing the number of pulses per burst.
During these drilling experiments we developed some hypotheses regarding the drilling process, and we wanted to try and confirm or affirm them. For example, we wanted to produce experimental evidence that the optical transmission decreases as a function of the hole depth and that the appearance of cracks on the inner walls would also decrease the transmission. To do so, we implemented a transmission measurement on bevel samples so as to study a large range of hole depth on a single sample. We identified a drilling limitation regarding the outlet diameter. We observed that no matter the number of bursts, the burst fluence or the repetition rate, the outlet diameter was nearly constant. Through several observations, we emitted the hypothesis that the plume played a crucial part in the drilling process and especially in the enlargement of the hole. The transmission measurement did support the two first hypotheses which suggest that indeed the hole acts as a waveguide for the laser beam to reach the tip of the hole for high aspect ratios. However, we needed to study the drilling dynamics and investigate the behaviour of the plume during the drilling and especially when drilling through holes.
In this optic, we implemented a pump-probe shadowgraphy setup to determine the behaviour of the plume in all three regimes as well as for through holes in the GHz-burst regime. This

study revealed that the plume has a much longer luminescence time in the case of the GHz-burst regime (12 µs in RSP & MHz-burst vs 17 µs in GHz-burst). Moreover, the repetitive single pulse regime displayed a significant shockwave within the material which was not the case in the other regimes probably due to a much lower pulse energy. Finally, when investigating through hole drillings, we observed that as soon as the hole is through, the plume leaks quite quickly from the hole by the rear side. Then, as soon as the plume is no longer contained inside the hole, the drilling is over and the final hole morphology and geometry are fixed.
In the end, during this drilling study, we have been able to determine the drilling process in GHz-burst mode. It turned out that the hole enlargement, which gives birth to those cylindrical holes only obtainable in the GHz-burst regime, is brought by the plume itself. The enlargement of the hole is not provoked by direct laser ablation anymore but by the interaction between the inner walls and the plume (which is composed by hot dense matter) either by mechanical erosion or by heat transfer. So, without the plume, there is no enlargement of the hole.

The fourth chapter is dedicated to crystalline materials and semiconductor percussion drilling. In crystalline dielectrics materials such as CaF_2 or sapphire, we identified the very same drilling stages than that was observed in glasses. However, we observed in CaF_2 that very particular behaviours could be observed with a defocused spot or with a high burst repetition rate, especially the creation of colour centres of fluoride. Unfortunately, CaF_2 is quite expensive so we did not pursue this investigation and chose to focus mainly on silicon in this chapter. In silicon, we investigated the influence of the burst duration as well as the burst shape and revealed that, contrarily to glass percussion drilling an increasing burst shape and bursts of 100 pulses would increase the depth.
We provided a comparative study between the repetitive single pulse, the MHz-burst and the GHz-burst regimes regarding percussion drilling in terms of depth and hole morphology. We revealed that, in the case of silicon, a MHz repetition rate within the burst could show beneficial as it produced very thin holes with excellent morphologies and depths up to 750 µm. Finally, we investigated a new wavelength in the range of the transparency window of silicon to try and produce at long term in-volume modifications in this material. As a first experience in the transparency domain of silicon and its non-linear properties, we implemented simple experiments in order to familiarize ourselves with this semiconductor. We investigated the transmission regarding the microscope objectives and the number of pulses per burst in order to try and identify a set of parameters susceptible of modifying silicon in volume. We revealed that the GHz-burst regime coupled with a high numerical aperture seems like an appropriate configuration.

The final chapter is dedicated to glass cutting by means of a Bessel beam. In a first part, we investigated glass cutting with the Bessel beam coupled with the GHz-burst regime by itself. This combination of spatial and temporal beam shaping had never been published before, to the best of our knowledge, so we led a preliminary study regarding the evolution of the surface quality as a function of the Bessel-to-Bessel pitch for several burst energies. We identified that the GHz-burst regime was quite appropriate for class cutting with samples up to 1 mm thick in the case of sodalime producing a very homogenous cutting plane. Note that we were also able to cut sapphire and fused silica with excellent surface qualities. In a second time, and in order to put the GHz-burst regime glass cutting into perspective, we compared it with the

state-of-the-art MHz-burst glass cutting. We provided experimental evidence that both these regimes show the very same behaviour regarding the evolution of the surface roughness as a function of the pitch. However, we observed that the GHz-burst regime required a much higher overlap as well as a higher burst energy. We identified the optimized process windows for both these regimes and distinguish 4 distinct zones. First, the optimum process window producing the best cutting results in terms of cutting feasibility, uniformity and surface roughness. The second zone represents a process window for which cutting is possible but with a lowered surface quality of the cutting plane due to a too high overlap (low pitch). The third zone represents the parameters for which cutting is not feasible due to insufficient bulk modification. The mechanical stress required for singulation is too high, resulting in an uncontrolled breaking of the sample. The fourth zone corresponds to very low pitches and/or too high burst energy leading to the thermal cutting regime which has been further discussed in the dedicated section. Despite the fact that no mechanical stress is required in this operating window, the cutting plane no longer follows the Bessel beam trajectory which can be critical in industrial applications. Finally, we investigated the impact of the pulse duration on the cutting quality as it has been shown that a pulse duration in a range of a few picoseconds could improve the energy deposition. We show that, although the surface roughness was lower than for shorter pulses with comparable energies, one should consider the effective length of the Bessel beam. This behaviour is quite similar to that was identified in the comparative study. A low pulse energy (which is the case in GHz-burst regime) can lead to a shortened effective Bessel beam. Stretching the pulse duration reduces the peak pulse energy which in turn induces the very same phenomenon.

In this manuscript, we experimentally investigated this relatively new regime of light-matter interaction, the GHz-burst mode. During the three years dedicated to this PhD, the main goal was to provide an extensive experimental study of femtosecond GHz-burst laser processing in order to bring a better understanding of this new regime. Up till 2021, the scientific community was still very divided regarding the real industrial potential of the GHz-burst mode. This discord among the community was supported by a lack of experimental studies. For three years, a lot of effort has been dedicated in contributing to the state of the art of GHz-burst femtosecond laser processing [124,125,127,136,138,140,141,151].

Perspectives

Of course, in this lapse of time, only a few processes were investigated along with a few materials. The first thing worth investigating are new materials. We already showed that semiconductors react differently than glasses, one should consider investigating other semiconductors or even different types of materials. New processes are also worth investigating such as surface structuring or welding. The GHz-burst regime, relying on thermal accumulation could show very useful for such processes. Further studies on the GHz-burst regime, for example pump-probe shadowgraphy on the cutting process, could be very interesting. Of course, this regime and the optimization of the processes would strongly benefit from a theoretical model of the GHZ-burst interaction which is yet to come.

Based on the observations made in Section 3 of Chapter 4, we tried to inscribe lines in silicon. To do so, we fixed the laser configuration with respect to the working parameters that were identified previously (128 ppb; 1.28 GHz; 50X HR). In this case, we tried to produce lines inside the silicon sample and observe them thanks to the setup depicted in Figure 4.13. Indeed, in the previous experiment we were not able to observe any *post mortem* in-volume modifications in silicon. However, we suspected that the modifications were too small to be observed or the processing times were too short. The experiment was divided in two parts, first we scribed a line on the surface, as a reference, and then we moved the focus within the sample such as to inscribe several lines with a fixed burst repetition rate of 10 kHz and a speed of 1 µm/s which corresponds to a very high overlap. The goal here is to benefit from burst-to-burst heat accumulation to pretend obtaining an index change inside silicon. We investigated the effect of the burst energy during this study. In this case, the focusing of the laser beam is done by the objective 50X HR (N.A = 0.65, the beam size upstream the objective has been adapted) and the observation is set with the 20X objective. Although a specific Z position was identified in Section 3 of Chapter 4, we chose to investigate the full range of the sample for us not to miss anything. The graphical representation of the whole study is depicted in Figure p.1. In this figure the red crosses represent the points for which there was surface ablation and the orange the point without surface ablation but with no in-volume modifications observed.

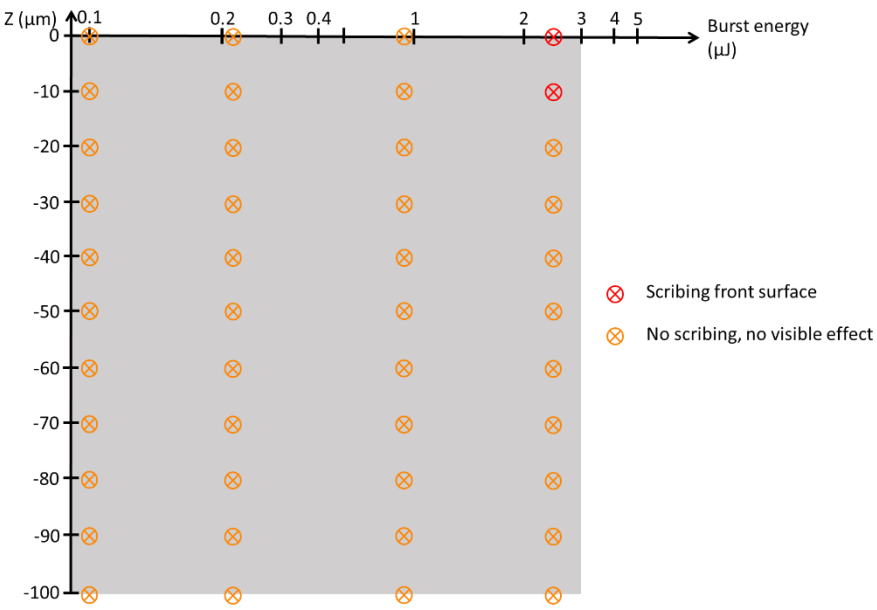

Figure p.1. Graphical representation of the line writing experiments realized with 128 ppb at 1.28 GHz and N.A = 0.65.

In this figure, one can observe that there were no visible in-volume modifications obtained in silicon for 128 ppb at 1.28 GHz no matter the burst energy nor the Z position. Note that the same experiment with repetition rates of 20 kHz and 40 kHz were implemented and did not gave better results. In addition to 128 ppb, we led a much larger study on every burst parameter at our disposal while changing the burst energy as well as the repetition rate. We did not obtain any visible in-volume modification. However, we cannot exclude the fact that our observation system is not adapted to such small modifications. Indeed, the spot size was measured about 5 µm which could result in a very small modification. In addition, the burst energy is quite low, this could mean that the effective energy deposition zone is very localized or longer processing times, i.e. slower sample translations might be necessary.

These preliminary results on in-volume silicon line scribing would require a whole parametric study to try and find the operating parameters for such a challenging task. Indeed, this investigation is part of an international ANR-DFG project that just started in collaboration with the IAP in Jena which is dedicated to the investigation of in-volume and backside modification in silicon with femtosecond pulses in GHZ-burst mode.

List of publications

Peer-reviewed journal articles:

1. J. Lopez, S. Niane, G. Bonamis, **P. Balage**, E. Audouard, C. Hönninger, E. Mottay, and I. Manek-Hönninger, Percussion drilling in glasses and process dynamics with femtosecond laser GHz-bursts, Optics Express, Vol. 30, No. 8 / 11 Apr 2022.
2. J. Lopez, S. Niane, G. Bonamis, **P. Balage**, and I. Manek-Hönninger, In-Situ Monitoring of Bottom-Up Percussion Drilling of Alkali-Free Alumina-Borosilicate Thin Glasses Using Single and Double Femtosecond Laser Pulses, JLMN-Journal of Laser Micro/Nanoengineering, Vol. 17, No. 1, 2022.
3. **P. Balage**, J. Lopez, G. Bonamis, C. Hönninger, and I. Manek-Hönninger, Crack-free high-aspect ratio holes in glasses by top-down percussion drilling with infrared femtosecond laser GHz-bursts, Int. J. Extrem. Manuf. 5 (2023).
4. **P. Balage**, G. Bonamis, M. Lafargue, T. Guilberteau, M. Delaigue, C. Hönninger, J. Qiao, J. Lopez, and I. Manek-Hönninger, Advances in femtosecond laser GHz-burst drilling of glasses: influence of the burst shape and length, Micromachines, 2023, 14, 1158.
5. **P. Balage**, T. Guilberteau, M. Lafargue, G. Bonamis, C. Hönninger, J. Lopez, and I. Manek-Hönninger, Bessel Beam Dielectrics Cutting with Femtosecond Laser in GHz-Burst Mode, Micromachines, 2023, 14, 1650.
6. **P. Balage**, M. Lafargue, T. Guilberteau, G. Bonamis, C. Hönninger, J. Lopez, and I. Manek-Hönninger, Comparative study of percussion drilling in glasses with femtosecond laser in single pulse, MHz-burst and GHz-burst regimes, Micromachines, 2023
7. **P. Balage**, T. Guilberteau, M. Lafargue, G. Bonamis, C. Hönninger, J. Qiao J. Lopez, and I. Manek-Hönninger, Advances on Percussion Drilling with Femtosecond Laser in GHz-burst Mode, The European Physical Journal Conferences.
8. **P. Balage**, M. Lafargue, T. Guilberteau, G. Bonamis, C. Hönninger, J. Lopez, and I. Manek-Hönninger, Femtosecond percussion drilling of silicon using repetitive single pulses, MHz- & GHz-burst regimes. Micromachines, 2024
9. **P. Balage**, J. Lopez, T. Guilberteau, M. Lafargue, G. Bonamis, C. Hönninger, and I. Manek-Hönninger, Laser drilling of through vias in gap materials using bursts of femtosecond pulses. JLMN-Journal of Laser Micro/Nanoengineering. (Submitted)

Conference Proceedings:

1. I. Manek-Hönninger, S. Niane, G. Bonamis, **P. Balage**, E. Audouard, C. Hönninger, E. Mottay, and J. Lopez, High aspect ratio and high-speed glass drilling with femtosecond GHz-bursts, Conference on Lasers and Electro-Optics (CLEO), 2022.
2. C. Hönninger, **P. Balage**, J. Lopez, G. Bonamis, I. Manek-Hönninger, Long and crack-free holes in glass by top-down drilling with femtosecond laser GHz-bursts, CLEO US 2023
3. I. Manek-Hönninger, **P. Balage**, J. Lopez, G. Bonamis, C. Hönninger, Femtosecond GHz-burst laser processing for percussion drilling applications, PW 2023.
4. I. Manek-Hönninger, **P. Balage**, G. Bonamis, C. Hönninger, J. Lopez, Gap materials drilling with femtosecond laser in GHz-burst mode, CLEO Europe.
5. **P. Balage**, J. Lopez, G. Bonamis, C. Hönninger, I. Manek-Hönninger, Bessel beam dielectric cutting with femtosecond laser in GHz-burst mode, CLEO Europe.

6. I. Manek-Hönninger, **P. Balage**, T. Guilberteau, M. Lafargue, G. Bonamis, M. Delaigue, C. Hönninger, J. Lopez, Ultrafast laser micromachining with GHz-bursts, Laser in Manufacturing
7. I. Gusachenko, **P. Balage**, D. Nuzhdin, M. Ziat, G. Bonamis, A. Douard, G. Pallier, C. Hönninger, J. Lopez, I. Manek-Hönninger, Dielectric materials cutting using Bessel beams with a femtosecond laser configured in MHz and GHz burst regimes, Lasers in Manufacturing.
8. **P. Balage**, J. Lopez, M. Lafargue, T. Guilberteau, G. Bonamis, C. Hönninger, and I. Manek-Hönninger, Ultrafast laser drilling of through vias in Sodalime glass using GHz-burst mode operation, Proceeding SPIE Photonics Europe.

Oral presentations at conferences:

P. Balage, G. Bonamis, M. Delaigue, E. Audouard, J. Lopez, and I. Manek-Hönninger, Drilling speed measurements of femtosecond laser GHz-bursts in glasses and silicon, Procédés Laser pour l'Industrie (PLI), 2022.

P. Balage, J. Lopez, G. Bonamis, C. Hönninger, and I. Manek-Hönninger, Top-down percussion drilling in silicon with GHz-burst mode femtosecond laser, Optique Nice, 2022.

I. Manek-Hönninger, **P. Balage**, G. Bonamis, C. Hönninger, and J. Lopez, High aspect-ratio percussion drilling in glasses with femtosecond laser GHz-bursts, Laser Precision Microfabrication (LPM), (2022), hybrid meeting.

J. Lopez, S. Niane, G. Bonamis, **P. Balage**, and I. Manek-Hönninger, Time-resolved pump-probe shadowgraphy of bottom-up percussion drilling of AF32 thin glasses using single and double femtosecond laser pulses, ICALEO, 2022.

P. Balage, J. Lopez, G. Bonamis, C. Hönninger, I. Manek-Hönninger, Bessel beam dielectric cutting with femtosecond laser in GHz-burst mode, CLEO Europe.

I. Manek-Hönninger, **P. Balage**, G. Bonamis, C. Hönninger, J. Lopez, Gap materials drilling with femtosecond laser in GHz-burst mode, CLEO Europe.

I. Manek-Hönninger, **P. Balage**, T. Guilberteau, M. Lafargue, G. Bonamis, M. Delaigue, C. Hönninger, J. Lopez, Ultrafast laser micromachining with GHz-bursts, Laser in Manufacturing.

I. Manek-Hönninger, **P. Balage**, G. Bonamis, C. Hönninger, J. Lopez, World of Photonics.

I. Gusachenko, **P. Balage**, D. Nuzhdin, M. Ziat, G. Bonamis, G. Pallier, C. Hönninger, J. Lopez, I. Manek-Hönninger, Dielectric materials cutting using Bessel beams with a femtosecond laser configured in MHz and GHz burst regimes, Lasers in Manufacturing.

Co-chair Early Stage Researcher Session EOSAM 2023, Dijon.

P. Balage, T. Guilberteau, M. Lafargue, G. Bonamis, C. Hönninger, J. Qiao, J. Lopez, and I. Manek-Hönninger, Advances on Percussion Drilling with Femtosecond Laser in GHz-burst Mode, EOSAM 2023.

P. Balage, T. Guilberteau, M. Lafargue, G. Bonamis, C. Hönninger, J. Lopez, and I. Manek-Hönninger, GHz-burst Bessel beam dielectric materials cutting, PLI 2023 September 2023.

I. Manek-Hönninger, **P. Balage**, T. Guilberteau, M. Lafargue, G. Bonamis, M. Delaigue, C. Hönninger, J. Lopez, ICALEO 2023.

P. Balage, T. Guilberteau, M. Lafargue, G. Bonamis, C. Hönninger, J. Lopez, and I. Manek-Hönninger, Dielectrics cutting with Bessel beam in femtosecond GHz-burst regime, Photonics West 2024.
→ **Best Student Paper Award**

P. Balage, M. Lafargue, T. Guilberteau, G. Bonamis, C. Hönninger, J. Lopez, and I. Manek-Hönninger, Ultrafast laser drilling of through via in gap materials using burst operation mode, Photonics Europe 2024. → **Best Student Paper Award**

P. Balage, M. Lafargue, T. Guilberteau, G. Bonamis, C. Hönninger, J. Lopez, and I. Manek-Hönninger, Ultrafast laser drilling of through via in gap materials using burst operation mode, LPM 2024.

P. Balage, M. Lafargue, T. Guilberteau, G. Bonamis, C. Hönninger, J. Lopez, and I. Manek-Hönninger, Silicon processing with bursts of femtosecond pulses, Optique Normandie 2024.

Poster presentations:

P. Balage, J. Lopez, G. Bonamis, C. Hönninger, and I. Manek-Hönninger, Percussion drilling in glasses with femtosecond laser in GHz-burst mode, Laserap, 2022.

P. Balage, M. Lafargue, T. Guilberteau, G. Bonamis, C. Hönninger, J. Lopez, and I. Manek-Hönninger, Femtosecond laser processing: a comparison of single pulse, MHz-burst and GHz-burst drilling, Photonics West 2024.

P. Balage, M. Lafargue, T. Guilberteau, G. Bonamis, C. Hönninger, J. Lopez, and I. Manek-Hönninger, Challenges and solutions in femtosecond laser drilling of through vias in Gap materials in burst regime, Optique Normandie 2024.

References

[1] L. A. Hof and J. A. Ziki, "Micro-hole drilling on glass substrates-A review." Micromachines 8, 1–23 (2017).

[2] M. T. Gonheim and M. Hussain, "Highly Manufacturable Deep (Sub-Millimeter) Etching Enabled High Aspect Ratio Complex Geometry Lego-Like Silicon Electronics." Advanced Science News, 13, 1601801 (2017).

[3] D. Homoelle, S. Wielandy, A.L Gaeta, N.F Borrelli, C. Smith, Infrared photosensitivity in silica glasses exposed to femtosecond laser pulses. Opt. Lett., 24, 1311, (1999).

[4] S. Juodkazis, S. Matsuo, H. Misawa, V. Mizeikis, A. Marcinkevicius, H.-B. Sun, Y. Tokuda, M. Takahashi, T. Yoko, J. Nishii, Application of femtosecond laser pulses for microfabrication of transparent media. Appl. Surf. Sci., 197–198, 705–709 (2002).

[5] M.H Hong, B. Luk'yanchuk, S.M. Huang, T.S. Ong, L.H. Van, T.C. Chong, Femtosecond laser application for high capacity optical data storage. Appl. Phys. A Mater. Sci. Process., 79, 791–794 (2004).

[6] E.N. Glezer, M. Milosavljevic, L. Huang, R.J. Finlay, T.-H. Her, J.P. Callan, E. Mazur, Three-dimensional optical storage inside transparent materials: Errata. Opt. Lett., 22, 422 (1997).

[7] A. Marcinkevicius, S. Juodkazis, M. Watanabe, M. Miwa, S. Matsuo, H. Misawa, J. Nishii, Femtosecond laser-assisted three-dimensional microfabrication in silica. Opt. Lett., 26, 277 (2001).

[8] K. Minoshima, A.M. Kowalevicz, I. Hartl, E.P. Ippen, J.G. Fujimoto, J.G. Photonic device fabrication in glass by use of nonlinear materials processing with a femtosecond laser oscillator. Opt. Lett., 26, 1516 (2001).

[9] C.B. Schaffer, A. Brodeur, J.F. García, E. Mazur, Micromachining bulk glass by use of femtosecond laser pulses with nanojoule energy. Opt. Lett., 26, 93 (2001).

[10] K.M. Davis, K. Miura, N. Sugimoto, K. Hirao, Writing waveguides in glass with a femtosecond laser. Opt. Lett., 21, 1729 (1996).

[11] K. Minoshima, A. Kowalevicz, E. Ippen, J. Fujimoto, Fabrication of coupled mode photonic devices in glass by nonlinear femtosecond laser materials processing. Opt. Expr., 10, 645 (2002).

[12] K. Mishchik, K. Gaudfrin, J. Lopez, Drilling of through holes in sapphire using femtosecond laser pulses. J. Laser Micro Nanoeng., 12, 321–324 (2017).

[13] K. Mishchik, R. Beuton, O.D. Caulier, S. Skupin, B. Chimier, G. Duchateau, B. Chassagne, R. Kling, C. Hönninger, E. Mottay, et al. "Improved laser glass cutting by spatio-temporal control of energy deposition using bursts of femtosecond pulses." Opt. Expr., 25, 33271–33282 (2017).

[14] B.N. Chichkov, C. Momma, S. Nolte, F. yon Alvensleben, A. Tünnermann, Femtosecond, picosecond and nanosecond laser ablation of solids. Appl. Phys. A, 63, 109–115 (1996).

[15] K. Sugioka, Y. Cheng, Ultrafast lasers—Reliable tools for advanced materials processing. Light Sci. Appl., 3, e149 (2014).

[16] S. Nisar, L. Li, M.A. Sheikh, Laser glass cutting techniques: A review. J. Laser Appl., 25, 042010 (2013).

[17] R. Meyer, R. Giust, M. Jacquot, J.M. Dudley, F. Courvoisier, Submicron-quality cleaving of glass with elliptical ultrafast Bessel beams. Appl. Phys. Lett., 111, 231108 (2017).

[18] B.N.M. Jenne, D. Flamm, T. Ouaj, J. Hellstern, J. Kleiner, D. Grossmann, M. Koschig, M. Kaiser, M. Kumkar, S. Nolte, High-quality tailored-edge cleaving using aberration-corrected Bessel-like beams. Opt. Lett., 43, 3164–3167 (2018).

[19] M.K. Bhuyan, F. Courvoisier, P.A. Lacourt, M. Jacquot, R. Salut, L. Furfaro, J.M. Dudley, High aspect ratio nanochannel machining using single shot femtosecond Bessel beams. Appl. Phys. Lett., 97, 8 (2010).

[20] J. Del Hoyo, R. Meyer, L. Furfaro, F. Courvoisier, Nanoscale confinement of energy deposition in glass by double ultrafast Bessel pulses. Nanophotonics, 10, 1089–1097 (2021).

[21] S. Mitra, M. Chanal, R. Clady, A. Mouskeftaras, D. Grojo, Millijoule femtosecond micro-Bessel beams for ultra-high aspect ratio machining. Appl. Opt., 54, 7358–7365 (2015).

[22] Y.V. White, X. Li, Z. Sikorski, L.M. Davis, W. Hofmeister, Single-pulse ultrafast-laser machining of high aspect nano-holes at the surface of SiO2. Opt. Expr.,16, 14411–14420 (2008).

[23] C. Kerse, H. Kalaycoglu, P. Elahi, B. Cetin, D. Kesim, O. Akçaalan, S. Yavas, M. Asik, B. Oktem, H. Hoogland, R. Holzwarth, F. O. Ilday, Ablation-cooled material removal with ultrafast bursts of pulses. Nature, 537, 84–88 (2016).

[24] P. Elahi, O. Akçaalan, C. Ertek, K. Eken, F. O. Ilday, H. Kalaycoglu, High-power Yb-doped all-fiber laser delivering 300 fs pulses for high-speed ablation-cooled materiel removal. Opt. Lett., 43, 535–538 (2018).

[25] E. Mazur and R. Gattass, "A round-up of recent papers in the field of photonics published by the physical sciences division of the Nature Publishing Group." Nat. Photonics 2, 251–251, (2008).

[26] J. Zhang, R. Qin, W. Zhu, J. Vorberger, Energy Relaxation and Electron–Phonon Coupling in Laser-Excited Metals. Materials, 15, 1902 (2022).

[27] N. W. Ashcroft, N. D. Mermin, and R. Smoluchowski, "Solid State Physics." Phys. Today 30, 61–65 (1977).

[28] M. Lenzner, J. Krüger, S. Sartania, Z. Cheng, C. Spielmann, G. Mourou, and F. Kautek, "Femtosecond optical breakdown in dielectrics." Phys. Rev. Lett. 80, 4076–4079 (1998).

[29] A. Brodeur and S. L. Chin, "Band-Gap Dependence of the Ultrafast White-Light Continuum." Phys. Rev. Lett. 80, 4406–4409 (1998).

[30] J. Shan, F. Wang, E. Knoesel, M. Bonn, and T. F. Heinz, "Measurement of the FrequencyDependent Conductivity in Sapphire." Phys. Rev. Lett. 90, 247401 (2003).

[31] J. Olivier and R. Poirier, "Electronic structure of Al2O3 from electron energy loss spectroscopy." Surf. Sci. 105, 347–356 (1981).

[32] R. Lindner, M. Reichling, R. T. Williams, and E. Matthias, "Femtosecond laser pulse excitation of electrons and excitons in CaF2 and SrF2." J. Phys. Condens. Matter 13, 2339–2346 (2001).

[33] B. Rethfeld, "Free-electron generation in laser-irradiated dielectrics." Phys. Rev. B 73, 035101 (2006).

[34] S. C. Jones, P. Braunlich, R. T. Casper, X.-A. Shen, and P. Kelly, "Recent Progress On LaserInduced Modifications And Intrinsic Bulk Damage Of Wide-Gap Optical Materials." Opt. Eng. 28, 281039 (1989).

[35] E. E. Serebryannikov and A. M. Zheltikov, "Quantum and Semiclassical Physics behind Ultrafast Optical Nonlinearity in the Midinfrared: The Role of Ionization Dynamics within the Field Half Cycle." Phys. Rev. Lett. 113, 043901 (2014).

[36] M. Gertsvolf, M. Spanner, D. M. Rayner, and P. B. Corkum, "Demonstration of attosecond ionization dynamics inside transparent solids." J. Phys. B At. Mol. Opt. Phys. 43, 131002 (2010).

[37] H. X. Deng, X. Xiang, W. G. Zheng, X. D. Yuan, S. Y. Wu, X. D. Jiang, F. Gao, X. T. Zu, and K. Sun, "Theory of absorption rate of carriers in fused silica under intense laser irradiation." J. Appl. Phys. 108, 103116 (2010).

[38] M. D. Perry, B. C. Stuart, P. S. Banks, M. D. Feit, V. Yanovsky, and A. M. Rubenchik, "Ultrashort-pulse laser machining of dielectric materials." J. Appl. Phys. 85, 6803–6810 (1999).

[39] D. Arnold and E. Cartier, "Theory of laser-induced free-electron heating and impact ionization in wide-band-gap solids." Phys. Rev. B 46, 15102–15115 (1992).

[40] M. Lebugle, N. Sanner, N. Varkentina, M. Sentis, and O. Utéza, "Dynamics of femtosecond laser absorption of fused silica in the ablation regime." J. Appl. Phys. 116, 063105 (2014).

[41] V. S. Popov, “Tunnel and multiphoton ionization of atoms and ions in a strong laser field (Keldysh theory).” Physics-Uspekhi, vol. 47, pp. 855-885 (2004).

[42] E. G. Gamaly, "The physics of ultra-short laser interaction with solids at non-relativistic intensities." Phys. Rep. 508, 91–243 (2011).

[43] D. Arnold, E. Cartier, and D. J. DiMaria, "Theory of high-field electron transport and impact ionization in silicon dioxide." Phys. Rev. B 49, 10278–10297 (1994).

[44] P. Balling and J. Schou, "Femtosecond-laser ablation dynamics of dielectrics: basics and applications for thin films." Reports Prog. Phys. 76, 036502 (2013).

[45] P. Martin, S. Guizard, P. Daguzan, G. Petite, P. D’Oliveira, P. Meynadier, and M. Perdrix, "Subpicosecond study of carrier trapping dynamics in wide-band-gap crystals." Phys. Rev. B - 215 Condens. Matter Mater. Phys. 55, 5799–5810 (1997).

[46] D. Grojo, M. Gertsvolf, S. Lei, T. Barillot, D. M. Rayner, and P. B. Corkum, "Exciton-seeded multiphoton ionization in bulk SiO2." Phys. Rev. B 81, 212301 (2010).

[47] B. Rethfeld, "Unified Model for the Free-Electron Avalanche in Laser-Irradiated Dielectrics." Phys. Rev. Lett. 92, 187401 (2004).

[48] M. Shimizu, M. Sakakura, M. Ohnishi, Y. Shimotsuma, T. Nakaya, K. Miura, and K. Hirao, “Mechanism of heat-modification inside a glass after irradiation with high-repetition rate femtosecond laser pulses”, J. App. Phys, 108, 7 (2010).

[49] M. Shimizu, M. Sakakura, S. Kanehira, M. Nishi, Y. Shimotsuma, K. Hirao and K. Miura, “Formation mechanism of element distribution in glass under femtosecond laser irradiation”, Opt. Lett., Vol. 36, No. 11 (2011).

[50] I. M. Burakov, N. M. Bulgakova, R. Stoian, A. Mermillod-Blondin, E. Audouard, A. Rosenfeld, A. Husakou, and I. V. Hertel, “Spatial distribution of refractive index variations induced in bulk fused silica by single ultrashort and short laser pulses.” Journal of Applied Physics, 101, 043506 (2007).

[51] I. Miyamoto, A. Horn, J. Gottmann, “Local Melting of Glass Material and Its Application to Direct Fusion Welding by Ps-laser Pulses”, JLMN-Journal of Laser Micro/Nanoengineering, Vol. 2, No. 1, (2007).

[52] I. Miyamoto, K. Cvecek, Y. Okamoto, M. Schmidt, “Internal modification of glass by ultrashort laser pulse and its application to microwelding”, Appl. Phys. A, 114, 187–208 (2014).

[53] Cyril Mauclair. Spatio-temporal ultrafast laser tailoring for bulk functionalization of transparent materials. Other [cond-mat.other]. Université Jean Monnet - Saint-Etienne, 2010.

[54] E. G. Gamaly, A. V. Rode, B. Luther-Davies, and V. T. Tikhonchuk, "Ablation of solids by femtosecond lasers: Ablation mechanism and ablation thresholds for metals and dielectrics." Phys. Plasmas 9, 949 (2002).

[55] S. S. Mao, F. Quéré, S. Guizard, X. Mao, R. E. Russo, G. Petite, and P. Martin, "Dynamics of femtosecond laser interactions with dielectrics." Appl. Phys. A Mater. Sci. Process. 79, 1695– 1709 (2004)

[56] R. Stoian, D. Ashkenasi, A. Rosenfeld, and E. E. B. Campbell, "Coulomb explosion in ultrashort pulsed laser ablation of Al2O3." Phys. Rev. B 62, 13167–13173 (2000).

[57] R. Stoian, A. Rosenfeld, D. Ashkenasi, I. V. Hertel, N. M. Bulgakova, and E. E. B. Campbell, "Surface Charging and Impulsive Ion Ejection during Ultrashort Pulsed Laser Ablation." Phys. Rev. Lett. 88, 097603 (2002).

[58] J. P. Colombier, P. Combis, R. Stoian, and E. Audouard, “High shock release in ultrafast laser irradiated metals: Scenario for material ejection.” Phys. Rev. B, vol. 75, p. 104105 (2007).

[59] S. Y. Kruchinin, F. Krausz, and V. S. Yakovlev, “Colloquium: Strong- field phenomena in periodic systems.” Reviews of Modern Physics, vol. 90, p. 021002 (2018).

[60] G. Bonamis, “Conception et réalisation d’une source laser femtoseconde GHz et applications au régime d’ablation très haute cadence.” Physique [physics]. Université de Bordeaux, 2020. Français.

[61] Y. Kuroiwa, N. Takeshima, Y. Narita, S. Tanaka, and K. Hirao, “Arbitrary micropatterning method in femtosecond laser microprocessing using diffractive optical elements,” Opt. Express 12, 1908–1915 (2004).

[62] Z. Kuang, W. Perrie, J. Leach, M. Sharp, S. P. Edwardson, M. Padgett, G. Dearden, and K. G. Watkins, “High throughput diffractive multi-beam femtosecond laser processing using a spatial light modulator,” Appl. Surf. Sci. 255, 2284–2289 (2008).

[63] A. Jesacher and M. J. Booth, “Parallel direct laser writing in three dimensions with spatially dependent aberration correction,” Opt. Express 18, 21090–21099 (2010).

[64] S. Hasegawa, H. Ito, H. Toyoda, and Y. Hayasaki, “Massively parallel femtosecond laser processing,” Opt. Express 24, 18513–18524 (2016).

[65] B. Neuenschwander, B. Jaeggi, M. Zimmermannn, V. Markovic, B. Resan, K. Weingarten, R. de Loor, and L. Penning, “Laser surface structuring with 100 W of average power and sub-ps pulses”, J. Laser Appl., 28, 022506 (2016).

[66] A. M. Streltsov, & N.F. Borrelli, N. F. “Fabrication and analysis of a directional coupler written in glass by nanojoule femtosecond laser pulses”. Opt. Lett. 26, 42–43 (2001).

[67] T. Tamaki, W. Watanabe, J. Nishii, K. Itoh, “Welding of Transparent Materials Using Femtosecond Laser Pulses.” Jpn. J. Appl. Phys. 44, L687 (2005).

[68] W. Watanabe, S. Onda, T. Tamaki, K. Itoh, J. Nishii, “Space-selective laser joining of dissimilar transparent materials using femtosecond laser pulses.” Appl. Phys. Lett. 89, 021106 (2006).

[69] W. Kautek, J. Krüger, M. Lenzner, S. Sartania, C. Spielmann, F. Krausz, “Laser ablation of dielectrics with pulse durations between 20 fs and 3 ps.” Appl. Phys. Lett. 69, 3146–3148 (1996).

[70] E. G. Gamaly, A. V. Rode, B. Luther-Davies, V. T. Tikhonchuk, “Ablation of solids by femtosecond lasers: Ablation mechanism and ablation thresholds for metals and dielectrics.” Phys. Plasmas 9, 949–957 (2002).

[71] J. Gottmann, M. Hörstmann-Jungemann, M. Hermans, Dennis Beckmann, “High Speed and High Precision Fs-laser Writing Using a Scanner with Large Numerical Aperture.” J. Laser Micro Nanoeng Vol.

[72] F. Courvoisier, P.-A. Lacourt, M. Jacquot, M. K. Bhuyan, L. Furfaro, and J. M. Dudley,”Surface nanoprocessing with nondiffracting femtosecond Bessel beams”.Opt. Lett. Vol. 34, No. 3, (2009).

[73] Y. Li, K. Itoh, W. Watanabe, K. Yamada, D. Kuroda, J. Nishii, Y. Jiang, “Three-dimensional hole drilling of silica glass from the rear surface with femtosecond laser pulses.” Opt. Lett., Vol. 26, No. 23 (2001).

[74] D. Grossmann, M. Reininghaus, C. Kalupka, M. Jenne, M. Kumkar, “In-situ microscopy of front and rear side ablation processes in alkali aluminosilicate glass using ultra short pulsed laser radiation.” Opt. Expr, Vol. 25, No. 23 (2017).

[75] R.M Herman, T.A Wiggins, “Production and uses of diffractionless beams.” J. Opt. Soc. Am. A, 8, 932–942 (1991).

[76] H.Shin, D. Kim, “Strength of ultra-thin glass cut by internal scribing using a femtosecond Bessel beam”. Opt. Las. Tech. 2020, 129, 106307 (2020).

[77] J. Dudutis, P. Gečys, G. Račiukaitis, “Non-ideal axicon-generated Bessel beam application for intra-volume glass modification.” Opt. Expr., 24, 28433–28443 (2016).

[78] F. Courvoisier, J. Zhang, M. Bhuyan, M. Jacquot, J.M. Dudley, “Applications of femtosecond Bessel beams to laser ablation.” App. Phys. A, 112, 29–34 (2013).

[79] Y. Yu, L. Jiang, Q. Cao, B. Xia, Q. Wang, Y. Lu, “Pump-probe imaging of the fs-ps-ns dynamics during femtosecond laser Bessel beam drilling in PMMA.” Opt. Expr., 23, 32728–32735 (2015).

[80] I.H Chowdhury, X. Xu, A.M. Weiner, “Ultrafast double-pulse ablation of fused silica.” Appl. Phys. Lett. 86, 151110 (2005).

[81] K. Gaudfrin, G. Duchateau, K. Mishchik, R. Kling, J. Lopez, “Fused silica ablation by double femtosecond laser pulses with variable delays.”, Proc. SPIE 10905, LAMOM XXIV, 10905H (2019).

[82] A. Semerok, C. Dutouquet, “Ultrashort double pulse laser ablation of metals.” Thin Solid Films, 453, 501–505 (2004).

[83] T. Donnelly, J.G. Lunney, S. Amoruso, R. Bruzzese, X. Wang, X. Ni, “Double pulse ultrafast laser ablation of nickel in vacuum.” J. Appl. Phys., 106, 013304 (2009).

[84] A.Y. Vorobyev, C. Guo,”Direct observation of enhanced residual thermal energy coupling to solids in femtosecond laser ablation.” Appl. Phys. Lett., 86, 011916 (2005).

[85] D. Scuderi, O. Albert, D. Moreau, P.P. Pronko, J. Etchepare, “Interaction of a laser-produced plume with a second time delayed femtosecond pulse.” Appl. Phys. Lett., 86, 071502 (2005).

[86] R. Le Harzic, D. Breitling, S. Sommer, C. Föhl, K. König, F. Dausinger, E. Audouard, “Processing of metals by double pulses with short laser pulses.” Appl. Phys. A, 81, 1121–1125 (2005).

[87] S. Noel, J. Hermann, “Reducing nanoparticles in metal ablation plumes produced by two delayed short laser pulses.” Appl. Phys. Lett., 94, 53120 (2009).

[88] Z. Lin, L. Ji, M. Hong, “Enhancement of femtosecond laser-induced surface ablation via temporal overlapping double-pulse irradiation.” Photon Res., 8, 271 (2020).

[89] D.J. Förster, S. Faas, R. Weber, T. Graf,” Thrust enhancement and propellant conservation for laser propulsion using ultra-short double pulses.” Appl. Surf. Sci., 510, 145391 (2020).

[90] M.E. Povarnitsyn, T.E. Itina, K.V. Khishchenko, P.R. Levashov, “Suppression of Ablation in Femtosecond Double-Pulse Experiements.” Phys. Rev. Lett., 103, 195002 (2009).

[91] M.E. Povarnitsyn, V.B. Fokin, P.R. Levashov, T.E. Itina, “Molecular dynamics simulation of subpicosecond double-pulse laser ablation of metals.” Phys. Rev. B, 92, 174104 (2015).

[92] W. Hu, Y.C. Shin, G. King, “Modeling of multi-burst mode pico-second laser ablation for improved material removal rate.” Appl. Phys. A, 98, 407–415 (2009).

[93] C.-W. Cheng, J.-K. Chen, “Drilling of Copper Using a Dual-Pulse Femtosecond Laser.” Technologies, 4, 7 (2016).

[94] G.D. Förster, L.J. Lewis, “Numerical study of double-pulse laser ablation of Al.” Phys. Rev. B, 97, 224301 (2018).

[95] J. Roth, A. Krauß, J. Lotze, H.-R. Trebin, “Simulation of laser ablation in aluminum: The effectivity of double pulses.” Appl. Phys. A, 117, 2207–2216 (2014).

[96] D.J. Förster, B. Jäggi, A. Michalowski, B. Neuenschwander, “Review on Experimental and Theoretical Investigations of Ultra-Short Pulsed Laser Ablation of Metals with Burst Pulses.” Materials, 14, 3331 (2021).

[97] K. Gaudfrin, J. Lopez, L. Gemini, M. Delaigue, R. Kling, G. Duchateau, “Fused silica ablation by double ultrashort laser pulses with dual wavelength and variable delays.” Opt. Expr., Vol. 30, No. 22 (2022).

[98] J. König, S. Nolte, A. Tünnerman, “Plasma evolution during metal ablation with ultrashort laser pulses”, Opt. Expr., Vol. 13, No. 26, 10597-10607 (2005).

[99] B. Bornschlegel, J. Finger, “In-Situ Analysis of Ultrashort Pulsed Laser Ablation with Pulse Bursts.” J. Laser Micro Nanoeng., 14, No. 1, 88-94 (2019).

[100] A. Žemaitis, M. Gaidys, P. Gečys, M. Barkauskas, M. Gedvilas, “Femtosecond laser ablation by bibursts in the MHz and GHz pulse repetition rates.” Opt. Expr., Vol. 29, No. 5, 7641-7653 (2021).

[101] T. Kramer, Y. Zhang, S. Remund, B. Jaeggi, A. Michalowski, L. Grad, B. Neuenschwander, “Increasing the Specific Removal Rate for Ultra Short Pulsed Laser-Micromachining by Using Pulse Bursts.” J. Laser Micro Nanoeng., 12, No. 2, 107-114 (2019).

[102] D. Metzner, P. Lickschat, and S. Weißmantel, “Optimization of the ablation process using ultrashort pulsed laser radiation in different burst modes.” J. Laser Appl. 33, 012057 (2021).

[103] B. Neuenschwander, T. Kramer, B. Lauer, B. Jaeggi, “Burst mode with ps- and fs-pulses: Influence on the removal rate, surface quality and heat accumulation.” Proc. SPIE 9350, LAMOM XX, 93500U (2015).

[104] T. Kramer, Y. Zhang, S. Remund, B. Jaeggi, A. Michalowski, L. Grad, B. Neuenschwander, “Increasing the Specific Removal Rate for Ultra Short Pulsed Laser-Micromachining by Using Pulse Bursts.” J. Laser Micro Nanoeng, 12, 107–114 (2017).

[105] K. Mishchik, G. Bonamis, J. Qiao, J. Lopez, E. Audouard, E. Mottay, C. Hönninger, I. Manek-Hönninger, “High-efficiency femtosecond ablation of silicon with GHz repetition rate laser source.” Opt. Lett. Vol. 44, 9, 2193-2196 (2019).

[106] G. Bonamis, E. Audouard, C. Hönninger, J. Lopez, K. Mishchik, E. Mottay, I. Manek-Hönninger, “Systematic study of laser ablation with GHz bursts of femtosecond pulses.” Opt. Expr., Vol. 28, No. 19, 27702-27714 (2020).

[107] P. P. Pronko, S. K. Dutta, D. Du, R. K. Singh, “Thermophysical effects in laser processing of materials with picosecond and femtosecond pulses”, J. Appl. Phys., 78, 6233-6240 (1995).

[108] H. Pantsar, T. Lauterborn, A. Knorz, H. Herfurth, S. Heinemann, “High rate laser drilling and texturing of silicon”, 28th International Congress on Applications of Lasers & Electro–Optics (ICALEO), (2008).

[109] H. Matsumoto, Z. Lin, J. N. Schrauben, J. Kleiner, “Ultrafast laser ablation of silicon with ∼GHz bursts”, J. Laser Appl. 33, 032010 (2021).

[110] G. Bonamis, K. Mishchick, E. Audouard, C. Hönninger, E. Mottay, J. Lopez, and I. Manek-Hönninger, “High efficiency femtosecond laser ablation with gigahertz level bursts.” J. Laser Appl. 31, 022205 (2019).

[111] T. Hirsiger, M. Gafner, S. Remund, M.V. Chaja, A. Urniezius, S. Butkus, B. Neuenschwander, “Machining metals and silicon with GHz bursts: Surprising tremendous reduction of the specific removal rate for surface texturing applications.” Proc. SPIE 11267, LAMOM XXV, 112670T (2020).

[112] S. Remund, M. Gafner, M.V. Chaja, A. Urniezius, S. Butkus, B. Neuenschwander, “Milling applications with GHz burst: Investigations concerning the removal rate and machining quality.” Procedia CIRP 94 850–855 (2020).

[113] S. Bruening, K. Du, A. Gillner, “Micro processing with ultrafast bursts of pulses.” Procedia CIRP 94, 856–862 (2020).

[114] S. Butkus, V. Jukna, D. Paipulas, M. Barkauskas and V. Sirutkaitis, “Micromachining of Invar Foils with GHz, MHz and kHz Femtosecond Burst Modes.” Micromachines, 11, 733 (2020).

[115] O.Balachninaitė, Viktorija Tamulienė, Laurynas Eičas, Virgilijus Vaičaitis, “Laser micromachining of steel and copper using femtosecond laser pulses in GHz burst mode.” Results in Physics, Vol. 22, 103487 (2021).

[116] J. Schille, U. Loeschner, R. Ebert, P. Scully, N. Goddard, H. Exner, “Laser micro processing using a high repetition rate femtosecond laser.” 29th International Congress on Applications of Lasers & Electro–Optics (ICALEO), (2010).

[117] M. Domke, V. Matylitsky, S. Stroj, “Surface ablation efficiency and quality of fs lasers in single-pulse mode, fs lasers in burst mode, and ns lasers.” Appl. Surf. Sci., Vol. 505, 144594 (2020).

[118] P. R. Herman, A. Oettl, K.P. Chen, and R. S. Marjoribanks, “Laser micromachining of 'transparent' fused silica with 1-ps pulses and pulse trains.”, Proc. SPIE 3616, Commercial and Biomedical Applications of Ultrafast Lasers, (1999).

[119] S. Hendow, H. Takahashi, M. Yamaguchi, J. Xu, “Enhanced ablation using GHz-pulsed fsec laser.” Proc. SPIE 11268, Laser based Micro- and Nanoprocessing XIV, 1126809 (2020).

[120] C. W. Carr, H. B. Radousky, A. M. Rubenchik, M. D. Feit and S. G. Demos, Localized dynamics during laser-induced damage in optical materials, Phys. Rev. Lett., 92, 087401 (2004).

[121] B. Neuenschwander, B. Jaeggi, D.J. Förster, T. Kramer, and S. Remund, “Influence of the burst mode onto the specific removal rate for metals and semiconductors.” J. Laser Appl., 31, 022203 (2019).

[122] S. Schwarz, S. Rung, C. Esen, R. Hellmann, “Enhanced ablation efficiency using GHz bursts in micromachining fused silica.” Opt. Lett., Vol. 46, No. 2 (2021).

[123] K. Sugioka, “Will GHz burst mode create a new path to femtosecond laser processing?” Int. J. Extreme Manuf., 3, 043001 (2021).

[124] J. Lopez, S. Niane, G. Bonamis, P. Balage, E. Audouard, C. Hönninger, E. Mottay and I. Manek-Hönninger, Percussion drilling in glasses and process dynamics with femtosecond laser GHz-bursts, Opt. Express, 30, 12533–44 (2022).

[125] J. Lopez, S. Niane, G. Bonamis, P. Balage, and I. Manek-Hönninger, “In-Situ Monitoring of Bottom-Up Percussion Drilling of Alkali-Free Alumina-Borosilicate Thin Glasses Using Single and Double Femtosecond Laser Pulses”, JLMN-Journal of Laser Micro/Nanoengineering, Vol. 17, No. 1, (2022).

[126] K. Yamamoto, N. Hasaka, H. Morita and E. Ohmura, Influence of thermal expansion coefficient in laser scribing of glass, Precis. Eng. 34 70–75 (2010).

[127] P. Balage, J. Lopez, G. Bonamis, C. Hönninger, I. Manek-Hönninger, Crack-free high-aspect ratio holes in glasses by top– down percussion drilling with infrared femtosecond laser GHz-bursts. Int. J. Extrem. Manuf., 5, 015002 (2023).

[128] O. D. Caulier, K. Mishchik, B. Chimier, S. Skupin, A. Bourgeade, C. Javaux Léger, R. Kling, C. Hönninger, J. Lopez, V. Tikhonchuk, G. Duchateau, Femtosecond laser pulse train interaction with dielectric materials, Appl. Phys. Lett., 107, 181110 (2015).

[129] K. Obata, K. Sugioka, K. Toyoda, and K. Midorikawa, Enhance refractive index modification of fused silica by multiwavelength excitation process using F2 and KrF excimer lasers, RIKEN Rev., 50, 42–46 (2003).

[130] D. Nieto, J. Arines, G. M. O'Connor, M. T. Flores-Arias, Single-pulse laser ablation threshold of borosilicate, fused silica, sapphire, and soda-lime glass for pulse widths of 500 fs, 10 ps, 20 ns, Appl. Opt., 54, 8596–601 (2015).

[131] D. V. Podlesnik, H. H. Gilgen and R. M. Jr. Osgood, Waveguiding effects in laser-induced aqueous etching of semiconductors, Appl. Phys. Lett., 48, 496–8 (1986).

[132] V. N. Tokarev, J. Lopez, S. Lazare and F. Weisbuch, High-aspect-ratio microdrilling of polymers with UV laser ablation: experiment with analytical model, Appl. Phys. A, 76, 385–96 (2003).

[133] S. Lazar, J. Lopez and F. Weisbuch, High-aspect-ratio microdrilling in polymeric materials with intense KrF laser radiation, Appl. Phys. A 69 S1–S6 (1999).

[134] F. Fraggelakis, G. Mincuzzi, J. Lopez, I. Manek-Hönninger, and R. Kling, Texturing metal surface with MHz ultra-short laser pulses, Opt. Express, 25, 18131–9 (2017).

[135] G. D. Tsibidis, M. Barberoglou, P.A. Loukakos, E. Stratakis, and C. Fotakis, Dynamics of ripple formation on silicon surfaces by ultrashort laser pulses in subablation conditions, Phys. Rev. B, 86, 115316 (2012).

[136] P. Balage, G. Bonamis, M. Lafargue, T. Guilberteau, M. Delaigue, C. Hönninger, J. Qiao, J. Lopez, I. Manek-Hönninger, Advances in Femtosecond Laser GHz-Burst Drilling of Glasses: Influence of Burst Shape and Duration., Micromachines, 14, 1158 (2023).

[137] D. Metzner, P Lickschat, C. Kreisel, T. Lampke, S. Weißmantel, Study on laser ablation of glass using MHz-to-GHz burst pulses, Appl. Phys. A, 128, 637 (2022).

[138] P. Balage, M. Lafargue, T. Guilberteau, G. Bonamis, C. Hönninger, J. Lopez, I. Manek-Hönninger, Comparative Study of Percussion Drilling in Glasses with a Femtosecond Laser in Single Pulse, MHz-Burst, and GHz-Burst Regimes and Optimization of the Hole Aspect Ratio, Micromachines, 14, 1754 (2023).

[139] D. Esser, S. Rezaei, J. Li, P. R. Hermann, J. Gottmann, Time dynamics of burst-train filamentation assisted femtosecond laser machining in glasses, Opt. Expr., 19, 25 (2011).

[140] P. Balage, J. Lopez, T. Guilberteau, M. Lafargue, G. Bonamis, C. Hönninger, I. Manek-Hönninger, Through glass via drilling using GHz-bursts of femtosecond pulses: challenges and implementation, Journal of laser Micro/Nanoengineering, submitted (2024).

[141] P. Balage, J. Lopez, T. Guilberteau, M. Lafargue, G. Bonamis, C. Hönninger, I. Manek-Hönninger, Femtosecond Laser Percussion Drilling of Silicon Using Repetitive Single Pulse, MHz-, and GHz-Burst Regimes, Micromachines, 15, 632 (2024).

[142] F. He, J. Yu, Y. Tan, W. Chu, C. Zhou, Y. Cheng & K. Sugioka, Tailoring femtosecond 1.5-μm bessel beams for manufacturing high-aspect-ratio through silicon vias. Scientific Reports, 7, 40785 (2017).

[143] J. C. Diels, W. Rudolph, Ultrashort Laser Pulse Phenomena, Academic Press, San Diego, CA 2006, Ch. 7.

[144] H. H. Li, "Refractive Index of Silicon and Germanium and Its Wavelength and Temperature Derivatives", J. Phys. Chem. Ref. Data 9, 561–658 (1980).

[145] H. R. Shanks, P. D. Maycock, P. H. Sidles, G. C, Danielson, "Thermal Conductivity of Silicon from 300 to 1400°K", Phys. Rev., Vol. 30, No. 5, 1743-1748 (1963).

[146] E. V. Zavedeev, V. V. Kononenko, V. M. Gololobov, V. I. Konov," Modeling the effect of fs light delocalization in Si bulk", Laser Phys. Lett., 11, 036002 (2014).

[147] M. Chambonneau, D. Grojo, O. Tokel, F. Ö. Ilday, S.s Tzortzakis, and S. Nolte, "In-Volume Laser Direct Writing of Silicon—Challenges and Opportunitie"s, Laser Photonics Rev., 2100140 (2021).

[148] R. M. Herman, T. A. Wiggins, Production and uses of diffractionless beams., J. Opt. Soc. Am. A, 8, 932–942 (1991).

[149] M. Jenne, D. Flamm, T. Ouaj, J. Hellstern, J. Kleiner, D. Grossmann, M. Koschig, M. Kaiser, M. Kumkar, S. Nolte, High-quality tailored-edge cleaving using aberration-corrected Bessel-like beams. Opt. Lett., 43, 3164–3167 (2018).

[150] H. D. Nguyen, E. Moreno, A. Rudenko, N. Faure, X. Sedao, C. Mauclair, J.-P. Colombier, R. Stoian, Super-efficient drilling of metals with ultrafast non-diffractive laser beams. Sci. Rep., 12, 2074 (2022).

[151] P. Balage, T. Guilberteau, M. Lafargue, G. Bonamis, C. Hönninger, J. Lopez, I. Manek-Hönninger, Bessel Beam Dielectrics Cutting with Femtosecond Laser in GHz-Burst Mode., Micromachines, 14, 1650 (2023).

[152] Y. Matsuoka, Y. Kizuka, T. Inoue, The characteristics of laser micro drilling using a Bessel beam. Appl. Phys. A, 84, 423–430 (2006).

[153] J. Lopez, K. Mishchik, B. Chassagne, C. Javaux-Leger, C. Hönninger, E. Mottay, R. Kling, Glass cutting using ultrashort pulsed Bessel beam. In Proceedings of the ICALEO, Atlanta, GA, USA, 18–22 October 2015; p. M404.

[154] K. Mishchik, B. Chassagne, C. Javaux-Léger, C. Hönninger, E. Mottay, R. Kling, J. Lopez, Dash line glass- and sapphire-cutting with high power USP laser. Proc. SPIE 2016, 9740, 97400W-1.

[155] J. Durnin, J. J. Jr. Miceli, Diffraction-Free Beams. Phys. Rev. Lett., 58, 1499–1501 (1987).

[156] L. Rapp, R. Meyer, L. Furfaro, C. Billet, R. Giust, F. Courvoisier, High speed cleaving of crystals with ultrafast Bessel beams. Opt. Expr., 25, 9312–9317 (2017).

[157] S. Burghartz, B. Schulz, Thermophysical properties of sapphire, AlN and MgAl,O, down to 70 K. J. Nucl. Mater., 212–215, 1065–1068 (1994).

[158] L. Gaverina, J.C. Batsale, A. Sommier, C. Pradere, Pulsed flying spot with the logarithmic parabolas method for estimation in-plane thermal diffusivity fields on heterogenous and anisotropic materials. J. Appl. Phys., 121, 115105 (2017).

Etude de l'interaction des matériaux à gap avec des lasers femtosecondes en mode rafales GHz.

Résumé : Ces deux dernières décennies, la technologie laser femtoseconde a gagné en maturité et fiabilité. Cette évolution lui a permis d'être mise en œuvre dans de nombreux secteurs industriels pour des applications de micro-usinage de précision pour lesquelles la brièveté de l'impulsion constitue un atout incontestable. Cependant, la pénétration de cette technologie dans l'industrie est freinée par le manque de productivité de ces procédés. En effet, cette productivité est bien en-deçà des attentes industrielles. Plusieurs stratégies sont à l'étude pour lever ce verrou technologique et optimiser la productivité des procédés de transformation de la matière par lasers femtosecondes. L'une de ces stratégies consiste à optimiser le dépôt d'énergie en utilisant des rafales d'impulsions femtosecondes de faible intensité plutôt que des impulsions uniques de haute intensité.

De récents travaux ont montré que l'utilisation du régime rafales GHz permettait d'obtenir des efficacités bien supérieures à celle obtenues en régime mono-impulsion classique. Cependant, ces premiers résultats ont été rapidement contestés par d'autres études attestant une efficacité plus faible ainsi que la présence de défauts d'usinage en régime rafale GHz. Afin de dégager un consensus concernant ce nouveau régime d'interaction et d'apporter des données objectives à l'état de l'art, il était nécessaire de mener des études expérimentales approfondies. Pour ce faire, nous avons mené en étroite collaboration avec la société Amplitude des travaux de recherche sur les procédés, tels que le perçage ou la découpe par faisceau de Bessel, en utilisant un laser femtoseconde de puissance moyenne 100 W délivrant des rafales GHz. Cette étude nous a permis d'étudier l'influence des paramètres liés aux rafales et de mener des études comparatives avec les régimes existant (mono-impulsion et rafales MHz). Nous avons également pu mettre en place une expérience pompe-sonde inédite qui nous a permis de révéler le mécanisme d'interaction laser-matière en rafales GHz. Les excellents résultats obtenus dans le cadre de ce travail de thèse démontrent la capacité unique des rafales GHz à usiner des matériaux comme les diélectriques et les semi-conducteurs.

Mots-clés : Interaction laser-matière, Procédés laser, Rafales GHz, Diélectriques, Semi-conducteurs.

Gap materials interaction with femtosecond lasers in GHz-burst mode

Abstract: Over the past two decades, femtosecond laser technology has become significantly more reliable which has particularly enabled its integration into industry, as the brevity of such pulses allows for high-precision micromachining. However, the adoption of this technology in the industry remains hindered by a lack of productivity. Indeed, the production rate remains well below the ever-evolving industry targets. To address this limitation, several methods are being studied to increase the throughput by optimizing femtosecond laser processes. One approach relies on optimizing the energy deposition by using bursts of low-intensity femtosecond pulses rather than single high-intensity pulses.

Recent studies have shown that using GHz-bursts can achieve ablation efficiencies far superior to those obtained with more conventional methods. However, these initial results have been quickly challenged by other studies reporting lower efficiency and the presence of machining defects. To reach a consensus on this new regime, comprehensive experimental studies are needed to add data to the current state of the art. To this end, process studies such as microdrilling experiments and cutting with a Bessel beam have been implemented using a 100 W Amplitude laser delivering GHz-bursts. Close collaboration with the company Amplitude has allowed for investigating numerous burst parameters and conducting comparative studies with existing regimes (single-pulse and MHz-bursts). Moreover, a pump-probe experiment has been set up revealing the laser-matter interaction mechanism in GHz-burst mode. Throughout this thesis work, excellent results have been obtained, demonstrating the unique capability of GHz-bursts for microprocessing materials like dielectrics and semiconductors.

Keywords: Light-matter interaction, Laser processing, GHz-bursts, Dielectrics, Semi-conductors.

CEntre Lasers Intenses et Applications
UMR 5107, Université de Bordeaux, France